Investigation of enzymes from the respiratory chain by using electrochemical and spectroscopic techniques

Sinan Sabuncu

UNIVERSITÉ DE STRASBOURG

ÉCOLE DOCTORALE DES SCIENCES CHIMIQUES

UMR 7140, Chimie de la matière complexe

LABORATOIRE DE BIOÉLECTROCHIMIE ET SPECTROSCOPIE

THÈSE présentée par :

Sinan Sabuncu

Soutenue le : **9 Mai 2017**

pour obtenir le grade de : **Docteur de l'université de Strasbourg**

Discipline/ Spécialité : Chimie

Investigation of enzymes from the respiratory chain by using electrochemical and spectroscopic techniques

THÈSE dirigée par :

Prof. Petra Hellwig Professeur, Université de Strasbourg

RAPPORTEURS :

Prof. Thorsten Friedrich Professeur, University of Freiburg

Dr. Mathieu Etienne Chargé de recherches, Université de Lorraine

---

AUTRES MEMBRES DU JURY :

Dr. Pierre-Antoine Bonnefont Maitre de conférences, Université de Strasbourg

Acknowledgement

First of all I would like to thank to my supervisor Prof. Petra Hellwig who gave me the opportunity to be a part of her research group and supported me during my studies. I am also grateful to Dr. Frédéric Melin for his guidance, support and patience during these four years. This is a huge achievement in my life and it would not be possible without you. I would like to thank to Prof. Robert Gennis and Dr. Sylvia Choi for providing me the protein samples and information that allowed me to work on bo_3 oxidase. I would like to thank to Prof. Pia Adelroth and Dr. Josy Ter Beek for providing the cNOR samples. I am grateful to the University of Strasbourg, the CNRS and the FRC for the financial support and providing me all opportunities to finish my thesis.

I would like to show my gratitude to all my lab members. It was a pleasure to be in this group with such nice people. Thank you for everything Anton, Natalia, Zahia, Filipa, Mireille, Alicia, Batoul, Maddy, Thomas and all the interns in our lab. You teach me how to be a part of a group and always helped me with all the problems that I faced. To be a part of this group provided me massive scientific knowledge and besides that teach me the life itself.

Finally, I dedicate this thesis to my parents Emel, Ahmet Tarik, Ahmet Can, Sophia and Irina. Thank you very much for all your support and endless love. Without you I could only come to Strasbourg for vacation. Dear Irina, thank you for understanding and helping me during the hard times and always believing in me.

Sinan Sabuncu

March
2017

List of Abrevations

ADP	Adenosine diphsophate
ATP	Adenosine triphosphate
ATR	Attenuated total reflection
cNOR	Cytochrome c dependent nitric oxide reducatase
CE	Counter electrode
CV	Cyclic voltammetry
DNA	Deoxyribonucleic acid
DTSP	Dithioscuccinimide
DDM	n-dodecyl-ß-D-maltoside
E. coli	*Escherichia coli*
FTIR	Fourier transform infrared spectroscopy
Tris	Tris(hydroxymethyl)aminomethane
MUA	Mercaptoundecanoic acid
mV	Millivolt
nm	Nanometer
NP	Nanoparticle
NAD	Nicotinamide adenine dinucleotide
Ox-red	Oxidized minuse reduced
KPi	Potassium phosphate
P. denitrificans	*Paracoccus denitrificans*
RE	Reference electrode
SEIRAS	Surface-enhanced infrared absorption spectroscopy
Q	Quinone

UV/Vis	Ultraviolet/visible
WT	Wild-type
WE	Working electrode

The twenty amino acids

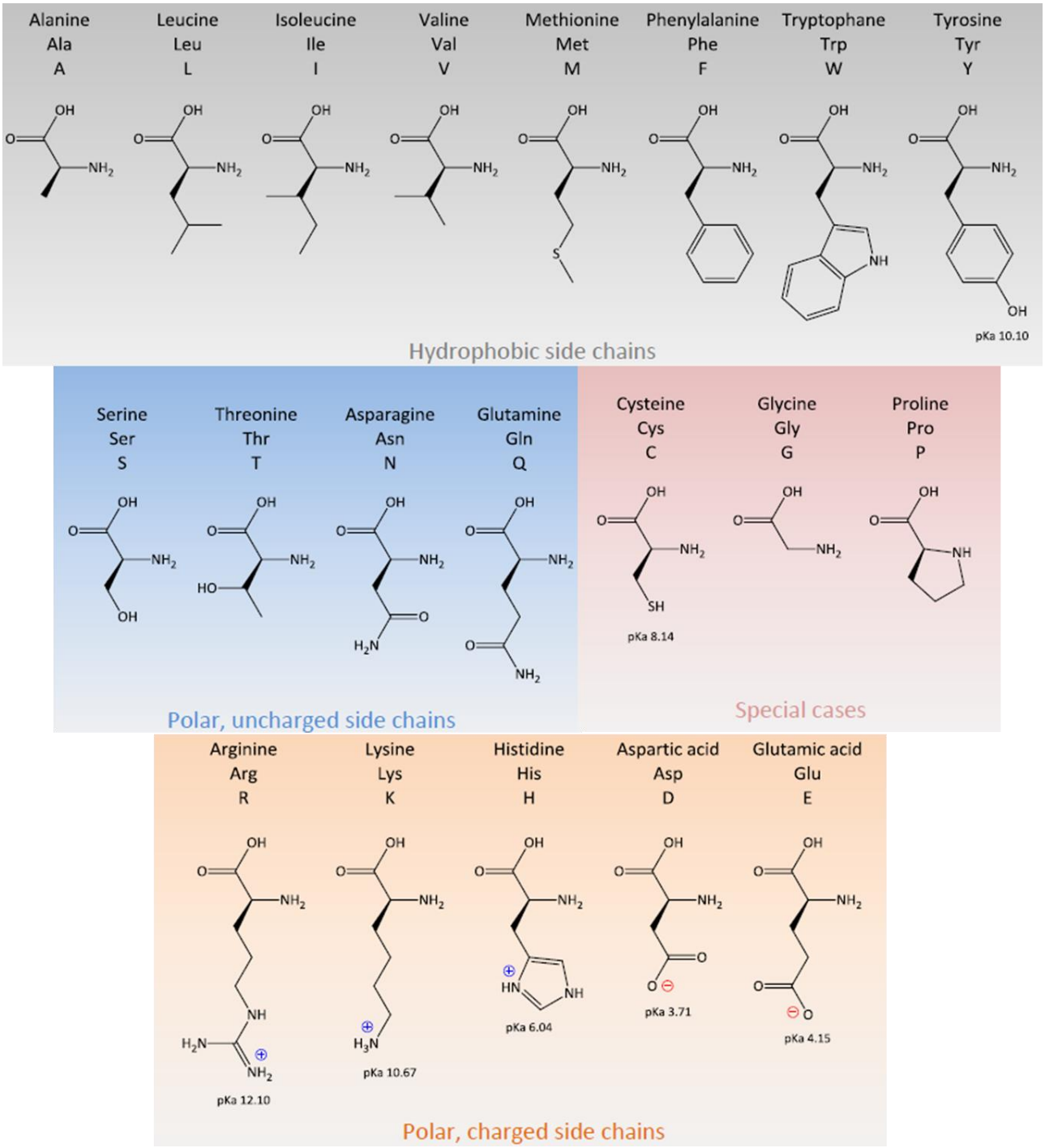

Table of contents

CHAPTER 1 Introduction

CHAPTER 2 Experimental Techniques

CHAPTER 3 Materials and Methods

CHAPTER 4 Results and Discussion

List of Figures

CHAPTER 1 Introduction

CHAPTER 2 Experimental Techniques

CHAPTER 3 Materials and Methods

CHAPTER 4 Results and Discussion

List of Tables

Rèsumè

L'objectif principal de cette thèse est de comprendre la structure et les différents mécanismes de protéines hémiques de la chaîne respiratoire. Afin d'atteindre cet objectif, nous avons combiné la spectroscopie vibrationnelle et l'électrochimie. Cette thèse est composée de deux parties principales : la première, est axée sur l'interaction de la protéine cytochrome bo_3 oxydase avec la quinone. La deuxième partie est focalisée sur la caractérisation de la cytochrome c réductase issue de l'organisme *Paracoccus denitrificans* via des techniques spectroscopiques (infrarouge différentielle, dosage électrochimique par spectroscopie UV/ Visible) ainsi que par électrochimie.

Concernant la première partie, nous nous sommes intéressés à la cytochrome bo_3 oxydase qui est une protéine membranaire de la chaîne respiratoire, et est également membre de la famille des oxydases hème-cuivre. Le rôle de cette protéine redox est de fonctionner comme une pompe à protons et de réduire l'oxygène libre en eau. La translocation de protons à travers la membrane produit une différence de potentiel qui est ensuite utilisée pour produire de l'ATP dans la cellule. La cytochrome bo_3 oxydase contient un hème *b*, un hème o_3 et un atome de cuivre Cu_B comme le montre la figure 1A. Cette protéine utilise un ubiquinol-8 en tant que donneur d'électrons au sein de la membrane qui se lie à l'enzyme et produit des électrons qui seront utilisés pour la réduction de l'oxygène. A l'heure actuelle, le nombre de site de liaison pour la quinone ainsi que sa position au sein de l'enzyme demeure un important sujet de débat.

Il est connu que plusieurs cofacteurs tels que les hèmes, la quinone et le Cu_B à l'intérieur de la cytochrome bo_3 oxydase sont en relation les uns avec les autres. Cependant, une étude poussée est nécessaire pour comprendre la relation entre ces cofacteurs. Ainsi, nous avons commencé à étudier l'interaction de la cytochrome bo_3 oxydase avec la quinone en réalisant un dosage électrochimique par spectroscopie UV/ Visible et par voltampérométrie cyclique.

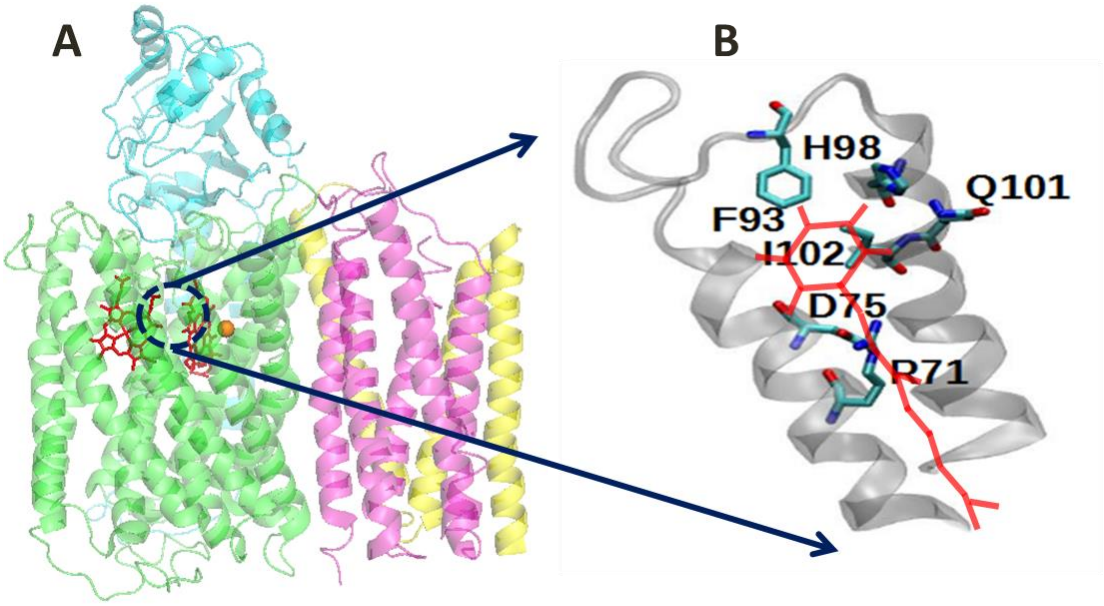

Figure 1. A) Structure cristallographique de la cytochrome bo_3 oxydase issu de l'*E. coli* **B)** Proposition du site de liaison da la quinone.

Le tableau 1 ci-dessous représente le potentiel de demi-vague des cofacteurs obtenus à partir du dosage électrochimique. Dans la bande de Soret, nous avons observé quatre contributions qui sont liées à la transition redox de l'interaction des hèmes. Nous avons également observé un déplacement dans les potentiels de demi-vague lors de la comparaison des échantillons avec et sans quinone. Afin de vérifier si le déplacement dans le potentiel de demi-vague des échantillons sans quinone est réversible, nous avons introduit la Q_2 manuellement. Nous avons observé qu'après l'insertion de la Q_2 les potentiels de demi-vague sont retournés à des valeurs négatives.

Table 1. Les potentiels redox obtenus en présence et absence de quinone comparés aux valeurs de la littérature [7]

WT *bo*$_3$ oxidase mV	Quinone extracted *bo*$_3$ oxidase mV	Q_2 + *bo*$_3$ oxidase mV	Menadione + *bo*$_3$ oxidase mV
- 249 +/-10	-	- 254 +/-10	- 254 +/-10
- 147 +/-10	+ 48 +/-10	- 140 +/-10	- 176 +/-10
- 49 +/-10	+ 158 +/-10	- 65 +/-10	-

Nous avons poursuivi notre étude en se focalisant sur les acides aminés qui sont susceptibles d'être situés au niveau du site de liaison de la quinone (figure 1B). Cette région a été proposée par le groupe de R. Gennis comme unique et présente une haute affinité pour le site de liaison de la quinone.

Différentes mutations de la cytochrome *bo*$_3$ oxydase telles que : D75N, H98F, I102N, Q101N, Q101M, Q101L, Q101T, Q101A, R71H, F93A and F93Y ont été caractérisées par spectroscopie infrarouge différentielle induite par électrochimie et par voltampérométrie cyclique. Les spectres différentiels obtenus nous donnent une idée générale sur la structure de la protéine (données non présentées). Des changements conformationnels qui se produisent au niveau de la bande amide I ont été observés.

Les activités catalytiques de tous les mutants ont été mesurées à partir du cyclovoltammogramme de la cytochrome *bo*$_3$ oxydase forme sauvage « Wild Ype (WT) ». Lors de la comparaison du potentiel de réduction et la courbe de réduction du *bo*$_3$ WT, nous avons observé un changement clair dans l'activité catalytique et dans les potentiels de réduction des échantillons. Le tableau 2 résume les modifications des activités catalytiques de tous les échantillons mesurés. Nous avons observé que les mutations des acides aminés F93, D75, H98, I102, R71 entrainent la perte totale de l'activité catalytique et qu'elles sont cruciales pour la liaison avec la quinone. Les mutations au niveau des acides aminés Q101M

and Q101A ont montré une activité électrochimique. Cependant, leur potentiel catalytique a été déplacé vers des valeurs négatives.

Table 2. Résumé des modifications électrochimiques dans la bo_3 WT et les différents mutants étudiés.

Sample	Catalytic potential (V)	Electrochemical reaction with O_2	k_{cat} (s^{-1})	Sigmoidal catalytic curve	Enzymatic activity *
Wild type	- 0.35	100%	14.8	Yes	100%
Q101N	-	1%		No	10%
Q101M	- 0.48	80%	11.8	Yes	50%
Q101T	- 0.40	50%	7.7	Yes	30%
Q101A	- 0.45	80%	12.9	Yes	30%
Q101L	-	1%		No	10%
F93A	-	1%		No	40%
F93Y	- 0.40	60%	10.2	Yes	80%
D75N#	-	0%		No	0%
H98F	-	10%		No	1%
I102N	-	10%		No	0%
R71H	-	10%		No	0%

#sans Quinone

La deuxième partie est focalisée sur la caractérisation de la cytochrome c réductase (cNOR) issue de l'organisme *Paracoccus. Denitrificans*. cNOR est une enzyme liée à la membrane et qui est responsable de la réduction de deux électrons de l'oxyde nitrique (NO) en oxyde nitreux (N_2O) selon l'équation suivante :

$$2NO + 2H^+ + 2e^- \rightarrow N_20 + H_2O \qquad \textbf{Equation 1}$$

La figure 2 montre la structure cristallographique de la cytochrome c réductase cNOR. Cette protéine est composée de deux sous-unités NorB et NorC. La sous-unité NorC contient un

hème *c* bas spin et la sous- unité NorB contient deux hèmes *b* (un hème *b* de bas spin et un hème b_3 de haut spin) et un atome de fer non hémique (Fe_B). A partir de la structure cristallographique, il a été montré que le cation Ca^{2+} est localisé entre l'hème *b* et l'hème b_3 avec des ligands Tyr-73, Gly-71 and Glu-135 (*P. aeruginosa* numbering). Le cation Ca^{2+} lie les propionates de l'hème *b* et l'hème b_3 afin de stabiliser les deux hèmes. Il est prévu qu'un donneur de protons doit être dans cette région. La cNOR est liée à la superfamille des oxydases hème-cuivre qui sont des protéines membranaires. La différence principale de la protéine cNOR avec les autres membres de la famille des oxydases est qu'elle ne pompe pas de protons, ce qui entraine la production d'aucun gradient électrochimique.

Tout d'abord, notre objectif était de comparer la cNOR à l'intérieur des liposomes et la cNOR dans le n-dodécyl-β-D-maltoside (DDM) via le dosage électrochimique par spectroscopie UV/ Visible et par la spectroscopie infrarouge différentielle induite par électrochimie dans le but de comparer les deux environnements. Il a été prédit que les liposomes pourraient fournir des environnements plus naturels à l'échantillon. Ainsi, nous pouvons obtenir un système plus stable et efficace.

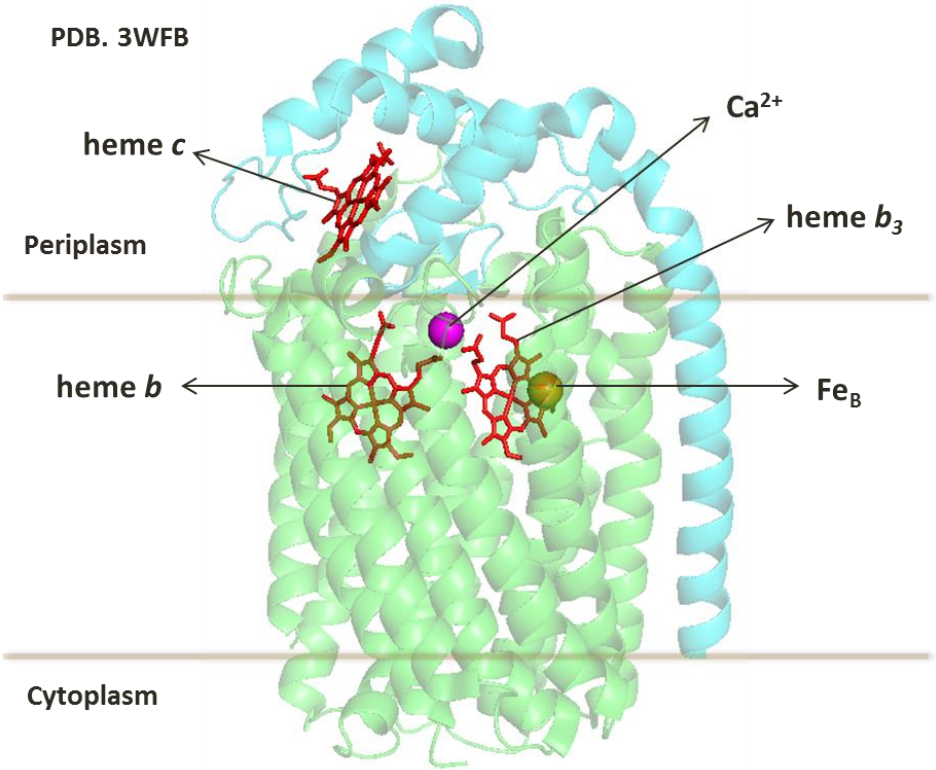

Figure 2. Structure cristallographique de la cytochrome c réductase cNOR from P. aeruginosa

La figure 3 illustre la comparaison entre les spectres différentiels (oxydé moins réduit) de la cytochrome c réductase cNOR avec les liposomes et la cytochrome c réductase cNOR en présence du DDM à pH 7.5. Lors de l'addition des lipides, nous avons observé deux bandes intenses situées à 1743 et 1709 cm^{-1} qui sont attribuées aux vibrations d'élongation ν (C=O) des lipides. De même dans la région comprise entre 1600 et 1400 cm^{-1}, nous avons noté la présence de deux bandes intenses à 1551 et 1402 cm^{-1} correspondant aux vibrations des lipides. Les lipides seuls ne présentent pas des spectres différentiels car ils ne subissent pas de changements structuraux au cours de la réaction d'oxydoréduction. Ainsi, les attributions de ces lipides sont en relation avec les changements d'orientation de ces derniers au cours de la réaction d'oxydoréduction des cNOR. Nous concluons donc que malgré la contribution importante de ces lipides dans les spectres différentiels, la cNOR est stable dans les liposomes.

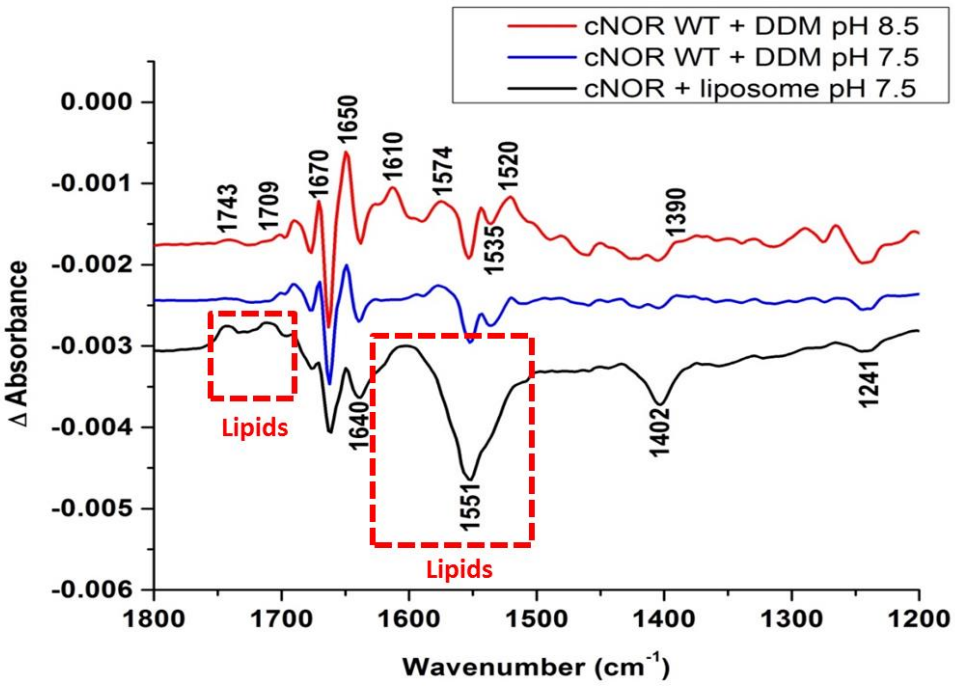

Figure 3. Spectres différentiels (forme oxydée-forme réduite de la cNOR avec DDM à pH 8.5, 7.5 et la cNOR avec liposomes dans le tampon Tris à pH 7.5.

Nous avons poursuivi notre étude en effectuant des dosages électrochimique par spectroscopie UV/ Visible de la cNOR en présence des liposomes et la cNOR avec du DDM. Les résultats obtenus sont représentés dans le tableau 3.

Table 3. Valeurs des potentiels redox obtenus pour la cNOR avec DDM et cNOR avec liposomes à pH 7.5

	cNOR +Liposome pH 7.5		cNOR+ DDM pH 7.5		cNOR+ DDM pH 8.5	
mV	Alpha band (551 nm)	Alpha band (558 nm)	Alpha band (551 nm)	Alpha band (558 nm)	Alpha band (551 nm)	Alpha band (558 nm)
heme *c*	103	85	97	101	92	98
heme *b*		167		178		172

- +/- 20 mV erreur

Nous avons également étudié la cNOR en se focalisant sur la translocation de la voie protonique dans la protéine. Afin de comprendre les donneurs de protons possibles, nous nous sommes focalisés sur la région d'intérêt contenant le cation Ca^{2+} pontant les propionates de l'hème b_3. Pour atteindre notre objectif, la forme sauvage WT de la cNOR ainsi que les mutants E122A, Y74F et Y74S ont été caractérisés dans le but d'étudier l'effet de ces mutants sur l'activité et la structure générale de la protéine.

La figure 4 représente les spectres différentiels de la protéine cNOR WT et des différents mutants. La comparaison du spectre différentiel de la cNOR WT avec les spectres des différents mutants a montré principalement des changements conformationnels qui ont eu lieu au niveau de la région amide I et amide II. Le mutant E122A était supposé induire des changements dans les vibrations d'élongation ν (C=O) de l'acide aspartique situées à 1741 et 1725 cm^{-1} qui peuvent être liés à l'absence du ligand Ca^{2+} (E122A).

Nous avons observé un déplacement de 3 cm^{-1} vers les hauts nombres d'onde, des modes de vibrations (CC) et (CH) de la tyrosine situés à 1522 cm^{-1} ainsi que des modes de vibrations (C-C) de la Tyr-OH situés à 1240 cm^{-1} pour le mutant Y74S et les modes (C-C) pour le

mutant Y74F. Comme la Tyrosine-74 à un rôle actif dans la conformation de l'hème *b* et b_3, il a été prévu de voir un changement structural en raison de la perte de cet acide aminé.

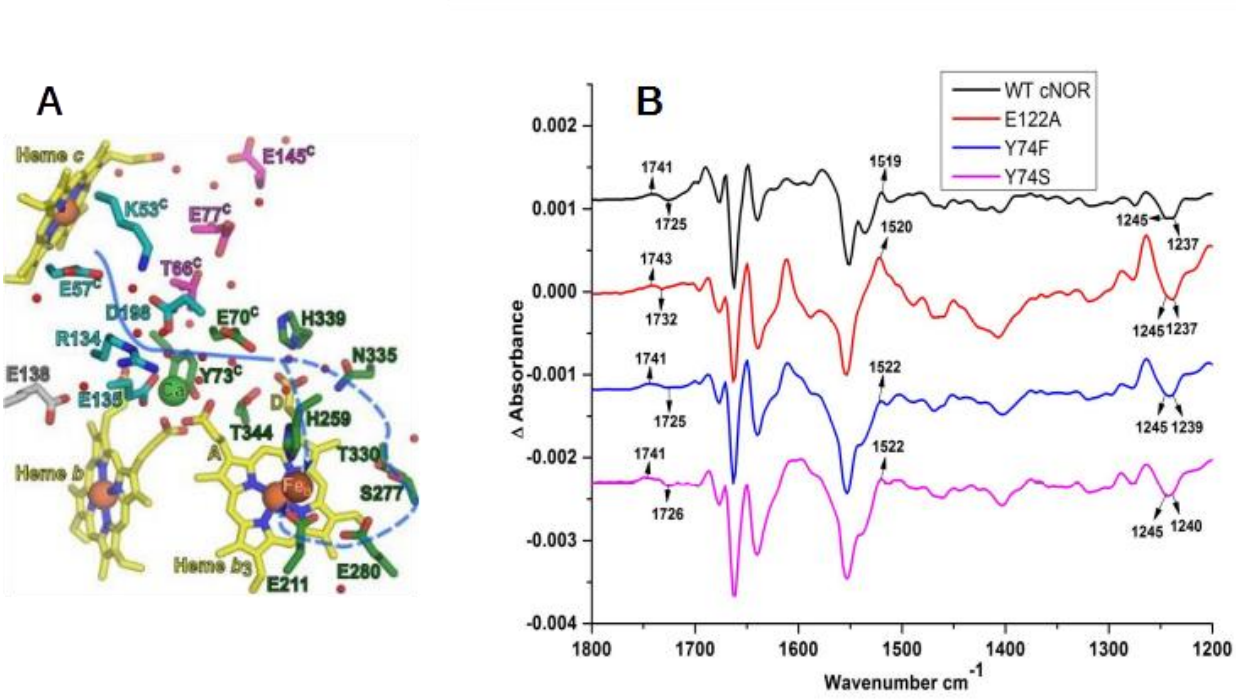

Figure 4. A) Proposition du chemin de proton et les résidus des acides aminés **B)** Spectres différentiels (forme oxydée- forme réduite) de la protéine cNOR WT et les différents mutants E122A, Y74F, Y74S.

Des dosages électrochimiques par spectroscopie UV/ Visible ont été réalisés sur ces différents mutants afin de voir l'effet de ces mutations sur les potentiels redox de l'hème. A partir du tableau 4, nous pouvons observer un déplacement dans les potentiels de demi-vague de ces hèmes. Le potentiel de demi-vague de l'hème *c* a été mesuré à partir de la bande située à 550 nm, l'hème b_3 à partir de la bande de Soret et l'hème *b* à partir de la bande à 560 nm. Ainsi, nous pouvons conclure que les potentiels de demi-vague de ces différents hèmes ont montré des déplacements pour tous les mutants étudiés. Nous avons réussi a observé une contribution claire de l'hème b_3 à partir de la bande de Soret avec un potentiel de demi-vague extrêmement négatif. Des mutations au niveau de la coordination du Ca^{2+} ont changé les propriétés électrochimiques plus précisément de l'hème *b* et l'hème b_3, ce qui montre l'importance du site Ca^{2+} dans la stabilité des transferts d'électrons entre les hèmes.

Table 4. Résumé des potentiels redox obtenus pour la cNOR WT et les différents mutants E122A, Y74F etY74S à pH 7.5 comparés avec les valeurs de la littérature

mV	WT cNOR Literature [1]	WT cNOR	E122A	Y74F	Y74S
Heme b_3	-177 (CTS band)	-271	-290	-295	-300
Heme *c*	+103	+97	+91	+50	+100
Heme *b*	+137	+163	+5	+40	+114

+/- 20 mV erreur

En conclusion, nous avons donc appliqué avec succès les techniques électrochimiques et spectroscopiques sur les protéines cytochrome c réductase (cNOR) et cytochrome bo_3 oxydase. La combinaison de l'électrochimie avec la spectroscopie infrarouge différentielle induite par électrochimie et le dosage électrochimique par spectroscopie UV/ Visible nous ont permis d'obtenir des informations combinées sur les propriétés structurales et électrochimiques de ces différentes protéines. Les mutations de divers acides aminés nous ont également permis de discuter la fonction et la structure de domaines cruciaux au sein de la protéine. Les résultats obtenus sont donc prometteurs dans l'investigation des protéines membranaires car ils pourront nous aider à comprendre de nombreux problèmes dans ce domaine.

1. INTRODUCTION

1.1 Energy Production in Cell

The cell is the building brick of all living organisms. They can be classified as prokaryotes (bacteria and archea) and eukaryotes (animals, plants, fungi, protozoa and chromista). The main differences in their cellular structure of eukaryotes and prokaryotes are the presence of membrane-bound organelles (nucleus, mitochondria and chloroplast), the cell wall and the structure of their DNA (Figure 1.1).

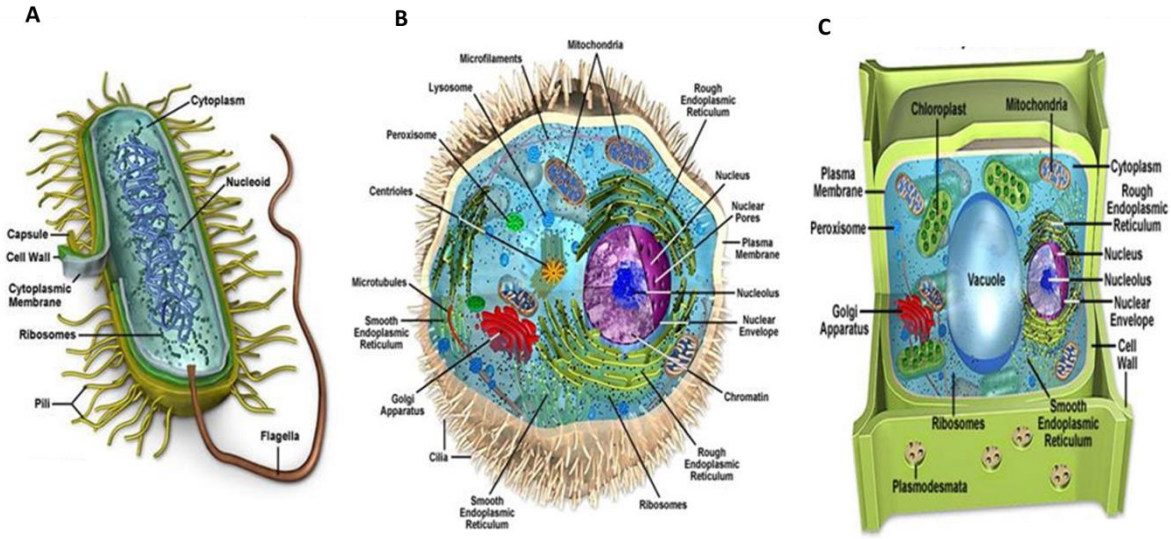

Figure 1.1 Representation of A) Bacterial B) Animal and C) Plant cell [1]

The cells perform various functions such as moving, growing or reproduction and most of these functions require energy. In order to obtain energy cells release the stored energy in molecules by using oxidation reactions such as respiration or light-dependent stage of photosynthesis [2- 4]. The released energy is stored in the form of Adenosine triphosphate (ATP) or nicotinamide adenine dinucleotide (NADH) [5- 7].

Photosynthesis is performed by plants and some bacteria, protozoa and archea. In photosynthesis the electrons obtained from O_2 production out of water (H_2O) are transported via the electron-transport chain [8]. During that process ATP and reduced Nicotinamide

Adenine Dinucleotide Phosphate (NADPH) are produced. ATP and NADPH are further used in the photosynthetic carbon-reduction cycle (Calvin cycle) [9]. In the Calvin cycle CO_2 is consumed to produce triose-phosphates (C_3 compounds).

Cellular respiration can be explained as follows. During glycolysis [10-12], glucose is converted into two molecules of pyruvic acid. During this process adenosine diphosphate (ADP) [13], nicotinamide adenine dinucleotide (NAD^+) [14, 15] and P_i are used to generate ATP and NADH by substrate level phosphorylation. The link reaction between the glycolysis and Krebs cycle [16] is the oxidative decarboxylation of pyruvate. At this step pyruvate is oxidized into acetyl-CoA [17] and CO_2 by the pyruvate dehydrogenase complex (PDC) [18]. PDC contains several copies of the three enzymes (pyruvate dehydrogenase [19], dihydrolipoyl transacetylase [20] and dihydrolipoyl dehydrogenase [19]) located in the mitochondria of the eukaryotic cells and in the cytosol of prokaryotic cells. Generated acetyl-CoA gets oxidized while NAD^+ is reduced into NADH during the Krebs cycle. NADH is then further metabolized into ATP by the electron transport chain (detailed information section 1.2) during oxidative phosphorylation. The eukaryotes Krebs cycle and the oxidative phosphorylation occur in the mitochondrial matrix and at the inner membrane of the mitochondria. A proton gradient is formed between out and inner sides of the inner membrane which is used by ATP Synthase enzyme (complex V) [21-24] to produce ATP from ADP by means of phosphorylation. Electrons that are used in this process are finally transported to exogenous oxygen (terminal electron acceptor) and (together with two protons) water is generated by complex IV. In aerobic prokaryotes (some respiring bacteria) these processes occur in the cytoplasmic membrane.

1.2 Respiratory Chain

The general concept of the respiratory chain, the main pathway for the transfer of electrons or protons from metabolites to oxygen, has been established as a result of several studies in the early twentieth century until the 1960s. There was a couple of milestones in this period of time such as the proposition of the proton-motive force theory by Mitchell in 1961 [25, 26] and purification of four respiratory complexes from mitochondria by Hatefi and coworkers in 1960s [26-31]. The chemiosmotic theory of Mitchell suggested that a proton-motive force,

which is generated through the translocation of the protons through ion pumps in the respiratory complexes, is further used by ATP synthase to drive the ATP production. In time it was understood that although the cells can produce sodium (Na^+), potassium (K^+) or calcium (Ca^{2+}) gradients, the role of the proton gradient was the most crucial amongst. The proton gradient has an important role for several functions in bacteria and archea such as photosynthesis, bacterial motility (flagellar motor) and homeostasis. Hatefi and coworkers purified the natural segments of the respiratory chain [26-31] and it helped understanding the reconstitution of the electron pathway together with coenzyme Q and cytochrome *c*. From the 90s to the present date most of the respiratory complexes were crystallized and their structures were determined.

Before introducing the respiratory complexes it is crucial to introduce the structure and the function of essential redox centers and electron carrying molecules since they are the main elements of electron transfer chain.

Cytochromes:

Cytochromes are iron-porphyrin containing, electron transferring proteins [32]. They are generally found in the aerobic cells and usually located in the inner mitochondrial membrane and for the prokaryotes in the cellular membrane. They are responsible for the transfer of electrons originating from the dehydrogenases in the respiratory complexes to the molecular oxygen. Cytochromes undergo Fe(II)-Fe(III) transition during the reduction/oxidation process. Cytochromes are classified by their energy absorption band such as cytochrome *c* (550 nm) and cytochrome *a* (605 nm). From the inner membrane of mitochondria and the cytoplasmic membrane of prokaryotes, 5 different types of cytochromes have been classified so far: cytochromes *b*, *c*, *d*, *a* and *o* [33-36].

The porphyrin ring is present in all cytochromes. Porphyrins can be classified depending on their side-chain substituent such as mesoporphyrins, uroporphyrins and protoporphyrins. The most common type of porphyrin is the protoporphyrins which contain four methyl groups, two vinyl groups and two propionic acid groups (Figure 1.2 A).

Protoporphyrins can form complexes with metal ions such as iron, magnesium, copper. The complex between protoporphyrins and Fe(II) is called heme (protoheme) and the same

complex with Fe(III) is called hemin (Figure 1.2 B). Four ligands of the heme form a planar structure with the iron center. The fifth and sixth ligands are perpendicular to the plane of the porphyrin ring. Myoglobins and hemoglobins are the most well-known hemeproteins and they contain an imidazole group (from histidine) in the fifth position while the sixth group can be either unoccupied or occupied by ligands such as O_2, CO. Most of the other hemeproteins contain R groups of aminoacids in the fifth and sixth position which prevents binding of the ligands such as O_2. Due to that myoglobins and hemoglobins acts as oxygen carriers and cytochromes as electron carriers [37, 38].

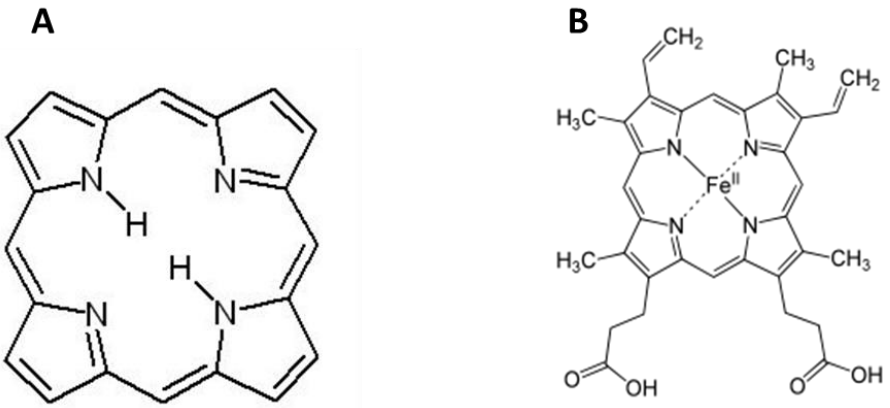

Figure 1.2 Structures of A) porphin (the simplest porphyrin) and B) protoheme (heme) [32]

The reduced or ferrous forms of cytochromes have three characteristic absorption bands in the UV/Vis range called α, β and Soret (γ) bands. These characteristic bands are used to distinguish the different types of cytochromes. *C* type cytochromes have a maximum between 550-558 nm, *b* and *o* types have a maximum between 555-565 nm, *a* type cytochromes have a maximum at 600 nm and *d* type cytochromes have a maximum at 630 nm [39]. In Figure 1.3 the structure of the different hemes are shown.

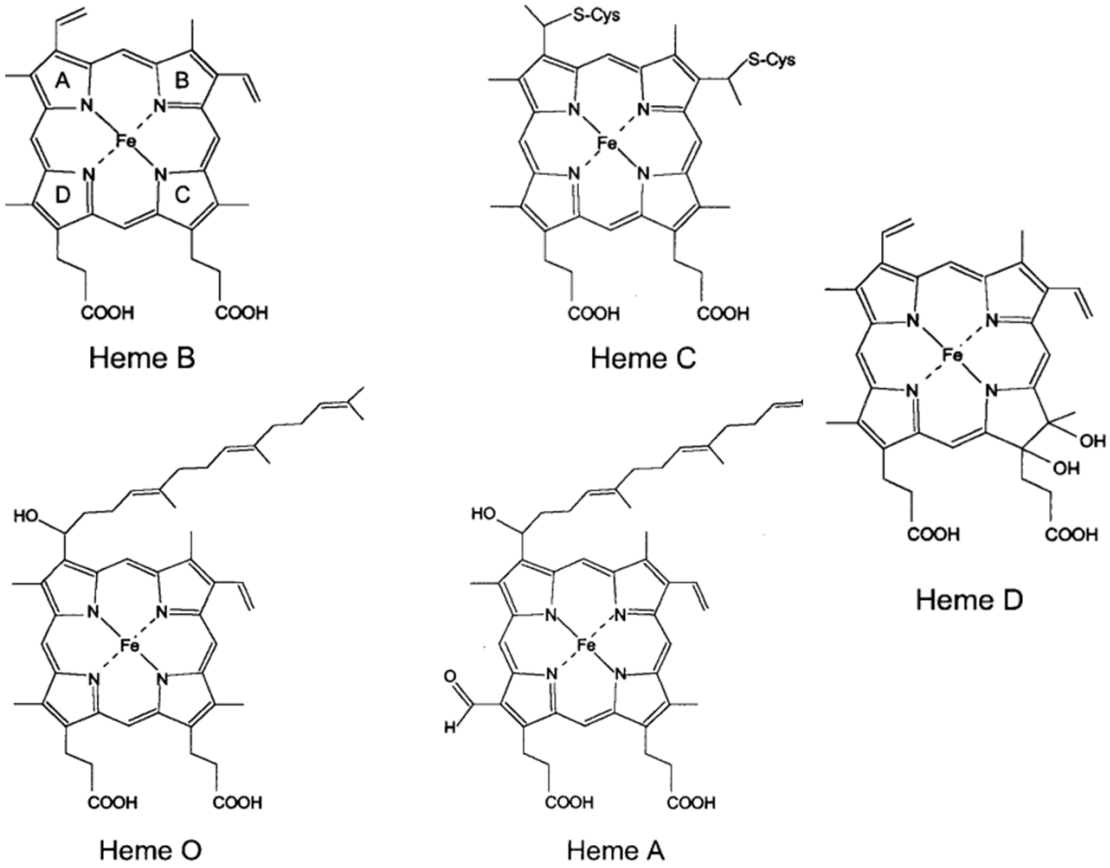

Figure 1.3 Structure of heme cofactors of cytochromes [39]

Ubiquinone (Coenzyme Q):

Ubiquinones are lipid-soluble electron transferring molecules. They are responsible for the transport of electrons between respiratory complexes, similar to the water-soluble cytochrome *c* molecules [40, 41]. Ubiquinones are coenzymes of respiratory complexes. They are composed of a quinone head group and a hydrophobic isoprenyl tail (Figure 1.4).

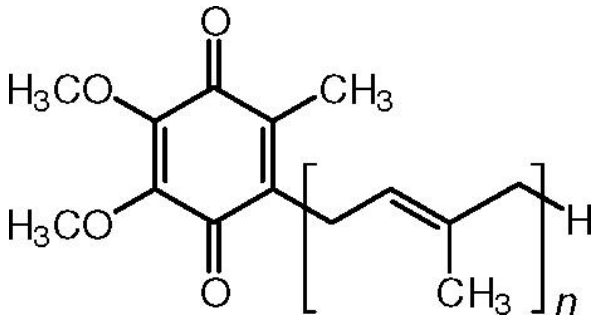

Figure 1.4 Structure of ubiquinone

Due to their hydrophobic nature they can move easily in the inner part of mitochondrial membrane (cell membrane in prokaryotes) by diffusion. There are several ubiquinones that were identified with respect to their length of the isoprenyl side chain. In microorganism ubiquinone-6 (6 isoprenyl units) [42] and in mitochondria ubiquinone-10 (10 isoprenyl units) [43] are commonly found. In particular, *E. coli* contains dominantly Q_8 and rarely Q_1, Q_7 and Q_9.

Ubiquinone has a characteristic absorption band at around 270 nm in the oxidized form [44]. When ubiquinone is reduced into quinol this band disappears.

a. Complex I (NADH:ubiquinone oxidoreductase):

In the respiratory chain electrons are transferred from NADH to O_2 through a chain of three protein complexes [45-48]. Electrons are carried from NADH-Q oxidoreductase [49-51] to another complex (III) which is Q-cytochrome *c* oxidoreductase by using coenzyme Q (Ubiquinone). The oxidation of NADH is coupled to the reduction of ubiquinone in the membrane part of the enzyme. During this process a free energy is generated and it is further used to pump four H^+ across the membrane to produce a proton gradient force.

NADH ubiquinone oxidoreductase (Complex I) catalyzes the following reaction [49];

$$\boldsymbol{NADH + ubiquinone + 5H_N^+ \leftrightarrows NAD^+ + ubiquinol + 4H_P^+}$$

where *N* and *P* represent the negative inner and positive outer membrane. This enzyme is the largest and most complex amongst the other respiratory chain proteins. The mitochondrial enzyme comprises several cofactors and up to 45 different subunits. In prokaryotes that contain complex I, this enzyme is constituted of 14 core subunits. Due to its complexity NADH ubiquinone oxidoreductase has remained the least understood member of the respiratory chain. It contains one flavin mononucleotide (FMN), several iron-sulfur clusters (Fe-S) (≈ 9) and a bound ubiquinone in its structure (Figure 1.5).

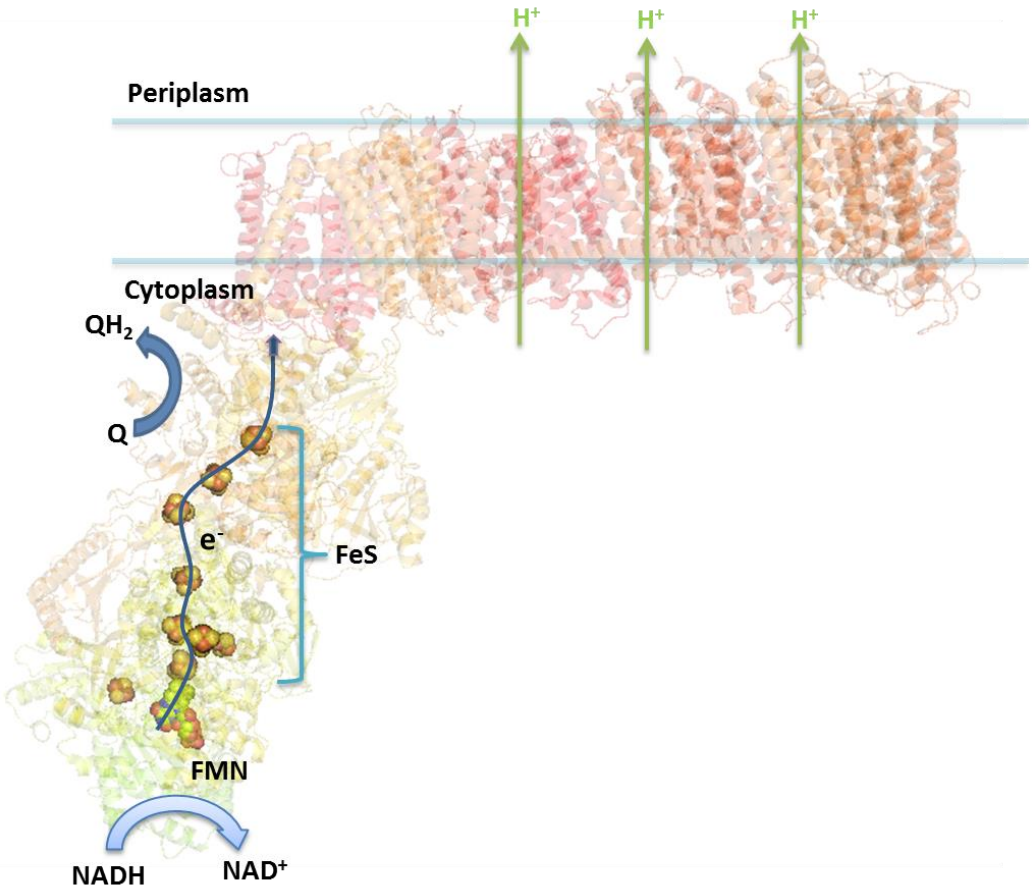

Figure 1.5 Structure of NADH ubiquinone oxidoreductase from *T. thermophilus.* The electron transfer and the proton pumping was illustrated (Complex I). (PDB. 4HEA)

Recent studies indicate that NADH ubiquinone oxidoreductase can produce superoxide and hydrogen peroxide through, at least, two pathways [52]. Excess amount of superoxide contribute to the cellular stress and it is linked to several neuromuscular diseases [53, 54]. Approximately 5% of the electrons flowing during the reverse and forward electron transfer in complex I can be diverted into superoxide formation [52].

b. Complex II (succinate dehydrogenase):

Succinate dehydrogenase is an enzyme from the citric acid cycle responsible for generating $FADH_2$ through the oxidation of succinate to fumarate [55-57]. During this process $FADH_2$ does not leave the complex and its electrons are transferred to Fe-S clusters and then to the ubiquinone for entring to the electron transport chain. Succinate dehydrogenase is the only protein in the respiratory chain that does not pump protons which is due to the low amount of

energy generated through the electron transfer (ΔE_o: 15 mV and ΔG_o: -2.9 KJ.mol^{-1}) [55]. Mitochondrial and most of the bacterial succinate dehydrogenases are composed of four subunits (Figure 1.6). Complex II from *E. coli* contains two hydrophilic subunits that are constituted of a flavoprotein (SdhA) and an iron-sulfur protein (SdhB). SdhA contains a FAD, succinate binding site and SdhB contains three iron-sulfur clusters (2Fe-2S, 4Fe-4S and 3Fe-4S). The other two hydrophobic subunits are SdcC and SdcD. These two subunits form a cytochrome *b* complex which contains one heme *b* and a ubiquinone binding site.

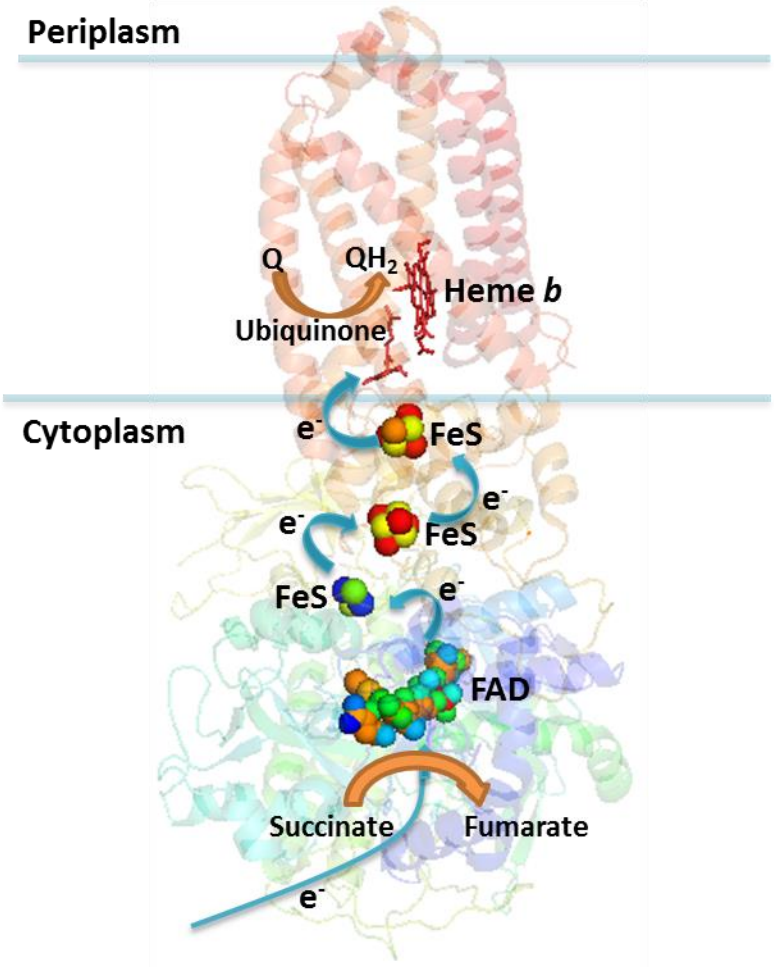

Figure 1.6 Structure of succinate dehydrogenase from *E. coli* (Complex II) showing the electron transport from FAD to ubiquinone. (PDB. 1NEK)

The succinate dehydrogenase catalyzes the following reaction;

$$\boldsymbol{Succinate + Q \leftrightarrows Fumarate + QH_2}$$

Recent studies indicate that reduced levels of succinate dehydrogenase enzyme have been observed in the brain of mice with Huntington`s disease [58]. Mutations in any of the hydrophobic or hydrophilic subunits of this enzyme can lead to several diseases such as Leigh syndrome [59], optic atrophy [60] and formation of superoxide ions together with tumorogenesis in chaffin cells [61].

c. Coenzyme Q-Cytochrome *c* oxidoreductase (Complex III)

Coenzyme Q-cytochrome *c* oxidoreductase is the second proton pump in the respiratory chain [62, 63]. The main function of this enzyme is to transfer electrons from reduced ubiquinol to another water-soluble electron transport molecule, cytochrome *c*, while generating a proton motive force. This process can be summarized as in the following reaction [62];

$$\boldsymbol{QH_2 + 2Cyt\ c_{ox} + 2H^+_{matrix} \leftrightarrows Q + 2Cyt\ c_{red} + 4H^+_{cytosol}}$$

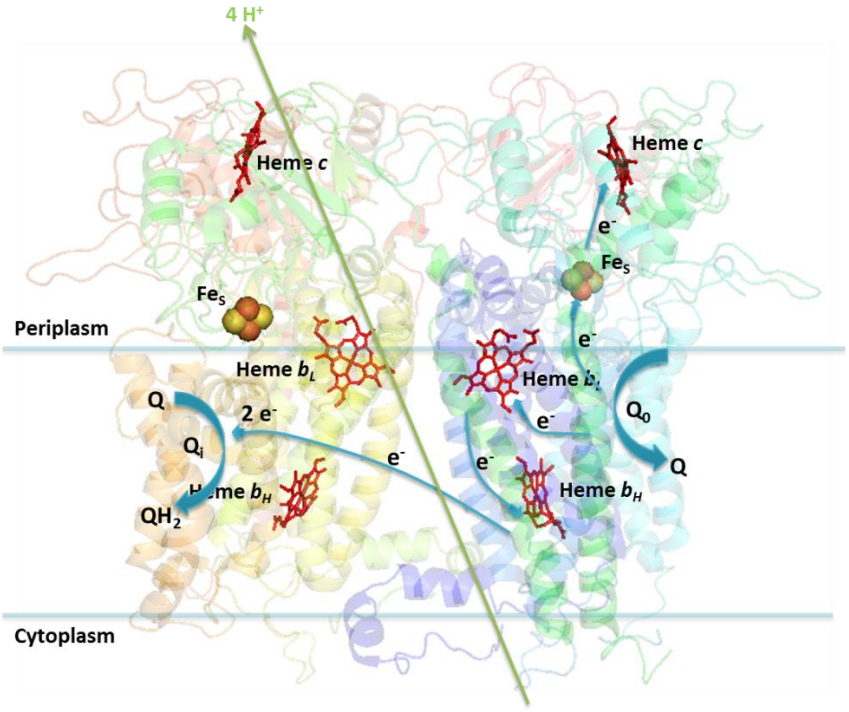

Figure 1.7 Structure of cytochrome *bc1* from *R. capsulatus* Complex III (Coenzyme Q-Cytochrome *c* oxidoreductase) showing the electron transfer between cofactors. (PDB. 1ZRT)

Complex III is a dimer and each of the monomers contains 11 subunits. It contains in total two *b*-type hemes (b_{Low} and b_{High}) and each dimer contains one *c*-type hemes together with an 2Fe-2S center (Figure 1.7). There are two ubiquinone binding sites (Q_o and Q_i) in complex III

which are distinguished by their location in the protein (In or Out). Two protons are released when the ubiquinol is oxidized at Q_o site. At the same time, two electron reduction of ubiquinone are used to reduce heme b_L and FeS cluster. The electrons of heme b_L are transferred to the Q_i through the heme b_H. The bound ubiquinone in this site is reduced to ubiquinol and 2 H^+ are taken from the inner, negative side of the membrane. The reduced FeS centers deliver the electrons to heme c_1. Finally electrons are donated to cytochrome *c*. As a summary, 2 H^+ are taken from the N side and 4 H^+ are pumped to the P side while two electrons are donated to cytochrome *c*.

Mutations in complex III related genes in humans leads to the formation of multisystem disorders, septo-optic dysplasia and exercise intolerance [64]. The group of Meunier studied several mutations in the mitochondrial cytochrome *b* [65] using yeast as a model system and showing that malfunction in complex III could be pathogenic in humans.

d. Cytochrome *c* oxidase (Complex IV)

Cytochrome *c* oxidase is the terminal oxidase in the respiratory chain [66-69]. It is responsible for the 4 electron reduction of O_2 into H_2O which is coupled to a proton pumping from negative, inner side to the positive side of the membrane. Cytochrome *c* oxidase is a member of a large family of terminal oxidases. There are several eukaryotic and prokaryotic cytochrome oxidases and quinol oxidases in the family of terminal oxidases. Members of this family use cytochrome *c* or quinone as an electron donor and a copper/heme center as an intermediate electron carrier.

All members of this family function as a proton pump which creates a proton gradient and this proton motive force is further used by ATPases (Complex V) to produce ATP. In prokaryotes they are located in the prokaryotic plasma membrane (between peri-plasm and cytoplasm) and in eukaryotic systems they are in the mitochondrial inner membrane.

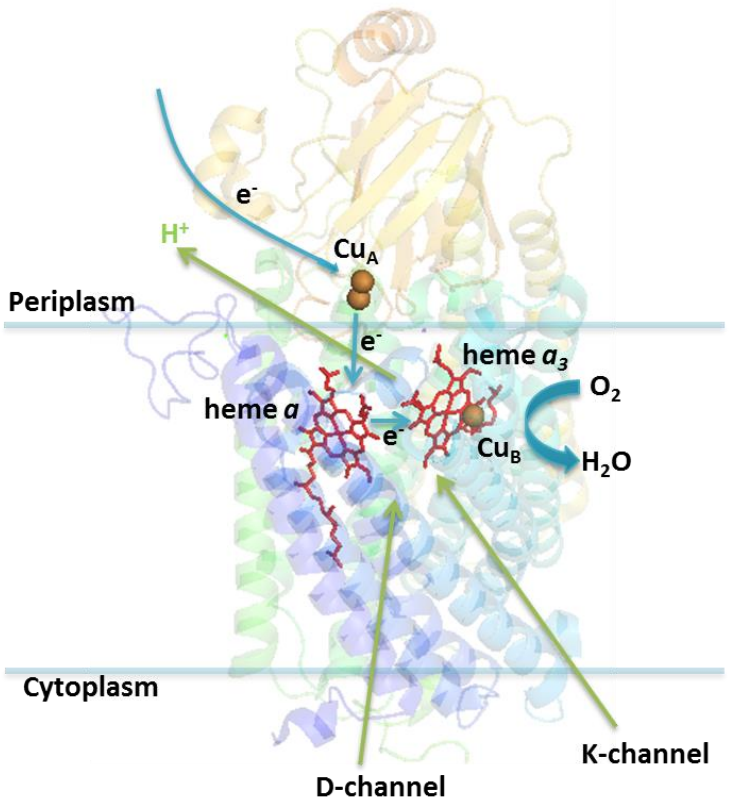

Figure 1.8 Structure of cytochrome *c* oxidase from *P. denitrificans* (Complex IV) showing the electron transfer between the cofactors. (PDB. 3HB3)

Mitochondrial cytochrome *c* oxidases are constituted of 13 different subunits [70]. Electron transfer is accomplished through 4 redox centers: one heme *a*, (can be heme *b* and heme *c* in other bacterial oxidases), one heme a_3 (can be heme o_3 and b_3 in other bacterial oxidases), one Cu_A (which is absent in quinol oxidase and cbb_3 oxidase) and one Cu_B center. In figure 1.8 the structure of cytochrome aa_3 oxidase from *P. denitrificans* is shown. In all oxidases reduction of O_2 into H_2O is performed in the bi-nuclear center which is constituted of heme a_3 (o_3/b_3) and Cu_B. Cu_A, in cytochrome *c* oxidase, is responsible for the oxidation of cytochrome *c* and delivering the electrons to the heme *a*. In the case of quinol oxidases electrons are directly delivered to the heme *b* and then to the bi-nuclear center. The electrons and protons that are transported to the bi-nuclear center are used to reduce O_2.

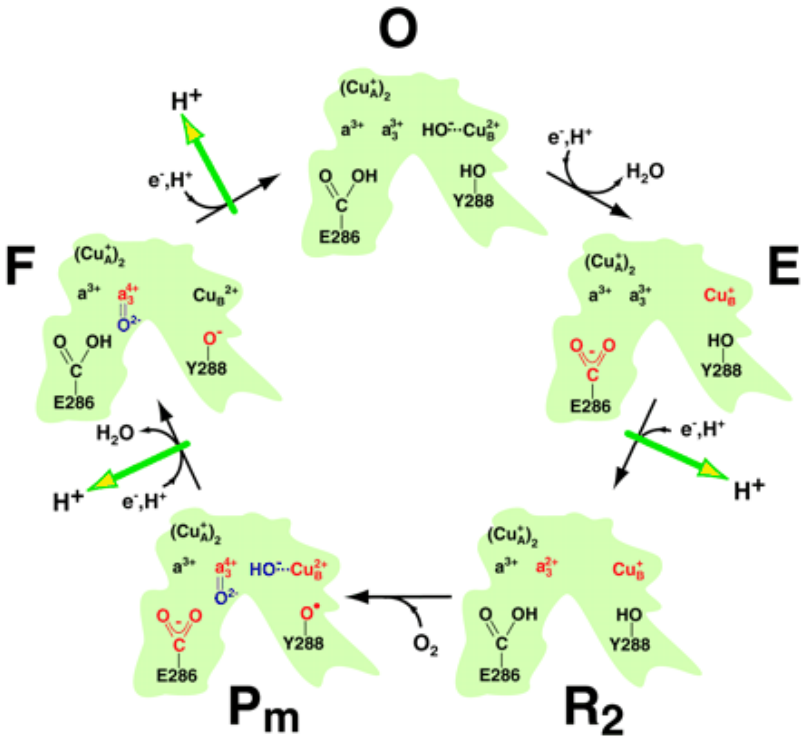

Figure 1.9 Five stages of the catalytic cycle of cytochrome *c* oxidase [71].

The electron transfer has a complicated pathway in cytochrome *c* oxidase and it is coupled with proton translocation. Electron transfer and O_2 reduction in the enzyme is usually studied by flow-flash technique where the enzyme is reduced under CO atmosphere, bound CO is dissociated with a laser flash and enzyme is mixed with an O_2 containing solution [72]. Results of this experiment show that O_2 rapidly bounds (≈ 10 μs) and electrons are transferred to heme *a*. In the next step, electrons are transferred to the bi-nuclear center (≈ 40 μs) and forming the peroxy state. During this process protons are transported from the solution (N side) to the bi-nuclear center (≈ 100 μs) and the ferryl state of the enzyme is formed. In the final step remaining electrons in the Cu_A-heme *a* equilibrium are transported to the bi-nuclear center and enzyme comes back to the oxidized form (≈ 1 ms) [72]. The complete catalytic cycle is shown in figure 1.9.

1.3 Heme-Copper Oxidase Superfamily

In the bacterial systems there are several distinct terminal oxidases rather than a single cytochrome *c* oxidase (eukaryotic mitochondrial system). This complex diversity of terminal oxidases has been studied in detail over the years to obtain a general classification [73-76].

Many studies in the past years showed that most of the bacterial oxidases use different substrates (cytochrome *c* or quinone), have different oxygen affinities and contain different heme/metal centers [76]. However, they are considered to be close relatives of a superfamily of heme-copper oxidases. The establishment of this classification triggered scientists to focus on the further comprehension of evolutionary links of the various respiratory systems.

The primary function of respiratory systems is to generate a proton motive force. However, this process is not always in the favor of the organism. Depending on the growth conditions the organisms can focus on the rate of respiration rather than the efficiency of proton translocation due to the importance of survival [73]. As a conclusion, the organism should work in balance, depending on the growth condition, to carry out the needs of an optimal respiratory chain. These needs can be summarized under three topics: maximal H^+/e^- ratio, rapid removal of excess reducing equivalents and oxygen reduction.

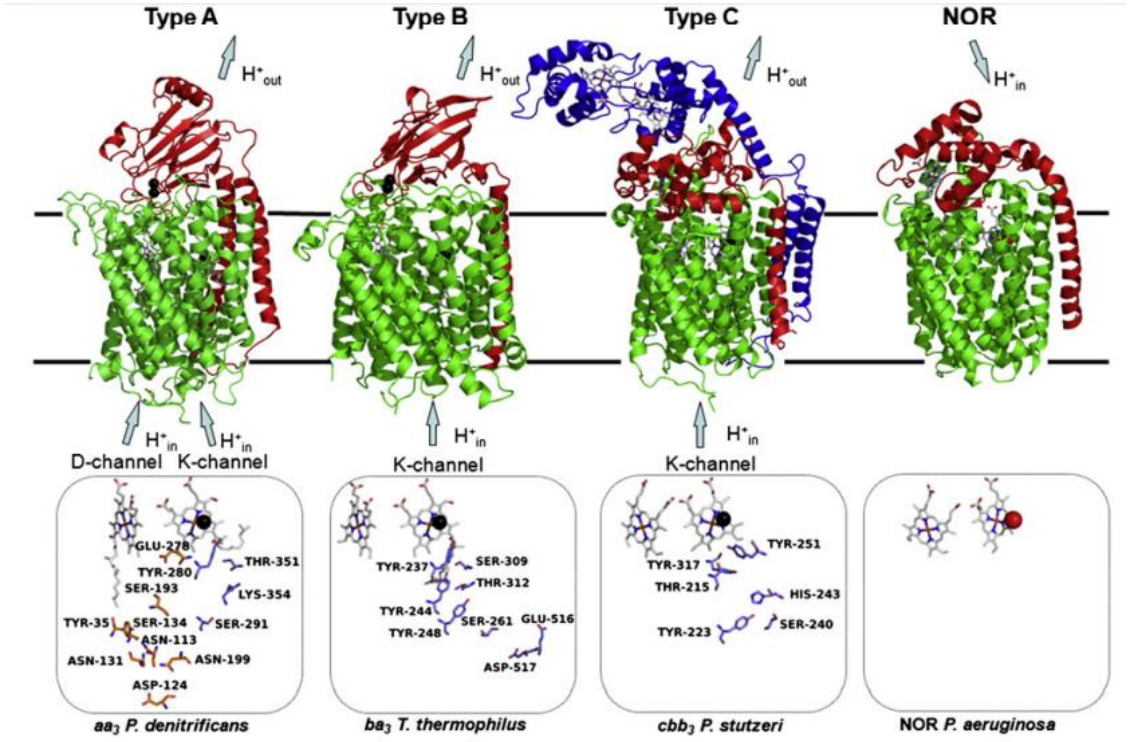

Figure 1.10 Crystal structures of the heme-copper oxidase super family. Catalytic subunits are shown in green and additional subunits are shown in red and blue. The amino acid residues in the proposed proton channels of different types of heme-copper oxidases are shown below [73].

The respiratory oxidases in prokaryotic systems vary between each other depending on the substrate type, substrate affinity and heme-copper composition. Thus heme-copper oxidases are divided into 3 major types: Type A (A1 and A2), type B and type C (Figure 1.10).

Type A:

Type A oxidases are the most studied and diverse type of heme-copper oxidases. Type A oxidases are divided into type A1 and type A2 oxidases. The main distinctive feature of type A1 oxidases are the two K and D proton channels. In aa_3 enzyme from *P. denitrificans*, the D channel starts with the conserved D124 residue in the negative side of the membrane and contains N199, N113, N131, Y35, S134, S193 and E278 (Ending of the channel) residues. K channel is constituted of highly conserved K362, S291, T359 and Y288 residues [67].

Type A2 enzymes also contain all the highly conserved residues in K and D channel in their structure except the E278 residue in helix VI. Studies with caa_3 oxidase from *Rhodothermus marinus* showed that a Tyr residue is present close to the position E278 and it has a role in the proton translocation process [77]. In addition, type A2 enzymes contain consecutive, conserved Ser residues suggested to take part in the proton translocation process. This concept is called YS motifs and it is a fingerprint of type A2 enzymes.

Type B:

The main difference between B type enzymes and the A type enzymes is the proton transport mechanisms. In type B enzymes the residues involved in the K and D proton channels are not conserved. Instead, it was proposed that the Lys-354, Thr351 and Ser291 residues in K channel have been replaced with threonine, serine and a tyrosine residues, respectively, and responsible for the proton translocation in the enzyme [73]. The best studied protein amongst type B oxidases is ba_3 from *T. thermophilus*. It was proposed that instead of a single K channel two proton channels (D and Q) were present in this enzyme [78]. However, the mutations in the residues proposed to be in the D and Q channels showed that the proton pumping ability of this enzyme was not perturbed. This fact indicates that the enzyme uses a single proton channel (K-channel).

Several members of type B heme-copper oxidases (such as ba_3 and aa_3 oxygen reductases from *T. thermophilus* and *A. ambivalens*, respectively) pump protons but with slower rate than type A oxidases [73, 79-81].

Type C:

The only member of type C heme-copper oxidases is cbb_3 oxygen reductase [82- 84]. It is generally constituted of four subunits (CcoN, CcoO, CcoP and CcoQ). In the catalytic sub-unit CcoN a low-spin heme *b* and a binuclear center, which is composed of a high-spin heme *b* and a Cu_B center, are present. The other two subunits CcoO and CcoP contain a low-spin heme *c* and two low-spin heme *c* respectively. cbb_3 oxidases use a single proton pathway which is related to the B type heme-copper oxidases with the exception of Thr-351 and Ser-291 (Instead contains serine and tyrosine) residues [85, 86]. A H^+/e stoichiometry between 0.6-1 was obtained with cbb_3 oxidase from *P. denitrificans* and *Rhodobacter sphaeroides* [82, 87].

Nitric oxide reductases (NORs):

NORs have two distinct types which are distinguished on the basis of the type of electron donor they use. cNORs use water soluble cytochrome *c* as the electron donor and qNORs use a lipid soluble ubiquinone. NORs do not pump protons thus they do not contain a proton channel connecting the two sides of the membrane. They contain a proton channel for the translocation of the protons that are used in the chemical reaction in the catalytic site. The catalytic site of NORs has the same core structure as heme-copper oxidases. The binuclear center of NOR is constituted of a high-spin heme b_3 and a Fe_B ion instead of Cu_B. Despite the differences in the terms of function and structure NORs are suggested to be evolutionary linked to the heme-copper oxidases [88, 89].

In this thesis, we focused on two members of heme-copper oxidase family: bo_3 oxidase from *E. coli* and cNOR from *P. denitrificans*.

1.5 Cytochrome bo_3 oxidase from *E. coli*:

The cytochrome bo_3 oxidase is a member of type A heme-copper oxidase superfamily [90, 91]. The main function of this enzyme is to generate a proton motive force through the

translocation of H^+ from the negative (N) side of the membrane to the positive (P) side and to catalyze the four electron reduction of O_2 to H_2O. Cytochrome *bo*$_3$ oxidase is constituted of four subunits. Subunit I contains all the redox centers such as a low-spin heme *b*, a high-spin heme o_3 and a Cu_B complex (Figure 1.11).

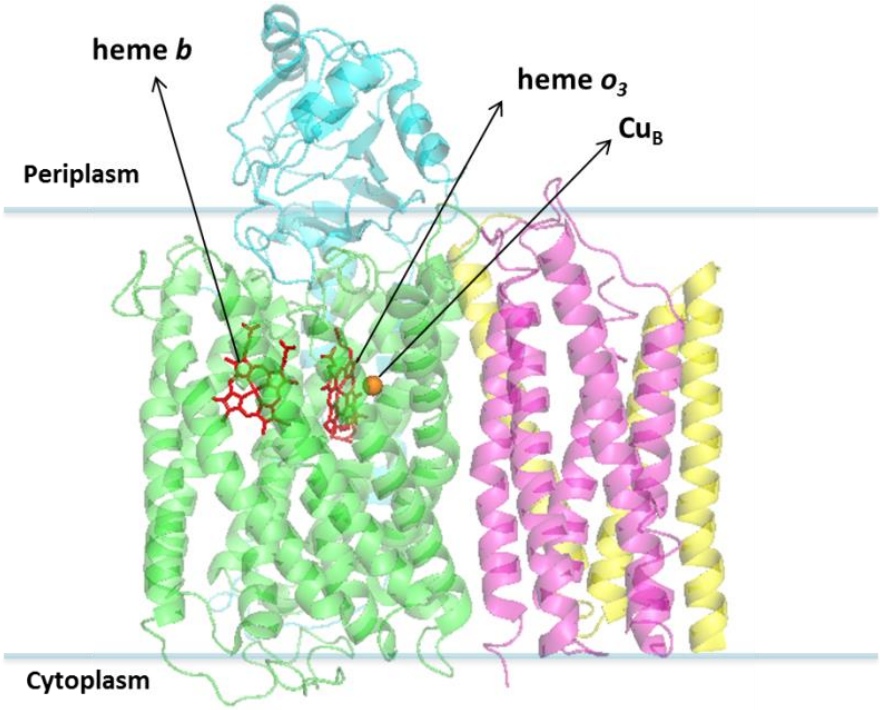

Figure 1.11 Structure of cytochrome *bo*$_3$ oxidase from *E. coli* (1FFT). Subunits I, II, III and IV are shown in green, blue, purple and yellow respectively.

The O_2 is reduced into H_2O in the binuclear center which is composed of these high-spin heme o_3 and a Cu_B ion in subunit I. Subunits I, II and III are homologous to the corresponding subunits of cytochrome *aa*$_3$ oxidase. It was shown that in both enzymes two hemes (heme *b* instead of heme *a* and heme o_3 instead of heme a_3) and the Cu_B contain histidine residues as ligands [91]. Subunit IV of *bo*$_3$ oxidase does not contain any conserved residues compared to other types of oxidases and its function is still under debate. *bo*$_3$ oxidase does not contain a Cu_A center (unlike *aa*$_3$ oxidase) and it uses a membrane soluble ubiquinol-8 as the electron donor. The electrons are directly transferred from the ubiquinol to low spin heme *b* and then to the binuclear center.

The electron transfer in *bo*$_3$ oxidase was extensively studied and it was shown that the four electron delivery to O_2 is a multiphasic process [92, 93]. The oxidation/reduction of redox centers does not commence at the same time and, in fact, there is a complex cooperativity between the redox centers. This means that oxidation/reduction of one of the hemes leads to easier reduction/oxidation of sequential heme in the enzyme. Flow-flash experiments with cytochrome *aa*$_3$ oxidase from bovine heart [94] demonstrated that the initial process of O_2 binding (≈120,000 s^{-1}) is followed by the oxidation of two hemes since the electrons are transferred to O_2 (≈30,000 s^{-1}). Afterwards, low-spin heme *b* is re-reduced with the incoming electrons from Cu_A (≈10,000 s^{-1}) and finally in the last step, O_2 is reduced into H_2O while the redox centers become fully oxidized. The lack of a Cu_A center in the structure of *bo*$_3$ oxidase raised the question about the similarity of the electron transfer mechanism. The absence of Cu_A should block the re-reduction of low spin heme *b* and the final reduction of O_2 to H_2O leaving a ferryl intermediate at the binuclear center. Recent studies showed that *bo*$_3$ oxidase could have either monophasic or multiphasic kinetics depending on the isolation of the enzyme. In 1999 Wikstrom and coworkers [94] showed that, actually, the amount of bound ubiquinone in the enzyme determines the electron transfer kinetics. They showed that in the absence of ubiquinone the enzyme undergoes a monophasic reaction resulting in the trapped ferryl intermediate in the binuclear center and in the presence of ubiquinone Cu_B can be re-reduced.

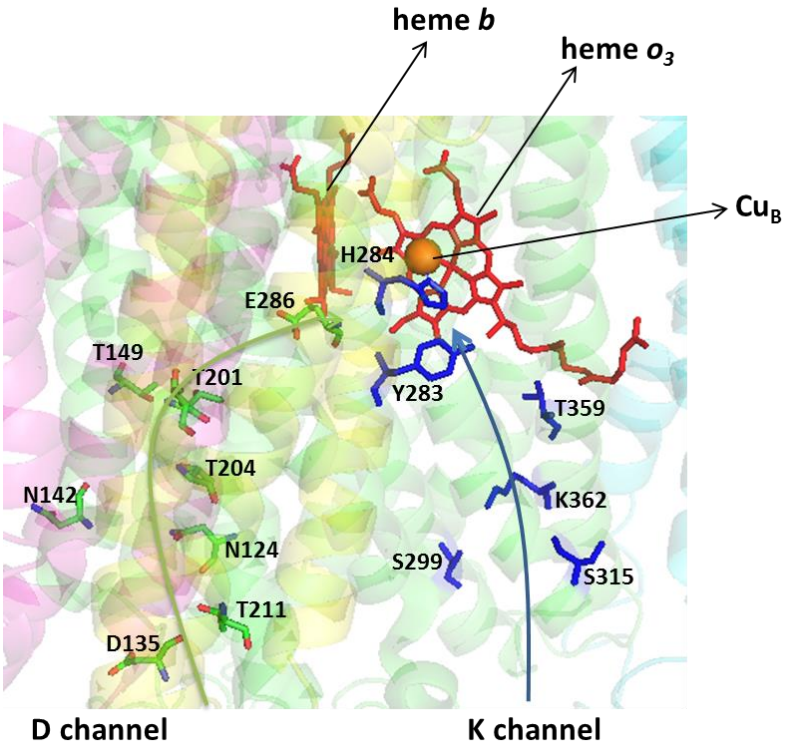

Figure 1.12 Two proton pathways, D and K channels in subunit I of *bo₃* oxidase from *E. coli*.

There are two proton channels present in *bo₃* oxidase from *E. coli*: D channel and K channel (Figure 1.12). These channels are responsible for the intake of protons from the cytosolic side and transporting them to the binuclear site. From the binuclear center the protons are either pumped to the other side of the membrane or used in the reduction of O_2 into H_2O.

The D channel is constituted of several conserved polar residues. It starts with the Asp 135 residue and proceeds through, Asn 124, Thr 211, Asn 142, Tyr 61, Thr 204, Ser 145, Thr 201, Thr 149 and terminates at Glu 286 [95, 96]. The K channel is also constituted of conserved polar residues such as Ser 315, Lys 362, Ser 299, Thr 359, the -OH group of the hydroxyethylfarnesyl tail of heme *o₃* and Tyr 283 [97- 99].

Cytochrome *bo₃* oxidase uses a membrane soluble ubiquinone as the electron donor. Phylogenetic studies showed that quinol oxidases are derived from cytochrome *c* oxidases. The subunits I, II and III are homologous in both *bo₃* oxidases and eukaryotic cytochrome *c* oxidases. The lack of Cu_A in its structure is the most distinctive property of *bo₃* oxidase. In the early 90s it was suggested that instead of the Cu_A center there could be a ubiquinone

binding site (low affinity Q_L). However, recent studies on the crystal structure of *bo*$_3$ oxidase showed that it is unlikely [91]. The isolation of the enzyme with more than one ubiquinone indicated that there might be more than one ubiquinone binding site in *bo*$_3$ oxidase (low affinity Q_L and high affinity Q_H) [100]. It was proposed that a quinone can bind from the quinone pool to the Q_L site and its electrons are delivered to the Q_H site where there is a tightly bound quinone. However, the most recent studies suggest that it is unlikely [100, 101, 107, 108].

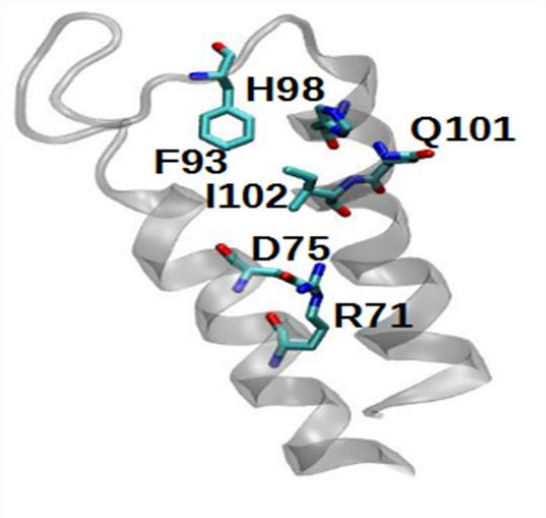

Figure 1.13 Structure of the proposed Q_H site in the helices I, II and III of subunit I in cytochrome *bo*$_3$ oxidase from *E. coli*.

From the crystal structure several residues were suggested to be in the Q_H site such as His 96, Gln 101, Ile 102, Arg 71 and Asp 75 (Figure 1.13). However, there was not a clear evidence for the presence of a Q_L site. Amongst the core residues of the Q_H site, D75 has been extensively studied [101-107]. Site directed mutations in the R71 and H98 residues resulted in the total loss of catalytic activity in the enzyme [108]. A site directed mutant of Q101 (Q101N) was studied by the group of Dr. Wikström [91] and they measured 24 % activity for the mutant and high K_m value was obtained. Recently a new residue, Phe 93, was proposed to be in this high affinity quinone binding site by the group of Pierri [109].

1.6 Cytochrome *c* dependent nitric oxide reductase (cNOR) from *P. denitrificans*

cNOR from *P. denitrificans* is a membrane protein and responsible for the reduction of nitric oxide (NO) into nitrous oxide (N_2O) in denitrifying bacteria. The catalytic reaction of NOR can be summarized as in the following reaction;

$$2NO + 2\,e^- + 2H^+ = N_2O + H_2O$$

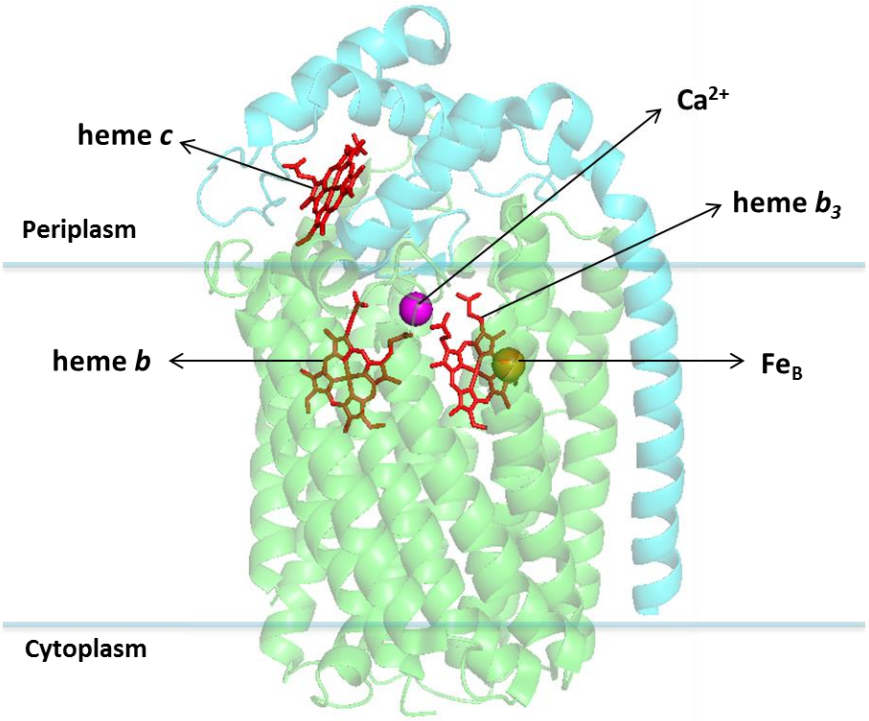

Figure 1.14 Structure of cNOR from *P. aeruginosa*. NorB and NorC subunits are shown in green and and blue respectively. PDB 3WFB

In the early 90s NOR was started to be considered as a member of the heme-copper oxidase family due to the structural similarities with cytochrome oxidases. Since NOR and cytochrome oxidases have similar catalytic subunits they demonstrate cross reactivity with respect to the substrates [88, 89]. It is suggested that NOR and cytochrome oxidases share a common ancestor. When the O_2 concentration was dramatically increased on the Earth the ancestral respiratory enzyme was converted to O_2 reducing cytochrome oxidase nonetheless, some of these enzymes have survived as NO reducing enzyme (NOR). Due to this reason there is significant interest to understand the structure and molecular mechanism of NOR.

Comparison of cytochrome oxidases to NOR may provide valuable information on the evolutionary links between respiratory enzymes.

NOR has two distinct classes such as quinone dependent NOR (qNOR) and cytochrome *c* dependent NOR (cNOR). The crystal structure of cNOR from *P. aeruginosa* (Figure 1.14) and qNOR from *G. stearothermophilus* were successfully determined [110, 111]. cNOR consists of two subunits, NorB and NorC. NorC subunit contains a low-spin heme *c* as a first electron acceptor from cytochrome *c* or azurin (copper protein). His and Met residues are the heme ligands. NorB subunit contains two *b*-type hemes (heme *b* and heme b_3) and a non-heme Fe_B center. The low-spin heme *b* contains two histidine residues (His 60 and His 349) as axial ligands [110]. The electrons are transferred from heme *c* to heme *b* and finally to the binuclear center that consists of high-spin heme b_3 and Fe_B. Heme b_3 contains His 347 as an axial ligand and the non-heme Fe_B has His 207, His 258 and His 259 as ligands [110]. It was suggested that heme b_3 and Fe_B are bridged by an oxygen atom which forms the μ-oxo-bridge [110].

From the crystal structure it was shown that Ca^{2+} binding site is located between hemes *b* and b_3 [110]. The Ca^{2+} ion has Tyr-73, Gly-71 and Glu-135 (*P. aeruginosa* numbering) as ligands (Figure 1.15) and they bridge the propionates of hemes *b* and b_3 [110]. There are five conserved Glu residues around the Ca^{2+} site which are Glu 135, Glu 138, Glu 211, Glu 215 and Glu 280 (*P. aeruginosa* numbering). Ca^{2+} site and the conserved Glu residues are essential for the catalytic activity of the enzyme [110].

In order to reduce NO into N_2O two molecules of NO must be delivered to the binuclear center in bacterial cNOR. From the crystal structure it was shown that there is not sufficient space in the binuclear center to fit two molecules of NO [110]. For this reason during the catalytic cycle of cNOR some conformational changes in the binuclear center are required to embed 2NO and to form the N-N bond. It was suggested that during the catalytic turnover the Glu ligand of the Fe_B may dissociate and open space for the binding of the second NO molecule [110]. The following mechanism was suggested for the bacterial reduction of NO (Figure 1.16):

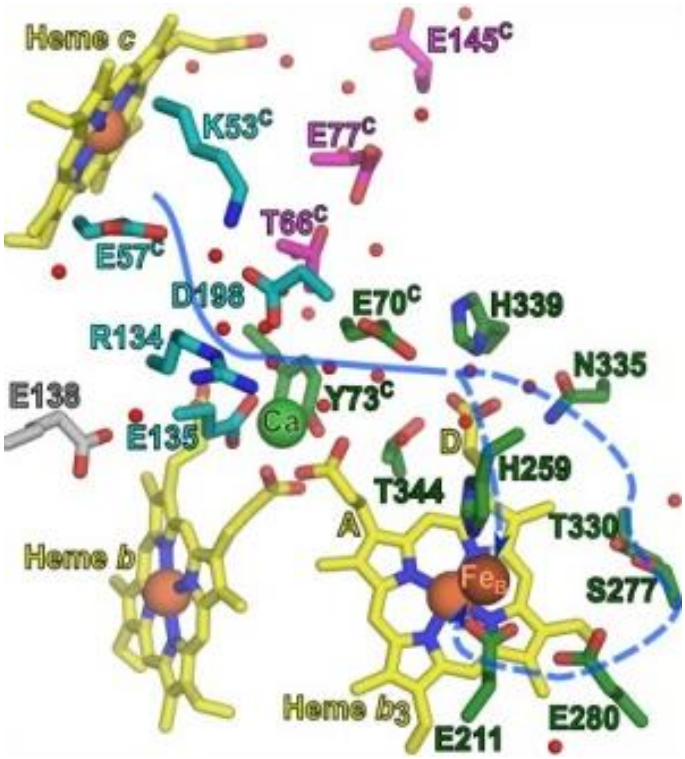

Figure 1.15 Suggested proton pathways for the wild type cNOR from *P. aeruginosa* [115].

1. In the resting state Fe_B (Ferric form) and heme b_3 are bridged by O, forming the µ-oxo-bridge.
2. In the oxidized state the µ-oxo-bridge disappears and non-bridged structure is observed in the binuclear center.
3. At the fully reduced step two NO molecules are bound to the heme b_3 and non-heme Fe_B. However, the exact mechanism of this process is still unclear. Most probably the Glu ligand of Fe_B dissociates to allow two molecules of NO to bind to the binuclear center.
4. After the transfer of electrons to the NO molecules N-N bond is formed between the two molecules. As a result a hyponitrite is formed as an intermediate. In this state the distance between heme b_3 and Fe_B should be at least 4.4 A. This indicates that the heme b_3 and Fe_B must shift from their original positions.
5. At the final stage, the protons are transferred from outside of the enzyme to the binuclear center through the proton pathway. Transferred protons promote the cleavage of N-O bond of hyponitrite and facilitate the N_2O and H_2O production.

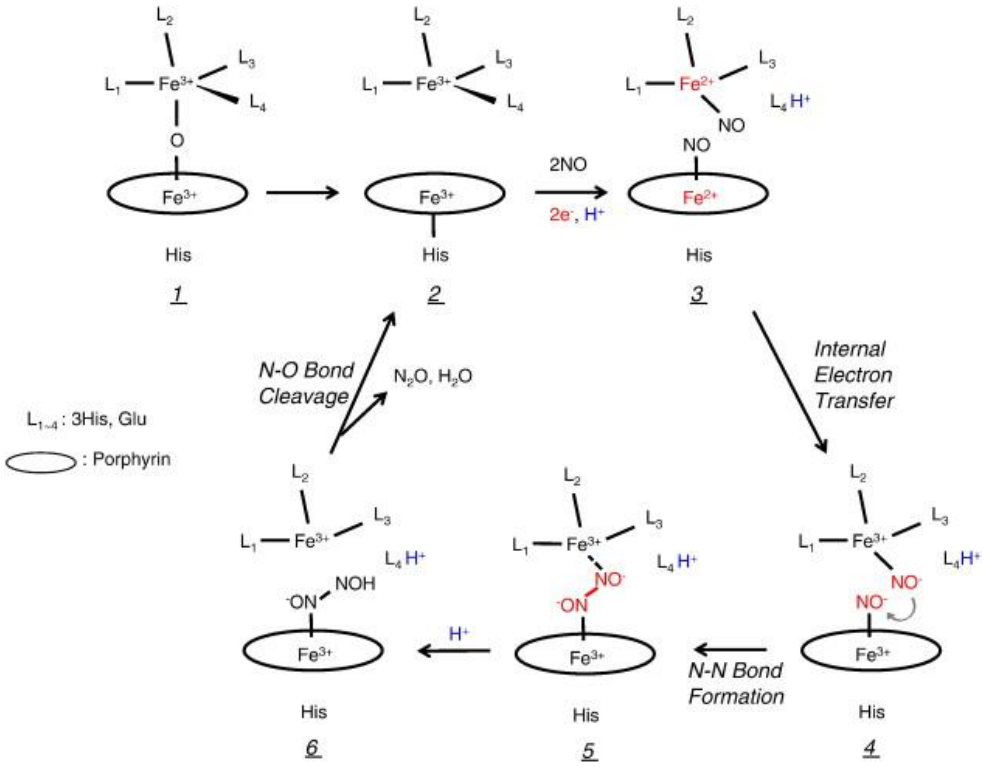

Figure 1.16 Proposed catalytic cycle for the reduction of NO into N_2O in cNOR [110]

The proton translocation in the enzyme is usually established by hydrogen-bonded water molecules and protonatable amino acids. Recent studies showed that cNOR from *P. denitrificans* use a single proton pathway [112- 116]. This proton pathway was suggested to be constituted of several amino acid residues such as Glu135, Asp198, Lys53, Arg134, Lys199, Glu70 and Glu57 (*P. aeruginosa* numbering) and the corresponding residues in *P. denitrificans* are Glu122, Asp185, Lys54, Arg121, Lys186, Glu71 and Glu58 respectively (Figure 1.15). The group of Dr. Adelroth suggested that there may be a final proton donor responsible for the delivery of the protons to the binuclear center [115]. Studies with the site-directed mutants of the E135 (E122 in *P. denitrificans*) residue revealed a large shift in the pK_a of the proton donor. After the crystal structure was determined it was understood that the E135 residue was the ligand of Ca^{2+}. As it was described previously Ca^{2+} was coordinated with Tyr73, Gly71 and one of the propionates of both hemes *b* and b_3. Mutating the residues around the Ca^{2+} and propionates of hemes *b* and b_3 resulted in the loss of Ca^{2+} from the enzyme [115].

1.7 Aim

In the first part of this thesis cytochrome *bo*$_3$ oxidase from *E. coli* was investigated. After the successful characterization of the wild-type enzyme the next focus was on the quinone-enzyme interaction. In this part quinone-free *bo*$_3$ oxidase was used as a control experiment. The interactions of quinone free *bo*$_3$ oxidase with quinones differ with respect to the length of the isoprenyl tails. By using various quinones with different tail lengths we aimed to understand the relation between the length of quinone and O_2 reduction activity of the enzyme. Added to that, we wanted to monitor the changes in the redox potentials of the cofactors after the reconstitution of *bo*$_3$ oxidase with various quinones. This may help us to understand how the quinone binding affects the redox properties of the cofactors.

The next step was to investigate the quinone binding site in *bo*$_3$ oxidase. Several site-directed mutants of the residues suggested to be involved in the high affinity quinone binding site (Q_H) were used in this part. Various properties such as functional groups, size and charge of these residues were changed after the mutations. Amongst the suggested residues in the high-affinity quinone binding site F93 is recently proposed to be also involved in this site. Working with these mutants may provide more detailed information about the Q_H site. The exact position of the quinone binding site and the quinone binding mechanism are still not fully understood.

In the second part, the enzyme cNOR from *P. denitrificans* was investigated. We focused on understanding the effect of environment on the structure of the enzyme and the redox properties of the cofactors. cNOR was inserted in liposomes and compared to the cNOR with DDM. It was expected that the liposomes may provide natural environment for the membrane proteins. Moreover, we wanted to monitor the stability of the enzyme at different pH values.

In the last part we focused on the proton translocation pathway in cNOR. The residues involved in the proton pathway were investigated and determined by the group of Dr. Adelroth [113-116]. The final proton donor that gives protons to the binuclear center is still under investigation. It was suggested that this proton donor may be one of the ligands of Ca^{2+} or is present in this area [113, 115]. We worked with the site directed mutants of the ligands of Ca^{2+} (E122, Y74).

1.8 References

1. Brooker, R. J., Vidmaier, E. P., Graham, L. E.and Stiling, P. D. (2011) Biology- 2nd edition.
2. Haddock, B. A., & Jones, C. W. (1977). Bacterial respiration. Bacteriological Reviews, 41(1), 47.
3. Pallardy, S. G. (2008). Photosynthesis. Physiology of Woody Plants, 107–167.
4. Songer, C. J., & Mintzes, J. J. (1994). Understanding cellular respiration: An analysis of conceptual change in college biology. Journal of Research in Science Teaching, 31(6), 621–637.
5. Bonora, M., Patergnani, S., Rimessi, A., de Marchi, E., Suski, J. M., Bononi, A., Pinton, P. (2012). ATP synthesis and storage. Purinergic Signalling.
6. Lin, H. (2007). Nicotinamide adenine dinucleotide: beyond a redox coenzyme. Organic & Biomolecular Chemistry, 5(16), 2541.
7. Lehninger, A. L., Nelson, D. L., and Cox, M. M. (2000). Lehninger Principles of Biochemistry. New York: Worth Publishers.
8. Blankenship, R. E. (2008). Molecular Mechanisms of Photosynthesis. Molecular Mechanisms of Photosynthesis.
9. Heineke, D., & Scheibe, R. (2009). Photosyntesis: The Calvin Cycle. Encyclopedia of Life Sciences, (March).
10. Lunt, S. Y., & Vander Heiden, M. G. (2011). Aerobic Glycolysis: Meeting the Metabolic Requirements of Cell Proliferation. Annual Review of Cell and Developmental Biology, 27(1), 441–464.
11. Reid, L. C. (1940). Cellular respiration. British Journal of Anaesthesia, 17(2), 41–56.
12. Krauss, S., Israel, B., & Medical, D. (2001). Mitochondria: Structure and Role in Respiration. Life Sciences, 1–6.
13. Gnaiger, E. (2001). Bioenergetics at low oxygen: Dependence of respiration and phosphorylation on oxygen and adenosine diphosphate supply. In Respiration Physiology (Vol. 128, pp. 277–297).
14. Lin, S. J., & Guarente, L. (2003). Nicotinamide adenine dinucleotide, a metabolic regulator of transcription, longevity and disease. Current Opinion in Cell Biology.

15. Lin, H. (2007). Nicotinamide adenine dinucleotide: beyond a redox coenzyme. Organic & Biomolecular Chemistry, 5(16), 2541.
16. Korla, K., & Mitra, C. K. (2014). Modelling the Krebs cycle and oxidative phosphorylation. Journal of Biomolecular Structure & Dynamics, 32(2), 242–56.
17. Acid, F., Colloquium, B., Sciences, L., Symposium, I., & Lipids, P. (2000). Fatty Acid Biosynthesis: Source of Acetyl-CoA and its. Society, 591–593.
18. Rardin, M. J., Wiley, S. E., Naviaux, R. K., Murphy, A. N., & Dixon, J. E. (2009). Monitoring phosphorylation of the pyruvate dehydrogenase complex. Analytical Biochemistry, 389(2), 157–164.
19. De Boer, V. C. J., & Houten, S. M. (2014). A mitochondrial expatriate: Nuclear pyruvate dehydrogenase. Cell.
20. Fuller, C. C., Reed, L. J., Oliver, R. M., & Hackert, M. L. (1979). Crystallization of a dihydrolipoyl transacetylase-dihydrolipoyl dehydrogenase subcomplex and its implications regarding the subunit structure of the pyruvate dehydrogenase complex from Escherichia coli. Biochemical and Biophysical Research Communications, 90(2), 431–438.
21. Boyer, P. D. (1997). The ATP synthase--a splendid molecular machine. Annual Review of Biochemistry, 66, 717–49.
22. Yoshida, M., Muneyuki, E., & Hisabori, T. (2001). ATP synthase--a marvellous rotary engine of the cell. Nature Reviews. Molecular Cell Biology, 2(9), 669–77.
23. Junge, W., & Nelson, N. (2015). ATP Synthase. Annual Review of Biochemistry, 84(1), 631–657.
24. Noji, H., & Yoshida, M. (2001). The rotary machine in the cell, ATP synthase. Journal of Biological Chemistry.
25. Mitchell, P. (1961) Coupling of phosphorylation to electron and hydrogen transfer by a chemi-osmotic type of mechanism, Nature 191, 144-148.
26. Mitchell, P. (2011). Chemiosmotic coupling in oxidative and photosynthetic phosphorylation. Biochimica et Biophysica Acta - Bioenergetics, 1807(12), 1507–1538.
27. Hatefi Y, Haavik AG, Fowler LR, Griffiths DE. (1962) Studies on the electron transfer system. XLII. Reconstitution of the electron transfer system. J Biol Chem 237: 2661–2669.

28. Hatefi Y, Haavik AG, Griffiths DE. (1962) Studies on the electron transfer system. XL. Preparation and properties of mitochondrial DPNH-Coenzyme Q reductase. J Biol Chem 237: 1676–1680.
29. Hatefi Y, Haavik AG, Griffiths DE. (1962) Studies on the electron transfer system. XLI. Reduced Coenzyme Q (QH2)-cytochrome c reductase. J Biol Chem 237: 1681–1685.
30. Hatefi Y, Haavik AG, Jurtshuck P. (1961) Studies on the electron transfer system. XXX. DPNH cytochrome c reductase I. Biochim Biophys Acta 52: 106–118.
31. Hatefi Y, Lest RL, Crane FL, Widmer C. (1959) Studies on the electron transport system. XVI. Enzymic oxidoreduction reactions of coenzyme Q. Biochim Biophys Acta 31: 490–501.
32. Liu, J., Chakraborty, S., Hosseinzadeh, P., Yu, Y., Tian, S., Petrik, I., Lu, Y. (2014). Metalloproteins containing cytochrome, iron-sulfur, or copper redox centers. Chemical Reviews.
33. Reedy, C. J., & Gibney, B. R. (2004). Heme Protein Assemblies. Chemical Reviews.
34. Li, T., Bonkovsky, H. L., & Guo, J. (2011). Structural analysis of heme proteins: implications for design and prediction. BMC Structural Biology, 11(1), 13.
35. Smith, L. J., Kahraman, A., & Thornton, J. M. (2010). Heme proteins-diversity in structural characteristics, function, and folding. Proteins: Structure, Function and Bioinformatics, 78(10), 2349–2368.
36. Paoli, M., Marles-Wright, J., & Smith, A. (2002). Structure-function relationships in heme-proteins. DNA and Cell Biology, 21(4), 271–280.
37. Reichlin, M. (1972). Hemoglobin and Myoglobin in Their Reactions with Ligands. Science, 178(4058), 296 LP-296.
38. Collman, J. P., Boulatov, R., Sunderland, C. J., & Fu, L. (2004). Functional Analogues of Cytochrome c Oxidase, Myoglobin, and Hemoglobin. Chemical Reviews, 104(2), 561–588.
39. Thöny-Meyer, L. (1997). Biogenesis of respiratory cytochromes in bacteria. Microbiology and Molecular Biology Reviews: MMBR, 61(3), 337–76.
40. Kawamukai, M. (2002). Biosynthesis, bio-production and novel roles of ubiquinone. Journal of Bioscience and Bioengineering.
41. Wang, Y., & Hekimi, S. (2016). Understanding Ubiquinone. Trends in Cell Biology.

42. Meganathan, R. (2001). Ubiquinone biosynthesis in microorganisms. FEMS Microbiology Letters.
43. Trumpower, B. L. (1981). New concepts on the role of ubiquinone in the mitochondrial respiratory chain. Journal of Bioenergetics and Biomembranes.
44. Land, E. J., Simic, M., & Swallow, A. J. (1971). Optical absorption spectrum of half-reduced ubiquinone. BBA - Bioenergetics, 226(2), 239–240.
45. Lenaz, G., & Genova, M. L. (2010). Structure and Organization of Mitochondrial Respiratory Complexes: A New Understanding of an Old Subject Structural Organization of the Respiratory Chain. Antioxidants & Redox Signaling, 12(8), 961–1008.
46. Hosler, J. P., Ferguson-Miller, S., & Mills, D. a. (2006). Energy transduction: proton transfer through the respiratory complexes. Annual Review of Biochemistry, 75, 165–187.
47. Vartak, R., Porras, C. A. M., & Bai, Y. (2013). Respiratory supercomplexes: Structure, function and assembly. Protein and Cell.
48. Schägger, H. (2002). Respiratory chain supercomplexes of mitochondria and bacteria. Biochimica et Biophysica Acta - Bioenergetics, 1555(1–3), 154–159.
49. Hirst, J. (2013). Mitochondrial complex I. Annual Review of Biochemistry, 82(March), 551–75.
50. Baradaran, R., Berrisford, J. M., Minhas, G. S., & Sazanov, L. a. (2013). Crystal structure of the entire respiratory complex I. Nature, 494(7438), 443–8.
51. Berrisford, J. M., Baradaran, R., & Sazanov, L. A. (2016). Structure of bacterial respiratory complex I. Biochimica et Biophysica Acta, 4–13.
52. Grivennikova, V. G., & Vinogradov, A. D. (2006). Generation of superoxide by the mitochondrial Complex I. Biochimica et Biophysica Acta - Bioenergetics.
53. Keeney, P. M., Xie, J., Capaldi, R. a, & Bennett, J. P. (2006). Parkinson's disease brain mitochondrial complex I has oxidatively damaged subunits and is functionally impaired and misassembled. The Journal of Neuroscience : The Official Journal of the Society for Neuroscience, 26(19), 5256–5264.
54. Mimaki, M., Wang, X., McKenzie, M., Thorburn, D. R., & Ryan, M. T. (2012). Understanding mitochondrial complex I assembly in health and disease. Biochimica Et Biophysica Acta-Bioenergetics, 1817(6), 851–862.

55. Cecchini, G. (2003). Function and structure of complex II of the respiratory chain. Annual Review of Biochemistry, 72, 77–109.
56. Sun, F., Huo, X., Zhai, Y., Wang, A., Xu, J., Su, D., Rao, Z. (2005). Crystal structure of mitochondrial respiratory membrane protein Complex II. Cell, 121(7), 1043–1057.
57. Iverson, T. M. (2013). Catalytic mechanisms of complex II enzymes: A structural perspective. Biochimica et Biophysica Acta - Bioenergetics.
58. Benchoua, A., Trioulier, Y., Zala, D., Gaillard, M. C., Lefort, N., Dufour, N., … Brouillet, E. (2006). Involvement of mitochondrial complex II defects in neuronal death produced by N-terminus fragment of mutated huntingtin. Mol Biol Cell, 17(4), 1652–1663.
59. Burgeois, M., Goutieres, F., Chretien, D., Rustin, P., Munnich, A., & Aicardi, J. (1992). Deficiency in complex II of the respiratory chain, presenting as a leukodystrophy in two sisters with Leigh syndrome. Brain & Development, 14(6), 404–8.
60. Taylor, R. W., Birch-Machin, M. A., Schaefer, J., Taylor, L., Shakir, R., Ackrell, B. A., Turnbull, D. M. (1996). Deficiency of complex II of the mitochondrial respiratory chain in late-onset optic atrophy and ataxia. Annals of Neurology, 39(2), 224–32.
61. Hoekstra, A. S., & Bayley, J. P. (2013). The role of complex II in disease. Biochimica et Biophysica Acta - Bioenergetics, 1827(5), 543–551.
62. Schagger, H., Cramer, W. A., & Vonjagow, G. (1994). Coenzyme Q reductase from liver plasma membrane: purification and role in trans-plasma-membrane electron transport. Analytical Biochemistry, 217(2), 220–230.
63. Xiaohang Yang, & Trumpower, B. L. (1986). Purification of a three-subunit ubiquinol-cytochrome c oxidoreductase complex from Paracoccus denitrificans. Journal of Biological Chemistry, 261(26), 12282–12289.
64. Bénit, P., Lebon, S., & Rustin, P. (2009). Respiratory-chain diseases related to complex III deficiency. Biochimica et Biophysica Acta - Molecular Cell Research.
65. Meunier, B., Fisher, N., Ransac, S., Mazat, J. P., & Brasseur, G. (2013). Respiratory complex III dysfunction in humans and the use of yeast as a model organism to study mitochondrial myopathy and associated diseases. Biochimica et Biophysica Acta - Bioenergetics.

66. Ostermeier, C., Iwata, S., & Michel, H. (1996). Cytochrome c oxidase. Current Opinion in Structural Biology, 6(8278), 460–466.
67. Iwata, S., Ostermeier, C., Ludwig, B., & Michel, H. (1995). Structure at 2.8 A resolution of cytochrome c oxidase from Paracoccus denitrificans. Nature.
68. Michel, H., Behr, J., Harrenga, A., & Kannt, A. (1998). Cytochrome c oxidase: structure and spectroscopy. Annual Review of Biophysics and Biomolecular Structure, 27, 329–356.
69. Behr, J., Michel, H., Mäntele, W., & Hellwig, P. (2000). Functional properties of the heme propionates in cytochrome c oxidase from Paracoccus denitrificans. Evidence from FTIR difference spectroscopy and site-directed mutagenesis. Biochemistry, 39(6), 1356–1363.
70. Wharton, D. C., & Tzagoloff, A. (1967). Cytochrome oxidase from beef heart mitochondria. Methods in Enzymology, 10(C), 245–250.
71. Nyquist, R. M., Heitbrink, D., Bolwien, C., Gennis, R. B., & Heberle, J. (2003). Direct observation of protonation reactions during the catalytic cycle of cytochrome c oxidase. Proceedings of the National Academy of Sciences of the United States of America, 100(5), 8715–8720.
72. Lucas, M. F., Rousseau, D. L., & Guallar, V. (2011). Electron transfer pathways in cytochrome c oxidase. Biochimica et Biophysica Acta, 1807(10), 1305–13.
73. Sousa, F. L., Alves, R. J., Ribeiro, M. A., Pereira-Leal, J. B., Teixeira, M., & Pereira, M. M. (2012). The superfamily of heme-copper oxygen reductases: Types and evolutionary considerations. Biochimica et Biophysica Acta - Bioenergetics, 1817(4), 629–637.
74. Lee, H. J., Reimann, J., Huang, Y., & Ädelroth, P. (2012). Functional proton transfer pathways in the heme-copper oxidase superfamily. Biochimica et Biophysica Acta - Bioenergetics, 1817(4), 537–544.
75. Pereira, M. M., Santana, M., & Teixeira, M. (2001). A novel scenario for the evolution of haem-copper oxygen reductases. Biochimica et Biophysica Acta - Bioenergetics, 1505(2–3), 185–208.
76. Garcia-Horsman, J. A., Barquera, B., Rumbley, J., Ma, J., & Gennis, R. B. (1994). The superfamily of heme-copper respiratory oxidases. Journal of Bacteriology, 176(18), 5587–5600.

77. Pereira, M. M., Sousa, F. L., Teixeira, M., Nyquist, R. M., & Heberle, J. (2006). A tyrosine residue deprotonates during oxygen reduction by the caa3 reductase from Rhodothermus marinus. FEBS Letters, 580(5), 1350–1354.
78. Soulimane, T., Buse, G., Bourenkov, G. P., Bartunik, H. D., Huber, R., & Than, M. E. (2000). Structure and mechanism of the aberrant ba(3)-cytochrome c oxidase from thermus thermophilus. The EMBO Journal, 19(8), 1766–76.
79. Sone, N., Koyanagi, S., & Sakamoto, J. (2000). Energy-Yielding Properties of SoxB-Type Cytochrome bo3 Terminal Oxidase: Analyses Involving Bacillus stearothermophilus K1041 and Its Mutant Strains. Journal of Biochemistry, 127(4), 551–557.
80. Gomes, C. M., Backgren, C., Teixeira, M., Puustinen, A., Verkhovskaya, M. L., Wikström, M., & Verkhovsky, M. I. (2001). Heme-copper oxidases with modified D- and K-pathways are yet efficient proton pumps. FEBS Letters, 497(2–3), 159–164.
81. von Ballmoos, C., Gennis, R. B., Ädelroth, P., & Brzezinski, P. (2011). Kinetic design of the respiratory oxidases. Proceedings of the National Academy of Sciences of the United States of America, 108(27), 11057–11062.
82. Toledo-Cuevas, M., Barquera, B., Gennis, R. B., Wikström, M., & García-Horsman, J. A. (1998). The cbb3-type cytochrome c oxidase from Rhodobacter sphaeroides, a proton-pumping heme-copper oxidase. Biochimica et Biophysica Acta - Bioenergetics, 1365(3), 421–434.
83. Pitcher, R. S., & Watmough, N. J. (2004). The bacterial cytochrome cbb3 oxidases. Biochimica et Biophysica Acta - Bioenergetics.
84. Buschmann, S., Warkentin, E., Xie, H., Langer, J. D., Ermler, U., & Michel, H. (2010). The structure of cbb3 cytochrome oxidase provides insights into proton pumping. Science (New York, N.Y.), 329(5989), 327–30.
85. Rauhamäki, V., Baumann, M., Soliymani, R., Puustinen, A., & Wikström, M. (2006). Identification of a histidine-tyrosine cross-link in the active site of the cbb3-type cytochrome c oxidase from Rhodobacter sphaeroides. Proceedings of the National Academy of Sciences of the United States of America, 103(44), 16135–40.
86. Hemp, J., Han, H., Jung, H. R., Kaplan, S., Martinez, T. J., & Gennis, R. B. (2007). Comparative genomics and site-directed mutagenesis support the existence of only one

input channel for protons in the C-family (cbb3 oxidase) of heme-copper oxygen reductases. Biochemistry, 46(35), 9963–9972.

87. De Gier, J. W. L., Lübben, M., Reijnders, W. N. M., Tipker, C. A., Slotboom, D. J., Van Spanning, R. J. M., Van Der Oost, J. (1994). The terminal oxidases of paracoccus denitrificans. Molecular Microbiology, 13(2), 183–196.
88. van der Oost, J., de Boer, a P., de Gier, J. W., Zumft, W. G., Stouthamer, a H., & van Spanning, R. J. (1994). The heme-copper oxidase family consists of three distinct types of terminal oxidases and is related to nitric oxide reductase. FEMS Microbiology Letters, 121(1), 1–9.
89. Zumft, W. G. (2005). Nitric oxide reductases of prokaryotes with emphasis on the respiratory, heme-copper oxidase type. Journal of Inorganic Biochemistry.
90. Rumbley, J. N., Nickels, E. F., & Gennis, R. B. (1997). One-step purification of histidine-tagged cytochrome bo3 from Escherichia coli and demonstration that associated quinone is not required for the structural integrity of the oxidase. Biochimica et Biophysica Acta - Protein Structure and Molecular Enzymology, 1340(1), 131–142.
91. Abramson, J., Riistama, S., Larsson, G., Jasaitis, A., Svensson-Ek, M., Laakkonen, L., Wikström, M. (2000). The structure of the ubiquinol oxidase from Escherichia coli and its ubiquinone binding site. Nature Structural Biology, 7(10), 910–917.
92. Schultz, B. E., & Chan, S. I. (1998). Thermodynamics of electron transfer in Escherichia coli cytochrome bo3. Proceedings of the National Academy of Sciences of the United States of America, 95(20), 11643–8.
93. Kaila, V. R., Verkhovsky, M. I., & Wikström, M. (2010). Proton-coupled electron transfer in cytochrome oxidase. Chemical Reviews, 110(12), 7062–7081.
94. Puustinen, a, Verkhovsky, M. I., Morgan, J. E., Belevich, N. P., & Wikstrom, M. (1996). Reaction of the Escherichia coli quinol oxidase cytochrome bo3 with dioxygen: the role of a bound ubiquinone molecule. Proceedings of the National Academy of Sciences of the United States of America, 93(4), 1545–1548.
95. Han, D., Morgan, J. E., & Gennis, R. B. (2005). G204D, a mutation that blocks the proton-conducting D-channel of the aa3-type cytochrome c oxidase from Rhodobacter sphaeroides. Biochemistry, 44(38), 12767–12774.

96. Han, D., Namslauer, A., Pawate, A., Morgan, J. E., Nagy, S., Vakkasoglu, A. S., Gennis, R. B. (2006). Replacing Asn207 by aspartate at the neck of the D channel in the aa 3-type cytochrome c oxidase from Rhodobacter sphaeroides results in decoupling the proton pump. Biochemistry, 45(47), 14064–14074.
97. Garcia-Horsman, J. A., Puustinen, A., Gennis, R. B., & Wikstrom, M. (1995). Proton transfer in cytochrome bo3 ubiquinol oxidase of Escherichia coli: Second-site mutations in subunit I that restore proton pumping in the mutant Asp135 Asn. Biochemistry, 34(13), 4428–4433.
98. Konstantinov, A. A., Siletsky, S., Mitchell, D., & Kaulen, A. (1997). The roles of the two proton input channels in cytochrome c oxidase from Rhodobacter sphaeroides probed by the effects of site-directed mutations on time-resolved electrogenic intraprotein proton transfer. Proceedings of the National Academy of Sciences, 94(August), 9085–9090.
99. Zaslavsky, D., & Gennis, R. B. (1998). Substitution of lysine-362 in a putative proton-conducting channel in the cytochrome c oxidase from Rhodobacter sphaeroides blocks turnover with O2 but not with H2O2. Biochemistry, 37(9), 3062–3067.
100. Yap, L. L., Lin, M. T., Ouyang, H., Samoilova, R. I., Dikanov, S. A., & Gennis, R. B. (2010). The quinone-binding sites of the cytochrome bo3 ubiquinol oxidase from Escherichia coli. Biochimica et Biophysica Acta - Bioenergetics, 1797(12), 1924–1932.
101. Yap, L. L., Lin, M. T., Ouyang, H., Samoilova, R. I., Dikanov, S. A., & Gennis, R. B. (2010). The quinone-binding sites of the cytochrome bo3 ubiquinol oxidase from Escherichia coli. Biochimica et Biophysica Acta - Bioenergetics, 1797(12), 1924–1932.
102. Hellwig, P., Barquera, B., & Gennis, R. B. (2001). Direct evidence for the protonation of aspartate-75, proposed to be at a quinol binding site, upon reduction of cytochrome bo3 from Escherichia coli. Biochemistry, 40(4), 1077–1082.
103. Hellwig, P., Yano, T., Ohnishi, T., & Gennis, R. B. (2002). Identification of the residues involved in stabilization of the semiquinone radical in the high-affinity ubiquinone binding site in cytochrome bo3 from Escherichia coli by site-directed mutagenesis and EPR spectroscopy. Biochemistry, 41(34), 10675–10679.
104. Lai, L. Y., Samoilova, R. I., Gennis, R. B., & Dikanov, S. A. (2007). Characterization of mutants that change the hydrogen bonding of the semiquinone radical at the QH site of

the cytochrome bo3 from Escherichia coli. Journal of Biological Chemistry, 282(12), 8777–8785.

105. Lin, M. T., Baldansuren, A., Hart, R., Samoilova, R. I., Narasimhulu, K. V., Yap, L. L., Dikanov, S. A. (2012). Interactions of intermediate semiquinone with surrounding protein residues at the QH site of wild-type and D75H mutant cytochrome bo3 from Escherichia coli. Biochemistry, 51(18), 3827–3838.
106. Lai, L. Y., Samoilova, R. I., Gennis, R. B., & Dikanov, S. A. (2006). Characterization of the exchangeable protons in the immediate vicinity of the semiquinone radical at the QH site of the cytochrome bo3 from Escherichia coli. Journal of Biological Chemistry, 281(25), 16879–16887.
107. Lin, M. T., Shubin, A. A., Samoilova, R. I., Narasimhulu, K. V., Baldansuren, A., Gennis, R. B., & Dikanov, S. A. (2011). Exploring by pulsed EPR the electronic structure of ubisemiquinone bound at the QH site of cytochrome bo3 from Escherichia coli with in vivo 13C-labeled methyl and methoxy substituents. Journal of Biological Chemistry, 286(12), 10105–10114.
108. Choi, S. K. (2015). The Interaction of Cytochrome bo3 from Escherichia Coli with its Substrates-Ubiquinone and Oxygen:Proposal for Dissertation Submitted by. University of Illinois at Urbana-Champaign.
109. Bossis, F., De Grassi, A., Palese, L. L., & Pierri, C. L. (2014). Prediction of high- and low-affinity quinol-analogue-binding sites in the aa3 and bo3 terminal oxidases from Bacillus subtilis and Escherichia coli1. The Biochemical Journal, 461(2), 305–14.
110. Shiro, Y., Sugimoto, H., Tosha, T., Nagano, S., & Hino, T. (2012). Structural basis for nitrous oxide generation by bacterial nitric oxide reductases. Philosophical Transactions of the Royal Society B-Biological Sciences, 367(1593), 1195–1203.
111. Matsumoto, Y., Tosha, T., Pisliakov, A. V, Hino, T., Sugimoto, H., Nagano, S., Shiro, Y. (2012). Crystal structure of quinol-dependent nitric oxide reductase from Geobacillus stearothermophilus. Nature Structural & Molecular Biology, 19(2), 238–245.
112. Reimann, J., Flock, U., Lepp, H., Honigmann, A., & Ädelroth, P. (2007). A pathway for protons in nitric oxide reductase from Paracoccus denitrificans. Biochimica et Biophysica Acta - Bioenergetics, 1767(5), 362–373.

113. Flock, U., Lachmann, P., Reimann, J., Watmough, N. J., & Ädelroth, P. (2009). Exploring the terminal region of the proton pathway in the bacterial nitric oxide reductase. Journal of Inorganic Biochemistry, 103(5), 845–850.
114. Flock, U., Reimann, J., & Adelroth, P. (2006). Proton transfer in bacterial nitric oxide reductase. Biochemical Society Transactions, 34, 188–190.
115. Beek, J. Ter, Krause, N., Reimann, J., Lachmann, P., & Ädelroth, P. (2013). The nitric-oxide reductase from paracoccus denitrificans uses a single specific proton pathway. Journal of Biological Chemistry, 288(42), 30626–30635.
116. Flock, U., Thorndycroft, F. H., Matorin, A. D., Richardson, D. J., Watmough, N. J., & Ädelroth, P. (2008). Defining the proton entry point in the bacterial respiratory nitric-oxide reductase. Journal of Biological Chemistry, 283(7), 3839–3845.

2. Experimental Techniques

2.1 Electrochemistry

Electrochemistry is the study of chemical reactions which take place in solution at the interface of an ionic conductor (electrolyte) and an electron conductor (electrode). In oxidation-reduction (redox) reactions, charge is transferred through the electrode by the movement of electrons. Typical electrodes are made of metals (e.g. Au, Pt), carbon (e.g. Graphite) and semi-conductors (e.g. Si, tin oxide) [1]. In our case, we used a three electrode electrochemical cell (Figure 2.1). A gold surface is used as the working electrode (WE), a platinum wire as a counter electrode (CE) and an Ag/AgCl in 3M KCl reference electrode (RE) (+208 mV vs. SHE). Using a CE prevents the polarization of RE and supports the equilibration of half –redox reactions. There are several methods (such as cyclic voltammetry (CV), chronoamperometry, coulometry etc.) that enable us to control the applied potential and to measure the resulting current.

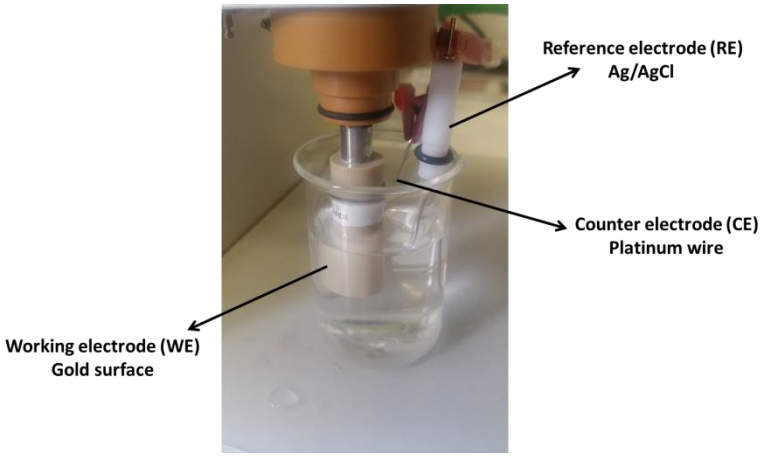

Figure 2.1 Electrochemical setup with three electrodes. Ag/AgCl reference electrode (RE) and platinum wire as counter electrode (CE) and a gold electrode as a working electrode (WE).

Direct electrochemistry is the study of the transfer of electrons from the electrode to the molecule of interest without the influence of diffusion of electron carrying molecules. Direct electrochemistry allows to study large molecules. The proteins or enzymes containing at least a single redox center close to their surface can be studied with direct electrochemistry. In order to enhance the electron transfer between electrode and the redox sites of the enzymes it

is possible to use metal nanoparticles (Au NPs [2]) and carbon-based structures (carbon nanotubes [3]). There are several studies on the direct electrochemistry of redox enzymes adsorbed on nanoparticles [4-6]. Direct electrochemistry has a wide application range since it is feasible to obtain information about the thermodynamics [7], kinetics of chemical reactions [8] and various features of redox enzymes (e.g. electron transfer, proton pumping [9, 10]).

In the case of large membrane proteins direct electron transfer is often too slow or not possible since their redox centers are buried in the polypeptide matrix. In this case transporter agents can be used for the acceleration of electron transfer. These transporter agents (such as mediators) assist the transfer of electrons to the proteins.

In this thesis we focused on the cyclic voltammetry of protein films which is called protein film voltammetry (PFV).

2.1.1 Cyclic Voltammetry

Within a cyclic voltammetry experiment an electrode is immersed in a solution and while the applied potential is swept the resulting current is recorded. The applied potential can be swept between two values with a triangular waveform (Figure 2.2). As it can be seen from the figure the potential is linearly altered in positive/negative directions and, finally, reach its initial value. This cycle can be repeated several times.

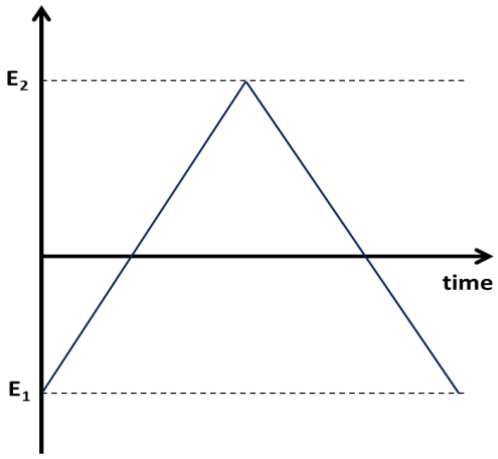

Figure 2.2 Voltage sweep between two values at a fixed rate in a cyclic voltammetry experiment.

In the case of the static electrode a typical peak shape of a cyclic voltammogram of electro-active species in solution and adsorbed on electrode surface can be seen from figure 2.3 With respect to this example, once the initial potential is applied, it is swept in the positive direction to obtain an anodic signal (current). The anodic wave correlates with the oxidation of the sample on the electrode. The oxidation signal will start to increase due to the applied oxidative potential until there is not enough oxidizable analytes in the system. This process is called *forward scan*. The reverse process (*reverse scan*) is observed when the reduction starts and cathodic current will increase as long as there is enough reducible analytes in the system. Finally the potential comes back to its initial value. The maximum point of the oxidation and reduction peaks are called peak potentials and the peak height is the distance between the maximum peak point and the baseline of the current approximation line. Values of peak potentials, peak height and peak position determine the reversibility of the reaction. Reversibility is related to the electrode kinetics depending on how fast or slow the electrons are transported from the molecule of interest to the electrode [12, 14, 15].

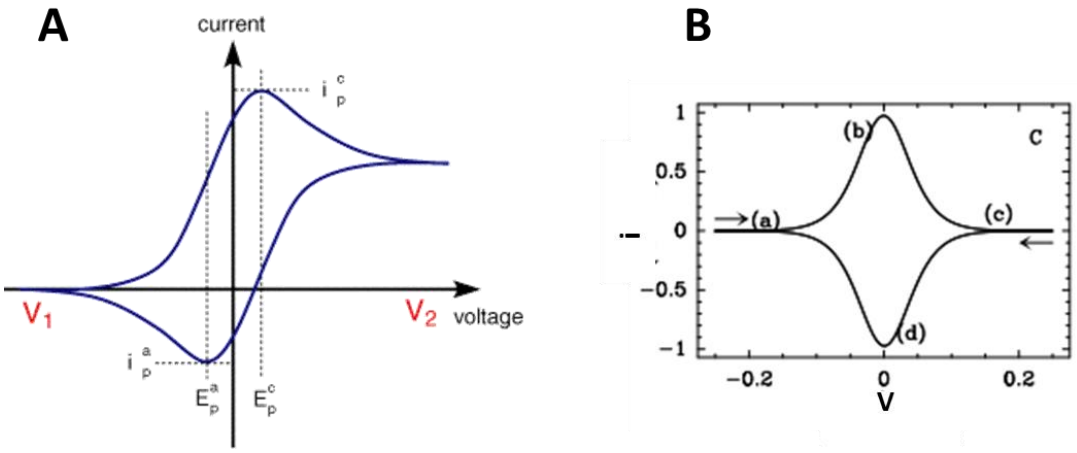

Figure 2.3 Cyclic voltammogram of; A) Redox species free to diffuse in solution [11], B) Redox species adsorbed on the surface of an electrode [12].

For a typical reversible cyclovoltammogram of a stationary electrode the oxidation and reduction signals should be symmetrical (adsorbed species, Figure 2.3 (B). Analysing the area under the oxidation/reduction peaks (figure 2.3A) provides information about the charge passed for the redox couple on the surface. For example while working with electroactive

enzymes on the electrode surface in the absence of substrate it is possible to calculate the amount of adsorbed electro-active species on the surface by using the equation [12] :

$$\Gamma = \frac{Q_F}{nFA} \qquad \textbf{Equation 2.1}$$

where, Q_f represents the integration of the oxidation/reduction peak, *n* is the number of electrons transferred, *F* is the Faraday constant and *A* is the area of the electrode.

The catalytic properties of enzymes can be studied by introducing substrate to the electrolyte solution. In such a situation, electrons will be transfered between electrode and the substrate via the enzyme which will be observed as catalytic current. In figure 2.14 a sigmoidal curve obtained with a rotating electrode and a typical cyclovoltammogram of a catalytic reaction with different rotation rates are shown. Catalysis is determined by the turnover frequency (k_{cat}) of the enzyme. By using rotating disk electrodes the electrode can be rotated along its axis and the solution is stirred. This generates a convective movement of the solution which increases the transport of electro-active species to the electrode surface. Since the concentration of reduced and oxidized species reach the equilibrium values the current reaches a limiting value (i_{lim}) as it can be seen from figure 2.4.

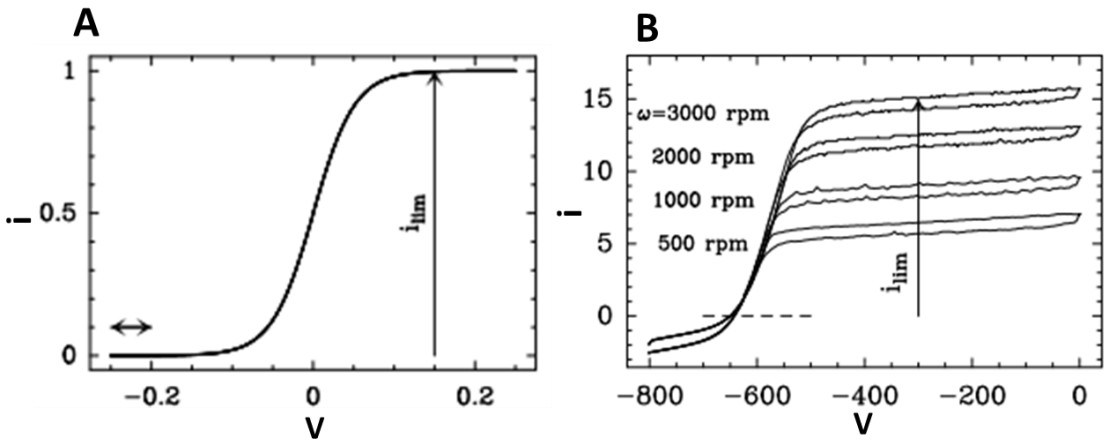

Figure 2.4 A) Sigmoidal wave obtained in a cyclic voltammetry of an electro-active species in solution at a rotating disk electrode, B) Catalytic wave of an adsorbed catalytic enzyme on the electrode surface showing the influence of rotation rate on the catalytic current [12]

The *Levich* equation shows that when a catalytic reaction is dependent on the rate of supply of substrate, the current will also be dependent on the rotation rate of the electrode [13].

$$i_{lim} = 0.62nFAD^{2/3}\omega^{1/2}v^{-1/6}c_0 \qquad \textbf{Equation 2.2}$$

where *n* is the number of transferred eletrons during the catalytic reaction, F is the Faraday constant, A is the surface area of the electrode, D is the diffusion coefficient, ω is the angular velocity, *v* is the kinetic viscosity and c_o is the concentration of electro-active species. After a certain rotation rate the current will reach a maximum value which can be calculated by plotting the reciprocal current against the reciprocal square root of the rotation rate according to the *Koutecky-Levich equation* [13],

$$\frac{1}{i_{lim}} = \frac{1}{i_{max}} + \frac{1}{0.62nFAD^{2/3}\omega^{1/2}v^{-1/6}c_0} \qquad \textbf{Equation 2.3}$$

2.1.2. Protein Film Voltammetry

Protein Film Voltammetry (PFV) was first introduced by F. Armstrong in the 1970`s with small redox proteins and later with soluble fragments of larger membrane proteins [14, 15]. Throughout PFV experiments protein is attached on the electrode surface and with small quantity a high resolution can be obtained. PFV technique can be used to study various properties of redox-active proteins such as, proton transfer [16], proton pumping [17, 18], inter- and intra-molecular electron transfer [19, 20], and several other applications [21].

In the course of a PFV experiment, proteins are adsorbed onto the electrode and direct electrochemistry is achieved. The application of a potential will induce an electron flow between substrate and the electrode. It is crucial to obtain a stable protein film on the electrode surface without losing the protein function and stability. Various strategies can be found in the literature for the protein adsorption on electrode surface [22-24], however we will focus on protein adsorption on gold surface via thiol-based monolayers. The metal electrode surface can be coated with thiol layer in order to prevent protein denaturation. Polarity and the morphology of the obtained thiol layer can be tuned to obtain appropriate protein adsorption [25]. It is possible to use gold nanoparticles to increase the surface area of the electrode. Preliminary results from our group showed that gold nanoparticles with

different sizes can be used to adsorb cytochrome bo_3 oxidase on gold electrode to obtain a direct electron transfer between electrode and the adsorbed protein [26].

In the absence of substrate, redox active proteins that are immobilized on the electrode give peak shaped signals. This peak can be attributed to the cofactors inside the proteins. By integrating this peak the surface coverage of the electrode can be calculated. However, after addition of substrate, peak signals transform into catalytic waves. For example in figure 2.5 the catalytic activity of cytochrome *bo_3* oxidase immobilized on a rotating disk electrode is shown. Electrons coming from the electrode pass to the redox centers in the protein and react with O_2 to produce water. Thus, the electrons passing from electrode to the protein do not return to the electrode, resulting in an irreversible sigmoidal-shaped signal.

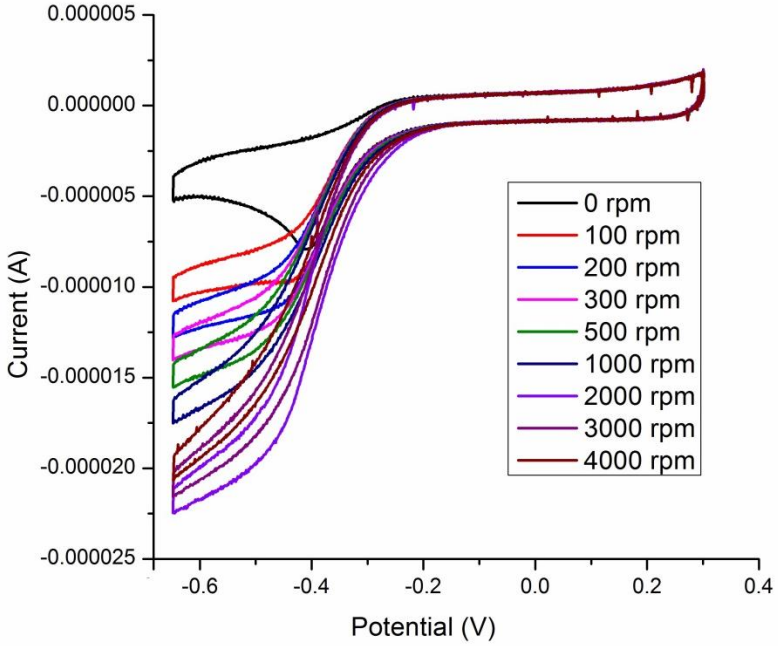

Figure 2.5 Cyclic voltammogram of cytochrome *bo_3* oxidase immobilized on a rotating gold disk electrode (in KPi buffer at pH 7.5) modified with Au nanoparticles and thiols (0.02 $V.s^{-1}$).

It is possible to estimate the number of moles of product produced per second by a saturated enzyme by calculating the k_{cat} value according to the formula;

$$\frac{1}{i_{max}} = \frac{C + K_m}{nFA\Gamma k_{cat} C} \qquad \textbf{Equation 2.4}$$

where K_m is the Michaelis-Menten constant, nF is the electrons per mole of adsorbed redox centers, Γ is surface concentration of electro-active species and A is the electrode surface. Usually the ratio of k_{cat}/K_m is calculated as a measure of enzyme efficiency. A large value of k_{cat} indicates rapid turnover and small value of K_m high affinity for substrate which together makes the k_{cat}/K_m ratio larger.

2.2 Spectroscopy

Spectroscopy was used to study small molecules and to characterize unknown chemicals for two centuries. Until 1960s spectroscopy was not applied to biological samples due to the limited sensitivity, lack of proper detectors, light source and the difficulty of sample preparation. However, nowadays it has been become one the most common techniques to study large and complex molecular systems.

In this thesis we focused on two main types of spectroscopy, UV/Vis spectroscopy and infrared spectroscopy.

Spectroscopy uses the interaction between matter and radiation. When a matter is exposed to electromagnetic radiation it can be reflected, scattered, absorbed, transmitted or can undergo photoluminescence (Figure 2.6)

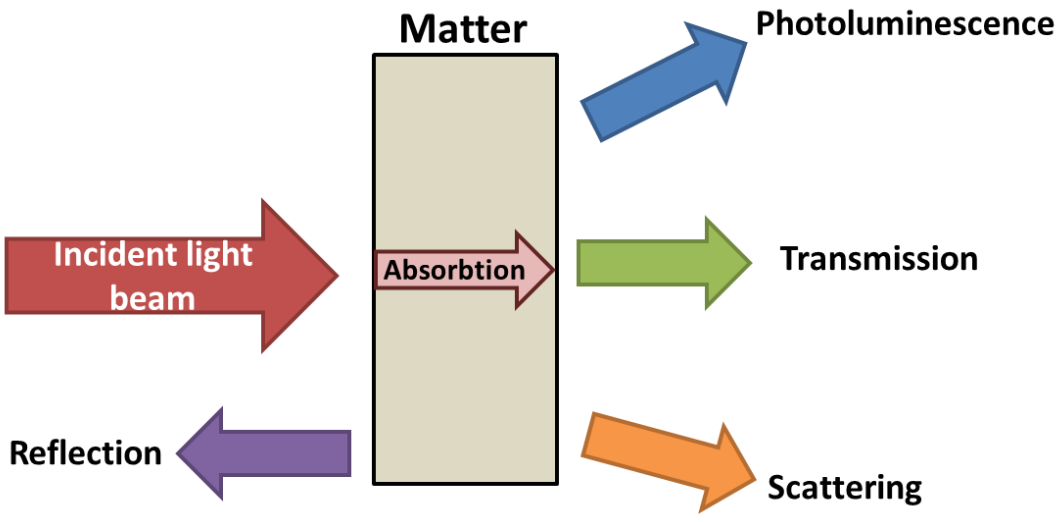

Figure 2.6 Interaction of matter and radiation.

It is important to understand that light has both wave and particle characteristics. The wave-like nature of light can be described with the frequency, wavelength and amplitude of the wave of light. The frequency (ν) of the wave is the number of oscillations it makes per second and the amplitude (A) of the wave is the maximum distance it moved from its original position. The wavelength (λ) of the light is the distance between the two maximum peak points of two consecutive waves.

The particles of light that have wave-like nature in movement are called photons. Energy of photons (E) can be calculated with the following equation,

$$E = h\nu \qquad \textbf{Equation 2.5}$$

where h is the Planck`s constant and ν is the frequency. Frequency is related to the wavelength according to the equation,

$$c = \lambda \nu \qquad \textbf{Equation 2.6}$$

where c is the speed of light and λ is the wavelength. The electromagnetic spectrum (Figure 2.7) is made of different domains which are developed with respect to the wavelength thus, the energy of the light.

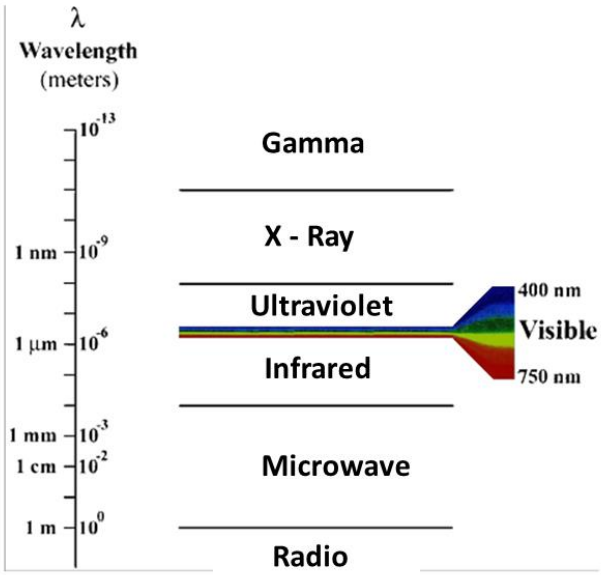

Figure 2.7 Electromagnetic spectrum [27].

2.2.1 UV/Vis Spectroscopy

When a material absorbs UV/Vis light outer electrons move from ground states to excited states. Materials have colors by absorbing certain wavelengths of light and transmitting the rest in the visible range. The promotion of electrons to excited states can also occur in the ultraviolet region (UV).

In the ground state, electrons are usually in three types of orbitals such as σ bonding, π bonding and non-bonding orbitals. When electrons are excited by electromagnetic radiation, they can move to anti-bonding orbitals (σ^* and π^*).

UV/Vis spectroscopy measures the transmittance (T) by measuring the light intensity after it passes the sample (I) and the intensity of incident light (I_0).

$$T = I / I_0 \qquad \textbf{Equation 2.7}$$

From the transmittance ratio the absorbance of light by the sample can be calculated (A) by,

$$A = - log\ T = - log\ (I / I_0) \qquad \textbf{Equation 2.8}$$

From the Beer-Lambert law [23], it is known that the absorbance of sample is dependent on the absorption coefficient of the sample (ε), the path length of the absorbing solution (l) and the concentration of the sample (c);

$$A = \varepsilon\ l\ c \qquad \textbf{Equation 2.9}$$

From an UV/Vis spectrum it is possible to determine the wavelength at which maximum absorption occurs (λ_{max}) and together with the absorption coefficient (ε) of the sample the concentration of the sample can be determined.

2.2.1.1 UV/Vis Spectroscopy coupled with Electrochemistry

Combination of electrochemistry with UV/Vis spectroscopy enables to study the samples in different redox states. Heme proteins are well studied with UV/Vis spectroscopy by focusing on the characteristic bands of hemes in their structure. In particular, *b* and *c* type hemes have absorption between 400-450 nm (soret band) and 500-550 nm (alpha band) [28, 29]. The

exact positions of these bands are dependent on axial ligands, spin states, oxidation/reduction state and nearby amino acids of the hemes (see table 2.1). In order to study redox active proteins we used an electrochemical cell [30] which is shown in figure 2.8.

Table 2.1 Attribution of main characteristic heme bands [28, 31-33].

	Position		Spin State
	Alpha band	Soret band	
Heme *c*	550 nm	426 nm	Low-spin
Heme *b*	560 nm	428 nm	Low-spin
Heme b_3	555 nm	430 nm	High-spin
Heme *o*	560 nm	428 nm	High-spin

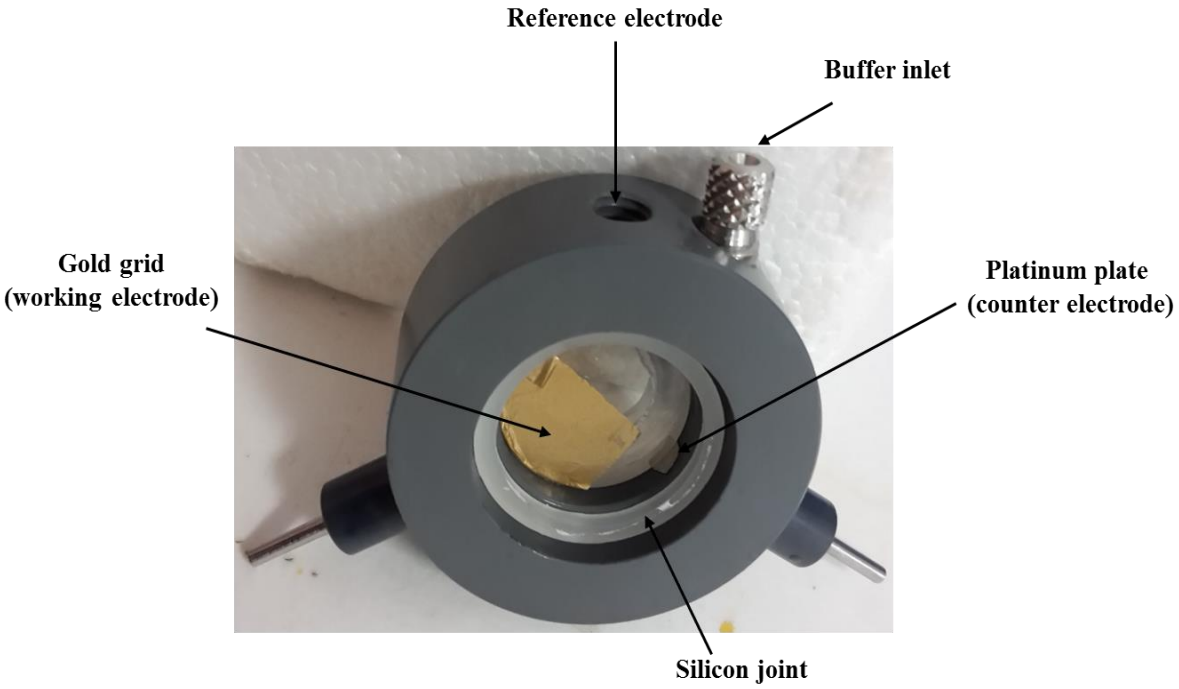

Figure 2.8 Thin layer electrochemical cell.

This electrochemical cell can also be used in infrared, Raman and fluorescence spectroscopy [34]. The cell contains two transparent calcium fluoride (CaF_2) windows attached on a pvc support, two plastic joints between the windows, a gold grid as working electrode, a platinum plate as counter electrode, inlets for reference electrode (Ag/AgCl) and inlet for the buffer injection into the cell. CaF_2 enables the transmission of IR, UV and Vis light. The gold grid is modified with a mixture of thiols (2mM 3-Mercaptopropionic acid and 2mM cysteamine) to prevent protein adsorption on the gold grid and eventually preventing denaturation. Protein sample is deposited on the previously modified gold grid and the temperature of the setup is controlled by pumping water in the cell continuously (5-12 C˚ depending on the stability of protein).

2.2.1.2 Potentiometric titrations

Most of the redox-active proteins contain one or more redox-active cofactors such as heme, FAD and NAD. These cofactors are crucial elements of the electron transportation and other reactions in the proteins which were explained in detail in section 1.5.2. If we consider a single cofactor, the equilibration between the two states (A_{oxd}/A_{red}) can be represented as;

$$\boldsymbol{A_{ox} + e^{-} \leftrightarrows A_{red}}$$

By using potentiometric titrations the reduction/oxidation potentials of cofactors can be determined with respect to the A_{oxd}/A_{red} by equilibrating the protein at different potentials. The potential can be applied by addition of oxidants and reductants or by coupling the system with a potentiostat. In small structures like cytochrome *c*, electron transfer to the protein is fast. However, in large proteins (membrane proteins) electron transfer to the active site of the protein is relatively slow. In order to accelerate the electron transfer electron transferring agents such as mediators are used. Utilization of a mixture of mediators allows obtaining fast equilibrium at different potentials.

During a typical redox titration of a membrane protein a reference spectrum is recorded in oxidized or reduced state and with each different applied potential, change in the absorbance value of the cofactors are recorded. In figure 2.9 potentiometric titration of nitric oxide reductase (NOR) from *P.denitrificans* is shown. In this example two distinctive bands of NOR (Soret and alpha bands) are present. The Soret band appears at about 420 nm and the

alpha band appears at about 550 nm with a shoulder at 560 nm. The Soret band emerges from π-π^* transitions and has a strong contribution in porphyrin containing structures [35]. The Soret band contains information about most of the hemes and it is not efficient to obtain detailed information on each heme by itself. Alpha band at about 550 nm and its shoulder at 560 nm, are also due to π-π^* transitions, however it has relatively small intensity [35]. The main band at 550 nm can be attributed to *c* type hemes and the shoulder at 560 nm to the *b* type hemes, thus it is the main band in focus to investigate the contributions of hemes separately.

The absorbance value of each potential step can be recorded and a titration curve can be fitted most generally by using Nernst equation fitting [36] or Gaussian fitting function [37]. In our case we used Gaussian fitting function to fit the first derivative of the absorbance values obtained from the titrations. The Gaussian model fits peaks with respect to the amplitude, center point (location), peak width and number of the components. Gaussian fitting process is described in detail in section 3.3.1 b.

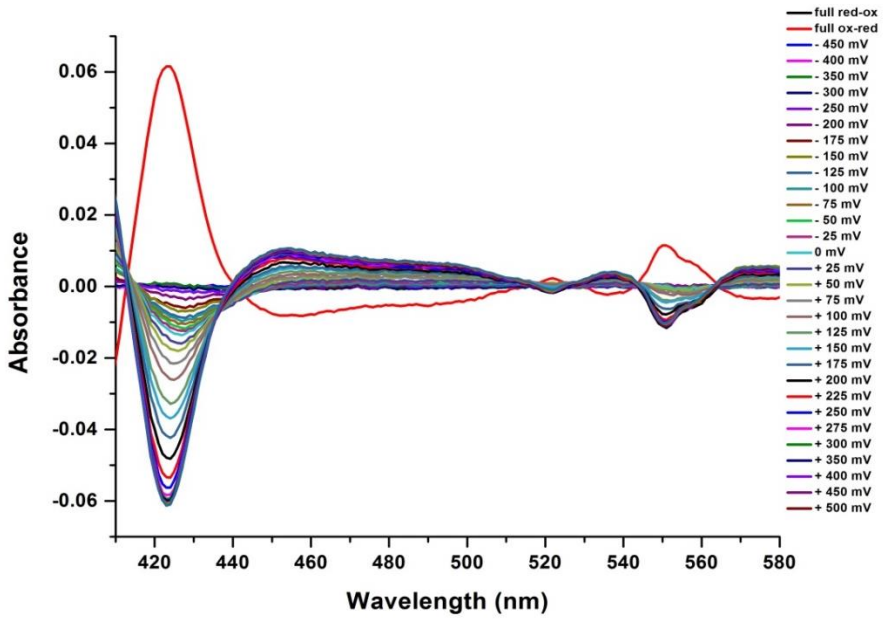

Figure 2.9 Potentiometric titration of cNOR from *P. denitrificans* in Tris buffer at pH 7.5 by using UV/Vis spectroscopy.

2.2.2 Infrared Spectroscopy

Infrared spectroscopy focuses on the vibrations of atoms in a molecule. A typical infrared spectrum is obtained by exposing the sample to infrared radiation and calculating the amount of absorbed radiation at a particular energy. Any peak in absorption spectrum is related to the frequency of a vibration from a part of the molecule of interest. The spectral range is divided into three regions; near infrared between 12500-4000 cm^{-1} (0.8-2.5 µm), mid infrared between 4000-667 cm^{-1} (2.5-15 µm), Far infrared between 667-50 cm^{-1} (15-200 µm). For a molecule to show an infrared absorption it must have a changing dipole moment during the vibration. These molecules are called 'infrared active' molecules.

For a triatomic molecule, the atoms of the molecule can move relative to each other. This means that bond length, angle can change or one of the atoms can move from its present state. These stretching and bending movements are called vibrations. Vibrations have various forms such as a change in bond length (stretching), a change in the bond angle (bending). The bonds can also stretch in-phase (symmetrical) or out-of-phase (asymmetrical). There are four types of bending vibrations: deformation, rocking, wigging and twisting that can be visualized by the movement of hydrogen atoms in the simple CH_2 system [38]. Figure 2.10 shows a summary of commonly seen stretching and bending vibrations in IR spectroscopy.

There are various methods to obtain an infrared spectrum. The most common and recent technique is the fourier-transform infrared spectroscopy (FTIR). This approach is based on the interference of two beams of radiation to obtain an *interferogram* [39].

Basic components of an FTIR instrument are the source, an interferometer, the detector, an amplifier, an analog-digital converter and a computer. The most common interferometer is the Michelson interferometer which is composed of one stationary and one moving mirror [40]. In figure 2.11 the schematic of a typical FTIR instrument with a Michelson interferometer is shown.

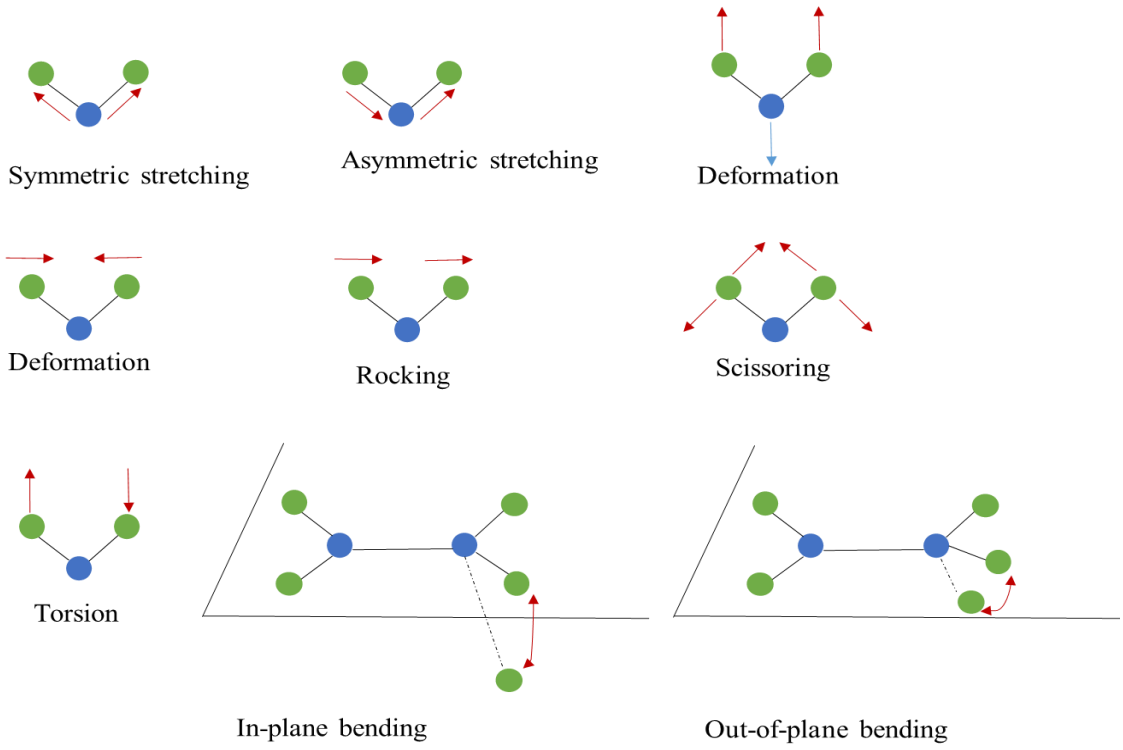

Figure 2.10 Normal vibrational modes commonly seen in IR spectroscopy [41].

When the incident beam collides to the beam splitter 50% of the beam will be reflected to the stationary mirror and the other 50% to the moving mirror and they both come together to the beam splitter and interfere before reaching the sample. Interference of two beams creates an interference profile called interferogram which is transformed into conventional spectrum by the Fourier-transformation. The moving mirror is an important part of the interferometer. It creates an optical path length difference ((n + ½) λ) and affects the interfered beams in a destructive or constructive way. The resolution of FTIR instrument is related to the maximum value of optical path length between the two beams generated by the moving mirror.

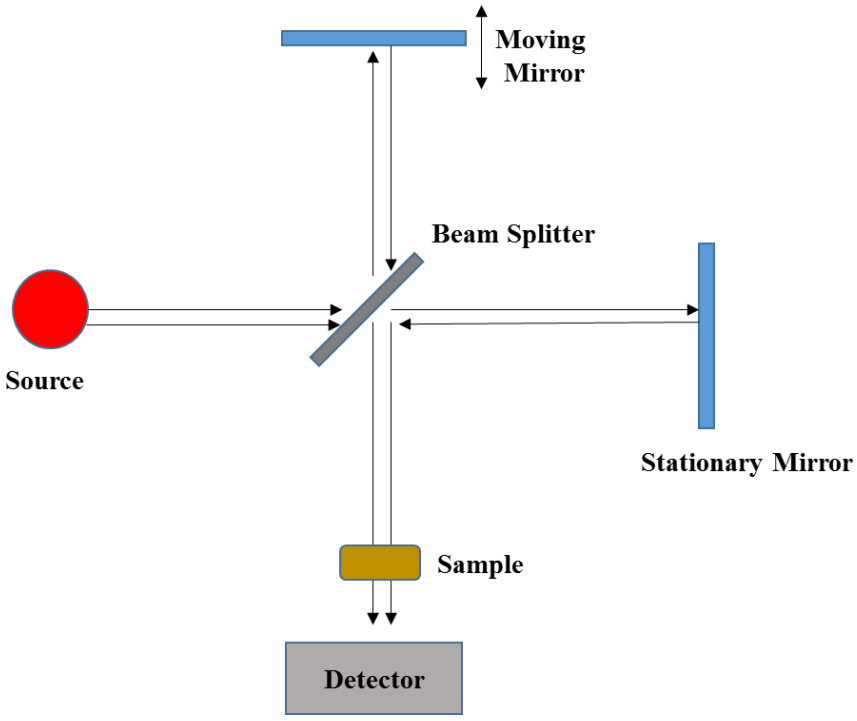

Figure 2.11 Schematic of a typical FTIR instrument with a Michelson interferometer.

Fourier transformation is a mathematical approach to translate the data in terms of '*time*' to the function of frequency [42]. There are two main formulas used in this transformation. First equation is:

$$\boldsymbol{I(\delta) = \int_{0}^{+\infty} B(v)\, cos(2\pi v\delta) dv} \qquad \textbf{Equation 2.10}$$

where $\boldsymbol{I(\delta)}$ is the intensity of beam on the detector, $\boldsymbol{v}$ is the spectral density at a wavenumber. It shows the relation between spectral density with the difference in the pathlength. Other pair of the fourier transformation given by $\boldsymbol{B(v)}$ is as following;

$$\boldsymbol{B(v) = \int_{-\infty}^{+\infty} I(\delta)\, cos(2\pi v\delta) d\delta} \qquad \textbf{Equation 2.11}$$

which shows the intensity in terms of wavenumber. Fourier transformation requires two interferograms with and without a sample to obtain spectra.

2.2.2.1 Infrared Spectroscopy of Proteins

Infrared spectroscopy is one of the most common techniques to study proteins [43-46]. It is a useful tool to obtain information on the chemical composition and orientation of residues in

proteins. It is also possible to investigate molecular mechanisms in proteins together with their structural properties. One of the advantages is the short measuring time and small amounts of sample demand. The mid-infrared region is the most studied spectral region for proteins since it contains many structural and functional information and perfectly studied in literature.

Proteins have several infrared-active bonds in their structures and it is possible to obtain information on several parameters of proteins such as their backbone structure, amino acid side chains and cofactors. Vibrational modes of the protein backbone are the most dominant features of proteins in IR absorption spectrum. In table 2.2 the vibrational modes of the amide group from the protein backbone are summarized.

Table 2.2 Vibrational modes of the amide group from the protein backbone [47]

Appellation	Position (cm^{-1})	Vibrational mode
Amide A	≈3300	ν(N-H)
Amide B	≈3100	ν(N-H) in resonance with an overtone of Amide II
Amide I	1700-1600	V(C=O) 80%, ν(C-N) 10%, δ(N-H) 10%
Amide II	1580-1510	δ(N-H) 60%, ν(C-N) 40%
Amide III	1400-1200	δ(C-N) 30%, δ(N-H) 30%, ν(C=O) 10%, δ(N-C=O) 10%

In figure 2.12 the characteristic IR absorption spectrum of *N*-methylacetamide (NMA) showing all normal modes of amide group is shown. Amide A and B modes (3300 cm^{-1} and 3070 cm^{-1}) originates from NH stretching vibrations and the latter is resonant with an overtone from amide II vibration. Amide I mode (1650 cm^{-1}) arises from the C=O stretching vibration dominantly and with small contributions from out-of-phase CN stretching vibrations and NH in-plane bending. The amide I band of proteins is sensitive to the secondary structure of the protein due to transition dipole coupling and secondary structural analysis can be done from this region by de-convoluting this band. α helices in the backbone structure of proteins

give rise to the band at 1655 cm^{-1}, antiparallel β-sheets have a strong signal at 1630 cm^{-1} and relatively weaker band at 1685 cm^{-1} in H_2O. Parallel β-sheets main band is ≈ 4 cm^{-1} away from the antiparallel β-sheet main band (1630 cm^{-1}) and can go as low as 1619 cm^{-1} in some proteins. Distinction between the main and side band of parallel β-sheets is less significant and the latter is sometimes not visible. The β-turn structure normal modes have a clear band at about 1672 cm^{-1} and disordered structures at ≈ 1654 cm^{-1}. In table 2.3 the summary of the assignments of secondary structures of amide I band is shown.

Table 2.3 Assignment of secondary structures of amide I band [48]

Secondary structure	Position cm^{-1} in H_2O	
	Average	**Extreme**
α-helix	1654	1648-1657
β-sheet	1633	1623-1641
	1684	1674-1695
Turns	1672	1662-1686
Disordered	1654	1642-1657

Amide I and amide A modes overlap with stretching and bending modes of water which is the major handicap for making assignments in these regions. The amide II mode (1550 cm^{-1}) arises mainly from the NH in-plane bending and CN stretching vibrations together with smaller contributions from CO in plane bending, CC and NC stretching vibrations. The amide II mode also provides structural information and together amide I and II modes are not strongly affected by side chain vibrations. The amide III mode (1400-1200 cm^{-1}) mainly arises from NH bending and CN stretching vibrations and together with small contributions from CO in plane bending and CC stretching.

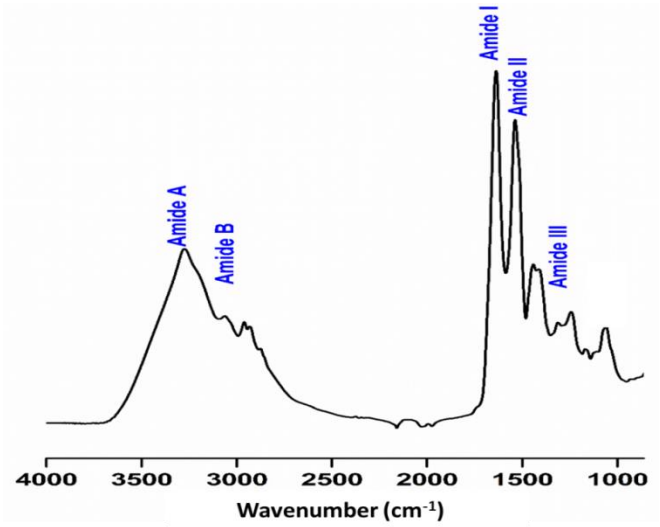

Figure 2.12 IR absorption spectrum of N-methylacetamide (NMA) showing all normal modes of an amide group [49]

2.2.2.2 Transmission mode

The transmission mode is the most common method in IR spectroscopy. Liquid, solid and samples in the gas can be measured with this mode. Proteins can be solubilized in various solvents in a special cell which has a tunable path length. These cells are made of special infrared transparent windows such as NaCl, KBr, CaF_2, KCl, CsBr and CsI and it is crucial to choose appropriate solvent for the sample not to damage the windows or the sample.

2.2.2.3 Differential IR Spectroscopy

FTIR difference spectroscopy is used to analyze proteins by perturbing the active site of the protein into two different states and subtracting their IR spectrum with each other [50-53, 21, 45]. Perturbation of the proteins active site can be induced by light, perfusion or electrochemical means. In this study we focused on the electrochemically-induced FTIR difference spectroscopy. Combination of electrochemistry and IR spectroscopy enabled us to probe all proteins with redox-active sites. A special thin-layer cell which was described previously in section 2.2.1.1 is necessary to perform IR differential experiments. With this technique the sample is reduced or oxidized in a electrochemical way and one of the states are used as a reference spectrum for the other. In figure 2.13 a typical reduced-oxidized spectrum of a protein is shown.

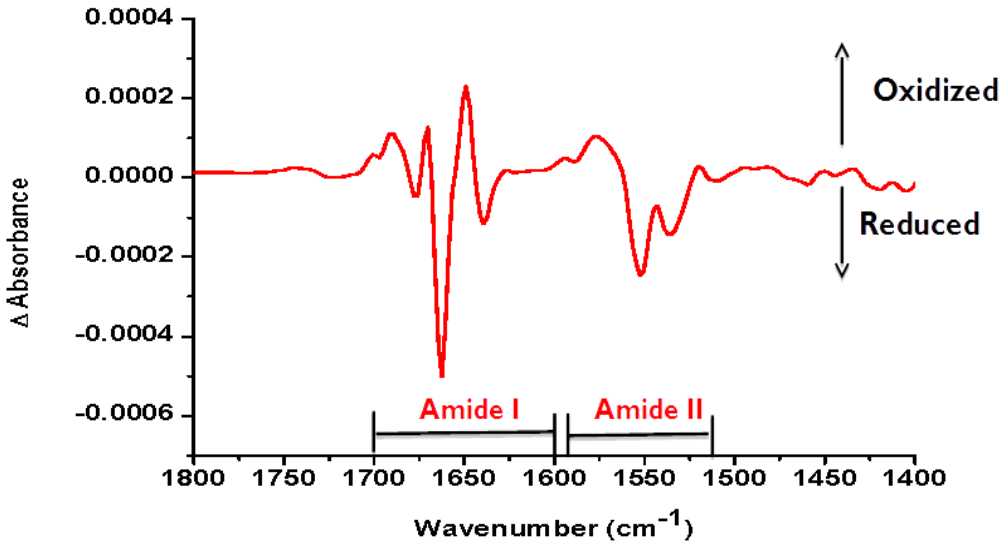

Figure 2.13 Electrochemically-induced infrared differential spectrum (ox-red) of cytochrome *bo*$_3$ from *E. coli* at pH 7.5

From the IR differential spectrum the changes in the frequencies, intensities of molecular vibrations which arise from conformational changes and coupled protonation changes during the redox reactions can be analyzed. It is possible to obtain information on the conformational changes, hydrogen bonding interaction of cofactors and redox intermediates, coupled electron and proton transfer (Asp, Glu protonation states).

Band assignments are usually made by comparing the protein spectra with the spectra recorded on a model compound [54, 55], by site-directed mutations [56, 57] or by isotopic labeling [58]. Contribution of cofactors or amino acids can be determined by comparison with the spectrum of isolated molecules (amino acids) [59].

Site-directed mutations are widely used in order to study the importance of crucial amino acids by replacing specific amino acids in protein structure and by comparing the IR spectrum of wild type protein with the mutant protein. The change in the IR signal in the spectrum of mutant can then be assigned to the mutated amino acid. However, it is important not to mutate crucial amino acids in protein in order not to inhibit protein function. Mutation of a specific amino acid can cause conformational changes in the protein and the effect of mutation on the IR spectrum should be studied carefully.

By using isotope labeling specific groups in proteins can be identified. Ligands, cofactors, protein side chains and backbone groups can be labeled without losing the function of protein and causing conformational changes. Labeled groups will have significant effects on their vibrational frequencies and the absorption bands will be shifted.

Heme-copper oxidases were widely studied by using various infrared spectroscopy approaches [21, 60, 61]. Cytochrome *c* oxidase is one of the most studied heme-copper oxidases. There are several studies to understand the proton translocation by focusing on the protonation sites. Glu-278 (*P. denitrificans*) was shown to be coupling the proton pathway to the catalytic center [62] and it was investigated by site directed mutagenesis [62]. The corresponding amino acid was studied in cytochrome bo_3 oxidase from *E. coli* (Glu-286) [64] and in *Rhodobacter sphaeroides* as well [65].

2.2.2.4 Reflectance Mode

Preparing samples for transmission measurement can be a complex task especially for liquid samples, since they should be poured into a special cell with a certain path length without forming bubbles inside. However, in attenuated total reflectance (ATR) spectroscopy mode sample preparation is generally fast and no preparation is needed. It has an excellent sample-to-sample reproducibility and minimal operator-induced variations.

There are several reflectance techniques which can be divided into two main groups; internal reflectance where an attenuated total reflectance is in contact with the sample and external reflectance where the infrared beam is reflected directly from the sample. In this study attenuated total reflectance spectroscopy is used. Under specific conditions if the IR beam is reflected into an ATR prism with high refractive index it will be internally reflected. If the angle of incidence between sample and crystal (θ) is larger than the critical angle (θ_c) and the refractive index of the crystal (n_1) is larger than the refractive index of the solvent (n_2) of sample, total interior reflection will be obtained (Figure 2.14).

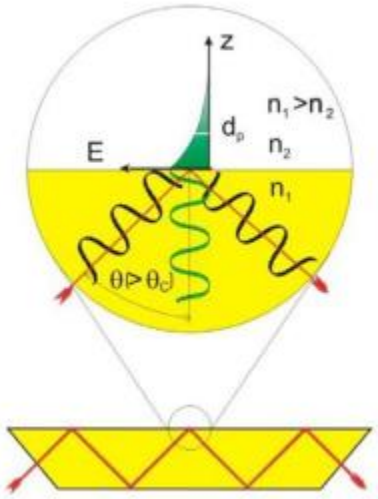

Figure 2.14 Schematic representation of an ATR crystal [66]. Incident IR beam makes three reflections and detailed explanation of the formation of evanescent waves

Each internal reflection of IR beam will create an evanescent field which can penetrate beyond the surface of the crystal if the sample absorbs IR radiation and is in close contact to the surface. Radiation can penetrate approximately 1 μm distance depending on θ and α and diminishes dramatically after. Distance of penetration can be calculated by using the formula [66];

$$d_p = \left(\lambda / n_1\right) \Big/ \left\{2\pi\left[\sin\theta - \left(\frac{n_1}{n_2}\right)^2\right]^{1/2}\right\} \qquad \textbf{Equation 2.12}$$

where, λ is the wavelength and d_p is the dept of penetration.

Proteins can be studied with ATR spectroscopy by adsorbing or drying them on the surface of the crystal [67, 68]. It requires less concentrated sample and less volume than in transmission mode. It is possible to obtain electrochemically induced differential spectra of proteins by using special setup and applying potential to the sample [69]. Another possibility to obtain difference spectra is to exchange the buffer or substrate via perfusion [72]. It is crucial not to detach the proteins on the surface during these manipulations, thus, the covalent attachment of proteins is better for more stable protein films on the surface. Several surface modification techniques are possible for the covalent attachment of proteins while preventing their

denaturation [22, 68-71]. Another efficient technique to protect the protein film is to use a dialysis membrane on top of the protein film [73].

2.2.2.5 Surface-enhanced Infrared Absorption Spectroscopy (SEIRAS)

In 1970s researchers found out that a surface enhancement effect of at least 10 times along the metal surfaces can be obtained with pyridine molecules in Raman spectroscopy [74]. In mid 1980s it was shown that the infrared signal of adsorbed molecules were also enhanced when they were in close contact with metal surfaces [75].This technique thus seems promising for the study of biological molecules.

Surface enhancement IR absorption is achieved by adsorbing molecules on nano-structured thin film surfaces such as densely packed gold metal islands [76]. When compared with standard ATR measurements SEIRA effect provides an enhancement up to three orders of magnitude.

Both local electromagnetic mechanism and chemical mechanism generate the surface enhancement along metal surfaces. Electromagnetic mechanism is based on the excitation of surface plasmons of metal surfaces by incident IR radiation. On metal islands dipole (d) is induced and it generates a local electromagnetic field which is stronger than the incident photon field around the metal island. This local electromagnetic field excites the molecular vibrations (V_{mn}) (Figure 2.15). The local electromagnetic field intensity decays dramatically when 10 nm of distance from the surface is exceeded.

The chemical enhancement mechanism is related to the adsorption of molecules on the metal surfaces. Chemical reactions between the surface and the molecule generate higher enhancement than the physical adsorption of molecules. This difference is due to the charge oscillations between molecular orbitals and the metal surface increasing the absorption coefficients of adsorbed molecules.

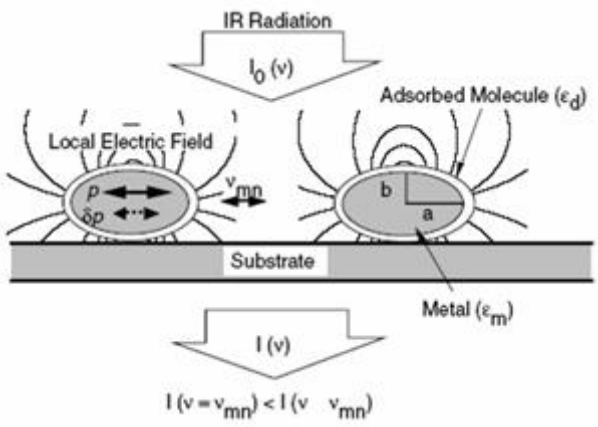

Figure 2.15 Schematic representation of electromagnetic enhancement mechanism on metal islands [77]

There are several factors affecting the enhancement properties. Topology of the metal surface has a crucial role in the enhancement mechanism and the best enhancement can be achieved with nano meter scale, rough surfaces. Metal islands on the surface together with the adsorbed molecules and the solvent have a contribution on the enhancement factor and can be calculated by the Bruggeman formula [22];

$$\boldsymbol{\varepsilon^{BR} = \varepsilon_h \frac{3(1-F)+F\alpha}{3(1-F)-2F\alpha}} \qquad \textbf{Equation 2.13}$$

where F is the packing density of metal islands, ε_h is the dielectric function of the solvent and α is the polarizability of the metal. It was shown that the shape and roughness of the metal particles affect the enhancement factor by directly affecting the polarization value α.

Surface enhancement is also dependent on the orientation of the adsorbed molecules. We observe a much more powerful enhancement in the vibrational modes if the change in the dipole moments is parallel to the surface. This rule can be used to study surface orientation of adsorbed molecules by comparing the SEIRAS spectra with the normal IR spectrum [77].

The study of a monolayer of proteins with ATR spectroscopy is limited due to the low signal intensity. Thus, SEIRAS is a promising technique to study proteins. As described previously the orientation of the protein on the surface is important for the enhancement factor. Water soluble and small proteins are easier to attach to the solid surfaces to form self-assembled monolayers (SAMs), by electrostatic or hydrophobic interactions. However, membrane

proteins have amphiphilic nature and low stability which make them harder to adsorb on the surfaces. Covalent attachment of membrane proteins enables to control their orientation on the surface and to retain their activity. As an example membrane enzymes can be attached on a gold surface through the *His-tag* which will be discussed in detail in section 3.3.2.2 [78].

References

1. Morrison, S.R. Electrochemistry at Semiconductor and Oxidized Metal Electrodes. United States: Plenum Press,New York, NY, 1980.
2. Pingarrón, J. M., Yáñez-Sedeño, P., & González-Cortés, A. (2008). Gold nanoparticle-based electrochemical biosensors. Electrochimica Acta, 53(19), 5848–5866.
3. Wang, J., Li, M., Shi, Z., Li, N., & Gu, Z. (2002). Direct electrochemistry of cytochrome c at a glassy carbon electrode modified with single-wall carbon nanotubes. Analytical Chemistry, 74(9), 1993–1997.
4. Hrapovic, S., Liu, Y., Male, K. B., & Luong, J. H. T. (2004). Electrochemical Biosensing Platforms Using Platinum Nanoparticles and Carbon Nanotubes. Analytical Chemistry, 76(4), 1083–1088.
5. Feng, J. J., Zhao, G., Xu, J. J., & Chen, H. Y. (2005). Direct electrochemistry and electrocatalysis of heme proteins immobilized on gold nanoparticles stabilized by chitosan. Analytical Biochemistry, 342(2), 280–286.
6. Meyer, T., Gross, J., Blanck, C., Schmutz, M., Ludwig, B., Hellwig, P., & Melin, F. (2011). Electrochemistry of Cytochrome c 1 , Cytochrome c 552 , and Cu A from the Respiratory Chain of Thermus thermophilus Immobilized on Gold Nanoparticles. The Journal of Physical Chemistry B, 115(21), 7165–7170.
7. Battistuzzi, G., Borsari, M., Sola, M., & Francia, F. (1997). Redox thermodynamics of the native and alkaline forms of eukaryortic and bacterial class I cytochromes c. Biochemistry, 36(51), 16247–16258.
8. Alwarappan, S., Joshi, R. K., Ram, M. K., & Kumar, A. (2010). Electron transfer mechanism of cytochrome c at graphene electrode. Applied Physics Letters, 96(26).
9. Thorp, H. H. (1992). Electrochemistry of proton-coupled redox reactions: Role of the electrode surface. Journal of Chemical Education, 69(3), 250–252.
10. Hirst, J., Duff, J. L. C., Jameson, G. N. L., Kemper, M. A., Burgess, B. K., & Armstrong, F. A. (1998). Kinetics and mechanism of redox-coupled, long-range proton transfer in an iron-sulfur protein. Investigation by fast-scan protein-film voltammetry. Journal of the American Chemical Society, 120(28), 7085–7094.
11. Yanpeng Xue. Voie innovante pour la nano micro texturation de surfaces metalliques a based assemblage de nanoparticules d'Auapplication superhydrophobe. Material chemistry. Universite Pierre et Marie Curie - Paris VI, 2014. French.

12. Léger, C. (2013). An Introduction to Electrochemical Methods for the Functional Analysis of Metalloproteins. Practical Approaches to Biological Inorganic Chemistry, 179–216.
13. Masa, J., Batchelor-McAuley, C., Schuhmann, W., & Compton, R. G. (2014). Koutecky-Levich analysis applied to nanoparticle modified rotating disk electrodes: Electrocatalysis or misinterpretation. Nano Research, 7(1), 71–78.
14. Armstrong, F. a., Hill, H. A. O., & Walton, N. J. (1988). Direct electrochemistry of redox proteins. Accounts of Chemical Research, 21, 407–413.
15. Armstrong, F. a, Hill, H. A., Oliver, B. N., Walton, N. J., & Letr, N. J. F. (1984). Direct Electrochemistry. Journal of American Chemical Society, 106(4), 921–923.
16. Chen, K., Hirst, J., Camba, R., Bonagura, C. A., Stout, C. D., Burgess, B. K., & Armstrong, F. A. (2000). Atomically defined mechanism for proton transfer to a buried redox centre in a protein. Nature, 405(June), 814–817.
17. Hammes-schiffer, S., Soudackov, A. V, & Pennsyl, V. (2008). Proton-Coupled Electron Transfer in Solution, Proteins, and Electrochemistry . The Journal of Physical Chemistry B, 112(45), 14108–14123.
18. Meyer, T., Melin, F., Richter, O. M. H., Ludwig, B., Kannt, A., Müller, H., Hellwig, P. (2015). Electrochemistry suggests proton access from the exit site to the binuclear center in Paracoccus denitrificans cytochrome c oxidase pathway variants. FEBS Letters, 589(5), 565–568.
19. Meyer, T., Melin, F., Xie, H., Von Der Hocht, I., Choi, S. K., Noor, M. R., Hellwig, P. (2014). Evidence for distinct electron transfer processes in terminal oxidases from different origin by means of protein film voltammetry. Journal of the American Chemical Society, 136(31), 10854–10857.
20. Shleev, S., Tkac, J., Christenson, A., Ruzgas, T., Yaropolov, A. I., Whittaker, J. W., & Gorton, L. (2005). Direct electron transfer between copper-containing proteins and electrodes. Biosensors and Bioelectronics.
21. Melin, F., & Hellwig, P. (2013). Recent advances in the electrochemistry and spectroelectrochemistry of membrane proteins. Biological Chemistry, 394(5), 593–609.
22. Ataka, K., Stripp, S. T., & Heberle, J. (2013). Surface-enhanced infrared absorption spectroscopy (SEIRAS) to probe monolayers of membrane proteins. Biochimica et Biophysica Acta - Biomembranes.
23. Butt, J. N., and Armstrong, F. A. (2008) Chapter 4 Voltammetry of Adsorbed Redox Enzymes: Mechanisms In the Potential Dimension, 91-128.

24. Eckermann, A. L., Feld, D. J., Shaw, J. A., & Meade, T. J. (2010). Electrochemistry of redox-active self-assembled monolayers. Coordination Chemistry Reviews.
25. Cecchini, G. (2003). Function and structure of complex II of the respiratory chain. Annual Review of Biochemistry, 72, 77–109.
26. Melin, F., Meyer, T., Lankiang, S., Choi, S. K., Gennis, R. B., Blanck, C., Hellwig, P. (2013). Direct electrochemistry of cytochrome bo_3 oxidase at a series of gold nanoparticles-modified electrodes. Electrochemistry Communications, 26(1), 105–108.
27. Hsu, C. P. S. (1997). Infrared Spectroscopy. Handbook of Instrumental Techniques for Analytical Chemistry, 247–284.
28. Salerno, J. C., Bolgiano, B., & Ingledew, W. J. (1989). Potentiometric titration of cytochrome-bo type quinol oxidase of Escherichia coli: Evidence for heme-heme and copper-heme interaction. FEBS Letters, 247(1), 101–105.
29. Rauhamäki, V., Bloch, D. A., Verkhovsky, M. I., & Wikström, M. (2009). Active site of cytochrome cbb3. Journal of Biological Chemistry, 284(17), 11301–11308.
30. Moss, D., Nabedryk, E., Breton, J., & Mäntele, W. (1990). Redox-linked conformational changes in proteins detected by a combination of infrared spectroscopy and protein electrochemistry. Evaluation of the technique with cytochrome c. European Journal of Biochemistry, 187(3), 565–572.
31. Kastrau, D. H. W., Heiss, B., Kroneck, P. M. H., & Zumft, W. G. (1994). Nitric oxide reductase from Pseudomonas stutzeri, a novel cytochrome bc complex. Phospholipid requirement, electron paramagnetic resonance and redox properties. European Journal of Biochemistry, 222(2), 293–303.
32. Butland, G., Spiro, S., Watmough, N. J., & Richardson, D. J. (2001). Two conserved glutamates in the bacterial nitric oxide reductase are essential for activity but not assembly of the enzyme. Journal of Bacteriology, 183(1), 189–199.
33. Bolgiano, B., Salmon, I., Ingledew, W. J., & Poole, R. K. (1991). Redox analysis of the cytochrome o -type quinol oxidase complex of Escherichia coli reveals three redox components. Biochemical Journal, 274(3), 723–730.
34. Chen, H., & Long, Y. (1999). Study of biomolecules by combining electrochemistry with UV/Vis, IR and surface enhanced Raman scattering spectroscopy by a novel flow microcell. Analytica Chimica Acta, 382(1–2), 171–177.
35. Gouterman, M. (1959). Study of the Effects of Substitution on the Absorption Spectra of Porphin. The Journal of Chemical Physics, 30(5), 1139.

36. Saroff, H. A. (2007). The Nernst equation applied to oxidation-reduction reactions in myoglobin and hemoglobin. Evaluation of the parameters. Biopolymers, 85(5–6), 450–455.
37. Bogachev, A. V., Bloch, D. A., Bertsova, Y. V., & Verkhovsky, M. I. (2009). Redox properties of the prosthetic groups of Na+-translocating NADH:Quinone oxidoreductase. 2. Study of the enzyme by optical spectroscopy. Biochemistry, 48(27), 6299–6304.
38. Hsu, C. P. S. (1997). Infrared Spectroscopy. Handbook of Instrumental Techniques for Analytical Chemistry, 247–284.
39. Stuart, B. H. (2004). Infrared Spectroscopy: Fundamentals and Applications. Methods (Vol. 8).
40. Subramanian, A., & Rodriguez-Saona, L. (2009). Fourier Transform Infrared (FTIR) Spectroscopy. In Infrared Spectroscopy for Food Quality Analysis and Control (pp. 145–178).
41. Neehaul, Y. (2012) Study of protein interactions in the respiratory chain by IR spectroscopy and electrochemistry, In *Institut de Chimie*, Universite de Strasbourg, Strasbourg
42. Perkins, W. D. (1986). Fourier transform-infrared spectroscopy: Part l. Instrumentation. Journal of Chemical Education, 63(1), A5.
43. Mäntele, W. (1993). Reaction-induced infrared difference spectroscopy for the study of protein function and reaction mechanisms. Trends in Biochemical Sciences, 18(6), 197–202.
44. Kong, J., & Yu, S. (2007). Fourier transform infrared spectroscopic analysis of protein secondary structures. Acta Biochimica et Biophysica Sinica, 39(8), 549–559.
45. Barth, A. (2007). Infrared spectroscopy of proteins. Biochimica et Biophysica Acta - Bioenergetics.
46. Tamm, L.K. and Tatulian, S.A. (1997) 'Infrared spectroscopy of proteins and peptides in lipid bilayers', Quarterly Reviews
47. Barth, A., and Zscherp, C. (2002) What vibrations tell us about proteins, Quarterly Reviews of Biophysics, 35, 369-430.
48. Arrondo, J. L., Muga, a, Castresana, J., & Goñi, F. M. (1993). Quantitative studies of the structure of proteins in solution by Fourier-transform infrared spectroscopy. Progress in Biophysics and Molecular Biology, 59(1), 23–56.
49. Khalil, M. (2016). Interactions et stabilité des protéines étudiées par spectroscopies infrarouge et Raman: Proposal for dissertation submitted by University of Strasbourg.

50. Moss, D. A., Fuechsle, K., Masuch, R., & Wolf, A. (2000). Biomedical applications of FTIR difference spectroscopy. Proc. SPIE-Int. Soc. Opt. Eng., 3918(Biomedical Spectroscopy: Vibrational Spectroscopy and Other Novel Techniques), 97–103.
51. Hellwig, P., Behr, J., Ostermeier, C., Richter, O. M. H., Pfitzner, U., Odenwald, A., Mäntele, W. (1998). Involvement of glutamic acid 278 in the redox reaction of the cytochrome c oxidase from Paracoccus denitrificans investigated by FTIR spectroscopy. Biochemistry, 37(20), 7390–7399.
52. Hielscher, R., Wenz, T., Stolpe, S., Hunte, C., Friedrich, T., & Hellwig, P. (2006). Monitoring redox-dependent contribution of lipids in fourier transform infrared difference spectra of complex I from Escherichia coli. Biopolymers, 82(4), 291–294.
53. Hellwig, P., Mogi, T., Tomson, F. L., Gennis, R. B., Iwata, J., Miyoshi, H., & Mäntele, W. (1999). Vibrational modes of ubiquinone in cytochrome bo3 from Escherichia coli identified by Fourier transform infrared difference spectroscopy and specific 13C labeling. Biochemistry, 38(44), 14683–14689.
54. Lutz, M., and Mantele, (1991)W. Vibrational spectroscopy of chlorophylls, in H. Scheer (Ed.), Chlorophylls, CRC press, Boca Raton, Florida, 855-902.
55. Ballschmiter, K., & Katz, J. J. (1972). Chlorophyll-chlorophyll and chlorophyll-water interactions in the solid state. BBA - Bioenergetics, 256(2), 307–327.
56. Belasco, J. G., & Knowles, J. R. (1980). Direct observation of substrate distortion by triosephosphate isomerase using Fourier transform infrared spectroscopy. Biochemistry, 19(3), 472–477.
57. Behr, J., Michel, H., Mäntele, W., and Hellwig, P. (2000). Functional properties of the heme propionates in cytochrome c oxidase from Paracoccus denitrificans. Evidence from FTIR difference spectroscopy and site-directed mutagenesis. Biochemistry, 39(6), 1356–1363.
58. Behr, J., Hellwig, P., Mäntele, W., & Michel, H. (1998). Redox dependent changes at the heme propionates in cytochrome c oxidase from Paracoccus denitrificans: Direct evidence from FTIR difference spectroscopy in combination with heme propionate 13C labeling. Biochemistry, 37(20), 7400–7406.
59. Wolpert, M., & Hellwig, P. (2006). Infrared spectra and molar absorption coefficients of the 20 alpha amino acids in aqueous solutions in the spectral range from 1800 to 500 cm^{-1}. Spectrochimica Acta - Part A: Molecular and Biomolecular Spectroscopy, 64(4), 987–1001.

60. Garcia-Horsman, J. A., Barquera, B., Rumbley, J., Ma, J., & Gennis, R. B. (1994). The superfamily of heme-copper respiratory oxidases. Journal of Bacteriology, 176(18), 5587–5600.
61. Gennis, R. B. (2003). Some recent contributions of FTIR difference spectroscopy to the study of cytochrome oxidase1. FEBS Letters, 555(1), 2–7.
62. Hellwig, P., Behr, J., Ostermeier, C., Richter, O. M. H., Pfitzner, U., Odenwald, A. Mäntele, W. (1998). Involvement of glutamic acid 278 in the redox reaction of the cytochrome c oxidase from Paracoccus denitrificans investigated by FTIR spectroscopy. Biochemistry, 37(20), 7390–7399.
63. Rost, B., Behr, J., Hellwig, P., Richter, O. M. H., Ludwig, B., Michel, H., & Mäntele, W. (1999). Time-resolved FT-IR studies on the CO adduct of Paracoccus denitrificans cytochrome c oxidase: Comparison of the fully reduced and the mixed valence form. Biochemistry, 38(23), 7565–7571.
64. Lübben, M., Prutsch, A., Mamat, B., & Gerwert, K. (1999). Electron transfer induces side-chain conformational changes of glutamate-286 from cytochrome bo_3. Biochemistry, 38(7), 2048–2056.
65. Nyquist, R. M., Heitbrink, D., Bolwien, C., Gennis, R. B., & Heberle, J. (2003). Direct observation of protonation reactions during the catalytic cycle of cytochrome *c* oxidase. Proceedings of the National Academy of Sciences of the United States of America, 100(5), 8715–8720.
66. Chalmers, J. M., and Griffiths, P. (2002). Handboook of vibrational spectroscopy (Vol 1-5), Wiley.
67. Chittur, K. K. (1998). FTIR/ATR for protein adsorption to biomaterial surfaces. Biomaterials.
68. Glassford, S. E., Byrne, B., & Kazarian, S. G. (2013). Recent applications of ATR FTIR spectroscopy and imaging to proteins. Biochimica et Biophysica Acta - Proteins and Proteomics, 1834(12), 2849–2858.
69. Kriegel, S., Uchida, T., Osawa, M., Friedrich, T., & Hellwig, P. (2014). Biomimetic environment to study E. coli complex i through surface-enhanced IR absorption spectroscopy. Biochemistry, 53(40), 6340–6347.
70. Murgida, D. H., Hildebrandt, P., & Todorovic, S. (2010). Immobilized redox proteins : mimicking basic features of physiological membranes and interfaces. Biomimetics, Learning from Nature, 21–49.

71. Ataka, K., & Heberle, J. (2006). Use of surface enhanced infrared absorption spectroscopy (SEIRA) to probe the functionality of a protein monolayer. Biopolymers, 82(4), 415–419.
72. Džafić, E., Klein, O., Screpanti, E., Hunte, C., & Mäntele, W. (2009). Flexibility and dynamics of NhaA Na+/H+-antiporter of Escherichia coli studied by Fourier transform infrared spectroscopy. Spectrochimica Acta - Part A: Molecular and Biomolecular Spectroscopy, 72(1), 102–109.
73. Giess, F., Friedrich, M. G., Heberle, J., Naumann, R. L., & Knoll, W. (2004). The Protein-Tethered Lipid Bilayer: A Novel Mimic of the Biological Membrane. Biophysical Journal, 87(5), 3213–20.
74. Fleischmann, M., Hendra, P. J., & McQuillan, A. J. (1974). Raman spectra of pyridine adsorbed at a silver electrode. Chemical Physics Letters, 26(2), 163–166.
75. Hartstein, A., Kirtley, J. R., & Tsang, J. C. (1980). Enhancement of the infrared absorption from molecular monolayers with thin metal overlayers. Physical Review Letters, 45(3), 201–204.
76. Osawa, M. (2001). Surface-Enhanced Infrared Absorption, In near-field Optics and Surface Plasmon Polaritons (Kawata, S., Ed.), 163-187, Springer Berlin Heidelberg.
77. Osawa, M., Ataka, K. I., Yoshii, K., & Nishikawa, Y. (1993). Surface-enhanced infrared spectroscopy: The origin of the absorption enhancement and band selection rule in the infrared spectra of molecules adsorbed on fine metal particles. *Applied Spectroscopy*, *47*(9), 1497–1502.
78. Ataka, K., Giess, F., Knoll, W., Naumann, R., Haber-Pohlmeier, S., Richter, B., & Heberle, J. (2004). Oriented attachment and membrane reconstitution of his-tagged cytochrome c oxidase to a gold electrode: In situ monitoring by surface-enhanced infrared absorption spectroscopy. Journal of the American Chemical Society, 126(49), 16199–16206.

3. Experimental Procedures

3.1 Preparation of protein samples

a. Preparation of cytochrome *bo₃* oxidase from *Escherichia coli*

Wild type (WT) cytochrome *bo₃* oxidase from *E. coli* was prepared by Dr. Sylvia Choi from the group of Robert B. Gennis (Center of Biophysics and Computational Biology, University of Illinois, Urbana Champaign, USA). The cell growth and protein purification procedure was described in detail in reference [1]. Proteins were mixed with nickel-nitrilotriacetic acid (Ni-NTA) resin and loaded in a column, which is a common technique to purify recombinant proteins carrying a His-tag. Obtained proteins were eluted in 50 mM potassium phosphate buffer (KPi) together with % 0.05 n-dodecyl-β-D-maltoside (DDM) at pH 7.5. Protein samples were concentrated in our laboratory by ultrafiltration (Amicon 50 kDa cut-off membrane, milipore) in a centrifuge (Eppendorf, Le Pecq, France) with a rotation speed of 7000 rpm/min for 20 minutes. Final concentration of ≈ 200 μM was obtained and samples were rapidly frozen in liquid nitrogen before storing them at -80℃.

Quinone extraction from wt cytochrome *bo₃* oxidase was performed by Dr. Sylvia Choi. Purified enzymes were mixed with methanol and petroleum ether solvent mixture and centrifuged in order to remove the tightly bound quinone from the sample [2]. Extracted ubiquinone was collected from the upper layer and remaining protein mixture was washed with the same solvent two more times.

Site directed mutations on the same enzyme at the proposed high affinity quinone binding site were also done by Dr. Sylvia Choi [3]. All mutant proteins were eluted in 50mM KPi and % 0.05 DDM at pH 7.5. Samples were concentrated as described previously to the final concentration of ≈ 200 μM and rapidly frozen in liquid nitrogen before storing them at -80℃. Steady state oxygen reduction activities of all the Q101, F93 and D75 mutant enzymes were measured. In table 3.1 enzymatic catalytic activities of all mutations are provided.

Table 3.1 Summary of mutations on the quinone binding site of cytochrome bo_3 oxidase from *E. coli* and their relative enzymatic activities [4-7].

Sample	Relative Enzymatic Activity
WT	% 100
Q101N	% 10
Q101M	% 50
Q101T	% 30
Q101A	% 30
Q101L	%10
F93A	% 40
D75N	% 0
H98F	% 1
I102N	% 0
R71H	% 0

b. Preparation of wild type (wt) cytochrome bo_3 oxidase with menadione, ubiquinone-2, ubiquinone-1 and ubiquinone-10

Different quinone molecules have been added to the quinone extracted bo_3 sample. A 1:2 protein to quinone ratio (molar) was used for all the samples. All quinone molecules were dissolved in ethanol and diluted to reach the desired final concentrations. After the evaporation of ethanol from the quinone samples, 5 µl of 100 µM wt bo_3 sample (containing no quinone) was added for the electrochemical experiments, whereas for the redox titration or differential infrared experiments 10 µl of 500 µM wt bo_3 sample (containing no quinone) was used. The protein sample was incubated with quinone in a shaker at 7℃ for 20-24 hours.

c. Preparation of cytochrome *c*-dependent nitric oxide reductase (cNOR) from *P. denitrificans*

Wild type cNOR from *P. denitrificans* was prepared by Dr. Josy Ter Beek from the group of Prof. Pia Adelroth (Department of Biochemistry and Biophysics, Stockholm University, Sweden). Cell growth and protein purification were performed according to the method described in reference [8]. Wild-type cNOR and mutants of the Ca^{2+} ligands E122A, Y74S and Y74F, were prepared according to the same protocol. Expressed

proteins were kept in 20 mM Tris buffer with 50 mM NaCl at pH 7.5. Heme *b* and heme *c* contents in all samples were verified by UV/Vis spectroscopy together with the concentrations of the samples (50-650 µM).

Another batch of cNOR was purified and inserted in liposomes. Lipid vesicles were formed with a mixture of 40 mg/ml α-phosphatidylcholine (type II-S from soybean) in 2% cholic acid and 50 mM Tris-HCl at pH 7.5. Afterwards in order to remove detergent without using Biobeads, samples were run over a PD10 column in 50 mM Tris-HCl at pH 7.5, and colored fractions were collected as described in the reference [8]. The proteoliposomes diameter was about ≈40 nm.

Protein samples were concentrated in our laboratory by ultrafiltration to achieve a final concentration of ≈ 200 µM and samples were rapidly frozen in liquid nitrogen before storing at - 80℃.

3.2 Electrochemistry

3.2.1 Synthesis of gold nanoparticles

Gold nanoparticles (Au NPs) were synthesized according to the protocol described by Frens [9]. 125 ml of Gold(III) chloride trihydrate ($HAuCl_4$, Sigma Aldrich) solution was prepared with a concentration of 1 mM together with 12.5 ml of sodium citrate tribasic dihydrate ($Na_3C_6H_5O_7$, Sigma Aldrich) solution with a concentration of 38.8 mM. The gold solution was heated until boiling and right after it was mixed with the citrate solution. After the solution turned dark red it was maintained under boiling for 10 minutes. Size of the synthesized Au NPs was estimated by UV/Vis spectroscopy from the A_{max}/A_{450} ratio [9].

3.2.2 Functionalization of electrode

For the protein film voltammetry experiments a 2 mm diameter gold electrode was used as a working electrode. The surface of the electrode was cleaned with micro polish alumina (0.3 µm, Buehler) powder and followed by 15 minutes of sonication. Electrode was activated by scanning at 1.5 V for 5 seconds, - 0.35 V for 10 second and after 100 cycles between - 0.35 V and 1.5 V in 0.1 M sulfuric acid (H_2SO_4) solution. The prepared Au NP solution was concentrated by centrifugation for 30 minutes at 10 000 rpm. Au NPs were deposited on the electrode by the drop casting method. An increase in the reduction peak

was observed after the addition of Au NPs in the cyclic voltammogram of the electrode measured in H_2SO_4 solution between – 0.35 V and 1.5 V potential. The prepared electrode was placed overnight in a mixture of 16 µl mercaptohexanol ($HS(CH_2)_6OH$) and 13 µl of hexanethiol ($CH_3(CH_2)_5SH$) solution in ethanol. An overview of the modification steps of the electrode is shown in figure 3.1. After the formation of thiols on Au NPs a background measurement was taken with buffer solution by scanning the electrode between – 0.65 V and 0.3 V. Finally, 3 µl of protein sample (≈100 µM) was deposited on the surface of the electrode by drop casting in absence of oxygen and the modified electrode was incubated overnight.

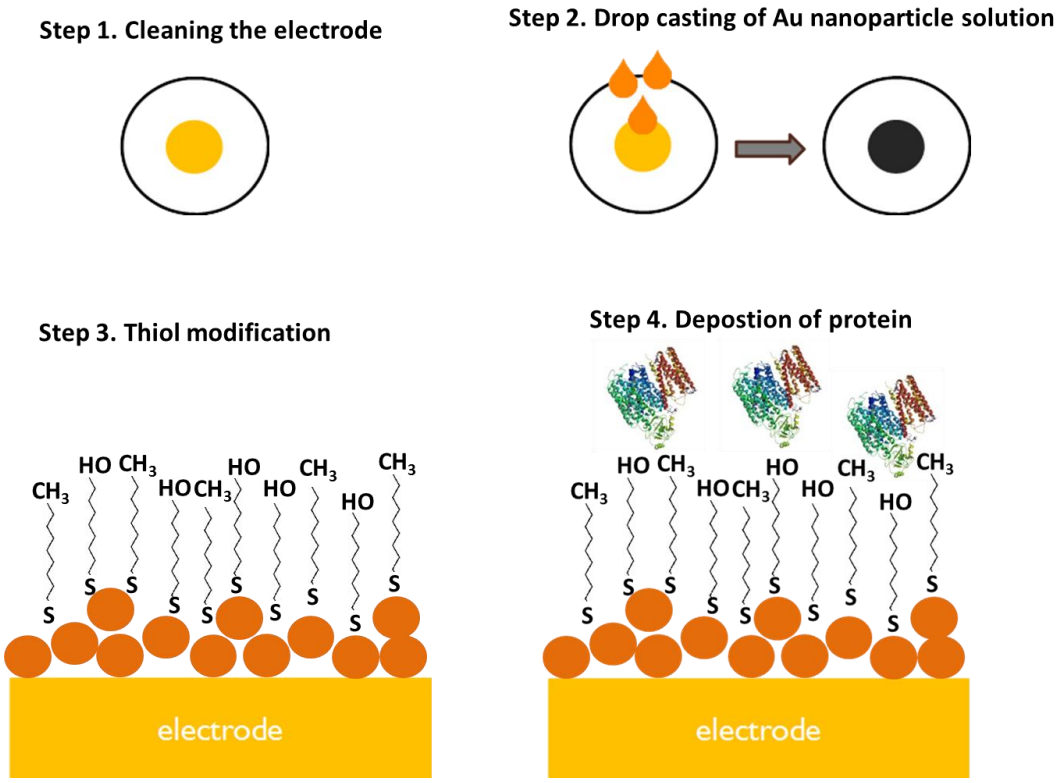

Figure 3.1 Schematic representation of the modification steps of a gold electrode.

All measurements described in this thesis were performed with a three electrode system connected to a Princeton Applied Research VERSASTAT 4 potentiostat. Reference electrode was Ag/AgCl 3M KCl which has - 208 mV difference related to the standard hydrogen electrode (SHE). The cyclic voltammograms were recorded in 50 mM KPi buffer at pH 7.5 with a scanning velocity of 0.02 $V.s^{-1}$. For measurements in absence of oxygen, the buffer was deoxygenized by flushing argon for 20 minutes.

3.3 Spectroscopy

3.3.1 UV/Vis Spectroscopy

a. Absorption measurements

The concentration of protein samples and the size of synthesized nanoparticles were measured by using UV/Vis absorption spectroscopy (UV/Visible VARIAN Carry 300). In order to determine protein concentrations, 1 µl protein sample was mixed with 700 µl buffer solution in a quartz cell. For both cytochrome *bo*$_3$ oxidase and nitric oxide reductase samples, $A_{560(ox)} - A_{580(ox)}$ and $A_{560(red)} - A_{580(red)}$ values were measured and concentration was determined according to the following formula,

$$\frac{C}{700} = \frac{\Delta A_{red} - \Delta A_{ox}}{\varepsilon} \qquad \textbf{Equation 3.1}$$

where *C* is the concentration of the sample and ε is the molar absorption coefficient for the enzyme.

The size of the synthesized Au NPs was estimated as it was mentioned in section 3.2.1. A_{max}, which is the maximum absorbance of plasmon band, is measured together with A_{450}. If the Amax/A450 value is between 1.56 and 1.65 Au NPs should have a diameter of 12-16 nm [9] which is the optimum size for the electrochemical experiments [10, 11].

b. Redox titrations

Redox titrations [12] were performed with the electrochemical cell which was previously described in the section 2.2.1.1 with CaF_2 windows.

For wt cytochrome *bo*$_3$ oxidase with and without quinone, potentiometric titrations were performed between the potential values of - 400 mV and + 400 mV and in the range of 300 - 800 nm. For a single measurement 10 µl of sample with a concentration of ≈25 µM was incubated in the mediator mixture (Table 3.2) for 20 minutes. These mediators have different reduction potentials and due to the low concentration they do not have any contribution during experiments [13, 14].

Table 3.2 List of mediators used in spectroelectrochemical experiments [13, 14].

Material	E (mV) [9] vs Ag/AgCl	Company	Solvent
Ferrocenylmethyltrimethylammoniumiodide	607	Strem chemicals	Ethanol
1,1`-ferrocenedicarboxylic acid	436	Fluka	Ethanol
Potassiumhexacyanoferrate(II) trihydrate	212	Riedel-de-Haen	Water
1,1`dimethylferrocene	133	Aldrich	Ethanol
Quinhydrone	70	Fluka	Ethanol
Tetrachloro-1,4-benzoquinone (p-Chloranil)	72	Aldrich	Acetone
N,N,N`,N`-tetramethyl-p-phenylenediamine dihydrochloride	62	Fluka	Water
2,6-dichlorophenolindophenol sodium salt hydrate	9	Biochemika	Ethanol
Hexaammineruthenium(III)chloride	-8	Aldrich	Water
Anthraquinone-2-sulfonic acid sodium salt	-23	Aldrich	Water
1,4 naphtaquinone hydrate	-63	Aldrich	Ethanol
Antraquinone	-108	Aldrich	Ethanol
5-hydroxy-1,4-naphtoquinone	-158	Aldrich	Ethanol
Duroquinone	-198	Sigma	Ethanol
Menadione	-220	Sigma	Acetone
2-hydroxyl-1,4 naphtoquinone	-333	Sigma	Ethanol
9,10-antraquinone-2,6-disulfonic acid disodium salt	-433	Sigma	Ethanol
Neutral red	-515	Sigma-Aldrich	Ethanol
Methyl viologen dichloride hydrate	-628	Aldrich	Water

50 mM KPi buffer was used together with 50 mM NaCl and 0.05% DDM at pH 7.5. For an oxidative titration a reference absorbance spectrum was taken for the fully reduced form (- 400 mV) and a potential was applied with 50 mV or 25 mV intervals (during the oxidation of hemes) until the fully oxidized form (+ 400 mV vs Ag/AgCl) was reached.

For a reductive titration a reference spectrum for the fully oxidized form was taken and same protocol was applied in the reverse direction. The absorbance of the Soret (428 nm) and alpha band (550 nm) was monitored during the titrations. For each potential step a series of measurements were taken until the equilibration of redox reaction was reached. Equilibration time between applied potentials varied between different samples depending on reduction/oxidation rate of redox centers in the protein. The obtained absorbance values in each interval were recorded. For the wt bo_3 15-30 minutes was required for the equilibration, however for the bo_3 sample without quinone equilibration time could go up to 45 minutes.

For cNOR with DDM, cNOR in liposomes and all mutants of the same enzyme, potentiometric titrations were performed between the potential values of – 425 mV and +425 mV and in the range of 300 - 800 nm by using the same procedure as described previously for cytochrome bo_3 oxidase. An oxidative titration was performed for cNOR samples. Equilibration time for the wt cNOR was 15-30 minutes for each step and for the mutants 20-45 minutes. The absorbance changes of the Soret band (426 nm) and alpha band (551 nm with a shoulder at 558 nm) were monitored. Potentiometric titrations were performed at three different pH values (pH 6.5, 7.5 and 8.5) with the cNOR with DDM and in liposomes. Samples were not stable at pH 6.5 and all measurements were performed at pH 7.5 and 8.5. The cNOR mutants (E122A, Y74S and Y74F) were studied only at pH 7.5. For all measurements 10 µl of protein solution with a concentration of ≈500 µM was incubated with a mixture of mediators (Table 3.2) for 20 minutes. For all cNOR samples except cNOR in liposomes, 50 mM Tris buffer was used together with 50 mM KCl and 0.05% DDM.

All measurements were performed at least twice. Gaussian fitting was applied to the first derivative values of all absorbance values obtained from the potentiometric titrations. This treatment is easier to use when there are several overlapping transitions. In figure 3.2 each step of fitting of a potentiometric titration by using Gaussian function is shown.

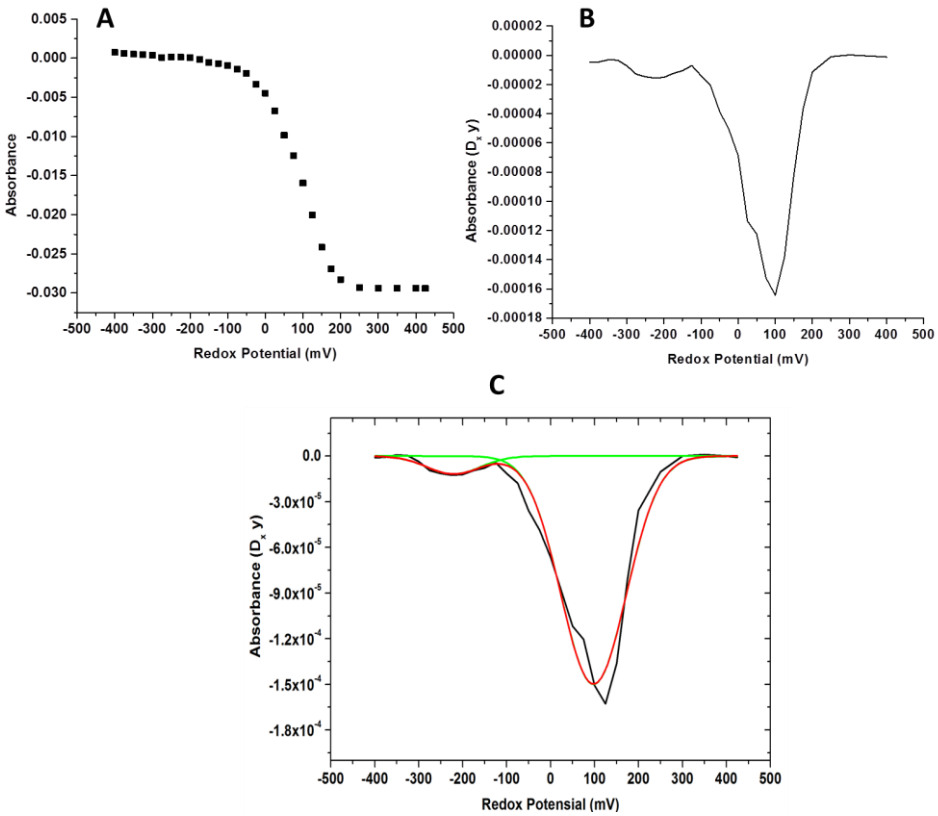

Figure 3.2 Potentiometric titration of cNOR from *P. denitrificans* at pH 7.5. Gaussian fitting of the first derivative of the absorbance values obtained from 551 nm band. A) Absorbance values obtained from each potential interval, B) First derivative of the absorbance values, C) Gaussian fitting of the first derivative values of the absorbance values.

The full width at half maximum (FWHM) version of Gaussian function uses the formula [15],

$$y = y_0 + \frac{A_e^{\frac{-4\ln(2)(x-x_c)^2}{w^2}}}{w\sqrt{\frac{\pi}{4\ln(2)}}} \qquad \textbf{Equation 3.2}$$

where, *w* is the value of FWHM. Manipulation of base, center and FWHM values is crucial for the perfect fitting and since the center value will determine the mid-point potential of the hemes. In Figure 3.3 an example Gaussian fitting and important components for the fitting process is shown.

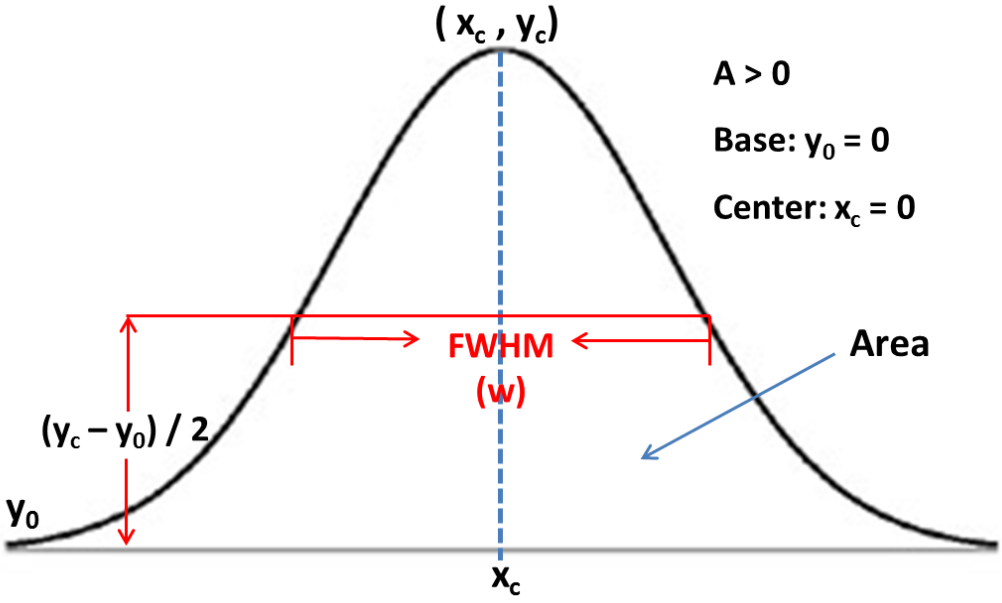

Figure 3.3 Example of a Gaussian curve showing the important components for the full width at half maximum (FWHM) version of Gaussian fitting function [15].

3.3.2 Infrared spectroscopy

3.3.2.1 Electrochemically induced differential spectroscopy

For the electrochemically-induced differential spectroscopy an electrochemical cell (see section 2.2.1.1) was used with CaF_2 windows. All samples were incubated with mediator mixture (Table 3.2) for 20 minutes before the measurements. After that, 10 µl protein sample (≈500 µM) was deposited on a gold grid which was previously modified with 1 mM cysteamine and 1mM 3-mercaptopropionic acid for 30 minutes.

Before starting the differential experiments of all samples a series of absorption spectra were measured in the transmission mode at 7℃. These spectra are measured to make sure that the absorbance of water at 1640 cm^{-1} is below 1. If it is not the case the cell is tightened again to decrease the path length below 10 µm. After 45 minutes the temperature of the cell was typically stable and the potentiostat was turned on.

a. Differential Spectra of cytochrome *bo₃* oxidase

For all *bo₃* samples 50 mM KPi with 50 mM NaCl and 0.05% DDM at pH 7.5 was used as buffer solution. Between the reduced state (-400 mV) and the oxidized state (+400 mV) several cycles of measurements were automatically generated. At each redox state 2 spectra which are an average of 256 scans, were taken and calculated into *oxidized-reduced* and *reduced-oxidized* spectra via the macro program of FTIR instrument. For the

wt *bo*$_3$ enzyme, equilibration time was 5 minutes and for the all mutants together with wt enzyme without quinone it was 10 minutes. At least 20 redox cycles were made to obtain better signal to noise ratio.

b. Differential Spectra of cNOR

For all cNOR samples 50 mM Tris with 50 mM KCl and 0.05% DDM was used as a buffer solution. For the redox state cycle, reduction potential was – 425 mV and the oxidation potential was + 425 mV for all the cNOR samples. Equilibration time between the redox states for the wt cNOR samples with DDM and inside liposomes was 5 minutes and for all the mutants it was 8 minutes. For wt cNOR samples with DDM and inside liposomes, differential spectra were obtained with three different pH values (6.5, 7.5 and 8.5). For E122A, Y74F and Y74S mutants all experiments were performed at pH 7.5.

3.3.2.2 Surface-enhanced Infrared Absorption Spectroscopy

Surface-enhanced infrared absorption spectroscopy (SEIRAS) measurements were performed in the ATR mode according to the protocol of Dr. Sebastien Kriegel [16]. On the surface of a semi-cylindrical silicon prism (r = 1 cm, h = 2.5 cm, Korth Krystalle) a thin gold layer was chemically deposited and the prism was inserted in a glass cell (courtesy of Prof. Masatoshi Osawa, Hokkaido University). A platinum wire was inserted in the glass cell as a counter electrode together with an Ag/AgCl reference electrode and the gold deposited ATR prism was the working electrode. The assembled electrochemical ATR cell can be seen in figure 3.4. Upon assembly, the glass cell was inserted on a support which is constituted of two gold coated side mirrors (Thorlabs) and a gold coated glass slide on a mirror holder (Thorlabs) in the middle. The aim of this optical setup is to reflect the incident IR beam on the prism with 60˚ angles and to the detector with 90˚ angles. All SEIRAS measurements were made with a Bruker Vertex 70 FTIR spectrometer (KBr Beamsplitter, LM-MCT detector) and 20 kHz scanning velocity.

Figure 3.4 A picture of the SEIRAS setup. The incident IR beam is guided through a gold-coated glass slide to the gold coated mirrors which were directed to the ATR crystal with 60° angles. Glass cell is mounted on the optical setup via metal holder stand.

a. Chemical deposition of gold on the ATR prism

Chemical deposition of gold layer on the prism was done according to the reference [17]. The surface of the prism was polished with a micro polish alumina (0.3 µm, Buehler) powder and rinsed with water, acetone and again with water. 40 % (w/v) ammonium fluoride solution was prepared and deposited on the prism for 45 seconds in order to increase the hydrophobicity of the prism surface. After that the prism was rinsed with water, dried with an argon stream and at the same time a plating solution was prepared. The plating solution was a mixture of 3 solutions (A, B and C) where A is 1 ml of 15 mM sodium tetrachloroaurate(III) dihydrate ($NaAuCl_4 \cdot 2H_2O$), B is a mixture of 500 µl of 150 mM sodium sulfite (Na_2SO_3), 250 µl of 50 mM sodium thiosulfate ($Na_2S_2O_3$) and 250 µl of 50 mM ammonium chloride (NH_4Cl), C is 1ml of % 2w/v hydrogen fluoride (HF). The plating solution was prepared by mixing A solution slowly to B solution and C solution to the A+B solution. The prepared plating solution and the ATR prism were placed on a hot plate to heat up to 65℃ for 10 minutes. Heated plating solution was poured on the heated

prism for 40 seconds and rapidly rinsed with water. As a result a thin gold film (about ≈50 nm) was formed on the prism.

b. His-tag modification on the gold surface of the ATR prism

After gold deposition the surface of the ATR prism was covered with a 10 mM solution of dithiobis(succinimidylpropionate) (DTSP) in dimethyl sulfoxide (DMSO). DTSP solution was left incubating for one hour while the formation of the monolayer was monitored by FTIR spectroscopy. DTSP forms a monolayer on the metal surface by covalent attachment of the sulfur groups. After formation of the monolayer, excess DTSP was washed away from the surface by rinsing the surface several times with DMSO and water. After, 100 mM of Nα,Nα-Bis(carboxymethyl)-L-Lysine hydrate (ANTA) solution was prepared in a buffer solution of potassium carbonate (K_2CO_3) at pH 9.8 (in water). DTSP monolayer was covered with the ANTA solution for three hours while formation of carboxamide linkage between the lysine and DTSP was monitored by FTIR spectroscopy. Then the excess ANTA was washed from the surface by rinsing the surface three times with water. In the last step DTSP-NTA modified surface was covered with a 50 mM Nickel(II) perchlorate ($Ni(ClO_4)_2$) solution (in water) and incubated for one hour while the ligation of Ni^{2+} with the three carboxylates of the NTA was monitored by FTIR spectroscopy. Excess nickel solution was washed by rinsing the surface three times with water.

Surface of the DTSP-NTA-Ni^{2+} modified prism was finally covered with 10 μM protein solution (cNOR and cytochrome bo_3 oxidase) and incubated until the surface was fully covered with protein. The protein adsorption process was monitored from the Amide I and the Amide II band by FTIR spectroscopy and the incubation was terminated when these two bands reached a stable intensity. In figure 3.5 each step of the His-tag modification process is shown.

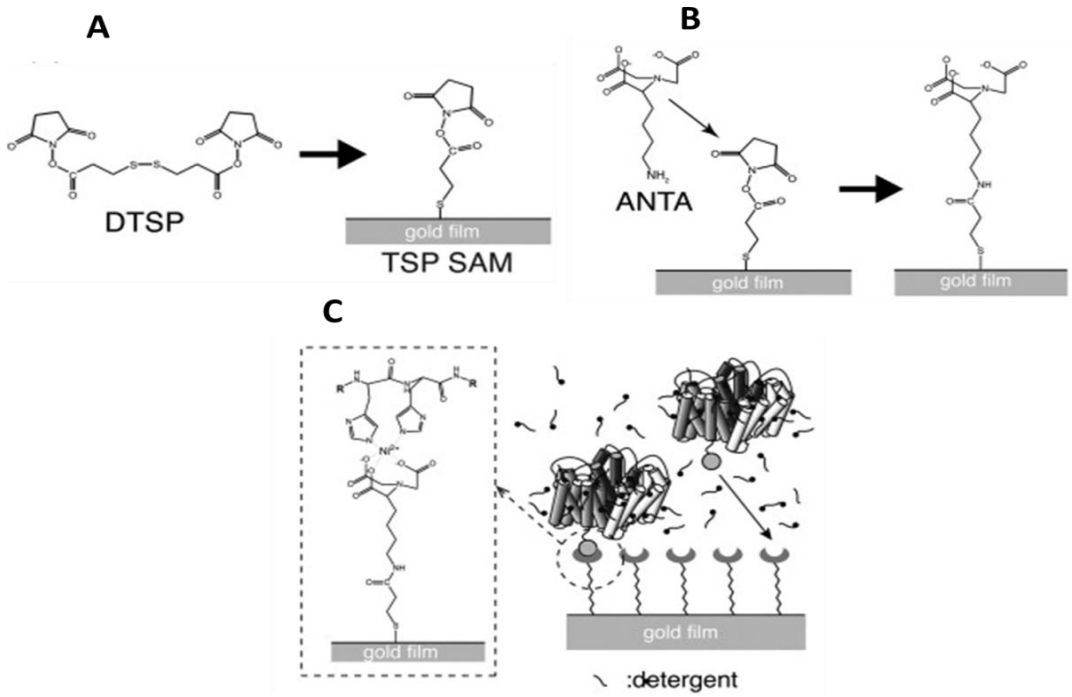

Figure 3.5 His-tag modification of the ATR crystal surface A) Self-assembly of TSP monolayer on the Au layer, B) Cross-linking of ANTA with TSP monolayer C) Adsorption of protein on the Ni-NTA modified Au surface via the His-tag [18].

c. Cyclic voltammetry and electrochemically induced difference spectroscopy of the adsorbed enzymes

Electrochemical activity of adsorbed enzymes was measured with a Princeton applied research VERSASTAT4 potentiostat. Potential was swept between +300 mV and -650 mV (vs Ag/AgCl) with 0.02 $V.sec^{-1}$ scan speed and current was measured.

After the verification process, the modified ATR cell was inserted in the FTIR spectrometer and was connected to a potentiostat. As described in section 3.3.2.1 macro program was used to obtain *oxidized-reduced* and *reduced-oxidized* spectra with the same conditions. All measurements were performed with an Ag/AgCl reference electrode.

References

1. Rumbley, J. N., Nickels, E. F., & Gennis, R. B. (1997). One-step purification of histidine-tagged cytochrome bo_3 from Escherichia coli and demonstration that associated quinone is not required for the structural integrity of the oxidase. Biochimica et Biophysica Acta - Protein Structure and Molecular Enzymology, 1340(1), 131–142.
2. Puustinen, a, Verkhovsky, M. I., Morgan, J. E., Belevich, N. P., & Wikstrom, M. (1996). Reaction of the Escherichia coli quinol oxidase cytochrome bo_3 with dioxygen: the role of a bound ubiquinone molecule. Proceedings of the National Academy of Sciences of the United States of America, 93(4), 1545–1548.
3. Lemieux, L. J., Calhoun, M. W., Thomas, J. W., Ingledew, W. J., & Gennis, R. B. (1992). Determination of the ligands of the low spin heme of the cytochrome o ubiquinol oxidase complex using site-directed mutagenesis. Journal of Biological Chemistry, 267(3), 2105–2113.
4. Choi, S. K. (2015). The Interaction of Cytochrome bo_3 from *Escherichia Coli* with its Substrates-Ubiquinone and Oxygen:Proposal for Dissertation Submitted by. University of Illinois at Urbana-Champaign.
5. Hellwig, P., Yano, T., Ohnishi, T., & Gennis, R. B. (2002). Identification of the residues involved in stabilization of the semiquinone radical in the high-affinity ubiquinone binding site in cytochrome bo_3 from Escherichia coli by site-directed mutagenesis and EPR spectroscopy. Biochemistry, 41(34), 10675–10679.
6. Yap, L. L., Lin, M. T., Ouyang, H., Samoilova, R. I., Dikanov, S. A., & Gennis, R. B. (2010). The quinone-binding sites of the cytochrome bo3 ubiquinol oxidase from Escherichia coli. Biochimica et Biophysica Acta - Bioenergetics, 1797(12), 1924–1932.
7. Lai, L. Y., Samoilova, R. I., Gennis, R. B., & Dikanov, S. A. (2007). Characterization of mutants that change the hydrogen bonding of the semiquinone radical at the QH site of the cytochrome bo3 from Escherichia coli. Journal of Biological Chemistry, 282(12), 8777–8785.
8. Reimann, J., Flock, U., Lepp, H., Honigmann, A., & Ädelroth, P. (2007). A pathway for protons in nitric oxide reductase from Paracoccus denitrificans. Biochimica et Biophysica Acta - Bioenergetics, 1767(5), 362–373.
9. Frens, G. (1973). Controlled Nucleation for the Regulation of the Particle Size in Monodisperse Gold Suspensions. Nature Physical Science, 241(105), 20–22.

10. Melin, F., Meyer, T., Lankiang, S., Choi, S. K., Gennis, R. B., Blanck, C., Hellwig, P. (2013). Direct electrochemistry of cytochrome *bo_3* oxidase at a series of gold nanoparticles-modified electrodes. Electrochemistry Communications, 26(1), 105–108.
11. Meyer, T., Gross, J., Blanck, C., Schmutz, M., Ludwig, B., Hellwig, P., & Melin, F. (2011). Electrochemistry of Cytochrome c 1 , Cytochrome c 552 , and Cu A from the Respiratory Chain of Thermus thermophilus Immobilized on Gold Nanoparticles. The Journal of Physical Chemistry B, 115(21), 7165–7170.
12. Moss, D., Nabedryk, E., Breton, J., & Mäntele, W. (1990). Redox-linked conformational changes in proteins detected by a combination of infrared spectroscopy and protein electrochemistry. Evaluation of the technique with cytochrome c. European Journal of Biochemistry, 187(3), 565–572.
13. Hellwig, P., Ostermeier, C., Michel, H., Ludwig, B., & Mäntele, W. (1998). Electrochemically induced FT-IR difference spectra of the two- and four-subunit cytochrome c oxidase from P. denitrificans reveal identical conformational changes upon redox transitions. Biochimica et Biophysica Acta - Bioenergetics, 1409(2), 107–112.
14. Hellwig, P., Behr, J., Ostermeier, C., Richter, O. M. H., Pfitzner, U., Odenwald, A., Mäntele, W. (1998). Involvement of glutamic acid 278 in the redox reaction of the cytochrome c oxidase from Paracoccus denitrificans investigated by FTIR spectroscopy. Biochemistry, 37(20), 7390–7399.
15. Mathematics, A., & Mathematics, R. (2008). Gaussian Function. History, (6), 8–10.
16. Kriegel, S., Uchida, T., Osawa, M., Friedrich, T., & Hellwig, P. (2014). Biomimetic environment to study E. coli complex i through surface-enhanced IR absorption spectroscopy. Biochemistry, 53(40), 6340–6347.
17. Miyake, H., Ye, S., & Osawa, M. (2002). Electroless deposition of gold thin films on silicon for surface-enhanced infrared spectroelectrochemistry. Electrochemistry Communications, 4(12), 973–977.
18. Ataka, K., Giess, F., Knoll, W., Naumann, R., Haber-Pohlmeier, S., Richter, B., & Heberle, J. (2004). Oriented attachment and membrane reconstitution of his-tagged cytochrome c oxidase to a gold electrode: In situ monitoring by surface-enhanced infrared absorption spectroscopy. Journal of the American Chemical Society, 126(49), 16199–16206.

4. Results and Discussion

4.1 Investigation of the cytochrome *bo₃* oxidase from *E. coli*

In the first part of the thesis, cytochrome *bo₃* oxidase from *E. coli* was the protein of interest. As the crystal structure of this enzyme was determined further details were revealed about the mechanism of oxygen reduction, proton translocation and quinone binding [1-4]. However, there are still several questions such as the position and number of quinone binding sites and interaction between the cofactors [5-18]. We aimed to answer some of these questions by using electrochemical and spectroscopic techniques.

4.1.1 Electrochemistry and FTIR difference spectroscopy of wild type cytochrome *bo₃* oxidase and K362M mutant

The electrochemical characterization of the cytochrome *bo₃* oxidase was done by cyclic voltammetry. Figure 4.2A displays the cyclic voltammogram of wild type cytochrome *bo₃* oxidase under zero oxygen conditions and under air at various rotation speed. When there is no oxygen present in the environment of the electrode, a reduction peak at – 0.42 V originating from the reduction of the cofactors in the adsorbed enzyme was observed. In the presence of oxygen a sigmoidal curve with an onset at – 0.12 V and half-wave value of -0.38 V is observed. As it was previously described, the Levich equation indicates that catalytic current is related to the rotation rate of the electrode. Acceleration of the rotation leads to an increase in the flux of electro-active species to the surface of the electrode and as a result a higher current value is measured [19-21]. In figure 4.2B the relationship between the limiting current and the rotation speed for *bo₃* oxidase is shown between 100 and 1000 rpm.

Characterization of *bo₃* oxidase was done by the comparison of wild-type enzyme with a K channel mutant (K362M, see figure 4.1) [7]. The cyclovoltammogram of K362M is shown in figure 4.3 and it shows that the O_2 reduction activity of the mutant is reduced as compared to the wt enzyme. K362 is located in the entrance of the proton pathway in cytochrome *bo₃* oxidase and mutation in this amino acid inhibits the uptake of the chemical protons to the enzyme. Thus, the enzyme can no longer reduce oxygen. As it can be seen from figure 4.3, there seems to be a small residual activity which results in a small reduction peak at around -0.25 V, however a sigmoidal curve was not observed.

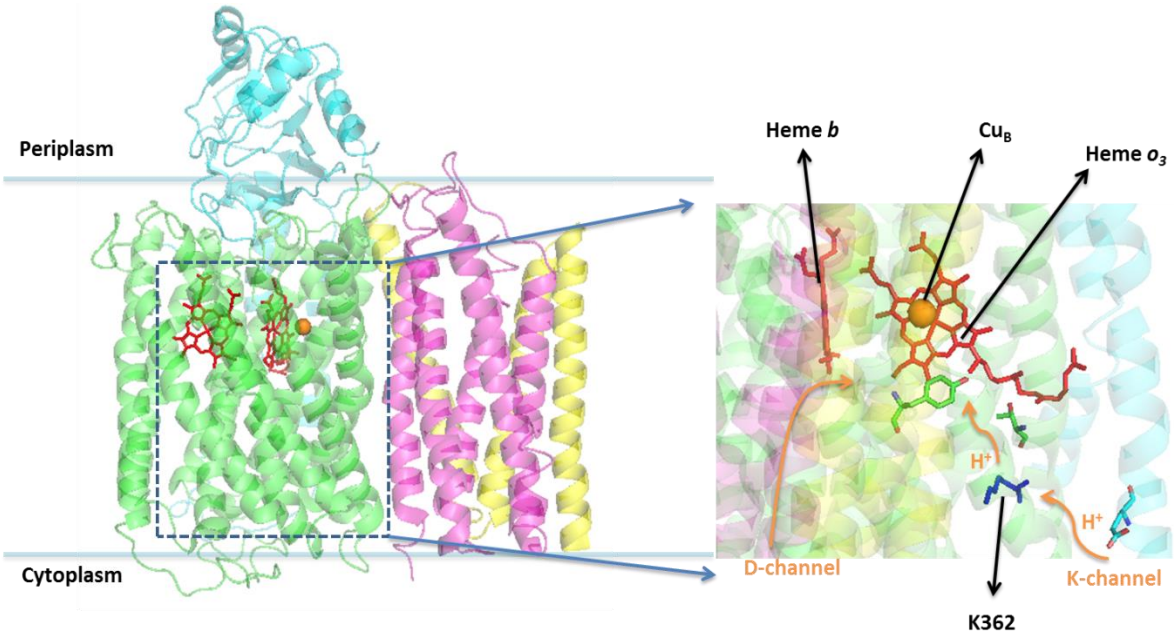

Figure 4.1 Structure of cytochrome *bo$_3$* oxidase from *E. coli*. Position of K362 in the K-channel (1FFT.pdb).

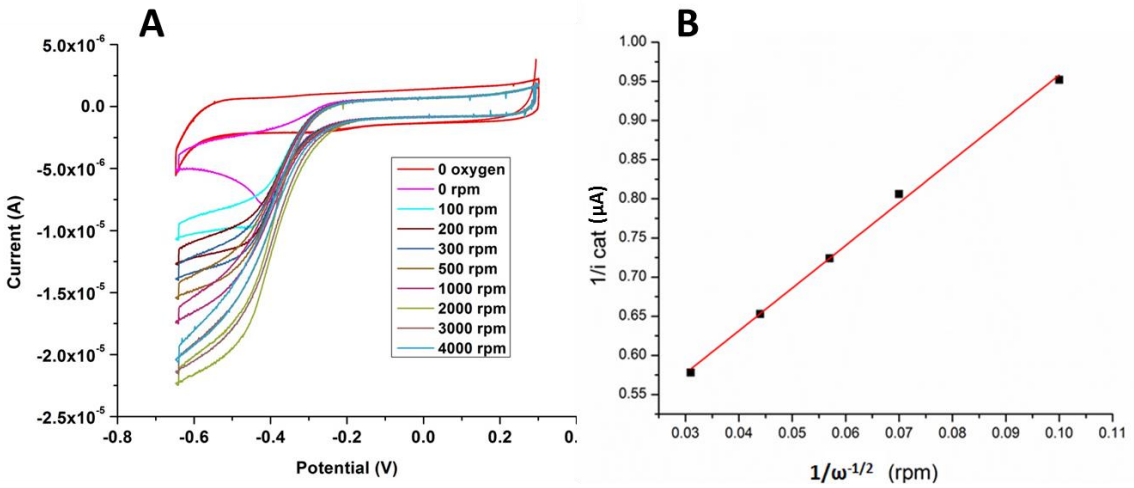

Figure 4.2 Cyclovoltammogram of wild-type cytochrome *bo$_3$* oxidase at pH 7.5, B) Relation between the catalytic current and rotation rate of the electrode (Scan rate of 0.02 V.s^{-1}).

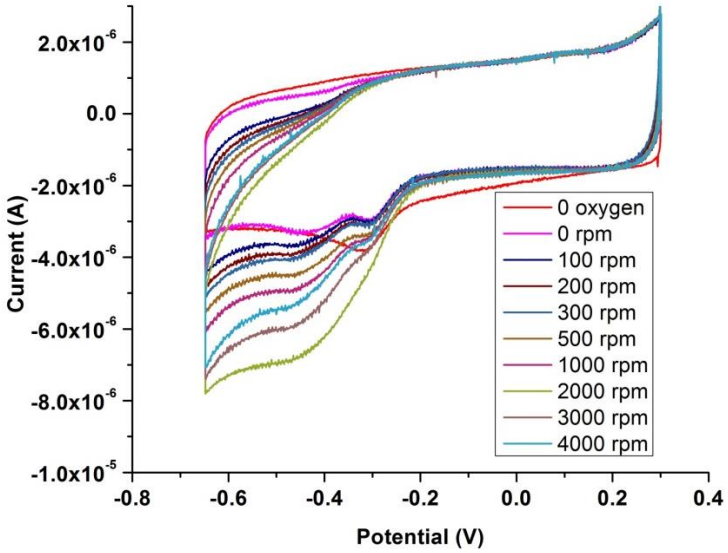

Figure 4.3 Cyclovoltammograms of K362M mutant of cytochrome *bo*$_3$ oxidase at pH 7.5 (Scan rate of 0.02 V.s^{-1})

The pH dependence cyclovoltammograms of both wild type *bo*$_3$ oxidase and K362M mutant were also studied. Although there was not a clear linear dependence of catalytic activity of the enzyme with changing pH, the samples were not perfectly stable at pH 6.5. In figure 4.4 the cyclovoltammograms of wt enzyme at pH 6.5, 7.5 and 8.5 (1000 rpm) were compared with K362M mutant. For the pH 6.5 measurement of wt enzyme catalytic signal was decreased after 1000 rpm. Highest O_2 reduction activity for the wild type *bo*$_3$ oxidase was measured at pH 7.5 and K362M mutant showed no clear O_2 reduction activity for any of the pH values.

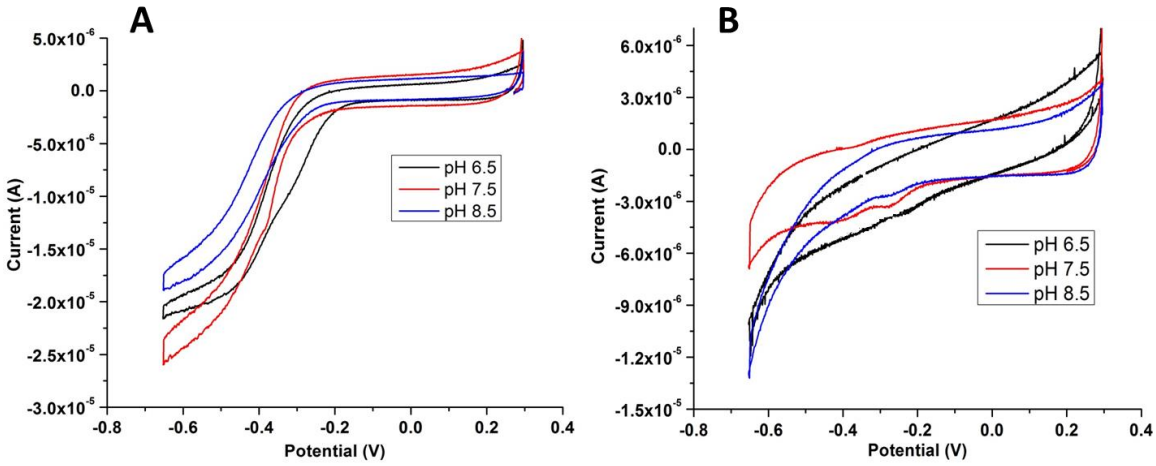

Figure 4.4 Comparison of electrochemical activities of A) Wild type cytochrome *bo*$_3$ oxidase, B) K362M mutant of cytochrome *bo*$_3$ oxidase, at different pH values (with oxygen, 1000 rpm rotation rate and scan rate of 0.02 V.s^{-1})

The K and D channels are widely studied in literature. A recent study with the site-specific mutants of these channels (K354M, D124N and K354M/D124N cytochrome *c* oxidase from *P. denitrificans*) on the oxygen reduction coupled to proton uptake was done by Dr. Meyer [50]. It was shown that when the proton entrance is blocked the enzyme may uptake protons from the exit of the proton pathways. The weak O_2 reduction activity that we observed with K362M mutant may be explained with the same reason. However, the sigmoidal O_2 reduction curve was not observed and this indicates the catalytic activity is perturbed in K362M.

Structural analysis of wild type cytochrome *bo*$_3$ oxidase and K362M mutant was made using FTIR difference spectroscopy. From redox difference spectra we aimed to obtain information about contributions of cofactors, secondary structure of protein and protonation/de-protonation of acidic residues [22-24]. In figure 4.5 the comparison of the FTIR difference (ox-red) spectra of wild type and K362M mutant at pH 7.5 is shown. The C=O vibrational modes of protonated Glu and Asp were observed above 1710 cm^{-1} [25, 12]. In the amide I range (1690-1620 cm^{-1}) signals at 1670, 1657, 1648 and 1630 cm^{-1} arise from conformational changes in the polypeptide backbone and Asn, Gln side chains (C=O vibrations) [12]. The signals at 1648, 1630 cm^{-1} and 1700, 1670 cm^{-1} indicate changes in the β-sheet secondary structure and loops [26]. The signals of protonated heme propionates can be seen at 1696 cm^{-1}[27]. In wild-type enzyme bound ubiquinone has a C=O vibration at 1668 cm^{-1} and 1656 cm^{-1} ant the C=C vibration at 1613 cm^{-1}. The $\delta(CH_3)$, $\delta(CH_2)$ vibrational modes of isoprenyl units of ubiquinone was observed at 1374 cm^{-1}, 1454 cm^{-1} and 1436 cm^{-1} and C-$COCH_3$ vibration at 1289 cm^{-1} and 1263 cm^{-1}[28]. Previous measurement with isolated arginine solution showed $CN_3H_5^+$ vibrational mode of this amino acid at 1672 and 1635 cm^{-1} [20]. With respect to this information the band at 1669 cm^{-1} can be attributed to the asymmetric $CN_3H_5^+$ vibrational mode and 1635 cm^{-1} to the symmetric $CN_3H_5^+$ vibrational mode of arginine, however, we need labeling or mutation studies to confirm that. In the amide II range (1570-1520 cm^{-1}) most dominant contributions arise from CN stretching and NH bending modes together with the C=C modes of heme porphyrin ring, COO^- modes of de-protonated heme propionates and Asp, Glu side chains [12]. The ring modes of protonated and reduced ubiquinone probably contributes at 1486, 1468, 1433 and 1388 cm^{-1} [28]. Oxidized ubiquinone has (C-OCH_3) vibrational modes at 1289, 1263 and 1206 cm^{-1} and below 1200 cm^{-1} the contribution

from the (P=O) modes of the phosphate buffer is present. In table 4.1 a summary of peak assignments for wt cytochrome bo_3 oxidase is shown.

For the K362M mutant, the band at 1656 cm^{-1} in amide I region is less intense and it can be due to the stronger C=O vibration of quinone in wild type bo_3 oxidase. From the double difference spectrum it was seen that the band at 1635 cm^{-1} was shifted to 1630 cm^{-1} and the band at 1689 cm^{-1} to 1687 cm^{-1}.

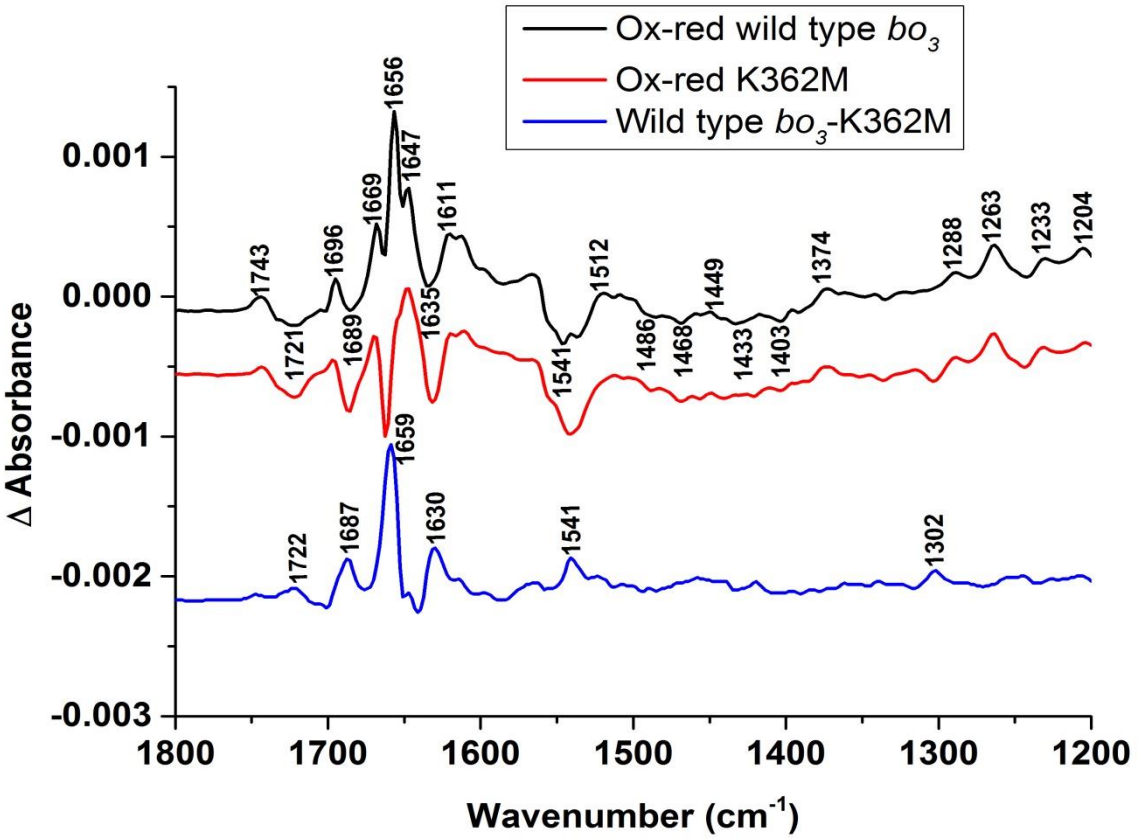

Figure 4.5 FTIR difference spectra of wild type cytochrome bo_3 oxidase, K362M mutant of the same enzyme (ox-red) and the double difference spectrum (Wild-type bo_3-K362M) at pH 7.5

Table 4.1 Assignments of principal bands of cytochrome *bo₃* oxidase redox difference spectra [29]

Band position in H_2O (cm^{-1})	Assignment
1743 (+)	Glu, Asp ν(C=O) COOH
1721 (-)	Glu, Asp ν(C=O) COOH
1696 (+)	Protonated heme propionates
1669 (+)	Asn and Gln ν(C=0), polypeptide backbone
1656 (+)	Asn and Gln ν(C=0), Quinone ν(C=0), polypeptide backbone
1647 (+)	Asn and Gln ν(C=O), polypeptide backbone
1635 (-)	Asn and Gln ν(C=O), polypeptide backbone
1611 (+)	Quinone ν(C=C)
1563 (+)	Deprotonated Glu, Asp $\nu(COO^-)^{as}$
1315, 1336 (+)	Deprotonated Glu, Asp $\nu(COO^-)^{s}$
1486, 1468, 1433, 1386 (-)	Ring modes of oxidized/reduced ubiquinol
1288, 1263, 1204 (+)	Oxidized ubiquinone $\nu(C\text{-}OCH_3)$
Below 1200	Phosphate buffer ν(P=O)

As a conclusion of this section, we worked with wild type cytochrome *bo₃* oxidase and K362M mutant which has a methionine instead of lysine in the entrance of the K-channel. Wild type *bo₃* oxidase was characterized by using cyclic voltammetry and FTIR difference spectroscopy. Comparison of wild type enzyme with K362M demonstrated the loss of catalytic activity in this mutant. The loss of catalytic activity of K362M is related with the perturbed proton transfer (chemical protons) in the enzyme which is coupled with the electron transfer to the catalytic center. From the FTIR difference spectra it was determined that the vibrational modes of ubiquinone in K362M mutant were weaker than wild type enzyme. K362M mutant was reconstituted with Q_2 to recover the catalytic activity of the enzyme. However, the enzyme still did not have O_2 reduction activity (Appendix, Figure 1) which indicates that the loss of activity in K362M is due to the blocked K channel.

4.1.2 Interaction of quinones with cytochrome *bo₃* oxidase

Our next aim was to further investigate the effect of quinone (as a cofactor) on the O_2 reduction activity of cytochrome *bo₃* oxidase and the redox properties of interacting hemes.

In this part various quinone types such as Q_1, Q_2, Q_{10} and menadione were used and their interaction with cytochrome *bo₃* oxidase was investigated. Iwamura *et al.* studied the role of isoprenyl tail of ubiquinone with bovine heart complex I and *bo₃* oxidase [9]. He reported that the double bonds in the isoprenyl tail enhance the quinone binding and different membrane enzymes recognize isoprenyl tail differently. The work of Dr. Sylvia Choi was consistent with this idea [10]. She showed that the energy required to dissociate the hydrophobic tail of the quinone from the enzyme is higher than the head group. She also showed that Q_1, Q_2 and Q_{10} can displace ubiquinone-8 in wild type *bo₃* oxidase while maintaining the enzymatic activity [10]. Our first aim was to regain the O_2 reduction activity which was perturbed due to the extraction of bound ubiquinone-8 (Q_8) from the wild type enzyme. In figure 4.5 the cyclovoltammograms of cytochrome *bo₃* oxidase (Quinone extracted) with Q_1, Q_2, Q_{10} and menadione is shown (2:1 quinone-enzyme ratio). Wild type *bo₃* oxidase with Q_2 showed a higher O_2 reduction activity than with Q_1. Q_{10} and menadione partially recovered the activity. This could support the idea that a long tail is crucial for stronger quinone binding. However, Q_{10} has a longer isoprenyl tail than original ubiquinone-8 and it could prevent perfect docking to the binding site. Studies of Dr. Sylvia Choi showed that Q_{10} can be successfully inserted in *bo₃* oxidase and she reported that it can form semiquinone [10] which indicates electrons are transferred to the heme *b*. On the other hand, the short tail length of Q_1 and Q_2 molecules enables them to be more soluble in water than Q_{10} and menadione, thus making it faster and easier diffusion into the enzyme. This could also explain the different measured activities. The cyclovoltammograms of quinone free *bo₃* oxidase is shown in appendix figure 2. The O_2 reduction activities of the wild type *bo₃* oxidase, quinone free *bo₃* oxidase and *bo₃* oxidase with quinones were compared at a rotation rate of 1000 rpm (highest activity) (Figure 4.6).

From the cyclovoltammogram of wt *bo₃* oxidase with Q_1 and Q_2 measured under zero-oxygen conditions, the reduction peak (- 0.30 V) and oxidation peak (only with Q_2) (+ 0.25 V) of quinone was determined (Figure 4.6). Due to the excess amount of un-bound quinones in solution and non-specific binding these signals overlap with the catalytic

signal of the enzyme. O_2 reduction activity of the *bo₃* with quinone was recovered with a sigmoidal oxygen reduction peak starting at – 0.20 V which is + 0.10 V shifted compared to the wild type cytochrome *bo₃* oxidase (Figure 4.2). It is possible to regain the catalytic activity of cytochrome *bo₃* enzyme by inserting quinone variants and Q_2 provided the highest activity. In the case of menadione the different head group structure could prevent proper docking in the quinone binding site. Repeating the experiments with Q_8 (natural substrate) could provide more apprehensible explanation to the relation between catalytic activity of the enzyme and the tail length of quinone.

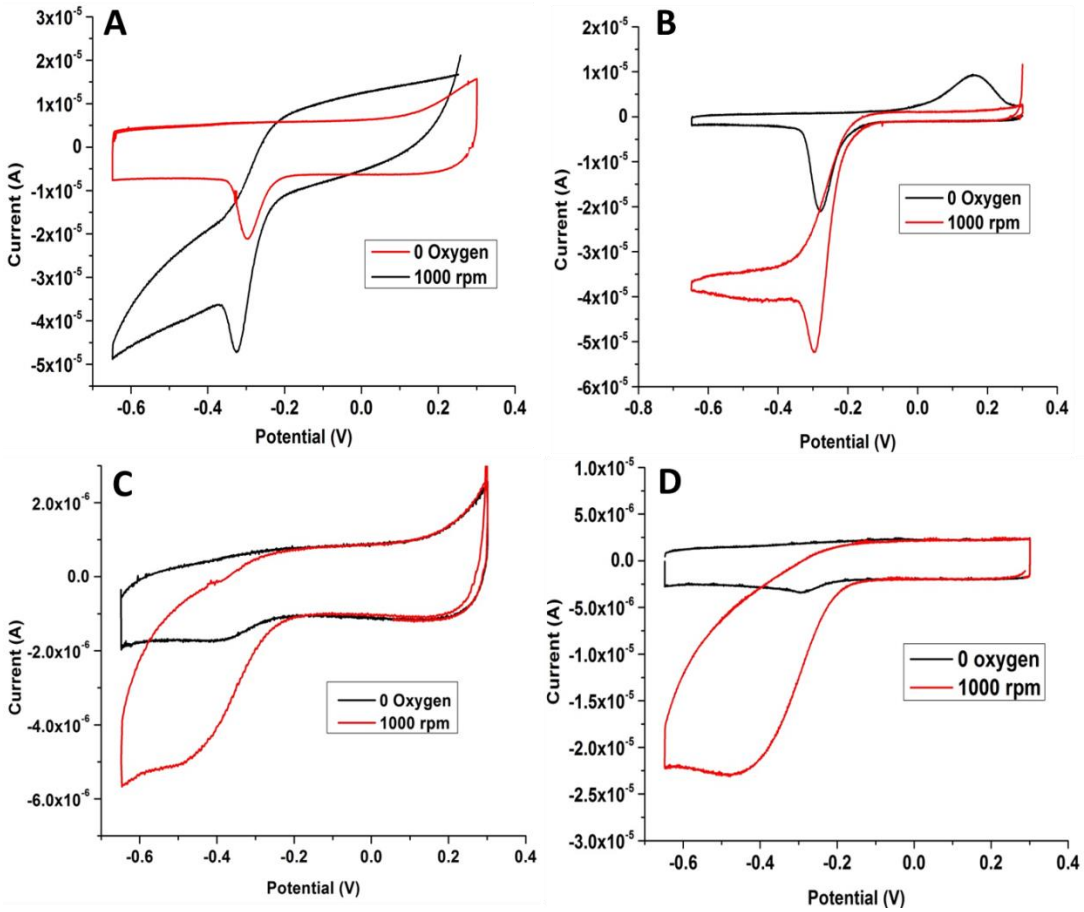

Figure 4.6 Cyclovoltammogram of A) *bo₃* + Q_1 B) *bo₃* + Q_2 C) *bo₃* + Q_{10} D) *bo₃* + menadione at pH 7.5 (scan rate of 0.02 $V.s^{-1}$)

In order to support our results we further investigated the role of quinone on the redox potentials of the heme cofactors in the enzyme via potentiometric titrations.

Potentiometric titrations were performed with wild type *bo₃* oxidase (with quinone), quinone free *bo₃* oxidase and cytochrome *bo₃* oxidase with Q_2 and menadione. We focused on Soret band at 428 nm in our experiments to determine redox potentials of

cofactors. In figure 4.7 the potentiometric titration of wild type *bo*$_3$ oxidase and the Gaussian fitting of the first derivative of obtained absorbance values is shown. Four different contributions were obtained from the titration of Soret band of wild type *bo*$_3$ oxidase (-249 mV, -147 mV, -49 mV and +146 mV). As it was described previously cytochrome *bo*$_3$ oxidase contains two hemes (*b* and *o*$_3$), Cu_B and a tightly bound ubiquinone-8 in its structure. There are several studies indicating that these cofactors are interacting with each other and there is cooperativity between them [6, 30, 31]. It means that reduction and oxidation of each heme is not happening sequentially but in conjunction of each other. However, it is not clear how bound quinone interacts with other cofactors.

Two of the determined contributions (-147 mV and – 49 mV) are originating from the interacting hemes in the *bo*$_3$ oxidase [6, 30, 31]. The high potential contribution at + 146 mV can be attributed to the coupling between heme *o*$_3$ and Cu_B which was reported in the literature to have a high potential value [6, 30, 31]. Added to that, we obtained a low-potential contribution at - 249 mV. This low-potential contribution may be originating from the heme-quinone interaction. It was shown that quinones have negative mid-point potentials [32]. The intensity of this low-potential contribution diminished in the titration of quinone free *bo*$_3$ oxidase (see figure 4.7) which supports our suggestion.

The same potentiometric titrations were repeated with quinone free *bo*$_3$ oxidase. In Figure 4.8 the results of the potentiometric titration of quinone free cytochrome *bo*$_3$ oxidase at pH 7.5 is shown. We see that the mid-point potentials of all contributions are positively shifted. Two contributions were determined with +48 mV and +158 mV mid-point potentials in Soret band. Fitting of alpha band showed similar two contributions with mid-point potentials of +46 mV and + 164 mV. Extremely slow electron transfer affects the equilibration time of all contributions during titration and this could result in hysteresis effect [33]. Removal of quinone does not completely block the electron transfer but makes it extremely slow as deduced from the longer time of equilibrium required and this could be due to the residual quinone in the sample. A negative contribution was observed in both Soret band (-289 mV) and alpha band (- 222 mV) however it was below the signal to noise ratio. Shifts in the redox potentials suggest that quinone-heme interaction has an important role in the redox properties of the enzyme.

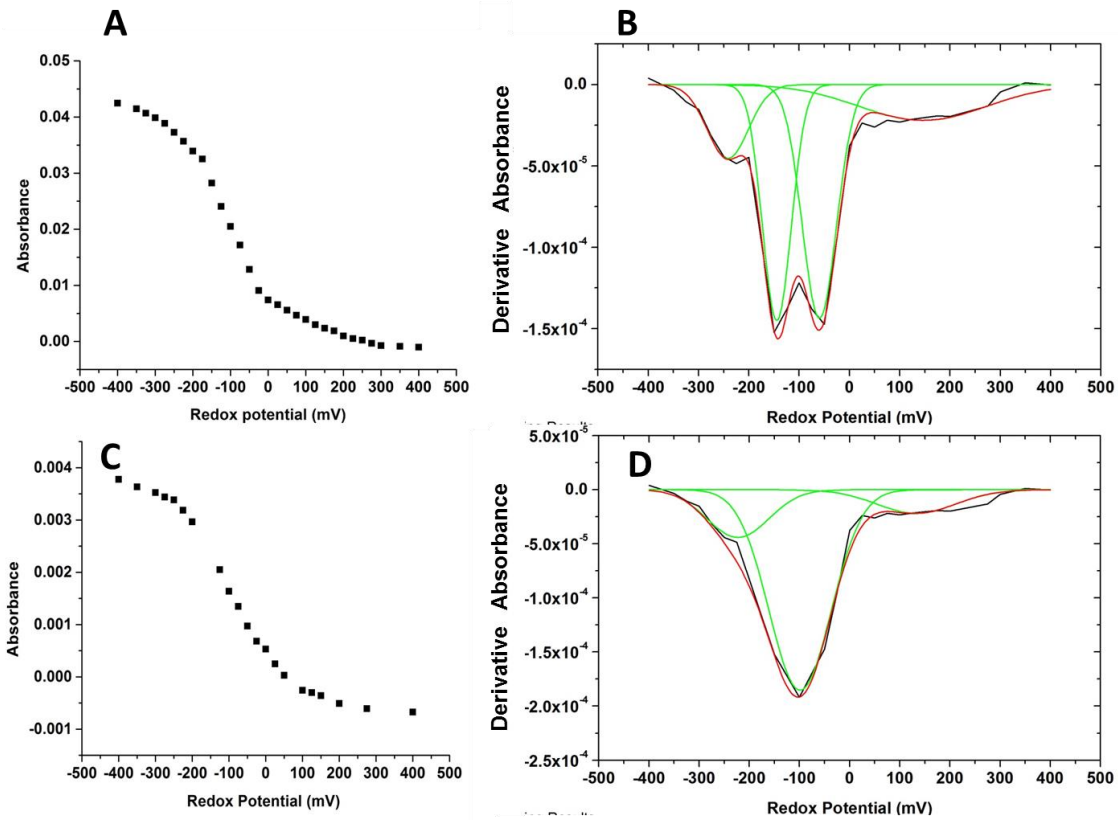

Figure 4.7 Potentiometric titration of wild type cytochrome *bo₃* oxidase at pH 7.5, A) Absorbance values from Soret band, B) Gaussian fitting of the first derivative of the absorbance values from Soret band, C) Absorbance values from alpha band, D) Gaussian fitting

In order to see if we could reverse these shifts in the redox potentials of cofactors, *bo₃* oxidase was reconstituted with menadione and Q_2 and then the potentiometric titrations were repeated. In figure 4.9 the results of the potentiometric titration of menadione inserted in the cytochrome *bo₃* oxidase at pH 7.5 is shown. After insertion of menadione we observed two contributions in the Soret band (-254 mV and –176 mV) which were closer to the values obtained with wild type enzyme (-249 mV and –147 mV). However, the contribution at -254 mV was not perfectly separated and had weak signal in Soret band. In the alpha band a dominant contribution was measured at -188 mV and relatively weak contribution at -275 mV.

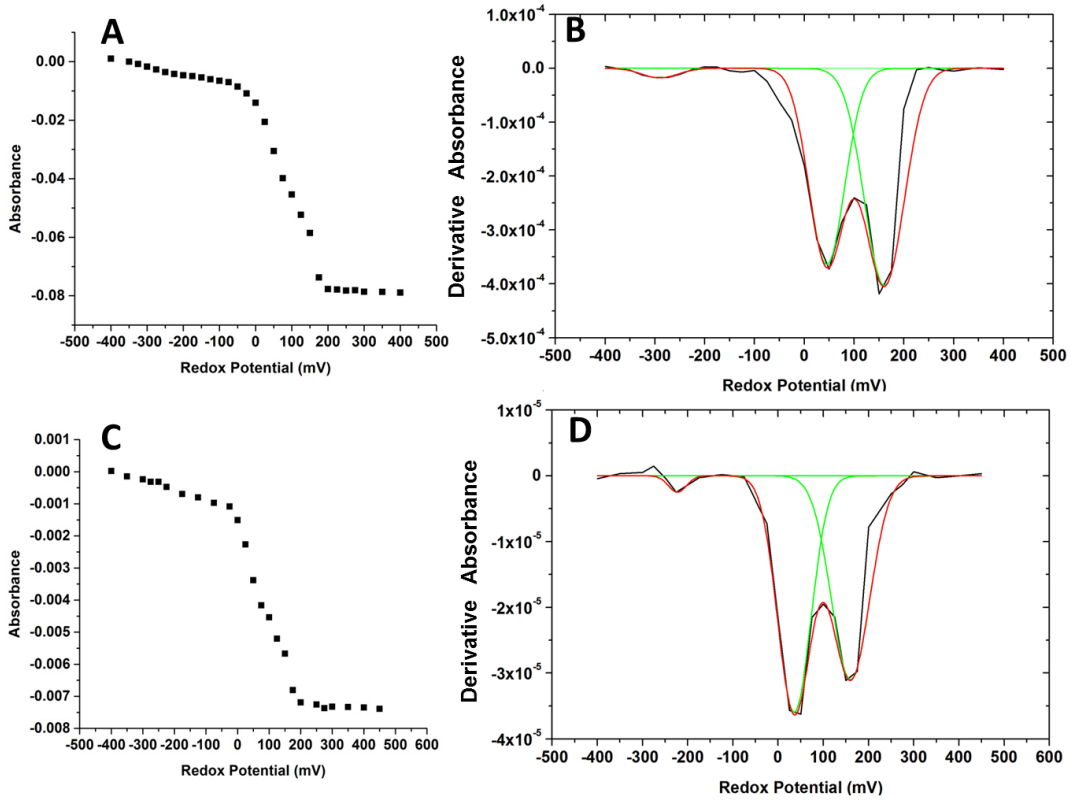

Figure 4.8 Potentiometric titration of quinone free cytochrome *bo*$_3$ oxidase at pH 7.5, A) Absorbance values from Soret band, B) Gaussian fitting of the first derivative of the absorbance values from Soret band, C) Absorbance values from alpha band, D) Gaussian fitting of the first derivative of the absorbance values from alpha band

From the cyclic voltammetry experiments it was determined that Q_2 provided the highest O_2 reduction activity (Figure 4.6). The potentiometric titrations were performed with cytochrome *bo*$_3$ oxidase with Q_2 to support our data. In figure 4.10 results of the potentiometric titration of cytochrome *bo*$_3$ enzyme with Q_2 is shown. From the Gaussian fitting of the first derivative of the absorbance values obtained from Soret band we determined three contributions at -256 mV, -140 mV and – 65 mV potentials which nearly corresponds to the three contributions measured in wild type *bo*$_3$ oxidase (-249 mV, -147 mV and -49 mV and +146 mV).

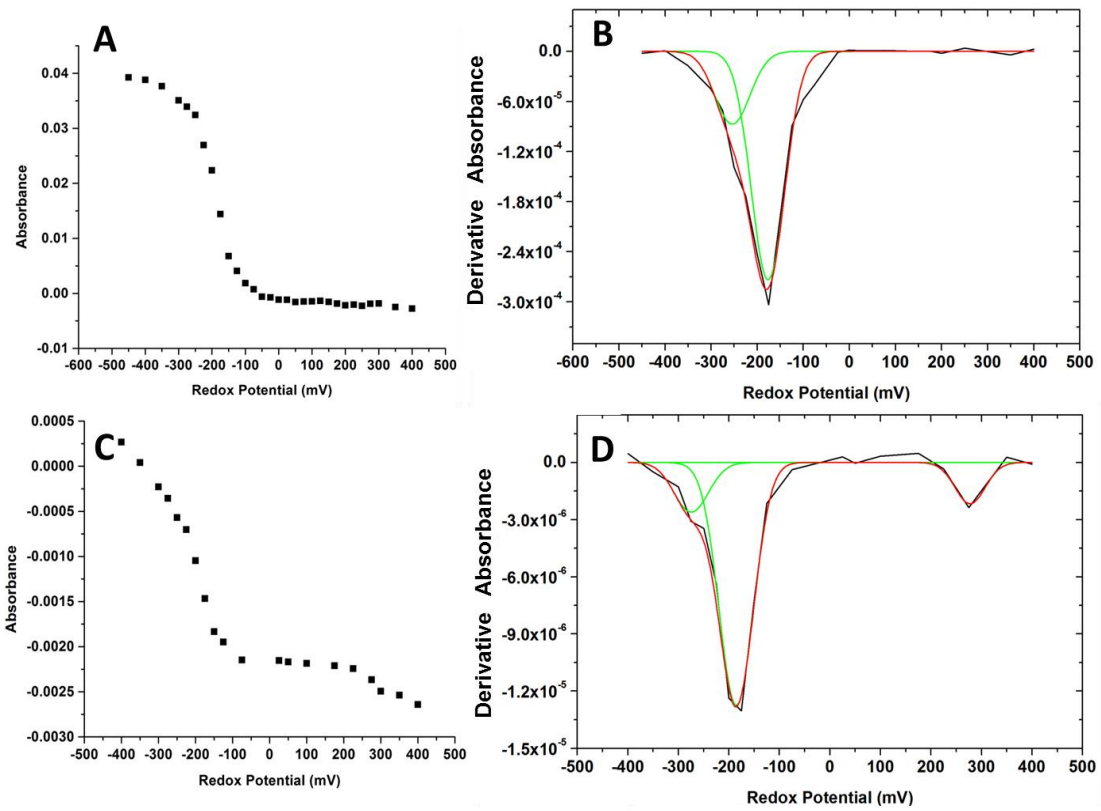

Figure 4.9 Potentiometric titration of cytochrome *bo*$_3$ oxidase with menadione at pH 7.5, A) Absorbance values from Soret band, B) Gaussian fitting of the first derivative of the absorbance values from Soret band, C) Absorbance values from alpha band, D) Gaussian fitting of the first derivative of the absorbance values from alpha band

In table 4.2 a summary of measured redox potentials of all contributions obtained from the potentiometric titration of cytochrome *bo*$_3$ oxidase with quinone variants at pH 7.5 is shown. Redox potentials of all contributions were shifted for the quinone free *bo*$_3$ oxidase. The *bo*$_3$ oxidase with Q_2 provided three negative redox potentials (similar to the wt values) corresponding to the interacting hemes and probably bound quinone. Titration of *bo*$_3$ oxidase with menadione showed two low-potential contributions in Soret band and they were compatible with the values from wild type enzyme however one contribution was still missing. These results are in line with the O_2 reduction activity. It was reported that small and soluble quinone variants (such as Q_1) could displace the head group of tightly bound ubiquinone-8 and it is mainly bound through the hydrophobic interaction with the tail [10]. However, if the tightly bound ubiquinone-8 is removed from the enzyme, the quinone variants can bind to the enzyme and retain the ability to form semiquinones. Repeating the same experiments with Q_8 could provide more detailed information on the role of tail length. For the future studies the addition of quinone variants to the quinone

free quinone binding site mutants could provide more information about the mechanism of quinone binding.

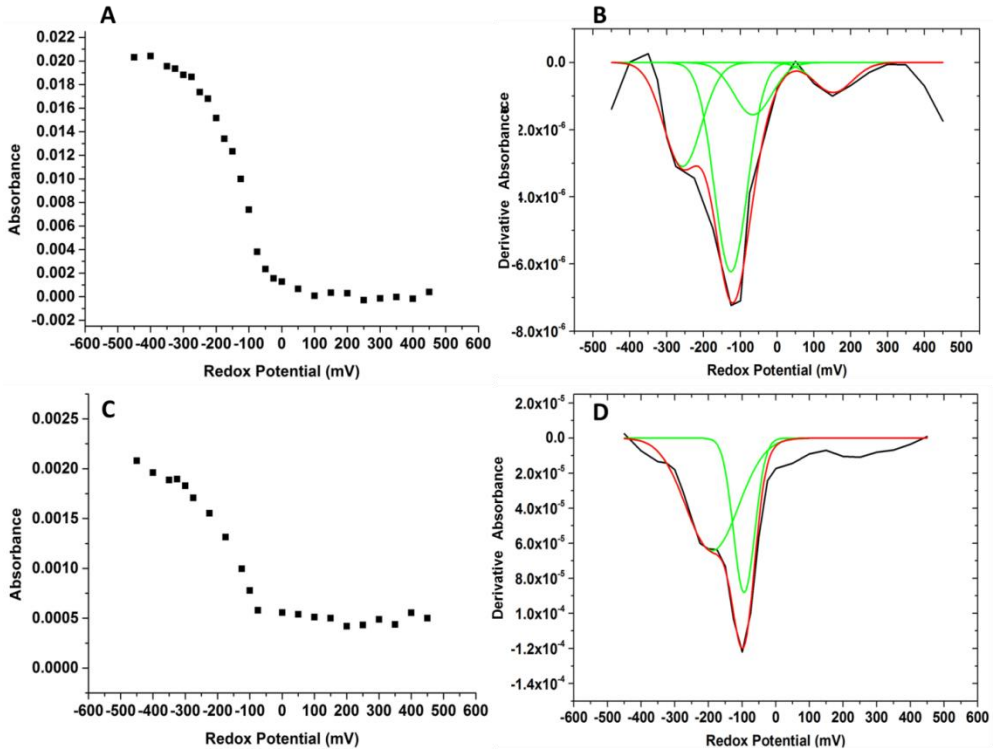

Figure 4.10 Potentiometric titration of cytochrome *bo₃* oxidase with Q_2 at pH 7.5, A) Absorbance values from the Soret band, B) Gaussian fitting of the first derivative of the absorbance values from Soret band, C) Absorbance values from the alpha band, D) Gaussian fitting of the first derivative of the absorbance values from alpha band

Table 4.2 Summary of redox potentials obtained from the potentiometric titration of cytochrome *bo₃* oxidase with quinone variants at pH 7.5.

WT *bo₃* oxidase (vs Ag/AgCl) mV	Quinone free *bo₃* oxidase (vs Ag/AgCl) mV	Q_2 + *bo₃* oxidase (vs Ag/AgCl) mV	Menadione + *bo₃* oxidase (vs Ag/AgCl) mV
-249 +/-10	-	**-256** +/-10	**- 254** +/-10
-147 +/-10	**+48** +/-10	**-140** +/-10	**-176** +/-10
-49 +/-10	**+158** +/-10	**-65** +/-10	-

As a conclusion, the highest O_2 reduction activity was measured with *bo₃* oxidase with Q_2, whereas Q_1, Q_{10} and menadione partially recovered the O_2 reduction activity of quinone free *bo₃* oxidase.

Further investigation of redox properties of the interacting hemes and quinone was done by potentiometric titrations in order to support the obtained electrochemical data. Mid-point potentials of all contributions were shifted for quinone free *bo₃* oxidase. The shifted potentials turn back to their original values when Q_2 was added into the quinone free *bo₃* oxidase. It was shown that Q_2 is the most suitable quinone variant amongst other studied quinone variants. There is a complex interaction between cofactors in *bo₃* oxidase and we believe that quinone also has a role in it as a cofactor-like behavior.

4.1.3 Investigation of the quinone binding site of cytochrome *bo₃* oxidase

In this part of the study we worked with several mutants of amino acids which were proposed to be at the quinone binding site of the cytochrome *bo₃* oxidase [1, 10-18] (Figure 4.11). Recent results of the group of Prof. Gennis strongly suggest that there is a single high-affinity quinone binding site in the structure of cytochrome *bo₃* oxidase [10-14, 16, 17]. With respect to these results the mutants listed in table 3.1 were investigated.

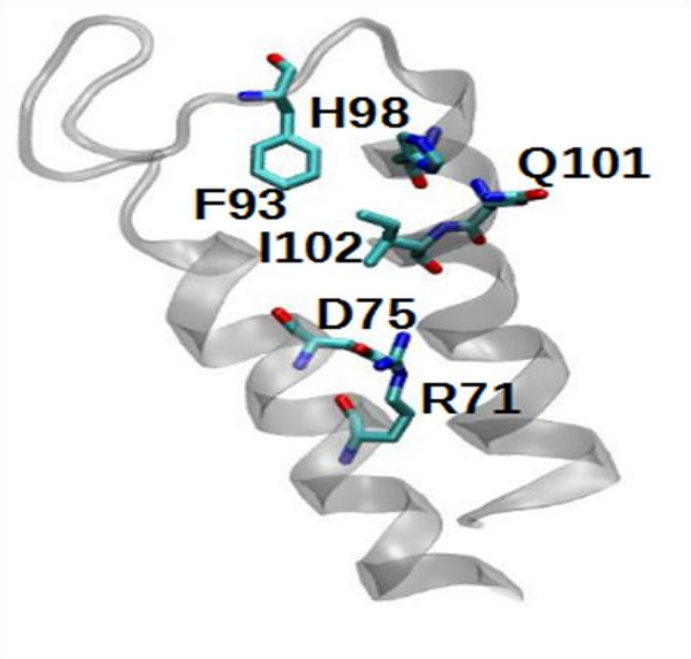

Figure 4.11 Proposed high affinity quinone binding site in cytochrome *bo₃* oxidase from *E. coli* (1FFT.pdb)

The cyclovoltammograms of all mutants were compared with wild type enzyme and the relative percentage O_2 reduction activities were calculated. The catalytic potential of each mutant was also determined for comparison. In figure 4.12 the comparison of cyclovoltammograms of wild type cytochrome *bo*$_3$ oxidase with F93A (1% relative activity), R71H (10% relative activity) and Q101M (80% relative activity) is shown. Q101N, Q101L, F93A, D75N, H98F, I102N, R71H mutants showed no catalytic activity (Appendix Figure 3 to11).

For the mutants that have high O_2 reduction activity, catalytic potentials were negatively shifted to – 0.48 V for Q101M, - 0.40 V for Q101T, - 0.45 for Q101A and -0.40 V for F93Y from the wild type enzyme value at – 0.35 V. Q101M and Q101A showed a wild type-like activity which was also in line with the enzymatic turnover measured by Dr. Sylvia Choi (Table 4.3). In the Q101A mutant enzyme glutamine was replaced with a smaller amino acid alanine and it enables water molecules to get to the binding site without perturbing the quinone binding. F93A had 1% relative O_2 reduction activity and F93Y had 60% when compared to the wt *bo*$_3$ oxidase. The difference in the relative O_2 reduction activity of these mutants may be explained by the different side chain lengths and the loss of aromatic ring.

Table 4.3 summarizes the data. The enzymatic turnover values were obtained in solution and the quinone in the enzyme was used as an electron donor. In our experiments the electrode acts as an electron donor which can be tuned depending on the applied potential and this can result in different O_2 reduction activity levels.

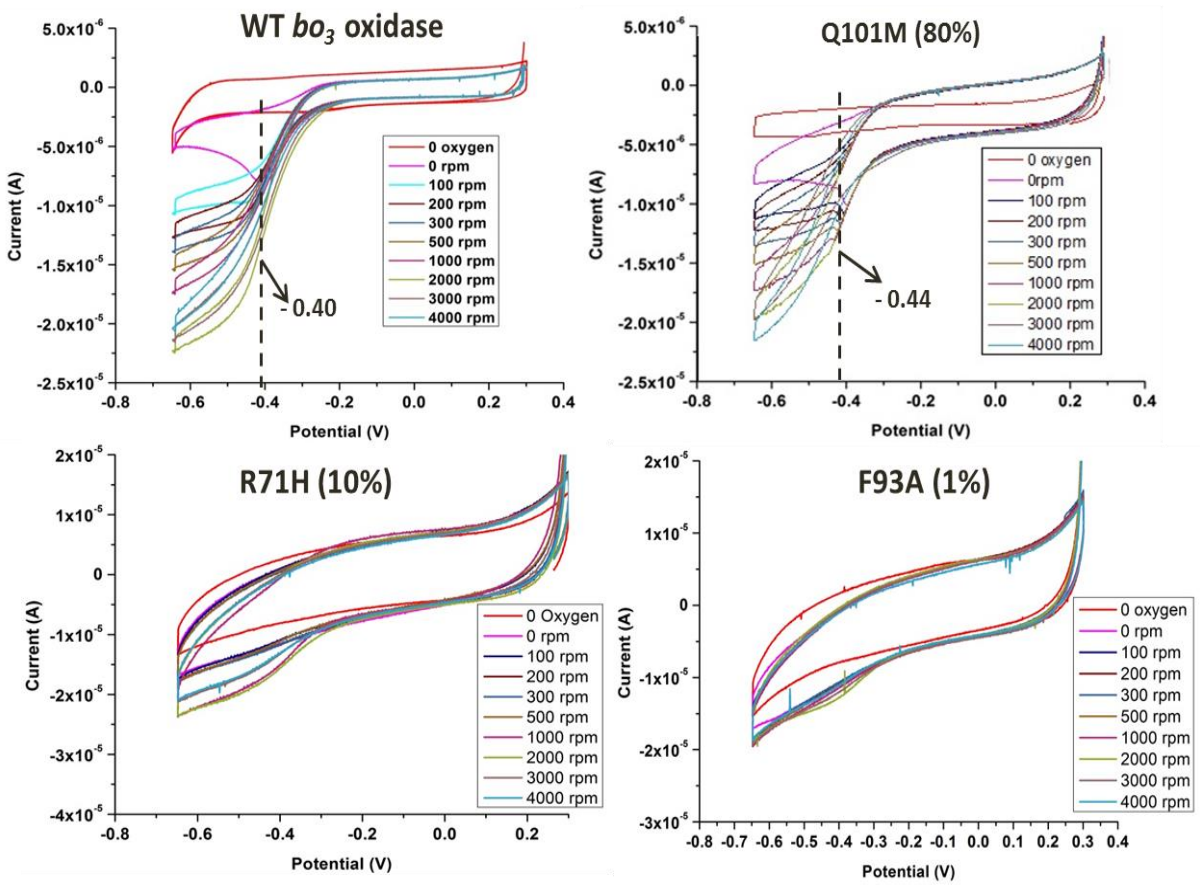

Figure 4.12 Cyclovoltammogram of wild-type cytochrome *bo₃* oxidase, Q101M (100% O_2 reduction activity), R71H (10% O_2 reduction activity) and F93A (1% O_2 reduction activity) mutants (scan rate of 0.02 $V.s^{-1}$)

Table 4.3 Summary of all electrochemical alterations in studied mutants with respect to wild-type cytochrome *bo₃* oxidase at pH 7.5 (≈ +/-5% error) [10, 13].

Sample	Catalytic potential (V)	Electrochemical reaction with O_2	k_{cat} (s^{-1})	Sigmoidal catalytic curve	Enzymatic activity *
Wild type	**- 0.35**	**100%**	**14.8**	**Yes**	**100%**
Q101N	**-**	**1%**		**No**	**10%**
Q101M	**- 0.48**	**80%**	**11.8**	**Yes**	**50%**
Q101T	**- 0.40**	**50%**	**7.7**	**Yes**	**30%**
Q101A	**- 0.45**	**80%**	**12.9**	**Yes**	**30%**
Q101L	**-**	**1%**		**No**	**10%**
F93A	**-**	**1%**		**No**	**40%**
F93Y	**- 0.40**	**60%**	**10.2**	**Yes**	**80%**
D75N#	**-**	**0%**		**No**	**0%**
H98F	**-**	**10%**		**No**	**1%**
I102N	**-**	**10%**		**No**	**0%**
R71H	**-**	**10%**		**No**	**0%**

*** Values provided by Dr. Sylvia Choi**

 # Quinone extracted

We continued our investigation of quinone binding site by using FTIR difference spectroscopy in order to obtain information about the structural changes in the enzyme due to the mutations in the quinone binding site. Since the natural environment of quinone binding site was disturbed it was expected to observe changes in quinone binding and the electron transfer to the binuclear site may also be affected.

In figure 4.13 and 4.14 the FTIR difference and double difference spectra of F93A and F93Y mutants are shown respectively. The C=O vibration of ubiquinone at 1655 cm^{-1}, the C=C vibration at 1610 cm^{-1}, the aromatic ring vibration of the reduced state (1390 cm^{-1}, 1470 cm^{-1}, 1488 cm^{-1}) and the C-OCH_3 vibration at 1264 cm^{-1} and 1286 cm^{-1} can be observed. Changes in the amide I and II bands provided information about the conformational changes in the secondary structure of the protein. In order to highlight the shifts the double difference spectra was calculated by normalizing all spectra with respect

to the quinone signals at 1264 cm^{-1} and 1286 cm^{-1} and subtracting the wild type spectrum from the mutant spectra. The problem with this normalization is that there may be different quinone content and shifts can look stronger than real.

F93 is a residue that has been suggested to play an important role in quinone binding site [18]. For the F93 mutants it was expected to observe a shift in the C=C ring mode of Phenylalanine (F) at 1498 cm^{-1} however, due to its non-polar structure it absorbs infrared radiation weakly. The double difference data of F93A and F93Y show changes in the amide I and II region which suggest conformational changes in the secondary structure of the protein. Comparison of the difference spectra of F93A with F93Y indicates that the mutation of Phe into Ala causes additional conformational changes in the polypeptide backbone of the enzyme. However, the broad amide I and II bands of F93Y indicates that the protein may be denatured. For this reason it was not possible to make detailed conclusion on the double difference data of F93Y.

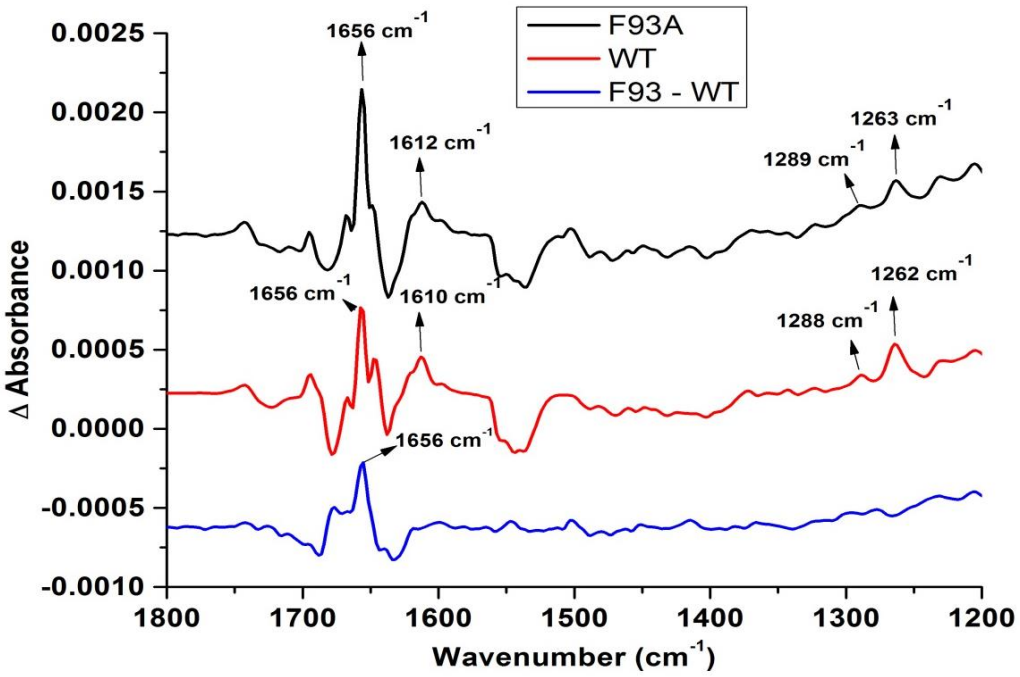

Figure 4.13 Oxidized-minus-reduced FTIR difference spectra of F93A, wild type cytochrome *bo₃* oxidase and double difference spectrum of F93A-WT at pH 7.5.

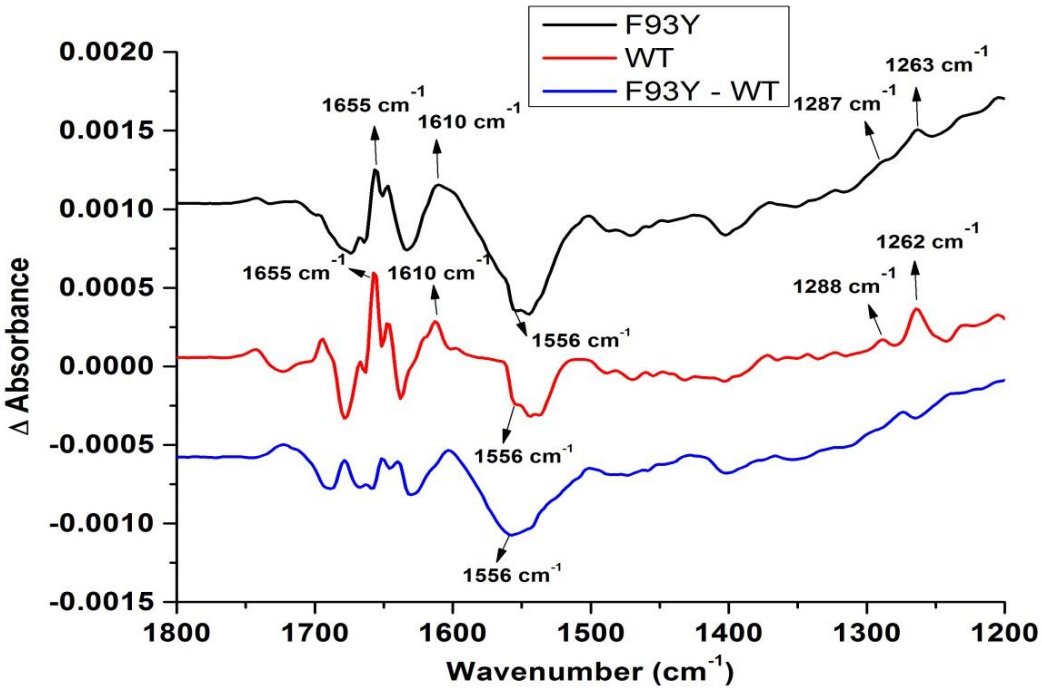

Figure 4.14 Oxidized-minus-reduced FTIR difference spectra of F93Y, wild-type cytochrome *bo*$_3$ oxidase and double difference spectrum of F93Y-WT at pH 7.5.

In figures 4.15, 4.16, 4.17, 4.18 and 4.19 the FTIR difference and double difference spectra of Q101N, Q101T, Q101M, Q101L and Q101A are shown. Glutamine has a low extinction coefficient thus it is not possible to make comments on the shifts of the vibrational mode of glutamine at 1672 cm^{-1}. In the amide I region shifts or intensity changes in the mode at 1655 cm^{-1} can be attributed to the weaker ubiquinone binding. The changes for the bands at 1685 cm^{-1} and 1635 cm^{-1} indicate changes in the polypeptide backbone of the protein. From the FTIR difference spectra it is not possible to make more specific assignments.

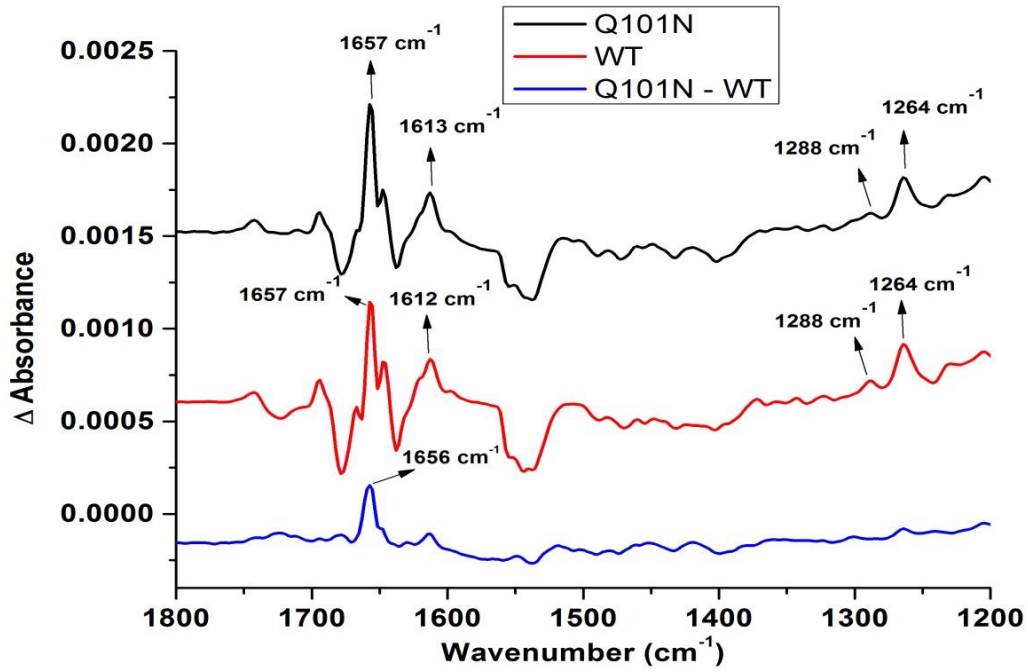

Figure 4.15 Oxidized-minus-reduced FTIR difference spectra of Q101N, wild-type cytochrome *bo₃* oxidase and double difference spectrum of Q101N-WT at pH 7.5.

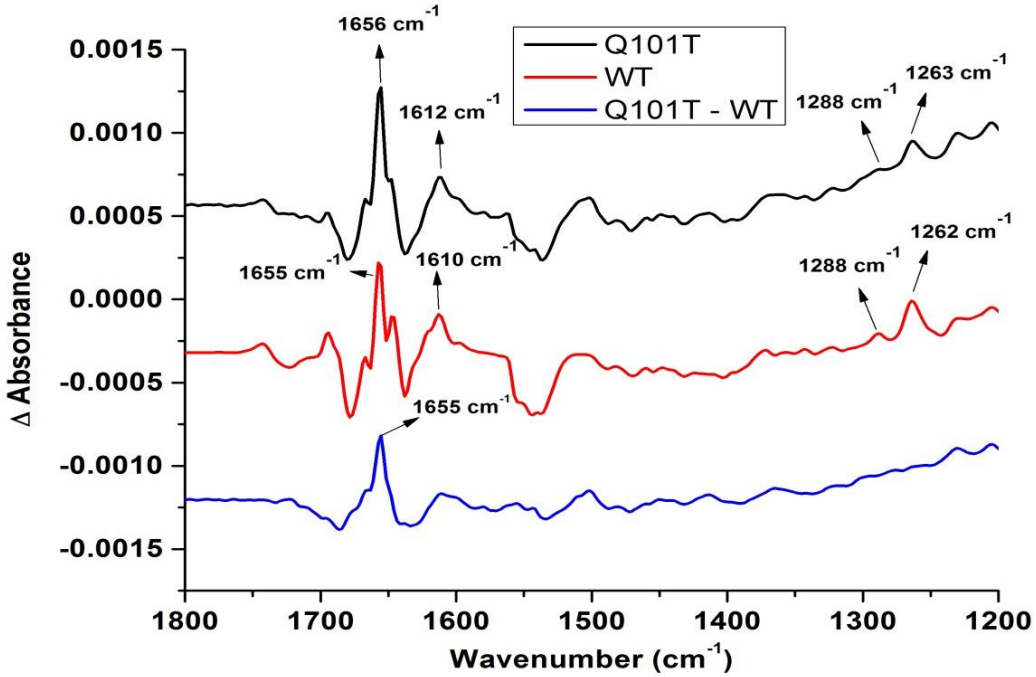

Figure 4.16 Oxidized-minus-reduced FTIR difference spectra of Q101T, wild-type cytochrome *bo₃* oxidase and double difference spectrum of Q101T-WT at pH 7.5.

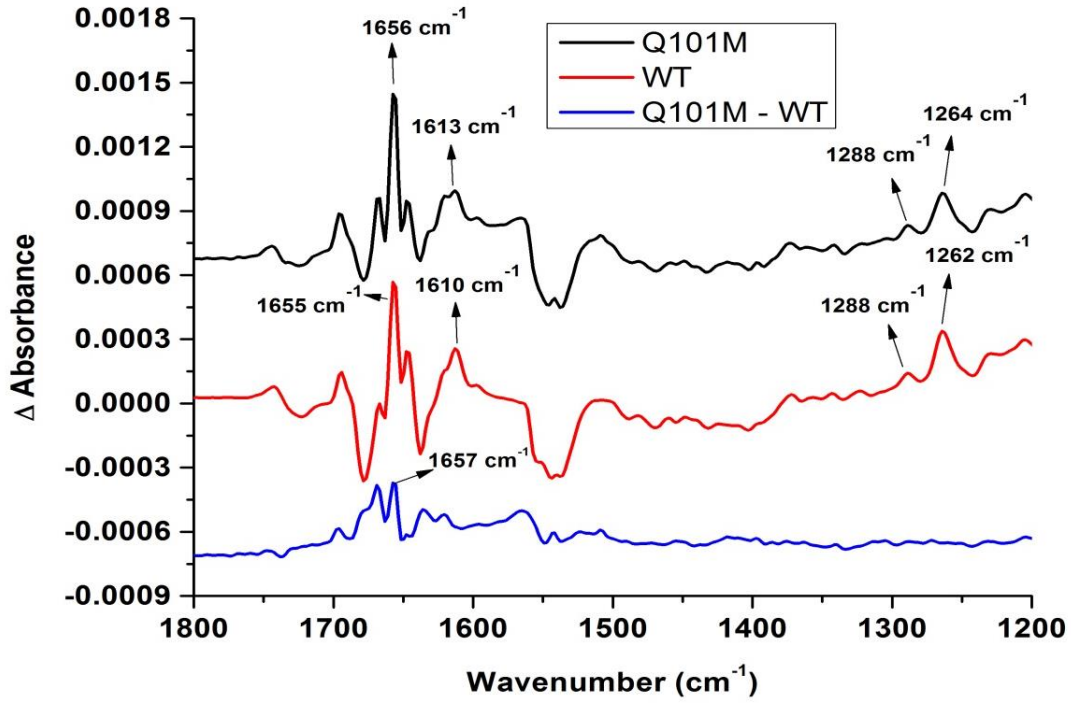

Figure 4.17 Oxidized-minus-reduced FTIR difference spectra of Q101M, wild-type cytochrome *bo*$_3$ oxidase and double difference spectrum of Q101M-WT at pH 7.5.

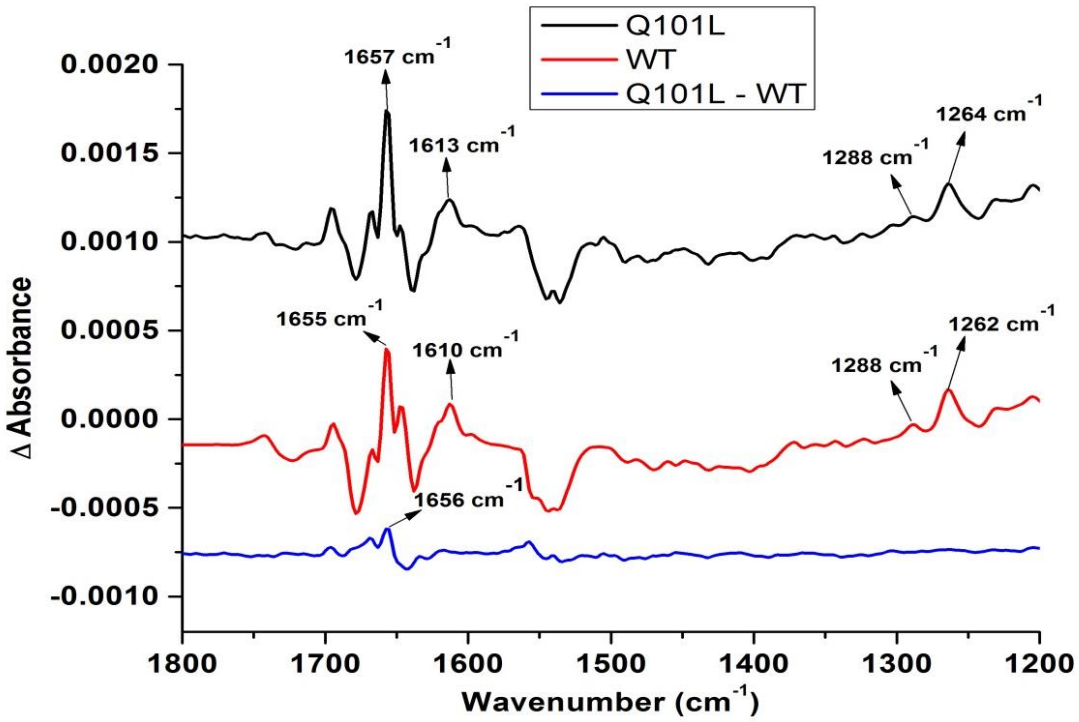

Figure 4.18 Oxidized-minus-reduced FTIR difference spectra of Q101L, wild-type cytochrome *bo*$_3$ oxidase and double difference spectrum of Q101L-WT at pH 7.5.

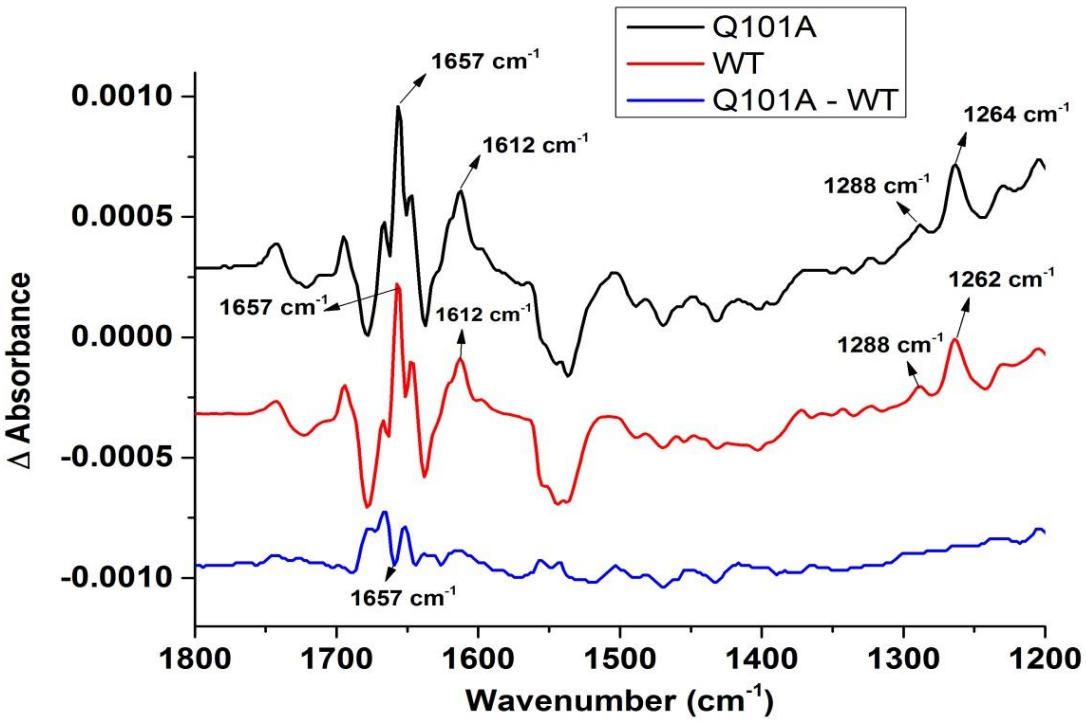

Figure 4.19 Oxidized-minus-reduced FTIR difference spectra of Q101A, wild-type cytochrome *bo₃* oxidase and double difference spectrum of Q101A-WT at pH 7.5.

In the final part of this chapter the residues at the high affinity quinone binding site of *bo*$_3$ oxidase have been investigated by working with several site-directed mutants. By using cyclic voltammetry the O_2 reduction activities were measured and with FTIR difference spectroscopy the possible structural changes in the enzyme were monitored.

As a conclusion, our results showed that all mutants in this proposed quinone binding site showed reduced O_2 reduction activity and shifts in the catalytic currents. Q101A and Q101M mutants showed high relative activity (80%) O_2 reduction activity and F93Y had 60% activity as compared to the wild type enzyme activity. The length and polarity of Glu-101 may have an important role in the quinone binding and electron transfer to the heme *b*. The S group of methionine may help to make H bonding with the reduced quinone and this may explain the high O_2 reduction activity with Q101M. Removal of aromatic ring in the structure of Phe-93 showed that this ring structure may be directly interacting with the head group of quinone and affecting the electron transfer to the heme *b*.

FTIR difference data showed that mutation of residues in the quinone binding site does not affect the FTIR spectra dramatically. Small shifts in the double difference spectra may indicate conformational changes in the secondary structure of the protein. However, the

normalization of the IR difference spectra with respect to the quinone vibrational modes may create artificial shifts in the double difference data. Thus, it was not possible to make more detailed analysis on the structural changes.

4.1.4 SEIRAS measurements of cytochrome *bo₃* oxidase

In the last part of this chapter surface-enhanced infrared absorption spectroscopy (SEIRAS) was studied as an alternative technique to study membrane proteins [34-38]. The aim was to immobilize proteins on a gold-coated ATR crystal and to couple it with electrochemistry. In the literature there are several methods to adsorb proteins on metal surfaces [39-43]. In this study we started working with a model compound, cytochrome *c*. Cytochrome *bo₃* oxidase was then immobilized on a gold coated ATR crystal via his-tag modification.

This technique was introduced by Dr. Sebastian Kriegel in our laboratory on Complex I [44].

a. Immobilization of Cytochrome *c* on a gold surface

Cytochrome *c* is already well studied by FTIR difference spectroscopy and cyclic voltammetry [45-48]. The protocol introduced by Jiang *et al*. was followed [49].

Chemical deposition of gold on ATR crystal was explained in detail in section 3.3.2.2. In appendix figure 12 the SEIRA spectra of MUA monolayer on the gold surface at different times after addition of MUA solution is shown. Upon the addition of cytochrome *c* solution, the amide I and amide II modes of cytochrome *c* at around 1659 cm^{-1} and 1551 cm^{-1} (Appendix figure 13), appeared immediately [49]. Maximum surface coverage was reached when the intensities of these bands stopped increasing.

After the adsorption of cytochrome *c* on the MUA layer, the electrochemical activity of the system was probed via cyclic voltammetry. In figure 4.20 cyclic voltammogram of cytochrome *c* adsorbed on the MUA/Au surface (Phosphate buffer at pH 7) is shown. Oxidation and reduction peaks of cytochrome *c* were observed upon sweeping the applied potential which indicates that electrons were transferred through the gold layer to the protein.

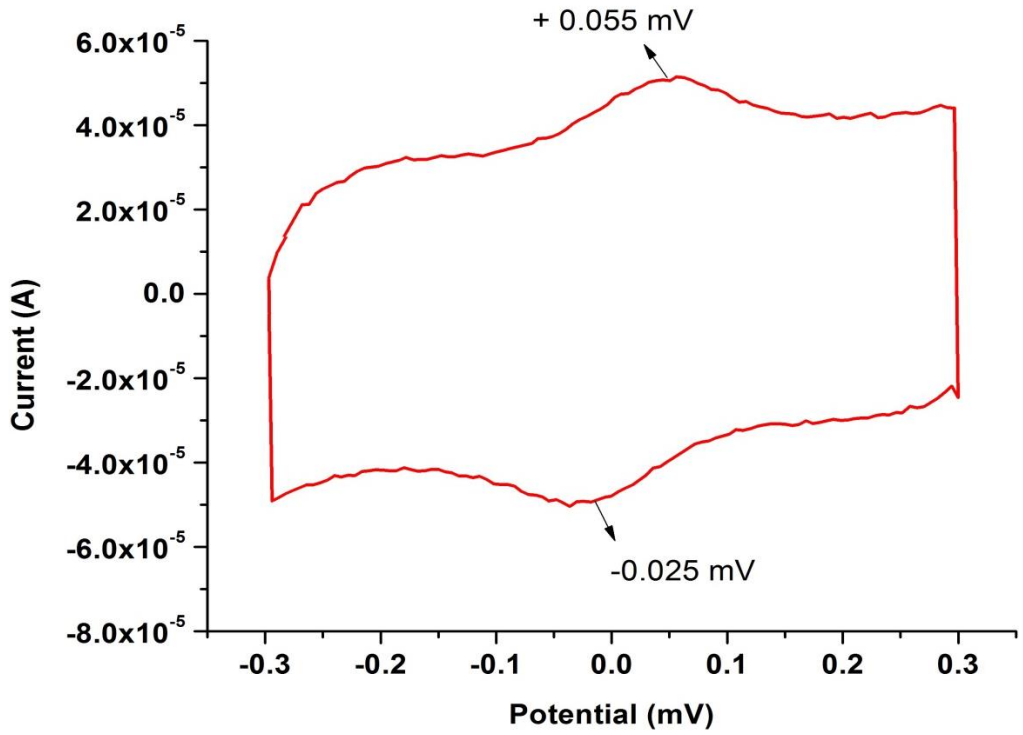

Figure 4.20 Cyclic voltammogram of cytochrome *c* adsorbed on the MUA/Au surface (Phosphate buffer at pH 7)

In order to measure the infrared difference spectrum of cytochrome *c* the system was inserted in the FTIR spectrometer and coupled with a potentiostat. In figure 4.21 potential-induced redox difference spectra of cytochrome *c* is shown. Ox-red spectrum of MUA layer showed that the band at 1681 cm^{-1}, which arises due to the C=O stretching mode of the carboxyl head groups of MUA [49],overlaps with the Amide I mode of the peptide backbone of cytochrome *c* at 1678 cm^{-1}. From cyclovoltammogram of adsorbed cytochrome *c* (Figure 4.20) the surface coverage was measured as 6.5 pmol cm^{-2}. This may indicate that the surface is not fully covered (Jiang *et. al.* 7.7 pmol cm^{-2} [49]). This suggests that water molecules on the surface of the crystal may contribute to the difference spectrum of cytochrome *c*. The broad band at around 1650 cm^{-1} is originating from the water molecules on the surface.

Comparison of the ox-red spectra of cytochrome *c* adsorbed on MUA layer and on Au nanoparticle modified MUA layer showed that IR signal was blocked due to the formation of a thick layer of Au nanoparticles on the ATR crystal. From the IR difference spectra the characteristic bands of cytochrome *c* were not observed for the reduced state at 1660 cm^{-1}, 1635 cm^{-1} and for the oxidized state at 1673 cm^{-1}, 1660 cm^{-1} and 1635 cm^{-1} [49].

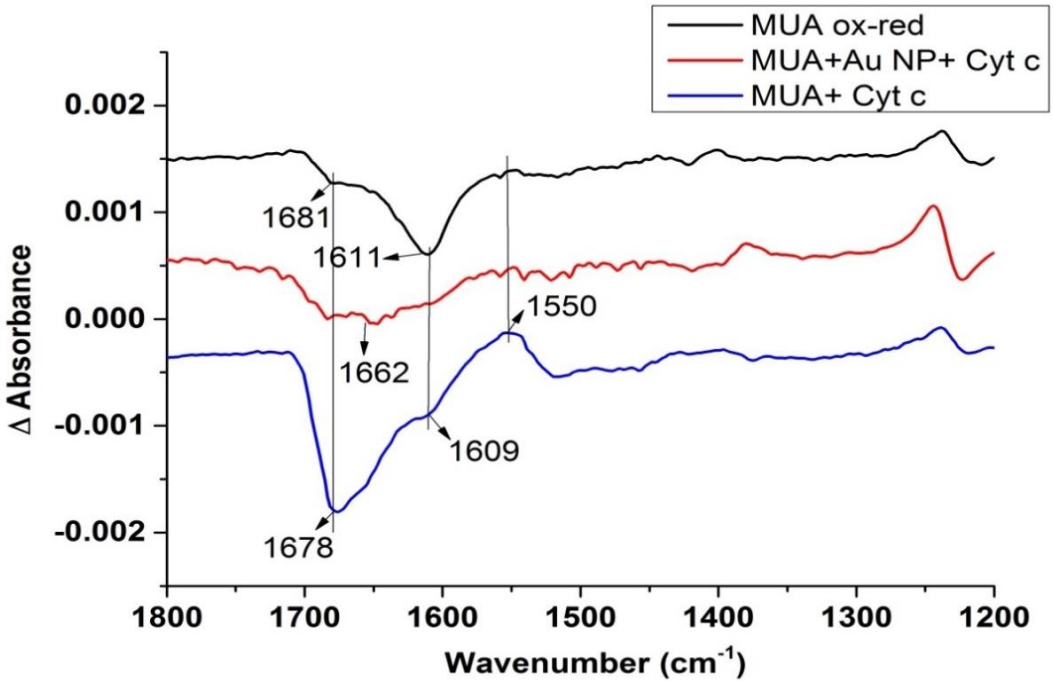

Figure 4.21 Surface-enhanced Infrared differential spectra (ox-red) of cytochrome *c* adsorbed on MUA layer and Au nanoparticle modified MUA layer

b. Immobilization of cytochrome bo_3 oxidase on a gold surface

The cytochrome bo_3 oxidase was immobilized from the His-tag in its structure on a Ni-NTA monolayer. This process was described in detail in section 3.3.2.2 b. Formation of Ni-NTA monolayer was monitored step by step using FTIR spectroscopy. Figure 4.22 shows the formation of DTSP monolayer on the gold coated ATR crystal. After the addition of DTSP solution on the gold surface the bands at 1740 cm^{-1} and 1790 cm^{-1} arise due to the asymmetric and symmetric C=O stretching modes of the succinimidyl ring of TSP respectively [44]. The band at 1431 cm^{-1} arises from the overlapping DTSP and DMSO signals.

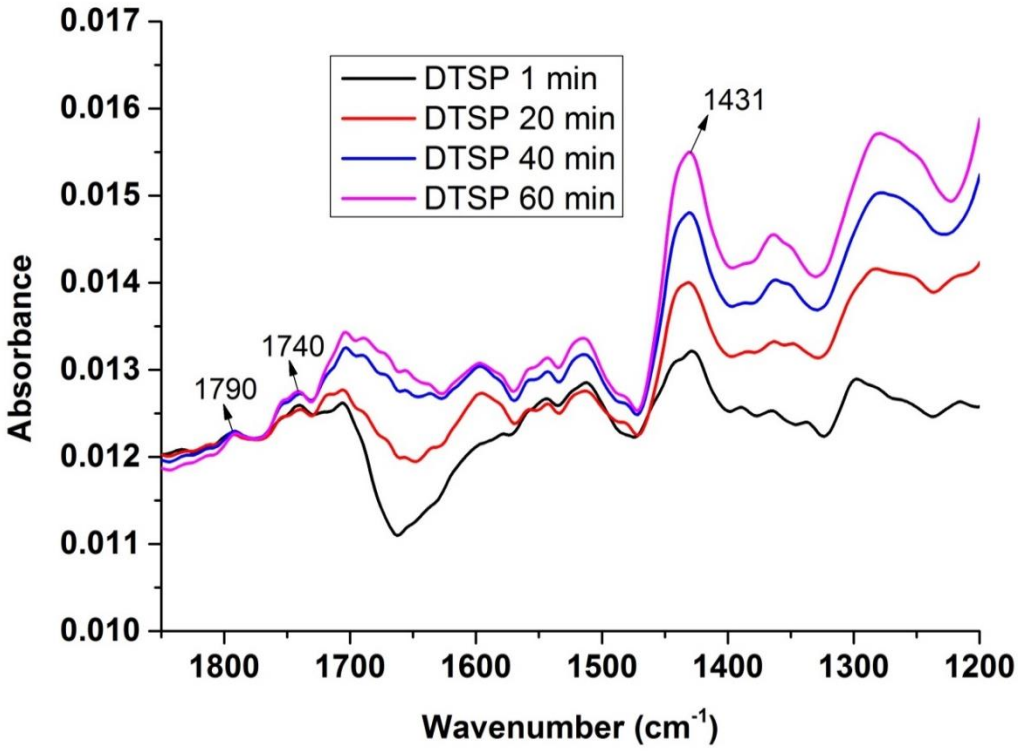

Figure 4.22 SEIRA spectra of the DTSP monolayer formation on the Au surface at different times after the addition of DTSP solution

Figure 4.23 shows the SEIRA spectra of the coupling of TSP to ANTA process. Cross-linking of TSP monolayer with the primary amine of ANTA forms a NTA surface which could ligate a Ni^{2+} ion. The amide bond formation between NTA and TSP was observed from the formation of amide I and II bands at 1650 cm^{-1} and 1565 cm^{-1}[44]. The bands at around 1404 cm^{-1} were assigned to the symmetric COO^- stretching vibrations [44].

After the formation of TSP-NTA layer, a $NiSO_4$ solution was added on the surface of the ATR crystal in order to obtain coordination between Ni^{2+} ions and the carboxyl groups of NTA (Lysine). Nitrogen atoms of the imidazole rings of the His-tag are binding to the Ni^{2+} ions [44]. In figure 4.24 SEIRA spectra obtained after the addition of $NiSO_4$ solution are shown. Ni^{2+} coordination does not provide major changes in the SEIRA spectra. Formation of the band at around 1430 cm^{-1} was attributed to the changes in the symmetric COO^- stretching mode of ANTA [44].

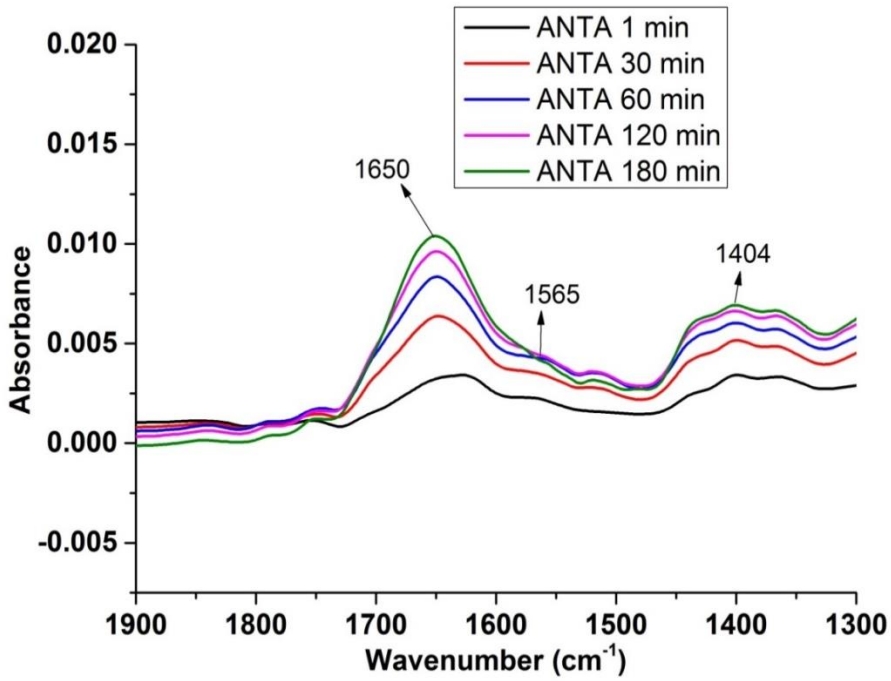

Figure 4.23 SEIRA spectra of the peptide coupling of DTSP with ANTA at different times after the addition of ANTA solution at pH 9.8 (in K_2CO_3)

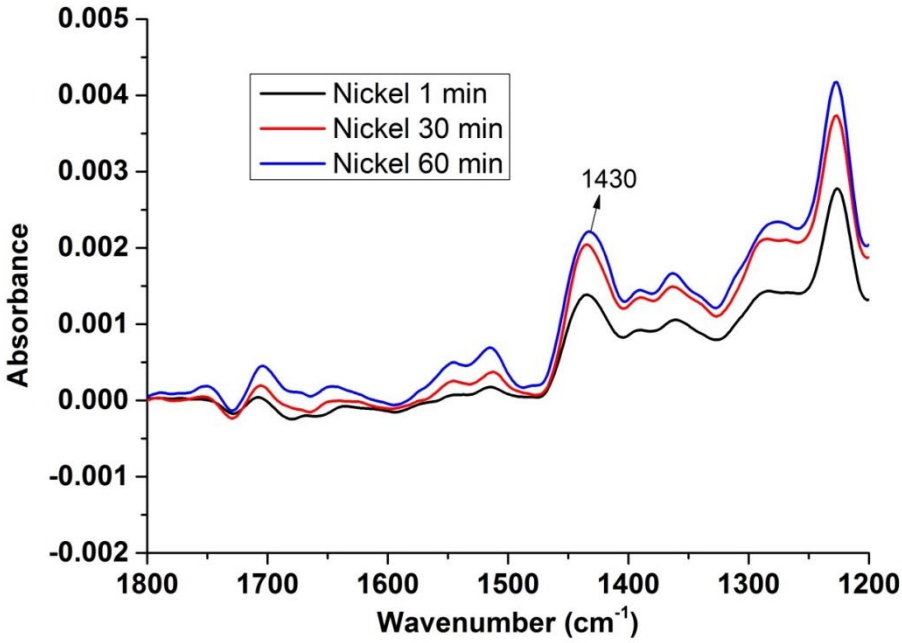

Figure 4.24 SEIRA spectra of the Ni^{2+} coordination of NTA at different times after the addition of $NiSO_4$ solution

Adsorption of cytochrome *bo*$_3$ oxidase and cNOR samples on the TSP-NTA surface was monitored via the formation of amide I and amide II bands. Figure 4.25A shows the SEIRA spectra of adsorbed cytochrome *bo*$_3$ oxidase on the ATR crystal via cross-linking

of NTA-Ni^{2+} to his-tag of the protein. The formation of amide I and amide II bands (1660cm^{-1} and 1540 cm^{-1} respectively) were observed right after the addition of protein solution on the surface [43]. After validating the formation of stable protein layer on the ATR crystal we aimed at checking the electrochemical activity of the adsorbed proteins by cyclic voltammetry. Figure 4.25 B shows the cyclovoltammogram of adsorbed cytochrome *bo₃* oxidase on the TSP-NTA modified gold surface. The CV shows that the adsorbed *bo₃* is interacting with O_2. The reduction peak at -0.3 V is corresponding to the potential values from the conventional CV measurements of *bo₃* oxidase (Figure 4.2).

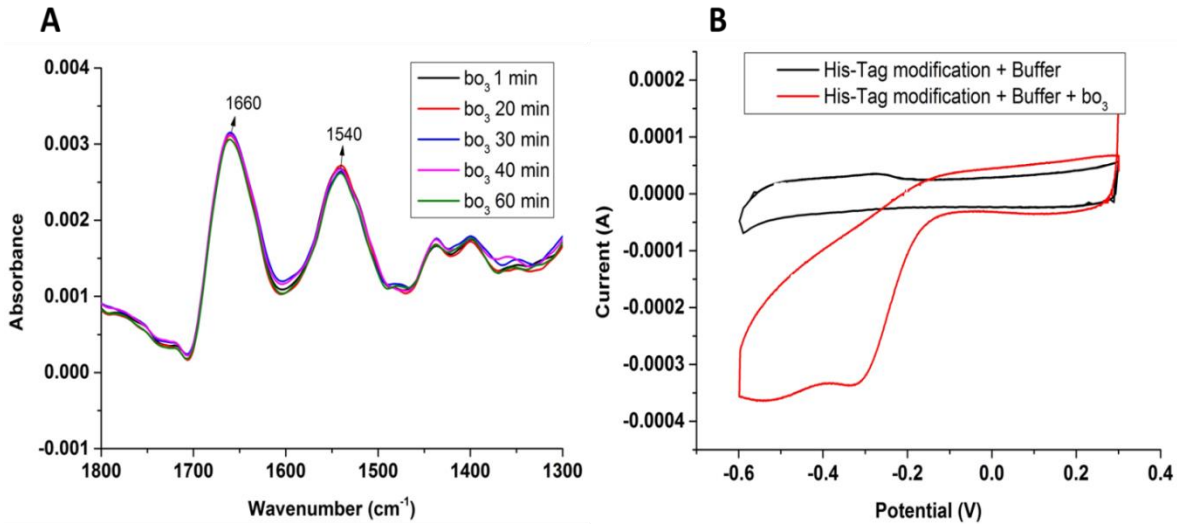

Figure 4.25 A) SEIRA spectra of cytochrome *bo₃* oxidase adsorption via cross-linking NTA-Ni^{2+} to His-tag in the protein structure at different times after the addition of protein solution, B) Cyclic voltammogram of cytochrome *bo₃* oxidase adsorbed on TSP-NTA layer (His-tag modification) at pH 7.

After that the system was connected to a potentiostat and potential-induced IR differential spectra were recorded. In figure 4.26 the comparison of the surface-enhanced infrared differential absorption (SEIDA) spectrum of adsorbed *bo₃* oxidase on the TSP-NTA modified surface, with the redox difference spectrum of *bo₃* oxidase obtained in transmission mode, is shown. Due to the strong absorption of water in mid-infrared range H_2O/D_2O exchange was done. The obtained SEIDA spectrum was featureless and shows no evidence of amide I and amide II signals. This could be explained by the low protein coverage on the surface or a complication in the orientation of the proteins. Cyclic voltammetry measurements showed that adsorbed proteins react with the O_2 however since this technique is more sensitive than FTIR spectroscopy low protein surface-coverage was not a limiting factor. However, in FTIR spectroscopy H_2O has strong

contribution and due to thelow surface coverage of proteins high amount of H_2O molecules interact with the gold surface.

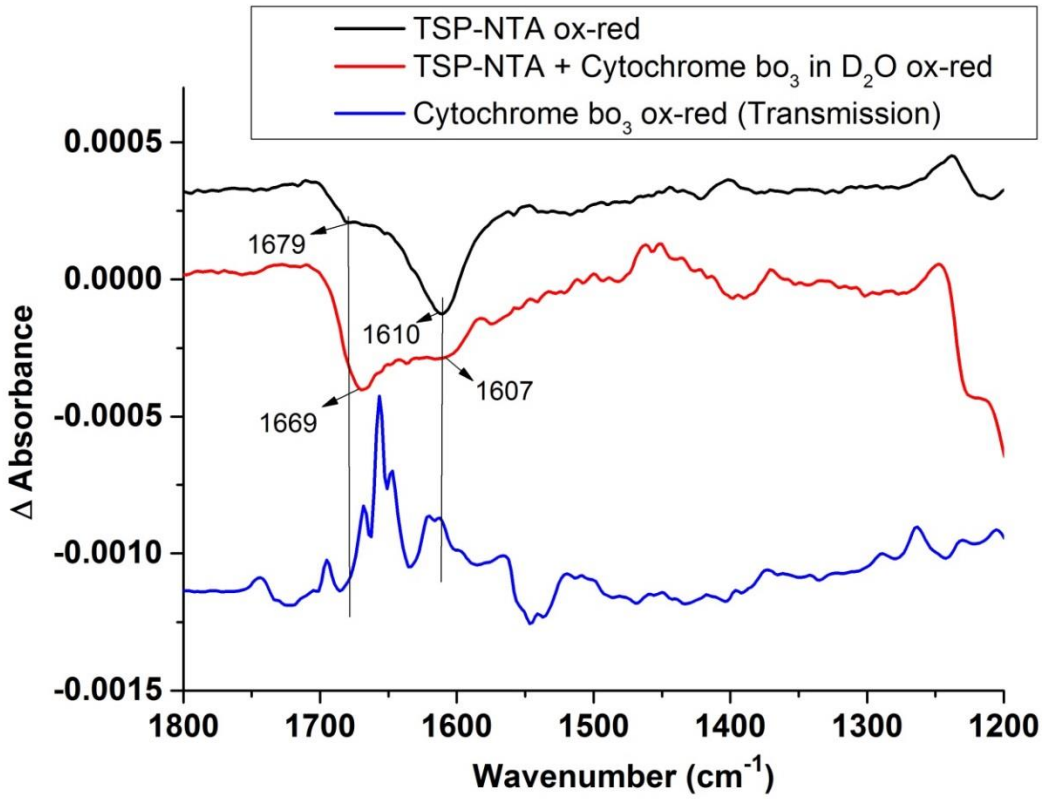

Figure 4.26 Comparison of surface-enhanced infrared differential absorption (SEIDA) spectra of adsorbed cytochrome *bo₃* oxidase on the TSP-NTA modified surface with the redox difference spectrum of cytochrome *bo₃* oxidase obtained in transmission mode.

As a conclusion, the surface modification process was monitored step by step and protein adsorption on the modified ATR crystal was not yet successful and needs further improvement. Further experiments are required to obtain variable SEIDA spectra of adsorbed enzymes. Changing the parameters such as incubation time of protein or thiols, concentration of adsorbed protein and the type of solvent could improve the quality of the differential spectra. SEIRAS technique has a high potential to study membrane proteins reactions in detail when compared to the conventional transmission mode FTIR difference spectroscopy.

References

1. Abramson, J., Riistama, S., Larsson, G., Jasaitis, A., Svensson-Ek, M., Laakkonen, L., Wikström, M. (2000). The structure of the ubiquinol oxidase from Escherichia coli and its ubiquinone binding site. Nature Structural Biology, 7(10), 910–917.
2. Puustinen, a, Verkhovsky, M. I., Morgan, J. E., Belevich, N. P., & Wikstrom, M. (1996). Reaction of the Escherichia coli quinol oxidase cytochrome bo_3 with dioxygen: the role of a bound ubiquinone molecule. Proceedings of the National Academy of Sciences of the United States of America, 93(4), 1545–1548.
3. Welter, R., Gu, L. Q., Yu, L., Yu, C. A., Rumbley, J., & Gennis, R. B. (1994). Identification of the ubiquinol-binding site in the cytochrome bo_3-ubiquinol oxidase of Escherichia coli. Journal of Biological Chemistry, 269(46), 28834–28838.
4. Garcia-Horsman, J. A., Puustinen, A., Gennis, R. B., & Wikstrom, M. (1995). Proton transfer in cytochrome bo_3 ubiquinol oxidase of Escherichia coli: Second-site mutations in subunit I that restore proton pumping in the mutant Asp135-Asn. Biochemistry, 34(13), 4428–4433.
5. Murray, L., Pires, R. H., Hastings, S. F., & Ingledew, W. J. (1999). Models for structure and function in quinone-binding sites: the Escherichia coli quinol oxidase, cytochrome bo_3. Biochemical Society Transactions, 27, 581–585.
6. Salerno, J. C., Bolgiano, B., Poole, R. K., Gennis, R. B., & Ingledew, W. J. (1990). Heme-copper and heme-heme interactions in the cytochrome bo-containing quinol oxidase of Escherichia coli. The Journal of Biological Chemistry, 265(8), 4364–8.
7. Chalovich, J. M., & Eisenberg, E. (2005). The quinone-binding sites of the cytochrome bo_3 ubiquinol oxidase from Escherichia coli. Biophysical Chemistry, 257(5), 2432–2437.
8. Sakamoto, K., Miyoshi, H., Takegami, K., Mogi, T., Anraku, Y., & Iwamura, H. (1996). Probing substrate binding site of the Escherichia coli quinol oxidases using synthetic ubiquinol analogues. Journal of Biological Chemistry, 271(47), 29897–29902.
9. Sakamoto, K., Miyoshi, H., Ohshima, M., Kuwabara, K., Kano, K., Akagi, T., Iwamura, H. (1998). Role of the isoprenyl tail of ubiquinone in reaction with respiratory enzymes: Studies with bovine heart mitochondrial complex I and Escherichia coli bo-type ubiquinol oxidase. Biochemistry, 37(43), 15106–15113.
10. Choi, S. K. (2015). The Interaction of Cytochrome bo_3 from *Escherichia Coli* with its Substrates-Ubiquinone and Oxygen:Proposal for Dissertation Submitted by. University of Illinois at Urbana-Champaign.

11. Yap, L. L., Lin, M. T., Ouyang, H., Samoilova, R. I., Dikanov, S. A., & Gennis, R. B. (2010). The quinone-binding sites of the cytochrome bo3 ubiquinol oxidase from Escherichia coli. Biochimica et Biophysica Acta - Bioenergetics, 1797(12), 1924–1932.
12. Hellwig, P., Barquera, B., & Gennis, R. B. (2001). Direct evidence for the protonation of aspartate-75, proposed to be at a quinol binding site, upon reduction of cytochrome bo3 from Escherichia coli. Biochemistry, 40(4), 1077–1082.
13. Hellwig, P., Yano, T., Ohnishi, T., & Gennis, R. B. (2002). Identification of the residues involved in stabilization of the semiquinone radical in the high-affinity ubiquinone binding site in cytochrome bo3 from Escherichia coli by site-directed mutagenesis and EPR spectroscopy. Biochemistry, 41(34), 10675–10679.
14. Lai, L. Y., Samoilova, R. I., Gennis, R. B., & Dikanov, S. A. (2007). Characterization of mutants that change the hydrogen bonding of the semiquinone radical at the QH site of the cytochrome bo3 from Escherichia coli. Journal of Biological Chemistry, 282(12), 8777–8785.
15. Lin, M. T., Baldansuren, A., Hart, R., Samoilova, R. I., Narasimhulu, K. V., Yap, L. L., Dikanov, S. A. (2012). Interactions of intermediate semiquinone with surrounding protein residues at the QH site of wild-type and D75H mutant cytochrome bo 3 from Escherichia coli. Biochemistry, 51(18), 3827–3838.
16. Lai, L. Y., Samoilova, R. I., Gennis, R. B., & Dikanov, S. A. (2006). Characterization of the exchangeable protons in the immediate vicinity of the semiquinone radical at the QH site of the cytochrome bo 3 from Escherichia coli. Journal of Biological Chemistry, 281(25), 16879–16887.
17. Lin, M. T., Shubin, A. A., Samoilova, R. I., Narasimhulu, K. V., Baldansuren, A., Gennis, R. B., & Dikanov, S. A. (2011). Exploring by pulsed EPR the electronic structure of ubisemiquinone bound at the QH site of cytochrome bo3 from Escherichia coli with in vivo 13C-labeled methyl and methoxy substituents. Journal of Biological Chemistry, 286(12), 10105–10114.
18. Bossis, F., De Grassi, A., Palese, L. L., & Pierri, C. L. (2014). Prediction of high- and low-affinity quinol-analogue-binding sites in the aa3 and bo3 terminal oxidases from Bacillus subtilis and Escherichia coli1. The Biochemical Journal, 461(2), 305–14.
19. J. Wang, (2006) Analytical Electrochemistry, 3rd ed., New York: John Wiley & Sons.
20. Léger, C. (2013). An Introduction to Electrochemical Methods for the Functional Analysis of Metalloproteins. Practical Approaches to Biological Inorganic Chemistry, 179–216.

21. Léger, C., Elliott, S. J., Hoke, K. R., Jeuken, L. J. C., Jones, A. K., & Armstrong, F. A. (2003). Enzyme electrokinetics: Using protein film voltammetry to investigate redox enzymes and their mechanisms. Biochemistry.
22. Melin, F., & Hellwig, P. (2013). Recent advances in the electrochemistry and spectroelectrochemistry of membrane proteins. Biological Chemistry, 394(5), 593–609.
23. Arrondo, J. L., & Goñi, F. M. (1999). Structure and dynamics of membrane proteins as studied by infrared spectroscopy. Progress in Biophysics and Molecular Biology, 72 VN-r(4), 367–405.
24. Surewicz, W. K., Mantsch, H. H., & Chapman, D. (1993). Determination of protein secondary structure by Fourier transform infrared spectroscopy: A critical assessment. Biochemistry, 32(2), 389–394.
25. Hellwig, P., Behr, J., Ostermeier, C., Richter, O. M. H., Pfitzner, U., Odenwald, A., Mäntele, W. (1998). Involvement of glutamic acid 278 in the redox reaction of the cytochrome c oxidase from Paracoccus denitrificans investigated by FTIR spectroscopy. Biochemistry, 37(20), 7390–7399.
26. Barth, A. (2007). Infrared spectroscopy of proteins. Biochimica et Biophysica Acta-Bioenergetics.
27. Behr, J., Michel, H., Mäntele, W., & Hellwig, P. (2000). Functional properties of the heme propionates in cytochrome c oxidase from Paracoccus denitrificans. Evidence from FTIR difference spectroscopy and site-directed mutagenesis. Biochemistry, 39(6), 1356–1363.
28. Hellwig, P., Mogi, T., Tomson, F. L., Gennis, R. B., Iwata, J., Miyoshi, H., & Mäntele, W. (1999). Vibrational modes of ubiquinone in cytochrome bo3 from Escherichia coli identified by Fourier transform infrared difference spectroscopy and specific 13C labeling. Biochemistry, 38(44), 14683–14689.
29. Wolpert, M., & Hellwig, P. (2006). Infrared spectra and molar absorption coefficients of the 20 alpha amino acids in aqueous solutions in the spectral range from 1800 to 500 cm-1. Spectrochimica Acta - Part A: Molecular and Biomolecular Spectroscopy, 64(4), 987–1001.
30. Bolgiano, B., Salmon, I., Ingledew, W. J., & Poole, R. K. (1991). Redox analysis of the cytochrome o -type quinol oxidase complex of Escherichia coli reveals three redox components. Biochemical Journal, 274(3), 723–730.

31. Salerno, J. C., Bolgiano, B., & Ingledew, W. J. (1989). Potentiometric titration of cytochrome-bo type quinol oxidase of Escherichia coli: Evidence for heme-heme and copper-heme interaction. FEBS Letters, 247(1), 101–105.
32. Urban, P. F., & Klingenberg, M. (1969). On the Redox Potentials of Ubiquinone and Cytochrome b in the Respiratory Chain. European Journal of Biochemistry, 9(4), 519–525.
33. Meyer, T. (2015). Caractérisation électrochimique et spectroscopique de proteins membranaires immobilisees sur des nanomteriaux: Proposal for Dissertation Submitted by. University Strasbourg.
34. Ataka, K., & Heberle, J. (2006). Use of surface enhanced infrared absorption spectroscopy (SEIRA) to probe the functionality of a protein monolayer. Biopolymers, 82(4), 415–419.
35. Ataka, K., & Heberle, J. (2007). Biochemical applications of surface-enhanced infrared absorption spectroscopy. Analytical and Bioanalytical Chemistry, 388(1), 47–54.
36. Ataka, K., Stripp, S. T., & Heberle, J. (2013). Surface-enhanced infrared absorption spectroscopy (SEIRAS) to probe monolayers of membrane proteins. Biochimica et Biophysica Acta - Biomembranes.
37. Glassford, S. E., Byrne, B., & Kazarian, S. G. (2013). Recent applications of ATR FTIR spectroscopy and imaging to proteins. Biochimica et Biophysica Acta - Proteins and Proteomics, 1834(12), 2849–2858.
38. Ataka, K., & Heberle, J. (2003). Electrochemically induced surface-enhanced infrared difference absorption (SEIDA) spectroscopy of a protein monolayer. Journal of the American Chemical Society, 125, 4986–4987.
39. H., D., Hildebrandt, P., & Todorovic, S. (2010). Immobilized Redox Proteins: Mimicking Basic Features of Physiological Membranes and Interfaces. In Biomimetics Learning from Nature. InTech.
40. Ataka, K., Giess, F., Knoll, W., Naumann, R., Haber-Pohlmeier, S., Richter, B., & Heberle, J. (2004). Oriented attachment and membrane reconstitution of his-tagged cytochrome c oxidase to a gold electrode: In situ monitoring by surface-enhanced infrared absorption spectroscopy. Journal of the American Chemical Society, 126(49), 16199–16206.
41. Todorovic, S., Verissimo, A., Wisitruangsakul, N., Zebger, I., Hildebrandt, P., Pereira, M. M., Murgida, D. H. (2008). SERR-spectroelectrochemical study of a cbb3 oxygen reductase in a biomimetic construct. The Journal of Physical Chemistry. B, 112(51), 16952–9.

42. Nowak, C., Schach, D., Gebert, J., Grosserueschkamp, M., Gennis, R. B., Ferguson-Miller, S., Naumann, R. L. C. (2011). Oriented immobilization and electron transfer to the cytochrome c oxidase. Journal of Solid State Electrochemistry, 15(1), 105–114.
43. Wiebalck, S., Kozuch, J., Forbrig, E., Tzschucke, C. C., Jeuken, L. J. C., & Hildebrandt, P. (2016). Monitoring the Transmembrane Proton Gradient Generated by Cytochrome bo3 in Tethered Bilayer Lipid Membranes Using SEIRA Spectroscopy. Journal of Physical Chemistry B, 120(9), 2249–2256.
44. Kriegel, S., Uchida, T., Osawa, M., Friedrich, T., & Hellwig, P. (2014). Biomimetic environment to study E. coli complex i through surface-enhanced IR absorption spectroscopy. Biochemistry, 53(40), 6340–6347.
45. Zhao, G.-C., Xu, M.-Q., Ma, J., & Wei, X.-W. (2007). Direct electrochemistry of hemoglobin on a room temperature ionic liquid modified electrode and its electrocatalytic activity for the reduction of oxygen. Electrochemistry Communications, 9(5), 920–924.
46. Chen, H., Wang, Y., Dong, S., & Wang, E. (2005). Direct electrochemistry of cytochrome c at gold electrode modified with fumed silica. Electroanalysis, 17(20).
47. Wright, W. W., Laberge, M., & Vanderkooi, J. M. (1997). Surface of cytochrome c: Infrared spectroscopy of carboxyl groups. Biochemistry, 36(48), 14724–14732.
48. Jiang, X., Ataka, K., & Heberle, J. (2008). Influence of the molecular structure of carboxyl-terminated self-assembled monolayer on the electron transfer of cytochrome c adsorbed on an Au electrode: In situ observation by surface-enhanced infrared absorption spectroscopy. Journal of Physical Chemistry C, 112(3), 813–819.
49. Melin, F., Meyer, T., Lankiang, S., Choi, S. K., Gennis, R. B., Blanck, C., Hellwig, P. (2013). Direct electrochemistry of cytochrome bo3 oxidase at a series of gold nanoparticles-modified electrodes. Electrochemistry Communications, 26(1), 105–108.
50. Meyer, T., Melin, F., Richter, O. M. H., Ludwig, B., Kannt, A., Müller, H., Hellwig, P. (2015). Electrochemistry suggests proton access from the exit site to the binuclear center in Paracoccus denitrificans cytochrome c oxidase pathway variants. FEBS Letters, 589(5), 565–568.

4.2 Investigation of cytochrome c dependent nitric oxide reductase (cNOR) from *P. denitrificans*

4.2.1 Electrochemical and structural investigation of wild type cNOR

In this part of the thesis cytochrome *c* dependent nitric oxide reductase (cNOR) from *P. denitrificans* (Figure 4.27) was studied. Wild type cNOR was characterized by using cyclic voltammetry, FTIR difference spectroscopy and potentiometric titrations.

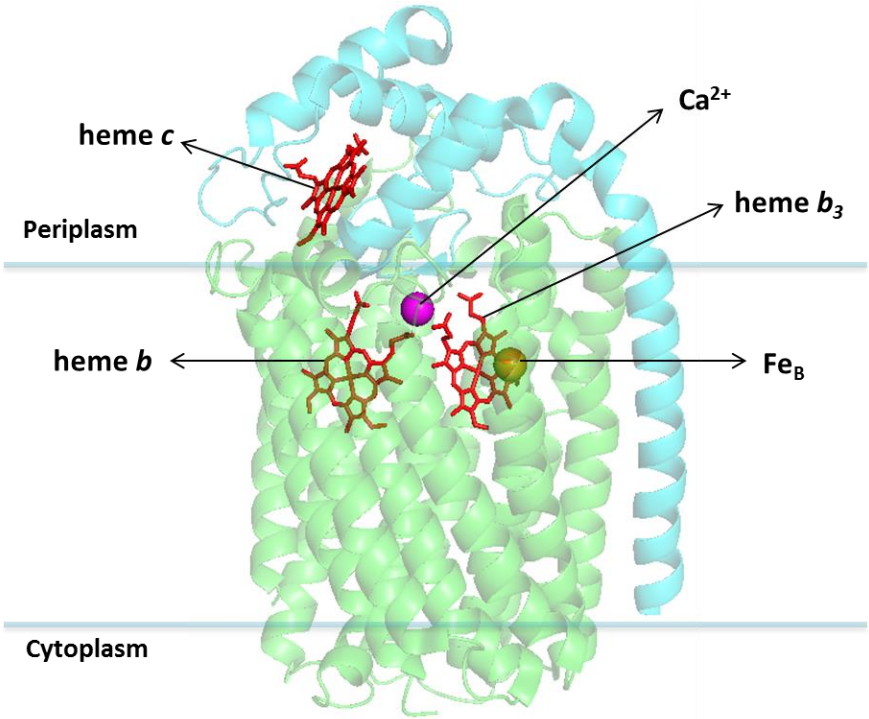

Figure 4.27 Structure of cNOR from *P. aeruginosa*. (3WFB.pdb)

Voltammetric studies:

In figure 4.28 the cyclic voltammograms of cNOR in O_2 and NO containing buffer with a scan rate of 0.02 $V.s^{-1}$ at pH7 are compared. In the presence of O_2 a weak oxidation signal at + 0.1 V and a reduction peak at -0.3 V was observed. It was reported that if not enough NO gas is present in the environment, cNOR can also catalyze O_2 reduction due to its similar binuclear center to other heme-copper oxidase proteins [1, 2]. NO gas was produced by the reaction of copper with nitric acid. Addition of NO gas into the O_2-free buffer resulted in a slightly more intense reduction signal at -0.38 V. This low-potential signal was previously assigned to binuclear center reduction in literature [3].

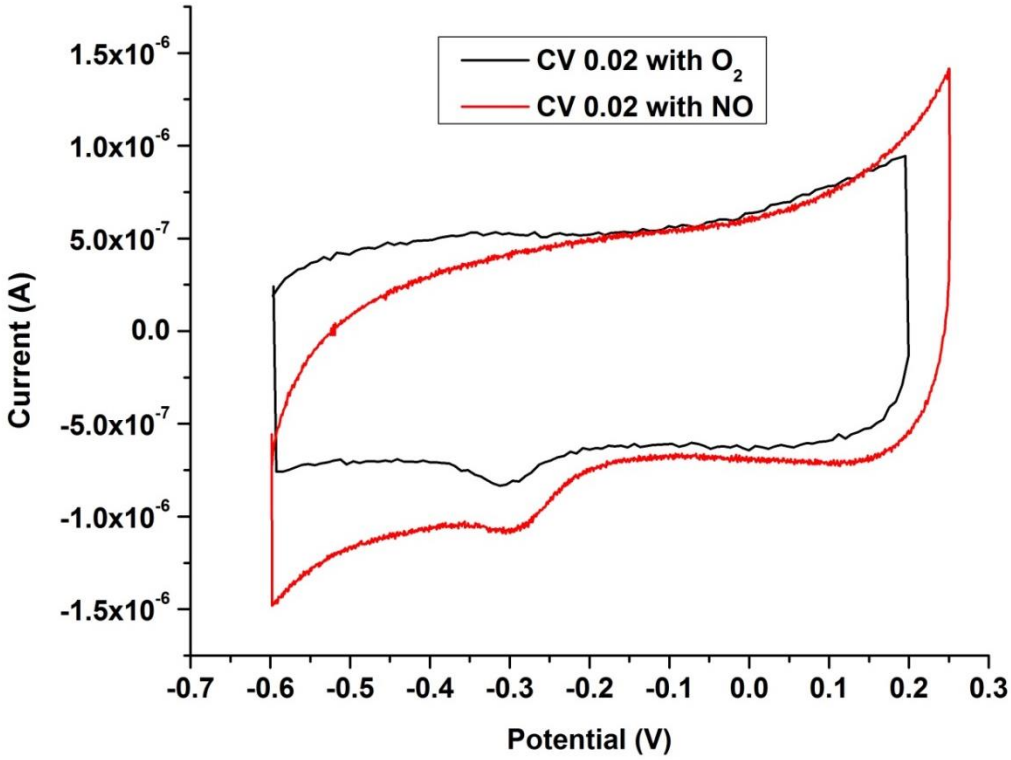

Figure 4.28 Cyclic voltammograms of cNOR in absence of NO (In solution with O_2) and with NO at pH 7.5.

It is noted that the NO obtained by the reaction of copper with nitric acid, was not very pure. Thus, we switched to the following reaction:

$$2KNO_2 + 2KI + 2H_2SO_4 \rightarrow 2NO + I_2 + 2H_2O + 2K_2SO_4$$

The KNO_2 is the limiting reactive so by the initial quantity of KNO_2 it is possible to control the concentration of produced NO. With this procedure NO was generated inside a solution with iodine and the solution with NO was added into our buffer before performing the cyclic voltammetry experiment. However, excess amount of I_2 which is produced together with NO gas, was causing baseline problems. Thus, excess amount of NO gas was isolated and introduced to the buffer solution to avoid contamination by I_2. As shown in figure 4.29 by inserting collected NO gas into the buffer a stronger reduction signal was obtained.

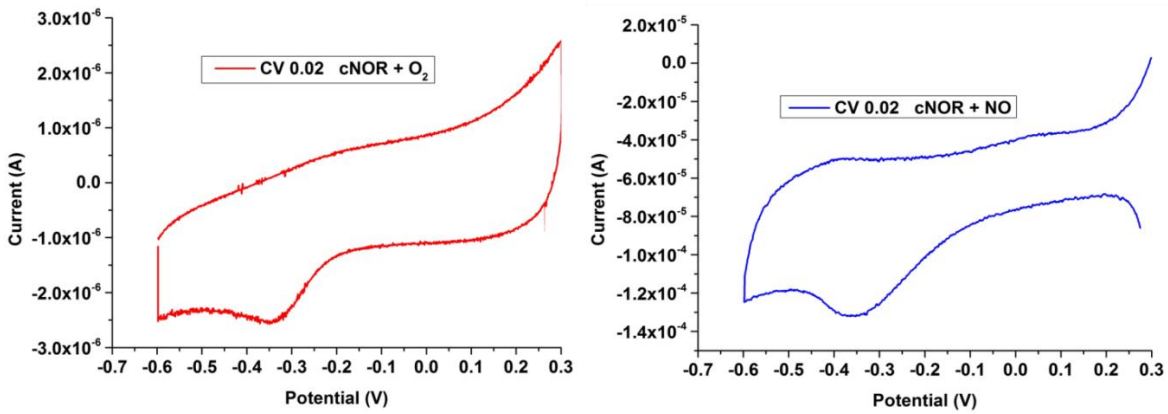

Figure 4.29 Cyclic voltammogram of cNOR Left: without NO gas (In solution with O_2), Right: Presence of NO in solution at pH 7.5.

In summary, the electrochemical characterization of cNOR was done by cyclic voltammetry. The reduction peak of binuclear center was obtained in the presence of NO and O_2. However, a catalytic curve for the reduction of NO or O_2 was not observed. It can be concluded that the cyclic voltammetry experiments needs to be optimized in order to observe catalytic activity.

Wild-type cNOR was further investigated by potentiometric titrations in order to measure the redox potentials of each heme.

Potentiometric titrations:

During the potentiometric titrations the Soret band (428 nm) and the alpha band (551 nm with a shoulder at 558 nm) were monitored. In the Soret band contribution of all hemes can be observed together and in the alpha band the contribution of hemes can be observed separately. We worked with two different batches of wt cNOR. In this section the results with the first batch is shown and other results are summarized in table 4.5. From the 2nd batch of cNOR we did not observe the contribution of heme b_3 which indicates a problem in the integrity of the 2nd batch of samples. This may be related to the purification process of the protein. The preliminary results obtained with the 2nd batch of samples should be repeated in order to make a clear conclusion. Gaussian fittings of the first derivative of the absorbance values obtained from the titration of the 2nd batch of wt cNOR are shown in appendix figures 16 and 17.

In figure 4.30 the Gaussian fitting of the first derivative of the absorbance values obtained from the titration of the Soret band of wt cNOR at pH 7.5 is shown. A large contribution

centered at +100 mV which arises from hemes *c* and *b* was obtained together with a contribution at -271 mV. In order to obtain mid-point potentials of hemes *c* and *b* the peak was de-convoluted into two peaks with mid-point potentials of +84 mV (heme *c*, +292 mV vs SHE) and +135 mV (heme *b*. + 343 mV vs SHE). The negative contribution with a mid-point potential of -271 mV was attributed to the heme b_3 (- 63mV vs SHE).

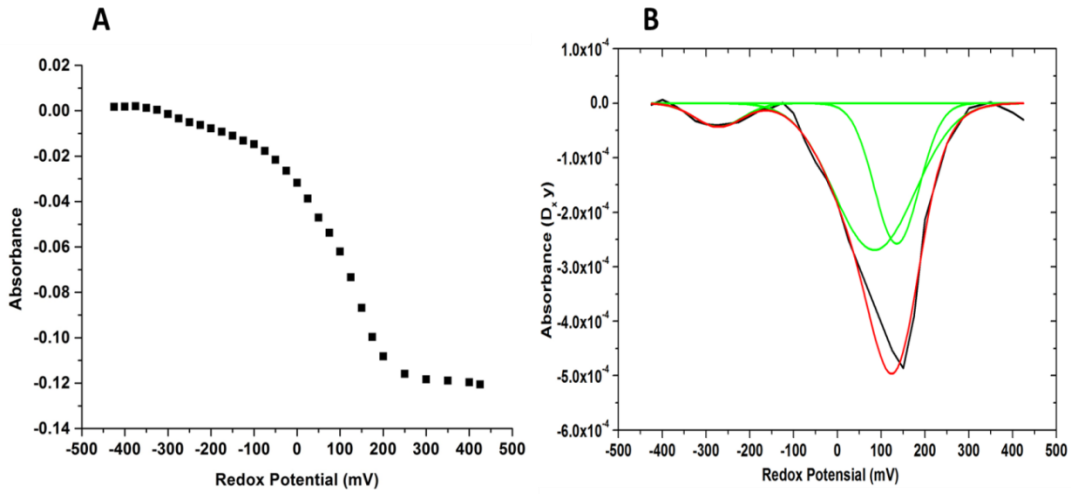

Figure 4.30 Potentiometric titration of wild type cNOR at pH 7.5, A) Absorbance values from Soret band, B) Gaussian fitting of the first derivative of the absorbance values from Soret band

In figure 4.31 the Gaussian fitting of the first derivative of the absorbance values obtained from the titration of the alpha band of wt cNOR pH 7.5 is shown. The mid-point potential of heme *c* was measured at +97 mV (+305 mV vs SHE) from the 551 nm band together with a weak signal of heme b_3 at -241 mV (-33 mV vs SHE). Heme b_3 contribution was stronger in the 558 nm band and the mid-point potential was measured at – 253 mV (-45 mV vs SHE). From the 558 nm band the mid-point potential of heme *b* and *c* were determined at +163 mV (+371 mV vs SHE) and +65 mV (+273 mV vs SHE) respectively. These values were similar to the values obtained with cNOR from *P. denitrificans* by the Butland`s group (for heme *c* + 310 mV, for heme *b* + 345mV and for heme b_3 +32 mV vs SHE) [4]. Added to that, the heme b_3 contribution is usually obtained from the charge transfer band (CTS band) [4, 5]. In our case the redox potential of heme b_3 were determined from the alpha band and Soret bands since it is unfeasible to study CTS band. The thin-layer electrochemical cell that we use in our experiments has a path-length of a few μm. Due to that reason it is not possible to observe CTS band with our setup.

A remarkable feature that was observed from the potentiometric titrations was the extremely negative mid-point potential of heme b_3 (-271 mV wt cNOR). This low redox

potential of heme b_3 hinders the delivery of electrons from heme *b* to the binuclear center. The reason behind the extremely negative mid-point potential heme b_3 is still under discussion. Recently it was suggested by Prof. Shiro`s group that the conserved glutamic acid residues in the structure of cNOR such as Glu-215, Glu-280, Glu 211 (*P. aeruginosa* numbering) could generate a large electro-negative environment at the catalytic center which could be the main reason of the low redox potential of heme b_3 [6, 30]. This extremely low potential of heme b_3 was also observed in cbb_3 oxidases [7] and it was explained by the presence of a highly conserved glutamic acid residue which is hydrogen-bonded to the histidine proximal ligand of the heme b_3. This similarities in the redox properties of heme b_3 indicate that NOR and other heme-copper oxidases could have evolved from a common ancestor [32].

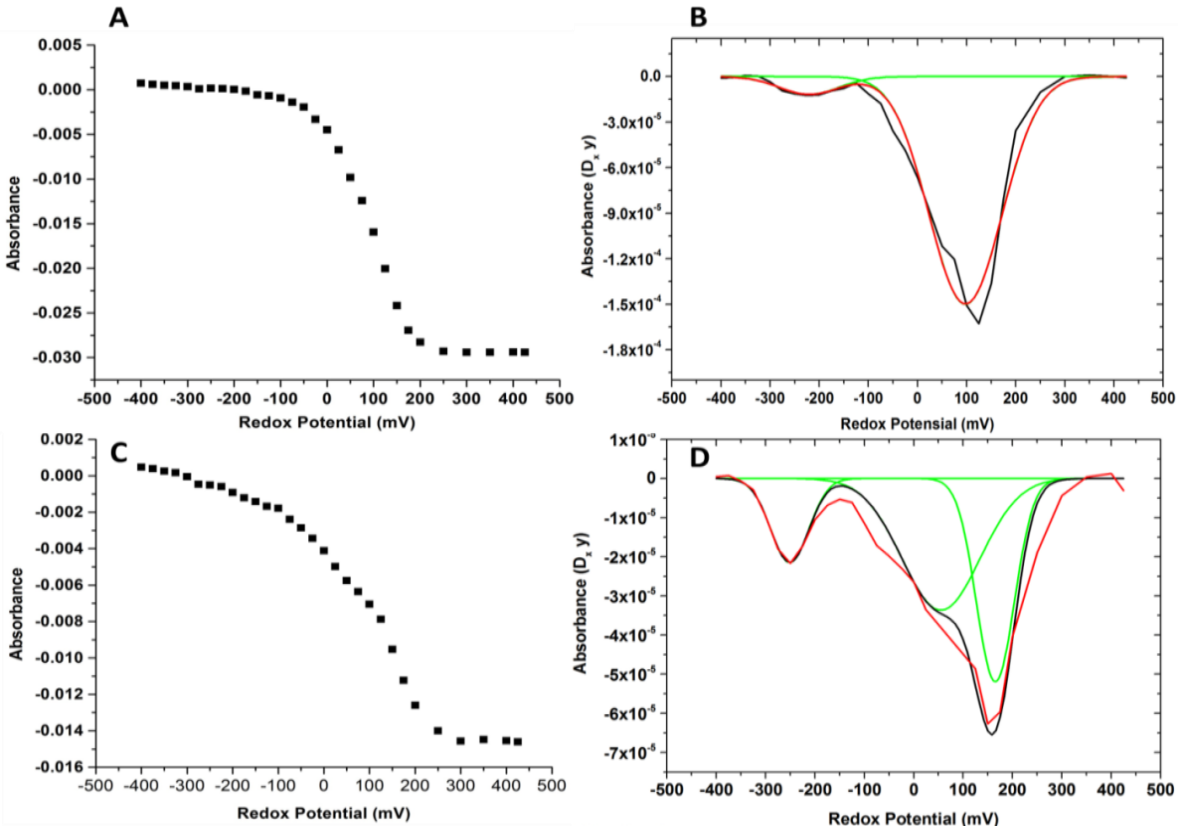

Figure 4.31 Potentiometric titration of wild type cNOR (1st batch) at pH 7.5, A) Absorbance values from alpha band at 551 nm, B) Gaussian fitting of the first derivative of the absorbance values from alpha band at 551 nm, C) Absorbance values from alpha band at 558 nm, D) Gaussian fitting of the first derivative of the absorbance values from alpha band at 558 nm

In table 4.4 the summary of the mid-point potentials obtained from the potentiometric titration of wild type cNOR (1st batch) at pH 7.5 is shown and they were compared with the literature values.

Table 4.4 Summary of redox potentials obtained from the potentiometric titration of wild type cNOR (1st batch) at pH 7.5.

mV	vs Ag/AgCl (pH 7.5)		vs SHE (pH 7.5)		Butland group [4] vs SHE (pH 7.5)	Zumft group [5] vs SHE (pH 7.5)
	550 nm	560 nm	550 nm	560 nm		
Heme *b*	-	+163	-	+ 371	+ 345	+ 322
Heme *c*	+ 97	+ 65	+ 305	+ 273	+ 310	+ 280
Heme b_3	- 241	- 253	- 33	- 45	+ 32	-

Table 2.5 Summary of redox potentials obtained from the potentiometric titration of different batches of wt cNOR at pH 7.5.

mV	1st Batch of wt cNOR pH 7.5 vs Ag/AgCl			2nd Batch of wt cNOR pH 7.5 vs Ag/AgCl		
	Soret 420 nm	550 nm	560 nm	Soret 420 nm	550 nm	560 nm
Heme *b*	+ 135	-	+ 163	+ 160	-	+ 178
Heme *c*	+ 84	+ 97	+ 65	+ 90	+ 97	+ 101
Heme b_3	- 271	- 241	- 253	-	-	-

FTIR difference spectroscopy:

Structural characterization of wt cNOR was made by FTIR difference spectroscopy. The tentative assignments are made based on the ox-red spectrum. In figure 4.32 the ox-red FTIR spectrum of wt cNOR at pH 7.5 is shown. The C=O vibration of protonated/deprotonated glutamic acid residues at 1745 cm^{-1} (positive) and 1724 cm^{-1}(negative) [8, 9. The bands at 1677, 1663, 1648 and 1638cm^{-1} arise from the C=O vibration of the polypeptide chain (Amide I region) [10]. The C=O vibration of Asn and Gln can also contribute at 1677 and 1663 cm^{-1}[11]. The anti-symmetric ($CN_3H_5^+$)

vibration of Arg also has contributions at 1677 cm^{-1} together with 1690 cm^{-1} and symmetric ($CN_3H_5^+$) vibration at 1663 and 1627 cm^{-1}[11]. The positive band at 1670 cm^{-1} arises from the C=O vibration of heme propionates [12]. At 1595 cm^{-1} the CC vibration of Tyr together with NH_2 vibration of Gln can be seen [11]. The anti-symmetric bending of heme propionates (COO^-) can be seen from the positive band at 1578 $cm^{-1}$and the negative band at 1535 cm^{-1}[12]. The amide II band at 1552 cm^{-1} arises from CN stretching vibration of the backbone structure of the protein [10]. It is not easy to make individual assignments for the amino acid side chains between 1500-1400 cm^{-1} where several vibrations of Phe, Trp, Pro and the COO^- vibration of heme propionates contribute [10-13]. The bands at 1245 cm^{-1} and 1239 cm^{-1} together with the contribution at 1519 $cm^{-1}$are originating from the vibrational modes of Tyr residues [11]. The tentative assignments for the ox-red spectrum of wild-type cNOR are summarized in table 4.6.

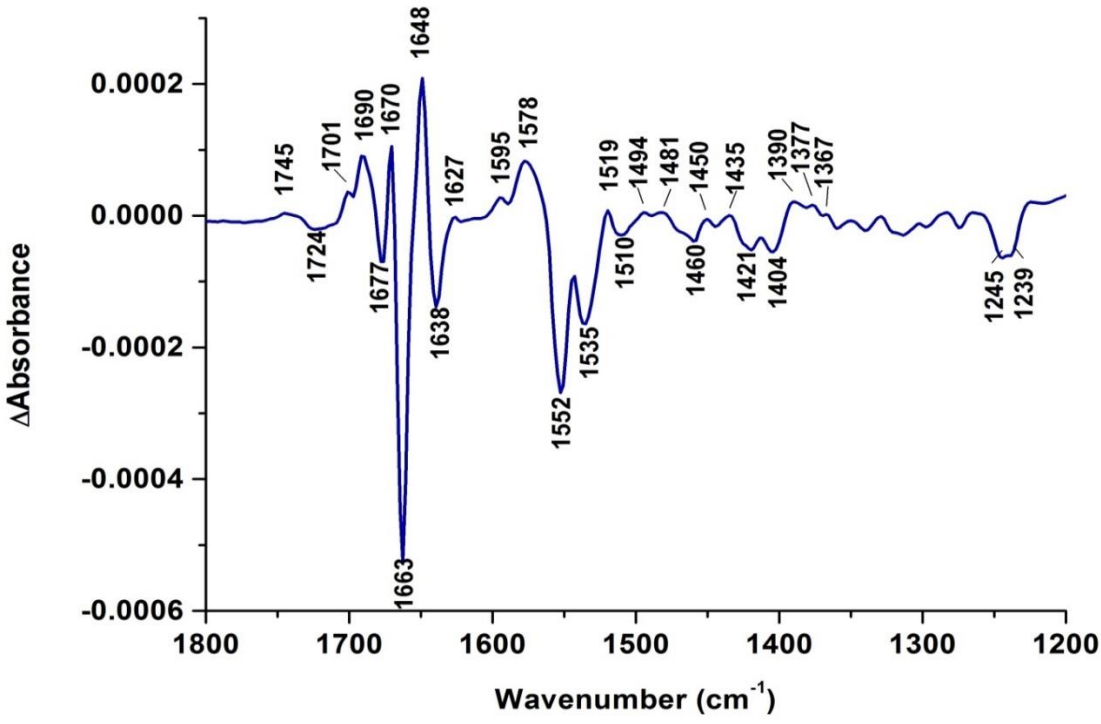

Figure 4.32 FTIR difference spectrum of wild type cNOR at pH 7.5 (ox-red).

Table 4.6 Tentative assignments of the electrochemical difference spectrum for wild type cNOR [8-11]

Band position in H_2O (cm^{-1})	Assignment
1745 (+)	Glu ν COOH
1724 (-)	Glu ν COOH
1701 (+)	Asn ν(C=O)
1690 (+)	Arg $\nu_{as}(CN_3H_5^+)$ – no salt bridge Gln ν(C=O)
1677 (-)	Amide I ν(C=O) Arg $\nu_{as}(CN_3H_5^+)$ Gln ν(C=O)
1670 (+)	ν (CO) COOH
1663 (-)	Amide I (C=O) Arg $\nu_{as}(CN_3H_5^+)$ Gln ν(C=O) Arg $\nu_s(CN_3H_5^+)$
1648 (+)	Amide I ν(C=O) Arg $\nu_s(CN_3H_5^+)$
1638 (-)	Amide I ν(C=O) Arg $\nu_s(CN_3H_5^+)$ – no salt bridge
1627 (+)	Amide I ν(C=O) Arg $\nu_s(CN_3H_5^+)$ – no salt bridge Lys $\delta_{as}(NH_3^+)$
1595 (+)	Tyr-OH ν(CC)
1578 (+)	$\delta_{as}COO^-$ heme propionate Asp $\nu_{as}(COO^-)$
1552 (-)	Amide II
1535 (-)	$\delta_{as}COO^-$ heme propionate
1519 (+)	Tyr-O^- ν(CC), δ(CH)
1494 (+)	Phe ν(CC ring)

1460 (-)	Trp δ(CH) ν(CC) ν(CN) Pro ν(CN)
1435 (+)	Trp δ(NH) ν(CC) δ(CH)
1421 (-)	Trp δ(NH) ν(CC) δ(CH)
1404 (-)	Glu $\nu_s(COO^-)$
1390 (+)	δs COO^- heme propionate
1245 (-)	Trp δ(CH) ν(CC) Asp/Glu ν(CO) Tyr-OH ν(CO) ν(CC)
1239 (-)	Tyr-OH ν(CO) ν(CC)

In summary, the structural characterization of cNOR was done by FTIR difference spectroscopy. The FTIR experiments showed signals that could be attributed to specific residues or secondary structure of the protein. The redox potentials of hemes were determined by the potentiometric titrations. Combined results of these two techniques with wild-type cNOR will be further used as a reference in this chapter.

4.2.2 Investigation of the effect of different environments on the stability and the function of wild type cNOR

In this section wild type cNOR samples in liposomes and detergent at different pH values were compared. One of the biggest challenges of membrane protein studies is the stability and function after isolation from the membrane [14-16]. It is crucial to provide a hydrophobic environment to keep the proteins in contact and at the same time to be in touch with an aqueous medium. There are several studies on the interaction of membrane proteins with different detergents [17-19], lipid bilayers [18-20] and liposomes [18-21]. We believe that liposomes can provide more natural environment to the enzyme then detergents, thus, resulting in a more stable and efficient system.

The structural stability of wild type cNOR was investigated (2^{nd} batch) at different pH values (6.5, 7.5 and 8.5) with DDM and inside liposomes (pH 7.5) by using FTIR difference spectroscopy. In figure 4.33 the comparison of FTIR difference spectra of wt cNOR at different pH values (pH 7.8 and 8.5) with DDM and in liposomes (pH 7.5) is shown. FTIR difference spectra of wt cNOR with DDM and in liposomes were compared at pH 7.5 since the system was stable and provided reproducible results at this pH value.

Samples were not stable at pH 6.5 so the data for this pH value is not shown here. Detailed assignments of the electrochemical difference spectrum for wild type cNOR at pH 7.5 were made in section 4.2.1. Main differences between the FTIR difference spectra at different pH values might be related to the protonation/de-protonation of heme propionates and acidic amino acids in the sample. The signals corresponding to the de-protonated residues overlap between 1600-1400 cm^{-1} and cannot be truly interpreted without site directed mutations or labeling. The band at 1610 cm^{-1} switched from negative to positive when the pH was increased and a possible explanation is that the changes in the environment of Gln/Asn amino acids (H bonding or de-protonation of surrounding amino acids) might have an effect on the vibration of these amino acids. The signal at 1241 cm^{-1} is attributed to the C-O and C-C stretching vibrations of de-protonated Tyrosine which has higher intensity at pH 8.5. At 1574 $cm^{-1}$and 1535 cm^{-1} we observed the anti-symmetric stretching of several amino acid residues and heme propionates and at 1390 cm^{-1} we can observe the COO^- symmetric stretching.

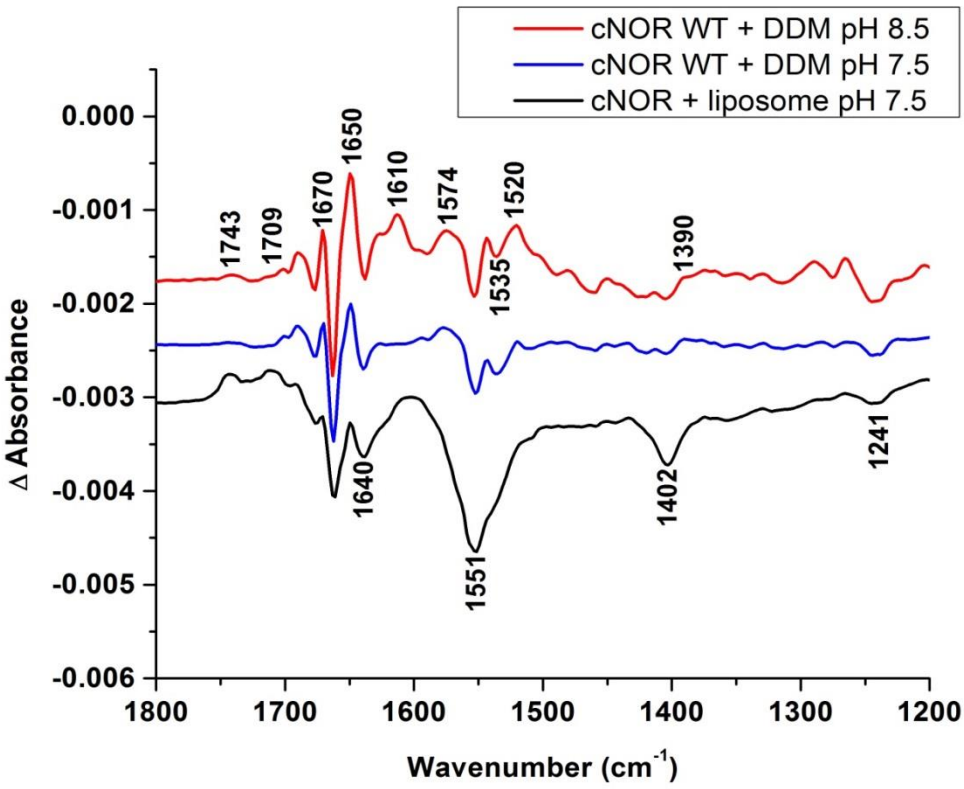

Figure 4.33 Ox-red spectra of wild type cNOR with DDM at pH 8.5, 7.5 and wild type cNOR in liposomes at pH 7.5 (Tris buffer).

Upon the addition of lipids strong bands at 1743 cm^{-1} and 1709 cm^{-1} originating from lipids C=O stretching were observed [22, 23]. The bands at 1551 cm^{-1} and at 1402 cm^{-1} originate from the NH_3^+ symmetric bending and $N^+(CH_3)_3$ anti-symmetric bending of lipids respectively [22, 23]. Since both amide II and NH_3^+ symmetric bending has negative signal in the same region a dominant band at 1551 $cm^{-1}$was observed. Lipids alone do not have differential spectra since they do not undergo structural changes during reduction and oxidation. Thus, these assignments of lipids could be related with the orientation changes of the lipids during the reduction and oxidation of cNOR. Due to these strong contributions of lipids the signals of heme propionates and amino acid side chains were not clearly observed, thus it was hard to make comments about the effect of pH on the sample with liposome.

In order to investigate the electrochemical properties of wt cNOR with DDM and in liposome potentiometric titrations were performed. pH 7.5 was chosen since it was the most stable pH value during the FTIR difference spectroscopy analysis.

Potentiometric titrations were analyzed by dividing the applied potentials into steps in order to observe each contribution of hemes separately and to visualize the shifts in the mid-point potentials. Mid-point potential of heme b_3 was expected to be between -300 and -100 mV, heme *c* between -100 and + 150 mV and heme *b* between +150 and +250 mV according to the wt cNOR measurements (see table 4.4). From the titration of Soret band of wt cNOR inside liposomes the contribution of all hemes were observed together thus the titration was divided into three steps to observe the contribution of each cofactor separately (Figure 4.34). Instead of the extremely negative mid-point potential of heme b_3, an extra contribution was obtained between 0 mV and + 100 mV (precise value was later obtained from the Gaussian analysis as +65 mV). This contribution could be attributed to the positively shifted heme b_3 contribution or the slightly negatively shifted heme *c* contribution. The “un-assigned” contribution was observed from the Soret band of the sample in liposomes and can be easily differentiated by comparing with the same performed steps for the cNOR with DDM (Figure 4.35A).

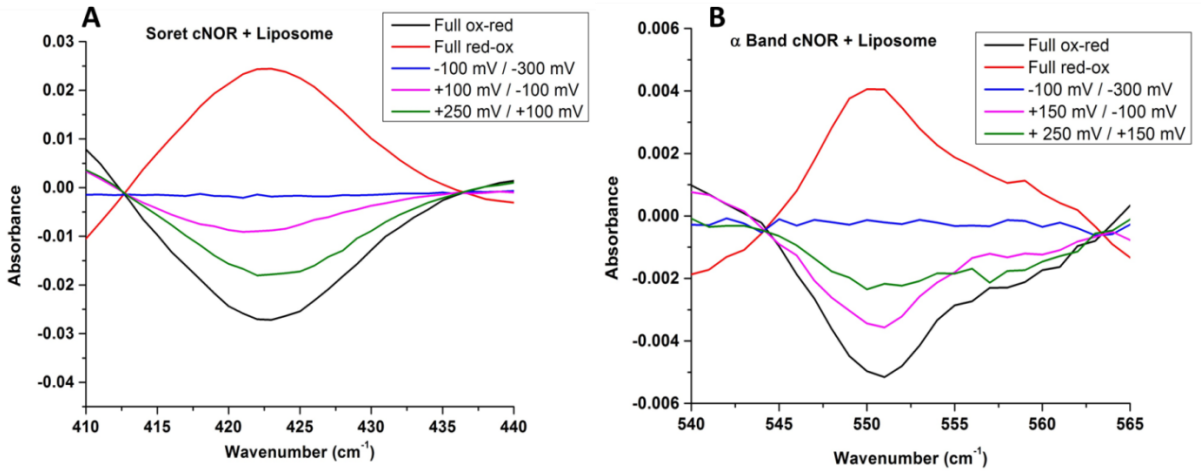

Figure 4.34 Investigation of the potentiometric titration of cNOR in liposome by steps, A) Soret band B) alpha band at pH 7.5.

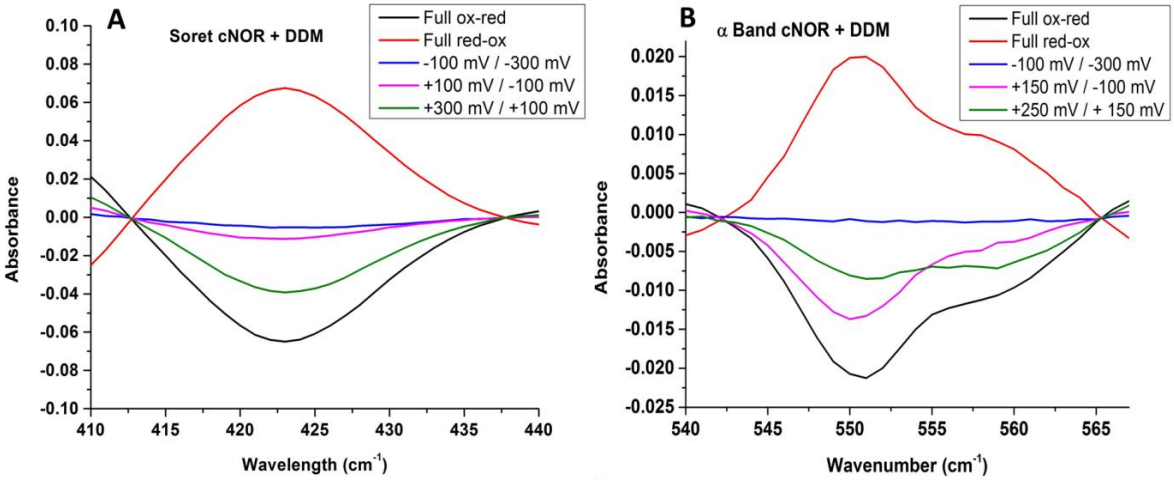

Figure 4.35 Investigation of the potentiometric titration of cNOR with DDM (2nd batch) by steps, A) Soret band B) alpha band at pH 7.5.

Comparison of figure 4.34 B and figure 4.35 B showed similar patterns for each potential interval. The "un-assigned" contribution was not observed in the alpha band step investigations. Both titrations did not show any heme b_3 contribution.

Gaussian fitting was applied to the first derivatives of the absorbance values of wt cNOR with DDM and in liposome.

The Gaussian fitting of the Soret band and the alpha band of wild type cNOR in liposome is shown in appendix figure 14 and figure 15, respectively. From the Soret band two contributions were obtained (+ 65 mV and + 145 mV). As it was described previously the signal at + 65 mV could be the negatively shifted heme *c* or positively shifted heme b_3

contribution. However since this contribution was not observed in the 551 nm band it is not possible to attribute it to heme *c* contribution. The contribution at +145 mV can be assigned to both hemes *c* and *b* together. From 551 nm band the mid-point potential of heme *c* was measured at + 103 mV and from 558 nm band heme *b* contribution as + 167 mV.

For the cNOR with DDM three pH values were chosen (6.5, 7.5 and 8.5) in order to see the effect of pH on the mid-point potentials of hemes. The samples were stable at pH 7.5 and 8.5 however; it was not possible to obtain reproducible spectra at pH 6.5. The Gaussian fitting of the Soret band and the alpha band of wild-type cNOR (2^{nd} batch) at pH 7.5 is shown in appendix figure 16 and 17. In table 4.7 a summary of measured mid-point potentials from the potentiometric titrations of wild-type cNOR in liposome at pH 7.5 and wt cNOR with DDM at pH 7.5 and 8.5 is shown.

As a brief reminder, from the titration of wild-type cNOR (2^{nd} batch) with DDM at pH 7.5 a single contribution was measured in the Soret band and it was de-convoluted. From the de-convolution two contributions with mid-point potentials of + 90 mV (heme *c*) and + 160 mV (heme *b*) were obtained. From the 551 nm the mid-point potential of heme *c* was measured at + 97 mV and from the 558 nm band heme *b* at + 178 mV.

In appendix figure 18 and 19 the potentiometric titration of the Soret band and alpha band of wt NOR with DDM at pH 8.5 is shown. From the Soret band a single large contribution was obtained with a mid-point potential of +101 mV. This single large contribution was originating from hemes *c* and *b* contribution together. From the alpha band the mid-point potential of heme *c* was measured at + 92 mV (551 nm) and heme *b* at + 172 mV (558 nm). These values were in accordance with the mid-point potentials obtained from the titration of wt cNOR with DDM at pH 7.5 (Table 4.4).

Table 4.7 Summary of redox potentials obtained from the potentiometric titrations of cNOR inside liposome at pH 7.5 and cNOR with DDM at pH 7.5 and 8.5.

	cNOR + Liposome pH 7.5			cNOR + DDM pH 7.5			cNOR + DDM pH 8.5		
	Soret band (mV)	Alpha band (551 nm) (mV)	Alpha band (558 nm) (mV)	Soret band (mV)	Alpha band (551 nm) (mV)	Alpha band (558 nm) (mV)	Soret band (mV)	Alpha band (551 nm) (mV)	Alpha band (558 nm) (mV)
heme *c*	65	103	85	90	97	101	101	92	98
heme *b*	145		167	160		178			172

We can conclude that cNOR was stable in liposomes. However, from the FTIR difference spectra we observed a strong contribution of lipids originating from the liposomes. The strong signals of lipids were dominating the protein signals and it was not possible to make detailed assignments for signals obtained with cNOR in liposome. cNOR was stable in pH 7.5 and 8.5 however, it was not possible to obtain a reproducible spectrum at pH 6.5.

Similar redox potentials were obtained for the samples at pH 7.5 and 8.5. From the titration of cNOR in liposome at pH 7.5, an "un-assigned" contribution was obtained at + 65 mV. This contribution may be assigned to negatively shifted heme *c* or positively shifted heme b_3.The major handicap was the absence of heme b_3 contribution. Normally the heme b_3 contribution should be visible in both Soret and alpha bands with an extremely negative potential. This absence could be due to a problem at the purification process of the 2nd batch of cNOR samples.

4.2.3 Investigation of site-directed mutants of the Ca^{2+} binding site of cNOR from *P. denitrificans*

Our final focus was on the Ca^{2+} ligation and the region around the heme b_3 propionates of cNOR in order to determine possible proton donors in the area of interest. Ca^{2+} bridges propionates of hemes *b* and b_3 in order to stabilize these two hemes. It is expected that a proton donor should be in this region [24-28]. When the crystal structure was resolved it was shown that Tyr-73 and Glu-135 (*Ps. aeruginosa* numbering) were ligands of Ca^{2+} (Figure 4.36) [29, 30]. For this purpose we worked with wild type cNOR and the site-directed mutants of the corresponding residues in *P. denitrificans*, E122A, Y74F and

Y74S [26]. The effect of mutations on the activity and general structure of protein was studied by FTIR difference spectroscopy and potentiometric titrations. Investigation of this area of cNOR could provide further information about the evolutionary link with the oxygen-reducing heme-copper oxidases [28, 31].

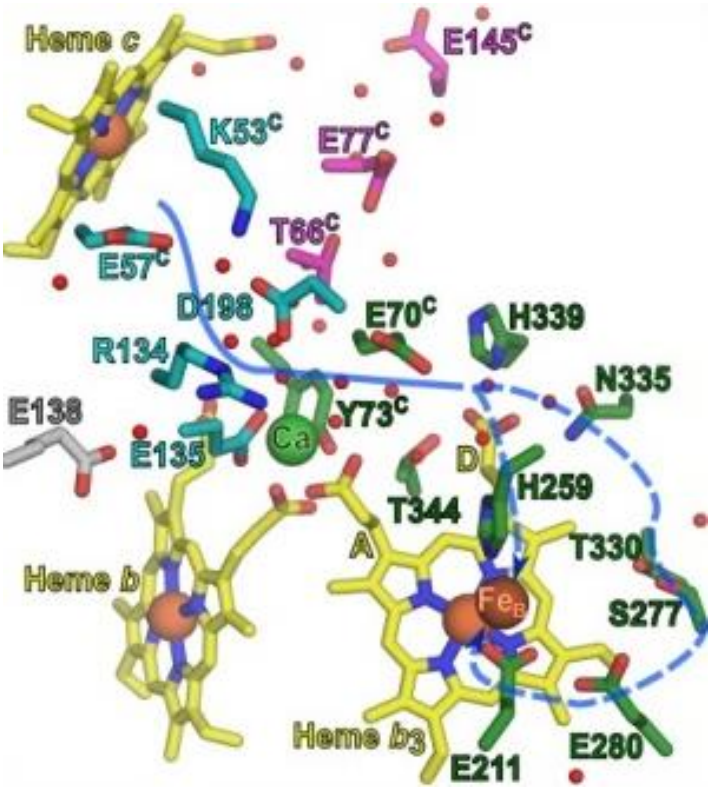

Figure 4.36 Suggested proton pathway for the wild type cNOR from *P. aeruginosa* [28].

Firstly, FTIR difference spectra of wt cNOR and E122A, Y74F and Y74S mutants were measured at pH 7.5 (Figure 4.37). Detailed band assignments for the wild type cNOR were made in section 4.2.1. As a brief reminder, the positive band at 1741 cm^{-1} and the negative band at 1725 cm^{-1} can be attributed to protonated glutamic acid residues. The bands at 1519 cm^{-1}, 1245 cm^{-1} and 1237 cm^{-1} can be respectively attributed to the (CC), (CH) and (C-O), (C-C) modes of Tyr-OH.

E122A mutant was expected to show alterations in the C=O vibration of glutamic acid assignments at 1741 cm^{-1} and 1725 cm^{-1}. From figure 4.37 an up-shift of 7 cm^{-1} at 1732 cm^{-1} and 2 cm^{-1} up-shift at 1743 cm^{-1} were observed which can be related with the removal of an active glutamic acid residue. Since E122 was a ligand of Ca^{2+} and has a role in the proton pathway mechanism [28] it was expected to observe changes in the heme propionates. However, vibrational signals of heme propionates overlap with the signals originating from the backbone of the protein (Amide I and II bands).

A 3 cm^{-1} up-shift in the (CC) and (CH) mode of Tyrosine was observed at 1522 cm^{-1} and 3 cm^{-1} up-shift in the (C-C) modes of Tyr-OH at 1240 cm^{-1} for Y74S mutant. The same shift in the (CC) and (CH) mode with 2 cm^{-1} shift in the (C-C) mode was observed for the Y74F mutant. Since Tyrosine-74 has an active role in the conformation of hemes *b* and b_3, it was expected to see some structural changes due to the loss of this Tyrosine. Added to that, the shape of the band at 1245 cm^{-1} and 1237 cm^{-1} was changed in the Y74S and Y74F mutants (Figure 4.37).

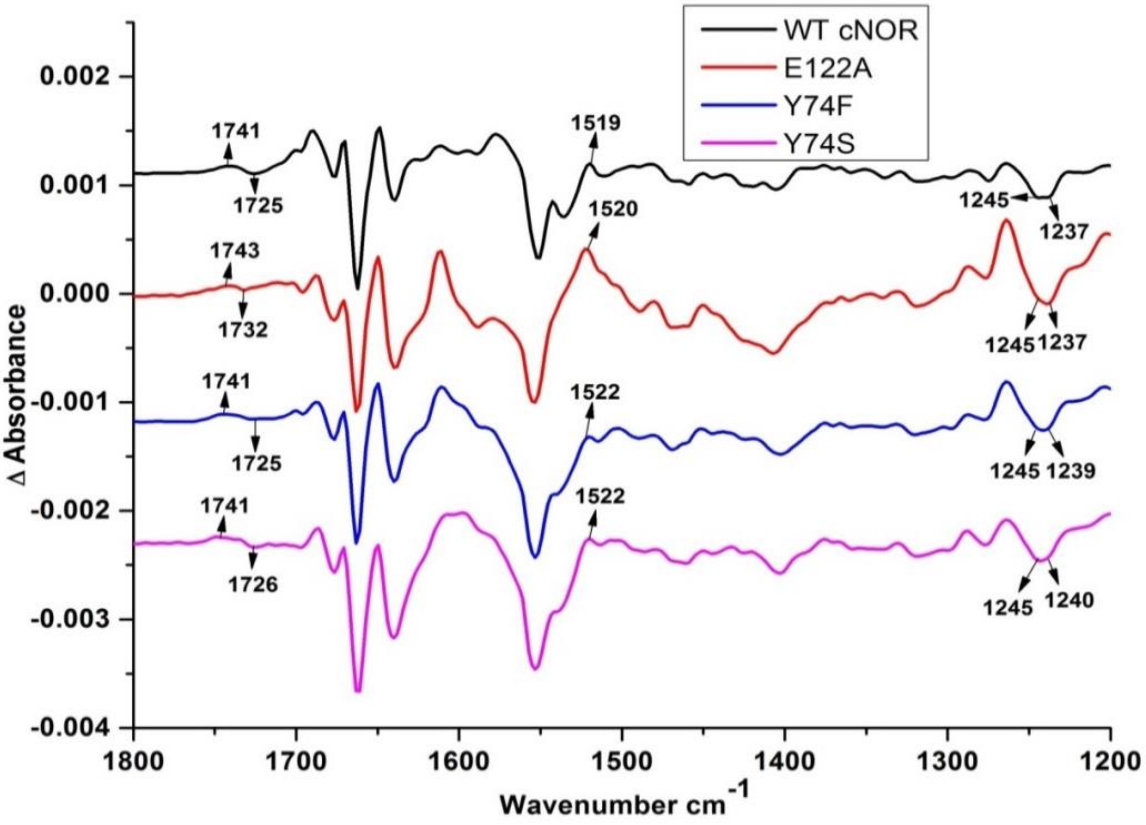

Figure 4.37 FTIR difference spectra (ox-red) of wild type cNOR and Y74F, Y74S mutants of the same enzyme at pH 7.5.

Potentiometric titrations were performed in order to study the effect of these mutations on the redox potentials of the hemes. It was described in section 1.6 that cNOR uses a single proton pathway which takes protons from the periplasmic side to be used for the NO (or O_2) reduction. It was suggested that Ca^{2+} site is responsible for maintaining the configuration of heme *b* and b_3 [30]. Due to these reasons, site directed mutations in this region could change the redox potentials of the hemes (In particular heme *b* and b_3).

The potentiometric titrations were interpreted by dividing the titration into steps in order to observe each heme contribution separately. The titrations were divided into three steps.

The – 425 mV /-150 mV step shows the extremely negative mid-point potential of heme b_3. Heme b_3 contribution was easily differentiated from its broad contribution in both Soret and alpha band. It was not possible to observe the contributions of hemes *c* and *b* separately from Soret band, however from alpha band between -150 mV /+100 mV heme *c* contribution was observed dominantly and between +100 mV/ +300 mV heme *b* contribution was observed from the shoulder of alpha band (558 nm).

The steps investigation of wild-type cNOR, E122A, Y74S and Y74F mutants were shown in appendix figures 20-23. The analysis of each step indicated that the mid-point potential of heme *b* was negatively shifted for all the mutants and the mid-point potential of heme *c* was shifted for only the Y74F mutant.

In order to determine the mid-point potentials of each heme more precisely we applied Gaussian fitting to the first derivative of the absorbance values obtained from the titrations of wt cNOR and the mutants. The Gaussian fitting of the wild-type cNOR (1^{st} batch) was shown in figure 4.30 and 4.31. Potentiometric titrations of E122A, Y74S and Y74F mutants are shown in the appendix section (Figures 24-29).

As a brief summary, for the wild type cNOR the mid-point potential of heme *c* was measured as +97 mV in the 551 nm band together with a weak signal of heme b_3 with -241 mV potential. Heme b_3 contribution was stronger at 558 nm and the mid-point potential was measured at – 253 mV. In the 558 nm band the mid-point potential of heme *b* and *c* were measured at +163 mV and +65 mV respectively.

First studied mutant was E122A and the Gaussian fitting of Soret band of this mutant at pH 7.5 is shown in appendix figure 24. From the Gaussian fitting of Soret band a single contribution was obtained which arises from hemes *c* and *b* together. It is more convenient to focus on alpha band in order to determine the mid-point potentials of hemes *c* and *b* separately. The mid-point potential of heme b_3 was measured at -290 mV. It is slightly negatively shifted as compared to the wt cNOR value (1^{st} batch, -271 mV). The Gaussian fitting of the alpha band of E122A at pH 7.5 is shown in appendix figure 25. From the 551 nm band the mid-point potential of heme *c* was measured at +91 mV. As it was shown before with steps investigation (Figure 4.39) heme *b* contribution was negatively shifted when compared to the wild-type value. From the Gaussian fitting of 558 nm band we measured the mid-point potentials of both hemes *c* (+ 98 mV) and *b* (+ 5 mV). Mid-point

potential of heme b_3 was determined from the 551 nm and 558 nm bands at -285 mV and -288 mV, respectively.

The next investigated mutant was Y74F and in Appendix figure 26 the Gaussian fitting of the Soret band of Y74F at pH 7.5 is shown. From the Soret band a single contribution was measured at +50 mV which arise from hemes *c* and *b* together. Heme b_3 contribution was easily separated in Soret band and the mid-point potential was measured at – 295 mV. The heme b_3 contribution is slightly negatively shifted as compared to the wt value (1st batch, -271 mV). The Gaussian fitting of the alpha band of Y74F at pH 7.5 is shown in Appendix figure 27. Similar fittings were obtained for both 551 nm and 558 nm bands and it shows that mid-point potentials of heme *c* and *b* are very close to each other. Investigation of Y74F by steps showed us that heme *c* had a slightly more negative potential than heme *b* (Appendix figure 21). With respect to that information, from the 551 nm band the mid-point potential of heme *c* was measured at + 50 mV and from the 558 nm band, the mid-point potential of heme *b* at + 40 mV. These values showed that the mid-point potentials of heme *c* and *b* were negatively shifted for Y74F mutant. Heme b_3 contribution was observed both in 551 nm (- 295 mV) and 558 nm (-260 mV) bands and in Soret band (-295 mV). These values show that the redox potential of heme b_3 was slightly negatively shifted when compared to the wt cNOR value (1st batch, -271 mV).

The last studied mutant was Y74S and the Gaussian fitting of Soret band of this mutant at pH 7.5 is shown in appendix figure 28. In Soret band a single contribution was obtained at around +100 mV which arises from heme *c* and *b* together. Mid-point potential of heme b_3 was measured at -300 mV which is still slightly negatively shifted when compared to the wt cNOR value (1st batch, -271 mV). The Gaussian fitting of the alpha band of Y74S at pH 7.5 is shown in appendix figure 29. From the 551 nm band the mid-point potential of heme *c* was determined at + 100 mV which is similar to the wt cNOR value (1st batch, +97 mV). From the 558 nm band a single contribution was obtained around + 95 mV and it arises due to heme *c* and *b* together. We tried to de-convolute this contribution in order to obtain the mid-point potential of heme *b*. From the steps investigation of Y74S mutant (Figure 4.41) it was determined that heme *b* had more positive mid-point potential than heme *c* similar to the wt cNOR (1st batch). According to this information the mid-point potential of heme *b* was measured at +114 mV from the de-convolution.

In table 4.8 the mid-point potentials of all hemes for wild-type cNOR (1st batch), E122A, Y74F and Y74S mutants are summarized.

Table 4.8 Summary of redox potentials obtained from the potentiometric titrations of wt cNOR, E122A, Y74F and Y74S mutants of the same enzyme at pH 7.5

	WT cNOR pH 7.5 Literature [4] (vs Ag/AgCl)	WT cNOR pH 7.5 (vs Ag/AgCl)	E122A pH 7.5 (vs Ag/AgCl)	Y74F pH 7.5 (vs Ag/AgCl)	Y74S pH 7.5 (vs Ag/AgCl)
Heme *b_3*	-177 (CTS band)	-271	-290	-295	-300
Heme *c*	+103	+97	+91	+50	+100
Heme *b*	+137	+163	+5	+40	+114

We can conclude that mutations in E122 and Y74 residues shifted the redox potential of heme *b*. As it was discussed previously in section 4.2.1 the extremely negative redox potential of heme b_3 was possibly related with the electro-negative environment provided by the glutamic acid residues close to the bi-nuclear center. The studied mutants of the Ca^{2+} binding site were not expected to contribute directly to this electro-negative environment at the catalytic center thus we did not measure major shifts in the redox potential of heme b_3 [30]. From the crystal structure it was shown that Ca^{2+} bridges propionates of hemes *b* and b_3 in order to stabilize these two hemes. This is consistent with the observed shifts for the redox potential of heme *b*. Mutation of Glu-122 into Ala did not affect the mid-point potential of heme *c* but negatively shifted the potential of heme *b*. Mutation of Tyr-74 into Phe shifted the mid-point potentials of heme *b* and *c* together. Since it was suggested that a proton donor could be close to Ca^{2+} site [28] these shifts could be related to the disturbed proton-coupled electron transfer in the protein. Protonation/de-protonation of the –OH group in Tyr may help the translocation of protons in cNOR. When mutating the Tyr into Phe, which is not possible to Protonate/deprotonate, the translocation of protons may be affected [28]. However, mutating Tyr into Ser, which is a shorter amino acid with an –OH group in its structure, did not change the mid-point

potentials of heme *c* and *b* (heme *b* was slightly negatively shifted). This could support our idea about the importance of –OH group in the proton translocation process.

References

1. Ducluzeau, A.-L., Schoepp-Cothenet, B., van Lis, R., Baymann, F., Russell, M. J., & Nitschke, W. (2014). The evolution of respiratory O2/NO reductases: an out-of-the-phylogenetic-box perspective. Journal of the Royal Society, Interface / the Royal Society, 11(98), 20140196.
2. De Vries, S., & Schröder, I. (2002). Comparison between the nitric oxide reductase family and its aerobic relatives, the cytochrome oxidases. Biochemical Society Transactions, 30(4), 662–667.
3. Cordas, C. M., Duarte, A. G., Moura, J. J. G., & Moura, I. (2013). Electrochemical behaviour of bacterial nitric oxide reductase - Evidence of low redox potential non-heme FeB gives new perspectives on the catalytic mechanism. Biochimica et Biophysica Acta - Bioenergetics, 1827(3), 233–238.
4. Butland, G., Spiro, S., Watmough, N. J., & Richardson, D. J. (2001). Two conserved glutamates in the bacterial nitric oxide reductase are essential for activity but not assembly of the enzyme. Journal of Bacteriology, 183(1), 189–199.
5. Kastrau, D. H. W., Heiss, B., Kroneck, P. M. H., and Zumft, W. G. (1994). Nitric oxide reductase from Pseudomonas stutzeri, a novel cytochrome bc complex. Phospholipid requirement, electron paramagnetic resonance and redox properties. European Journal of Biochemistry, 222(2), 293–303.
6. Hino, T., Nagano, S., Sugimoto, H., Tosha, T., & Shiro, Y. (2012). Molecular structure and function of bacterial nitric oxide reductase. Biochimica et Biophysica Acta, 1817(4), 680–7.
7. Melin, F., Xie, H., Meyer, T., Ahn, Y. O., Gennis, R. B., Michel, H., & Hellwig, P. (2016). The unusual redox properties of C-type oxidases. Biochimica et Biophysica Acta - Bioenergetics, 1857(12), 1892–1899.
8. Hellwig, P., Behr, J., Ostermeier, C., Richter, O. M. H., Pfitzner, U., Odenwald, A., Mäntele, W. (1998). Involvement of glutamic acid 278 in the redox reaction of the cytochrome c oxidase from Paracoccus denitrificans investigated by FTIR spectroscopy. Biochemistry, 37(20), 7390–7399.
9. Hellwig, P., Barquera, B., & Gennis, R. B. (2001). Direct evidence for the protonation of aspartate-75, proposed to be at a quinol binding site, upon reduction of cytochrome bo3 from Escherichia coli. Biochemistry, 40(4), 1077–1082.

10. Barth, A. and Zscherp, C. (2002) ‘What vibrations tell about proteins’, Quarterly Reviews of Biophysics, 35(4), pp. 369– 430.
11. Wolpert, M., & Hellwig, P. (2006). Infrared spectra and molar absorption coefficients of the 20 alpha amino acids in aqueous solutions in the spectral range from 1800 to 500 cm-1. Spectrochimica Acta - Part A: Molecular and Biomolecular Spectroscopy, 64(4), 987–1001.
12. Behr, J., Hellwig, P., Mäntele, W., & Michel, H. (1998). Redox dependent changes at the heme propionates in cytochrome c oxidase from Paracoccus denitrificans: Direct evidence from FTIR difference spectroscopy in combination with heme propionate 13C labeling. Biochemistry, 37(20), 7400–7406.
13. Pinakoulaki, E., & Varotsis, C. (2008). Resonance raman spectroscopy of nitric oxide reductase and cbb3 Heme-Copper oxidase. Journal of Physical Chemistry B, 112(6), 1851–1857.
14. Henry, G. D., & Sykes, B. D. (1994). Methods to study membrane protein structure in solution. Methods in Enzymology, 239(1992), 515–535.
15. Chang, Y.-C., & Bowie, J. U. (2014). Measuring membrane protein stability under native conditions. Proceedings of the National Academy of Sciences of the United States of America, 111(1), 219–24.
16. White, S. H., & Wimley, W. C. (1999). Membrane protein folding and stability: physical principles. Annual Review of Biophysics and Biomolecular Structure, 28, 319–365.
17. Tanford, C., & Reynolds, J. A. (1976). Characterization of membrane proteins in detergent solutions. Biochimica et Biophysica Acta (BBA) - Reviews on Biomembranes, 457(2), 133–170.
18. Le Maire, M., Champeil, P., & Møller, J. V. (2000). Interaction of membrane proteins and lipids with solubilizing detergents. Biochimica et Biophysica Acta - Biomembranes, 1508(1–2), 86–111.
19. Seddon, A. M., Curnow, P., & Booth, P. J (2004). Membrane proteins, lipids and detergents: Not just a soap opera. Biochimica et Biophysica Acta - Biomembranes, 1666(1–2), 105–117.
20. Wagner, M. L., & Tamm, L. K. (2000). Tethered polymer-supported planar lipid bilayers for reconstitution of integral membrane proteins: silane-polyethyleneglycol-lipid as a cushion and covalent linker. Biophys J, 79(3), 1400–1414.

21. Rigaud, J. L., Pitard, B., & Levy, D. (1995). Reconstitution of membrane proteins into liposomes: application to energy-transducing membrane proteins. BBA - Bioenergetics, 1231(3), 223–246.
22. Asher, I. M., & Levin, I. W. (1977). Effects of temperature and molecular interactions on the vibrational infrared spectra of phospholipid vesicles. Biochimica et Biophysica Acta (BBA) - Biomembranes, 468(1), 63–72.
23. Butland, G., Spiro, S., Watmough, N. J., & Richardson, D. J. (2001). Two conserved glutamates in the bacterial nitric oxide reductase are essential for activity but not assembly of the enzyme. Journal of Bacteriology, 183(1), 189–199.
24. Beek, J. Ter, Krause, N., Reimann, J., Lachmann, P., & Ädelroth, P. (2013). The nitric-oxide reductase from paracoccus denitrificans uses a single specific proton pathway. Journal of Biological Chemistry, 288(42), 30626–30635.
25. Thorndycroft, F. H., Butland, G., Richardson, D. J., & Watmough, N. J. (2007). A new assay for nitric oxide reductase reveals two conserved glutamate residues form the entrance to a proton-conducting channel in the bacterial enzyme. The Biochemical Journal, 401, 111–119.
26. Reimann, J., Flock, U., Lepp, H., Honigmann, A., & Ädelroth, P. (2007). A pathway for protons in nitric oxide reductase from Paracoccus denitrificans. Biochimica et Biophysica Acta - Bioenergetics, 1767(5), 362–373.
27. Flock, U., Thorndycroft, F. H., Matorin, A. D., Richardson, D. J., Watmough, N. J., & Ädelroth, P. (2008). Defining the proton entry point in the bacterial respiratory nitric-oxide reductase. Journal of Biological Chemistry, 283(7), 3839–3845.
28. Ter Beek, J., Krause, N., and Adelroth, P. (2016). Investigating the proton donor in the NO reductase from Paracoccus denitrificans. PLoS ONE, 11(3), 1–26.
29. Shiro, Y. (2012). Structure and function of bacterial nitric oxide reductases: Nitric oxide reductase, anaerobic enzymes. Biochimica et Biophysica Acta - Bioenergetics, 1817(10), 1907–1913.
30. Hino, T., Matsumoto, Y., Nagano, S., Sugimoto, H., Fukumori, Y., Murata, T., Shiro, Y. (2010). Structural basis of biological N_2O generation by bacterial nitric oxide reductase. Science (New York, N.Y.), 330(6011), 1666–1670.
31. Tosha, T., & Shiro, Y. (2013). Crystal structures of nitric oxide reductases provide key insights into functional conversion of respiratory enzymes. IUBMB Life, 65(3), 217–226.
32. Grönberg, K. L. C., Roldán, M. D., Prior, L., Butland, G., Cheesman, M. R., Richardson, D. J., Watmough, N. J. (1999). A low-redox potential heme in the dinuclear center of

bacterial nitric oxide reductase: Implications for the evolution of energy-conserving heme-copper oxidases. Biochemistry, 38(42), 13780–13786.

5. Conclusion

In this thesis two members of the heme-copper oxidase family were studied through different approaches. In the first part cytochrome *bo*$_3$ oxidase from *E. coli* was studied. The wild-type *bo*$_3$ was characterized by using cyclic voltammetry (CV) and FTIR difference spectroscopy. Obtained data were compared with a mutant enzyme that does not have a catalytic activity (K362M). By using potentiometric titrations we determined the redox potentials of the hemes in wild-type *bo*$_3$ oxidase. In the next step we focused on the quinone-protein interaction. In order to do that quinone free *bo*$_3$ oxidase and reconstituted *bo*$_3$ oxidase with various quinones were used. The cyclic voltammetry experiments showed that addition of Q_2 provided the highest O_2 reduction activity. We showed that the tail length has an important role in the quinone-protein interaction. Further experiments with different quinones are needed to make more specific conclusion.

In the next step the residues suggested to be in the high affinity quinone binding site (Q_H) of *bo*$_3$ oxidase was studied. From the CV measurements it was shown that the mutations in the Q101, F93, D75, H98, I102 and R71 residues reduced the O_2 reduction activity of the enzyme. For the Q101M and Q101A mutants showed wt-like O_2 reduction activity. When the Gln was replaced with a smaller amino acid (Ala) the water molecules may fill the space and quinone can bind to the protein. The mutations in the Phe-93 showed that the ring structure may be interacting with the head group of quinone and removal of it results in reduced O_2 reduction activity. From the FTIR difference spectra of mutants dramatic changes were not observed. Small shifts in the double difference spectra may indicate conformational changes in the secondary structure of the protein. However, the normalization of the IR difference spectra with respect to the quinone vibrational modes may create artificial shifts in the double difference data. Thus, it was not possible to make more detailed analysis on the structural changes.

SEIRAS was introduced as an alternative technique to study membrane proteins. From the CV measurements it was shown that the proteins on the surface react with the O_2. However, the SEIRAS difference spectrum was not obtained. Further studies are required to obtain stable SEIRAS difference spectra.

In the second part of the thesis cNOR from *P. denitrificans* was studied. Wild-type cNOR was successfully characterized by using FTIR spectroscopy and CV. In this part we worked with two batches of cNOR. By using potentiometric titrations the redox potentials of the hemes in the wild-type cNOR (Both batches) were determined. Firstly, the effect of environment on the stability of cNOR was investigated by working at different pH values (6.5, 7.5 and 8.5) and by reconstituting the enzyme in liposomes. The FTIR difference spectra showed that the samples were stable in liposomes. However, strong lipid contributions of liposomes were dominating the spectra. The cNOR samples with DDM at pH 7.5 and 8.5 were stable during FTIR and UV/Vis titration measurements. We could not manage to obtain reproducible results at pH 6.5. From the potentiometric titrations it was shown that redox potentials of the hemes were similar for the samples in liposomes and at different pH values. The main handicap we faced with the second batch of cNOR was the absence of heme b_3 contribution.

In the last part the last proton donor that transfers protons to the binuclear site of cNOR was investigated. For this purpose the mutants of the ligands of Ca^{2+} (E122A, Y74S and Y74F) was studied. The potentiometric titrations showed that mutation of Glu-122 into Ala did not affect the mid-point potential of heme *c* but negatively shifted the potential of heme *b*. Mutation of Tyr-74 into Phe shifted the mid-point potentials of heme *b* and *c* together. However Tyr-Ser change did not affect the redox potential of heme c and b dramatically. This indicates that the –OH group may have an important role in the proton translocation process.

6. Appendix

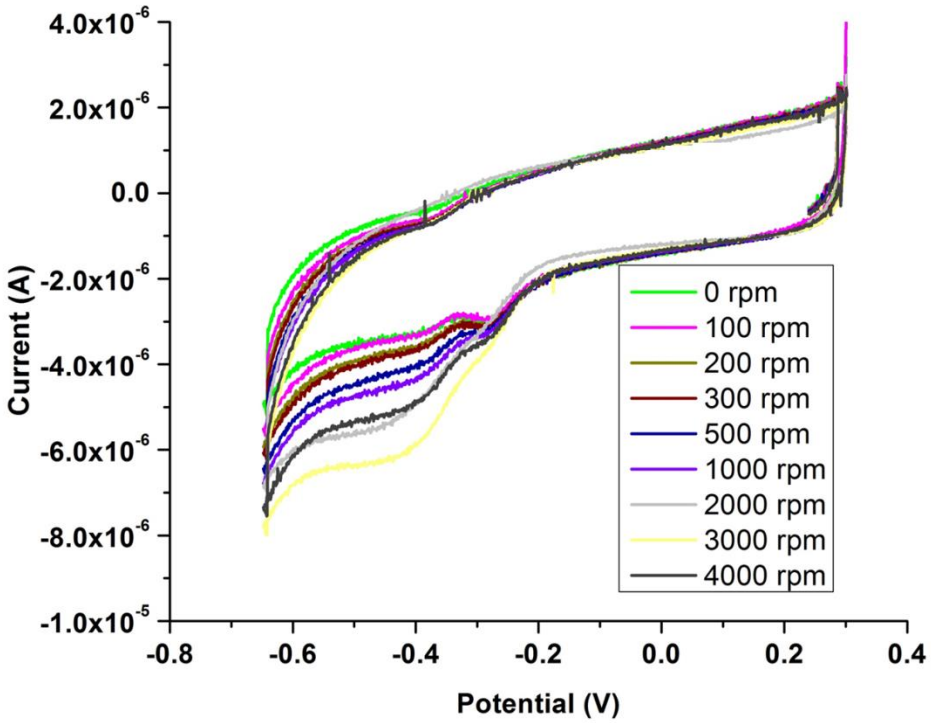

Figure 1. Cyclovoltammogram of K362M with Q_2 at pH 7.5 (Scan rate of 0.02 $V.s^{-1}$)

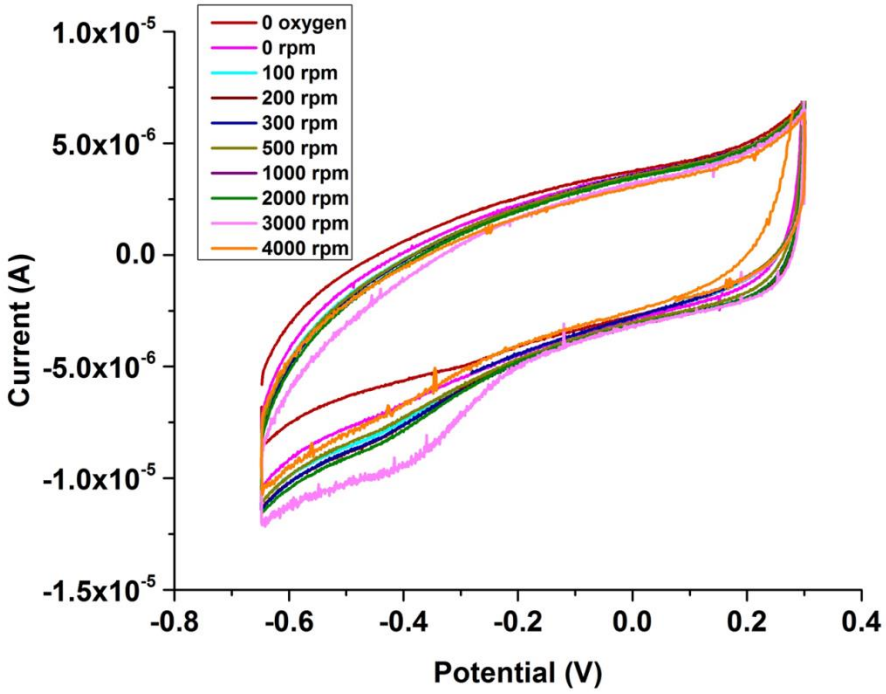

Figure 2. Cyclovoltammogram of quinone free *bo*$_3$ oxidase at pH 7.5 (Scan rate of 0.02 $V.s^{-1}$)

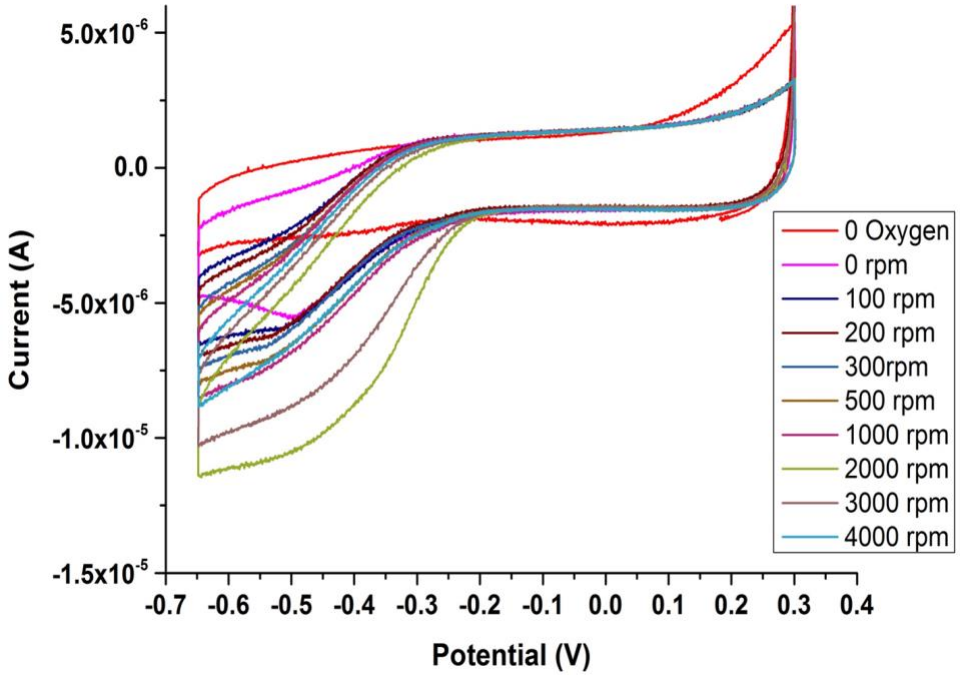

Figure 3. Cyclovoltammogram of F93Y at pH 7.5 (Scan rate of 0.02 $V.s^{-1}$)

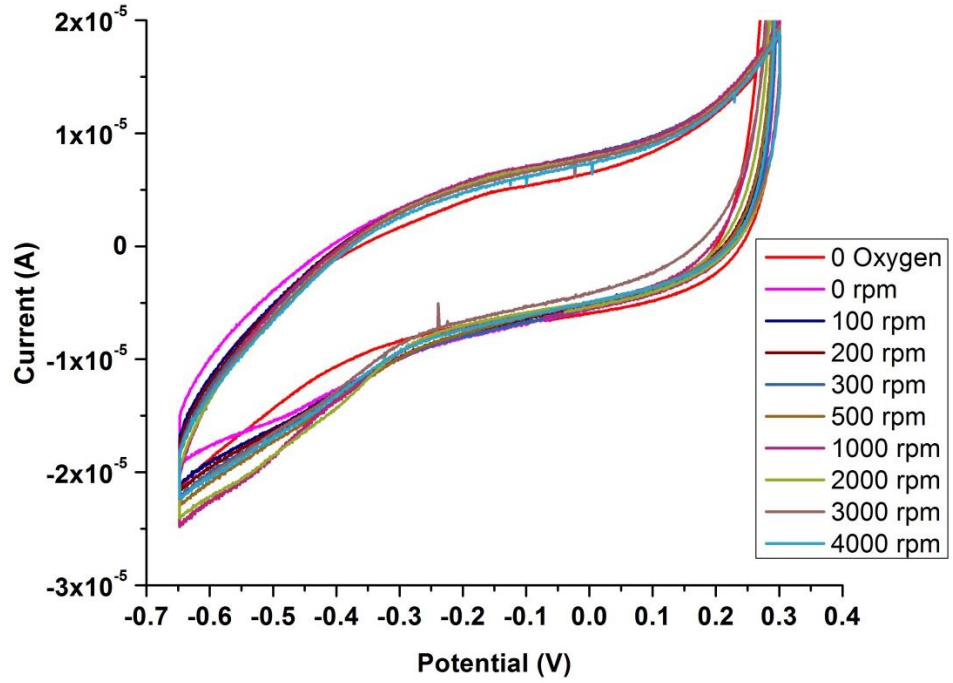

Figure 4. Cyclovoltammogram of Q101N at pH 7.5 (Scan rate of 0.02 $V.s^{-1}$)

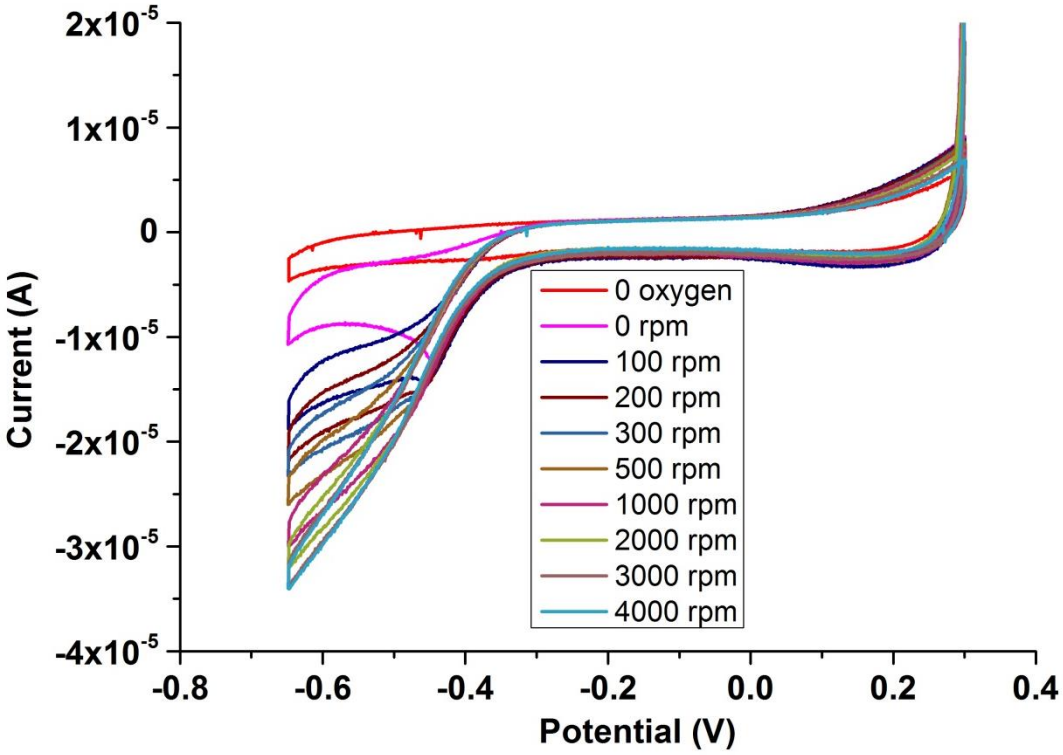

Figure 5. Cyclovoltammogram of Q101A at pH 7.5 (Scan rate of 0.02 $V.s^{-1}$)

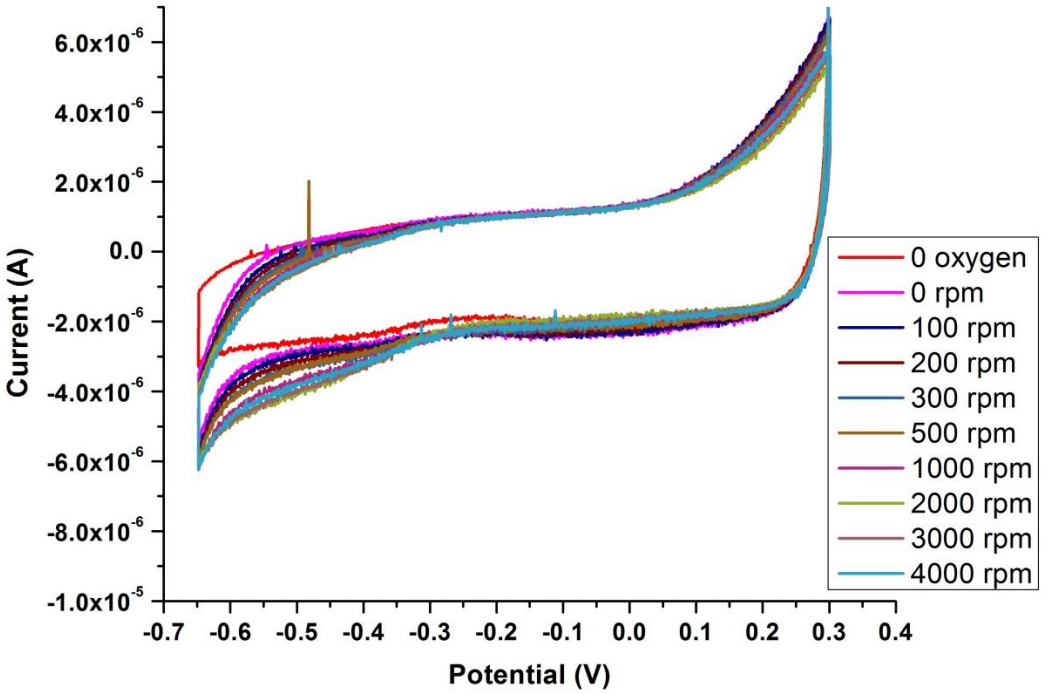

Figure 6. Cyclovoltammogram of Q101L at pH 7.5 (Scan rate of 0.02 $V.s^{-1}$)

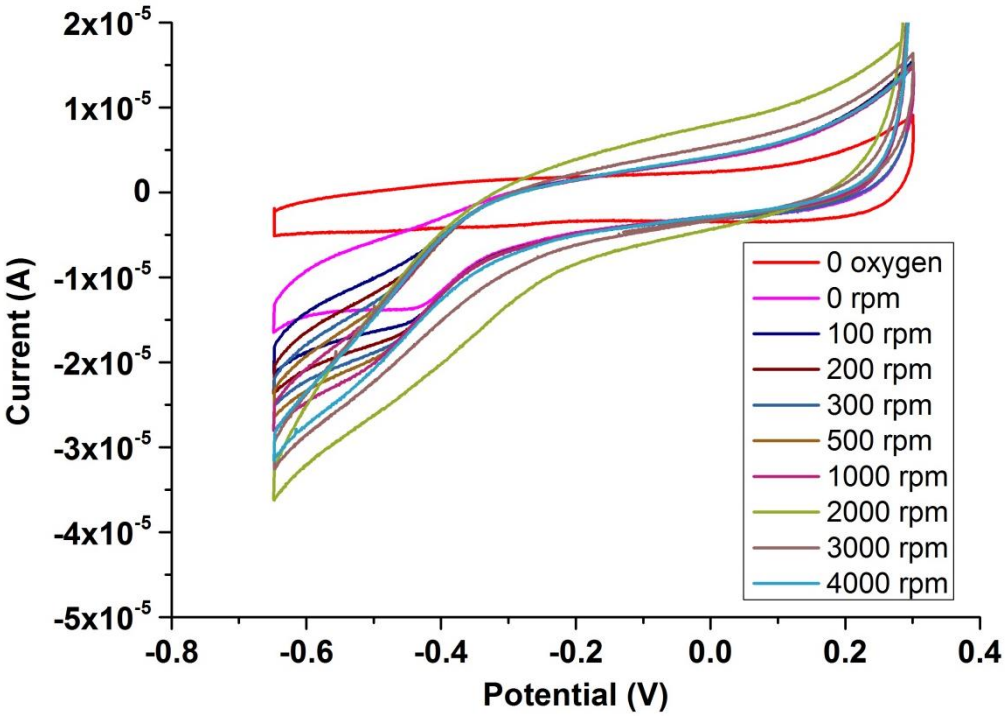

Figure 7. Cyclovoltammogram of Q101T at pH 7.5 (Scan rate of 0.02 $V.s^{-1}$)

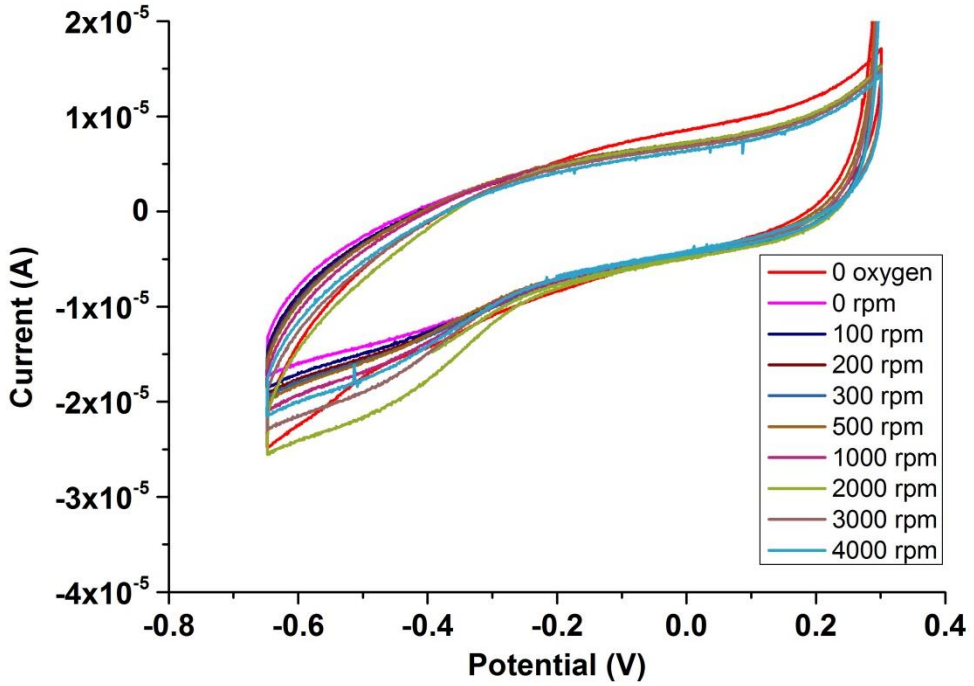

Figure 8. Cyclovoltammogram of I102N at pH 7.5 (Scan rate of 0.02 $V.s^{-1}$)

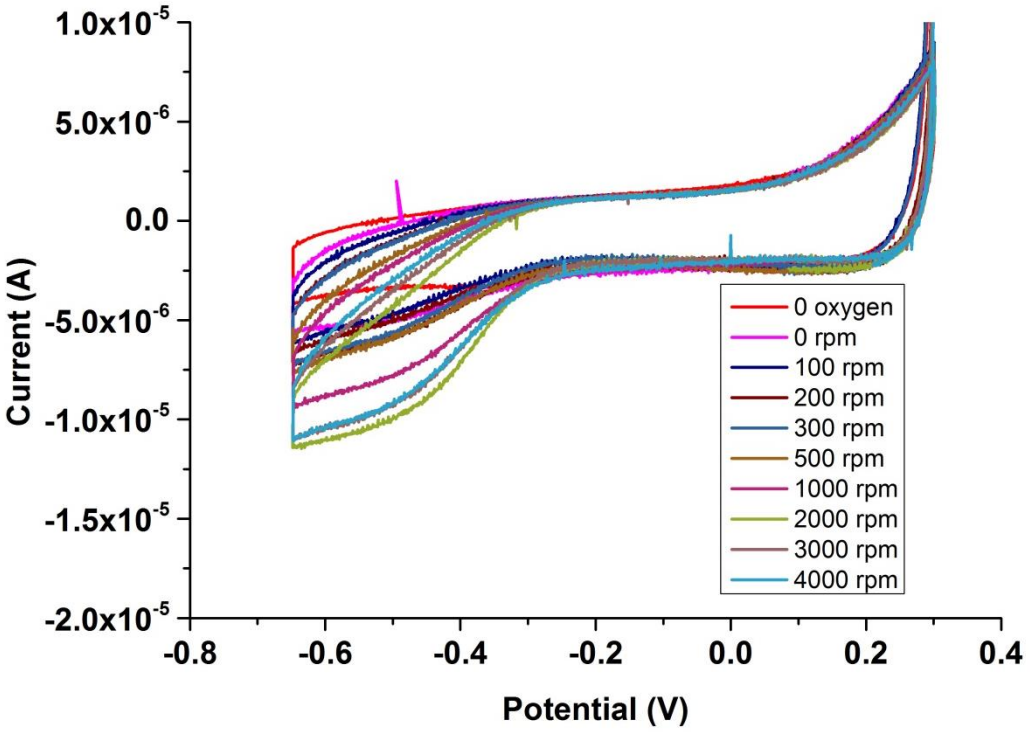

Figure 9. Cyclovoltammogram of H98F at pH 7.5 (Scan rate of 0.02 $V.s^{-1}$)

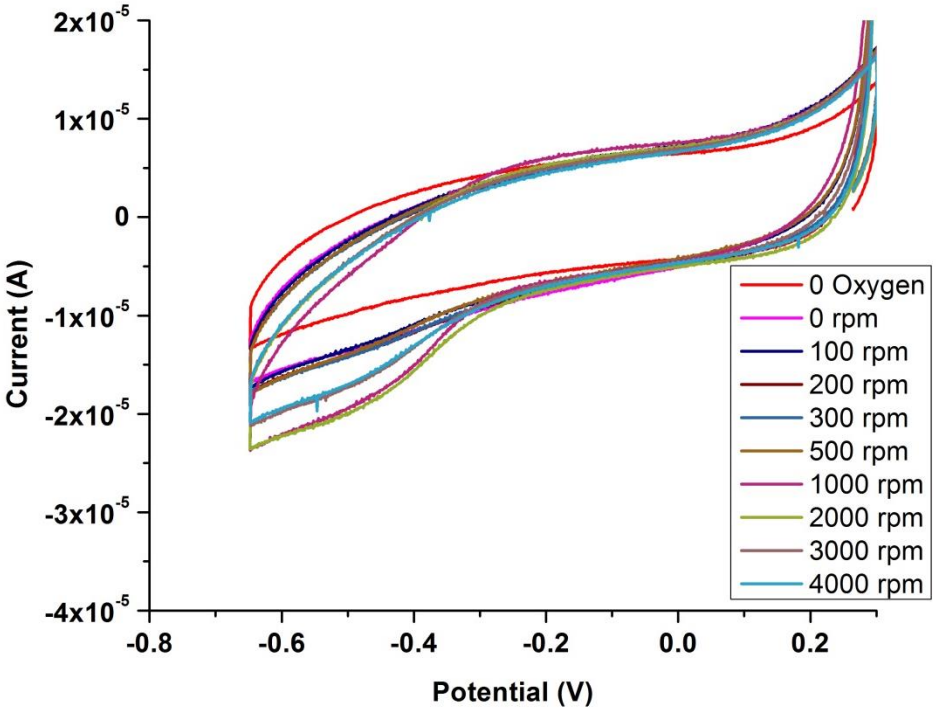

Figure 10. Cyclovoltammogram of R71H at pH 7.5 (Scan rate of 0.02 $V.s^{-1}$)

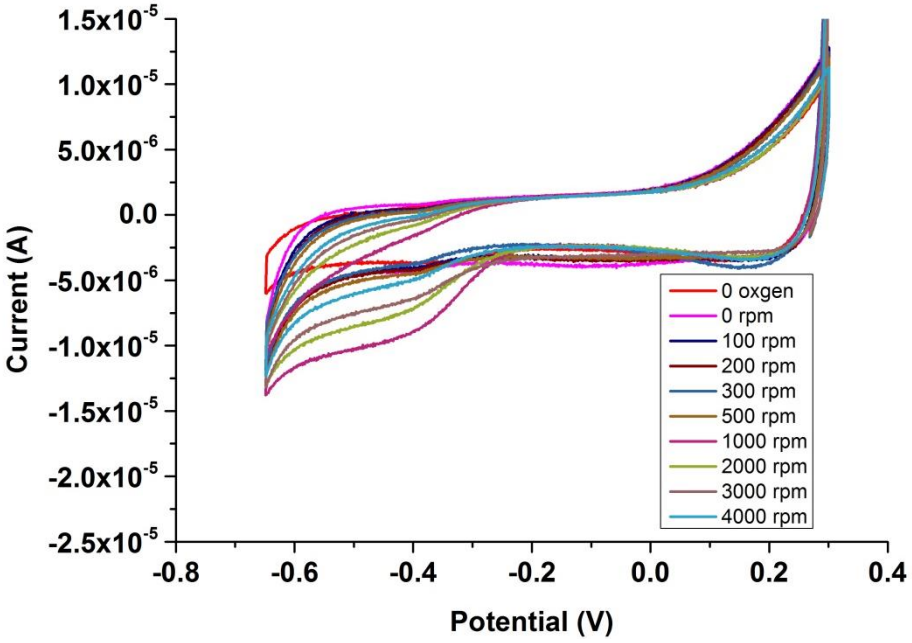

Figure 11. Cyclovoltammogram of quinone free D75N at pH 7.5 (Scan rate of 0.02 $V.s^{-1}$)

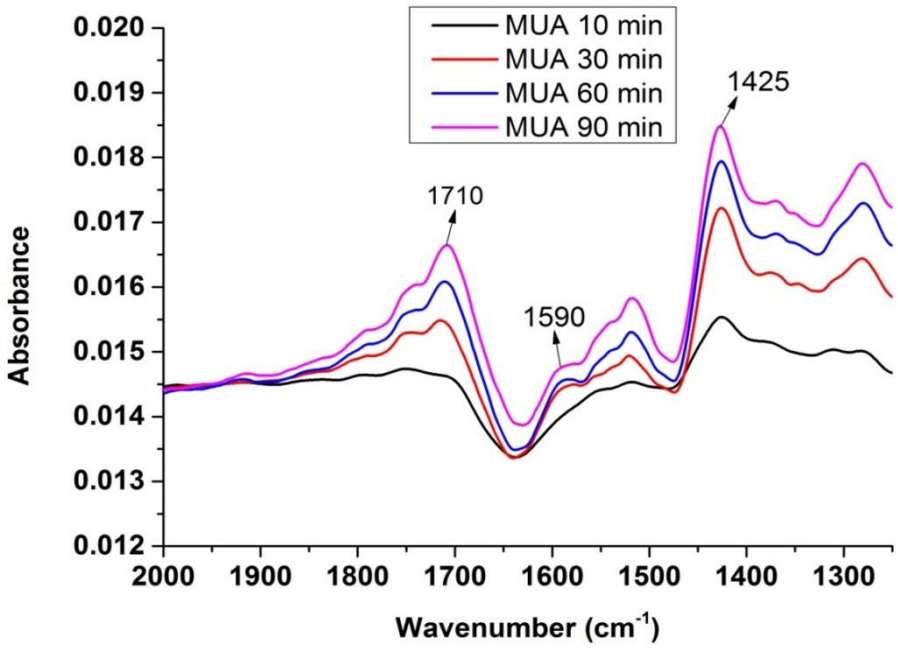

Figure 12. SEIRA spectra of MUA monolayer on the gold surface at different times after addition of MUA solution (in ethanol).

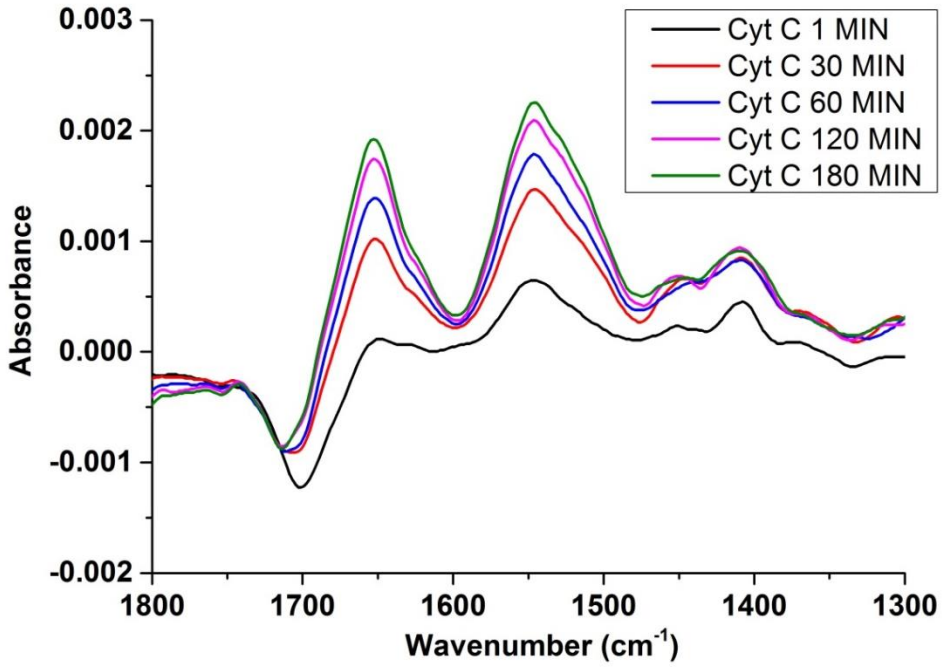

Figure 13. SEIRA spectra of cytochrome *c* adsorbed on MUA monolayer at different times after the addition of cytochrome *c* solution in 10 mM phosphate buffer at pH 7

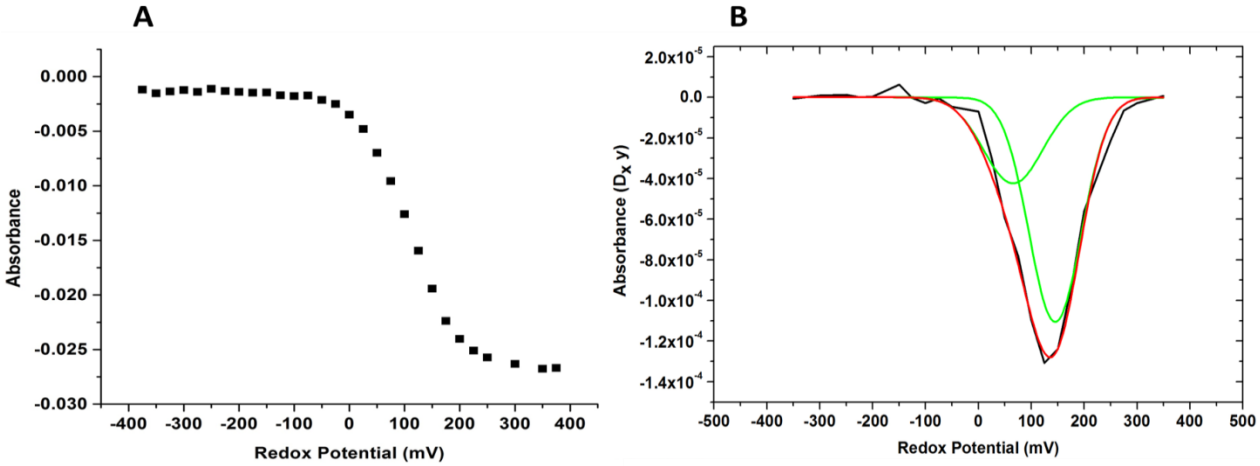

Figure 14 Potentiometric titration of wild type cNOR in liposome at pH 7.5, **A)** Absorbance values from Soret band, **B)** Gaussian fitting of the first derivative of the absorbance values from Soret band

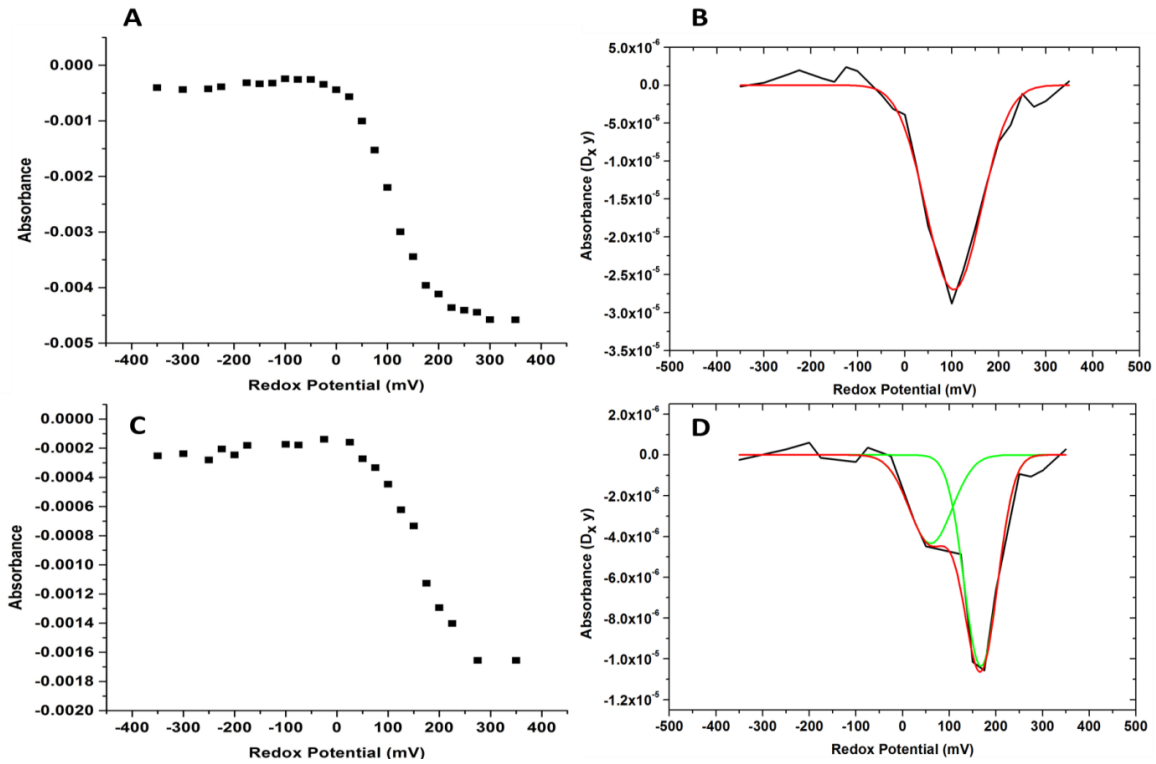

Figure 15 Potentiometric titration of wild type cNOR in liposome at pH 7.5, **A)** Absorbance values from alpha band at 551 nm, **B)** Gaussian fitting of the first derivative of the absorbance values from alpha band at 551 nm, **C)** Absorbance values from alpha band at 558 nm, **D)** Gaussian fitting of the first derivative of the absorbance values from alpha band at 558 nm

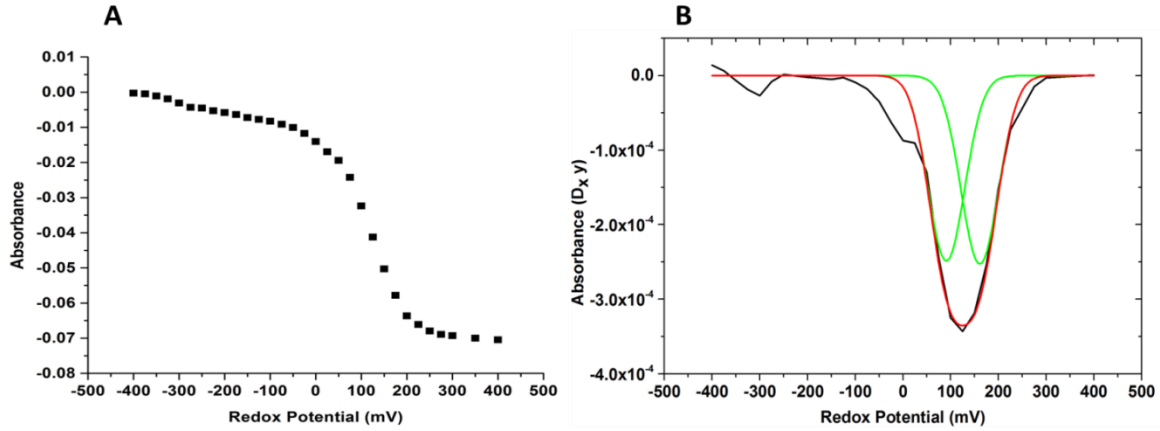

Figure 16 Potentiometric titration of wild type cNOR with DDM (2nd batch) at pH 7.5, **A)** Absorbance values from Soret band, **B)** Gaussian fitting of the first derivative of the absorbance values from Soret band

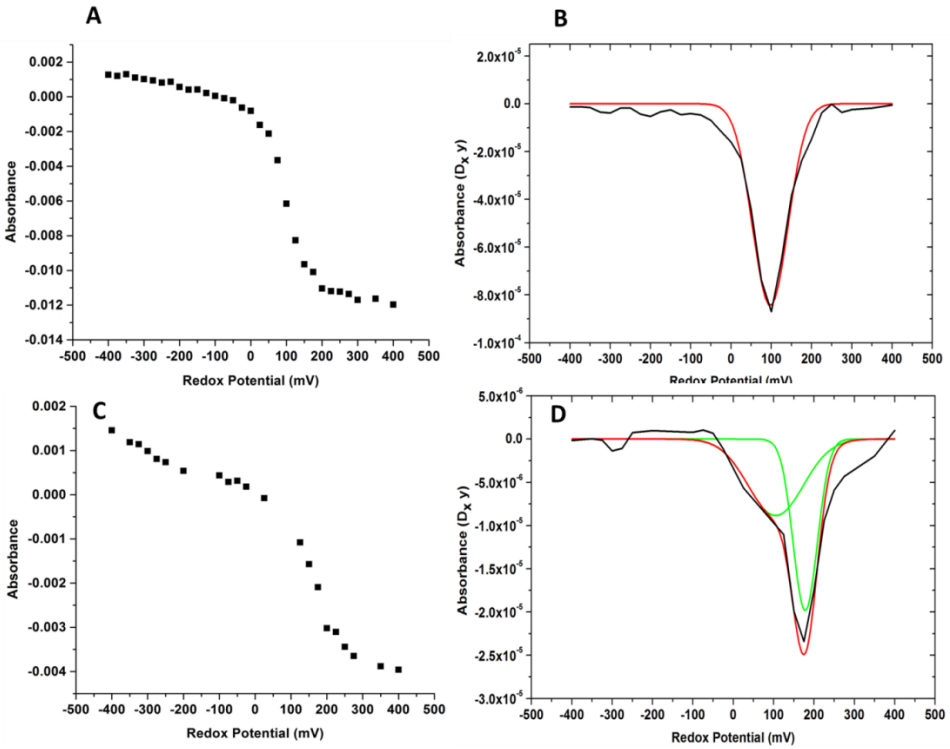

Figure 17 Potentiometric titration of wild type cNOR with DDM (2nd batch) at pH 7.5, **A)** Absorbance values from alpha band at 551 nm, **B)** Gaussian fitting of the first derivative of the absorbance values from alpha banat d 551 nm, **C)** Absorbance values from alpha band at 558 nm, **D)** Gaussian fitting of the first derivative of the absorbance values from alpha band at 558 nm

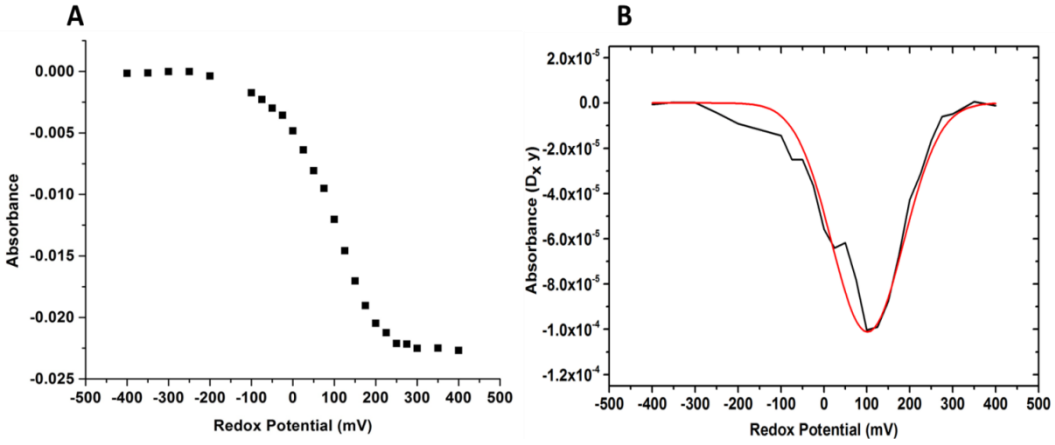

Figure 18 Potentiometric titration of wild type cNOR with DDM at pH 8.5, **A)** Absorbance values from Soret band, **B)** Gaussian fitting of the first derivative of the absorbance values from Soret band

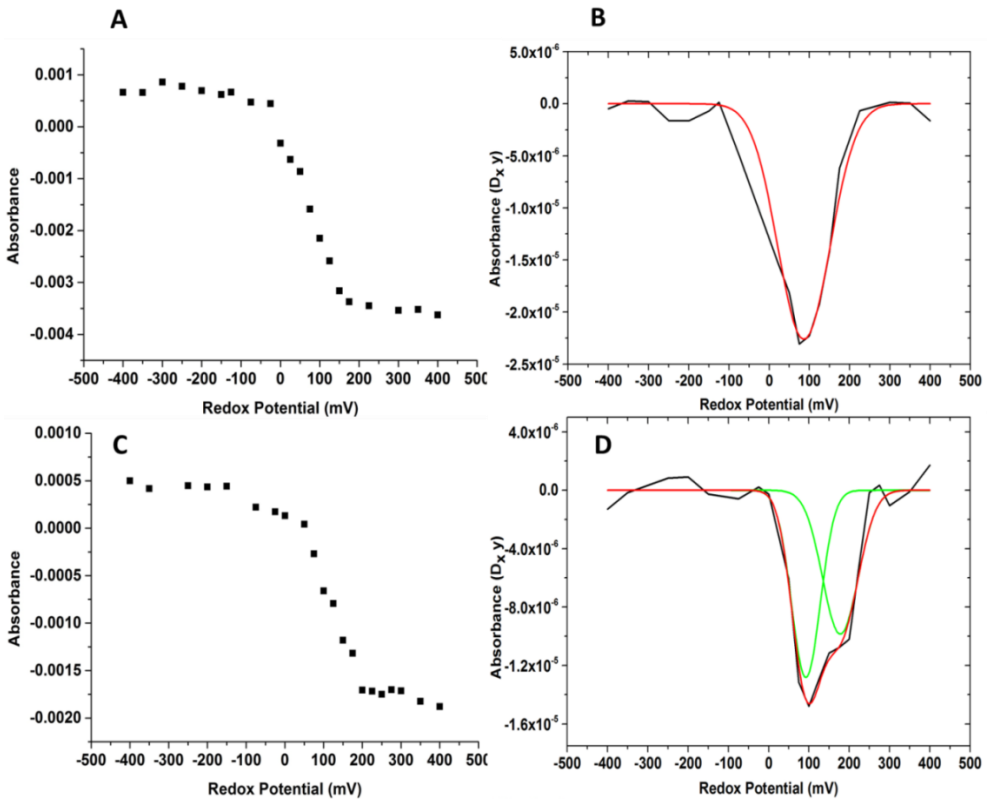

Figure 19 Potentiometric titration of wild type cNOR with DDM at pH 8.5, **A)** Absorbance values from alpha band at 551 nm, **B)** Gaussian fitting of the first derivative of the absorbance values from alpha band at 551 nm, **C)** Absorbance values from alpha band at 558 nm, **D)** Gaussian fitting of the first derivative of the absorbance values from alpha band at 558 nm

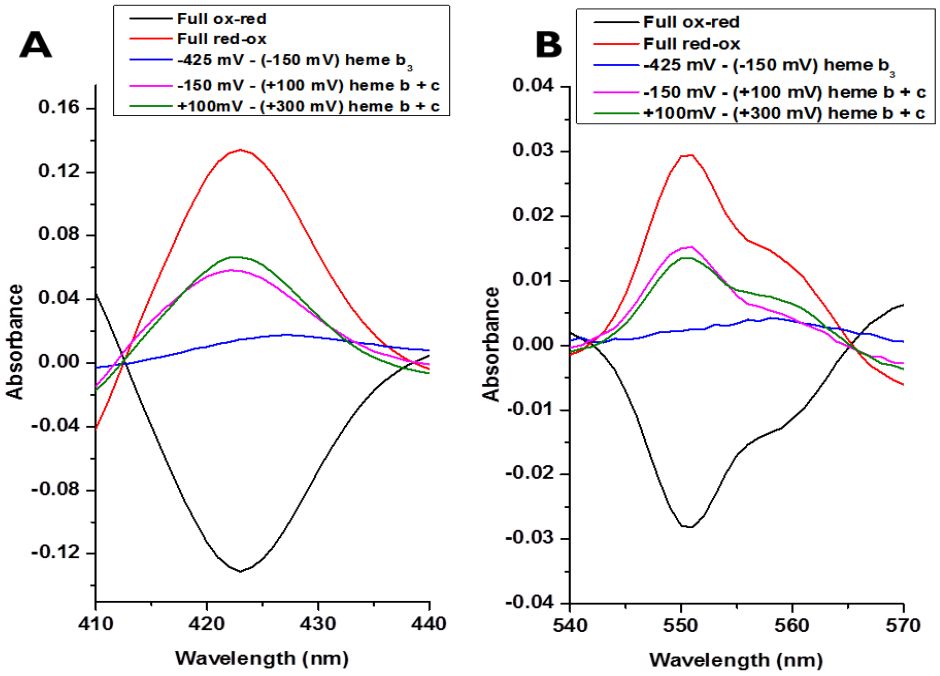

Figure 20 Investigation of the potentiometric titration of wild type cNOR (1st batch) by steps, **A)** Soret band **B)** alpha band at pH 7.5.

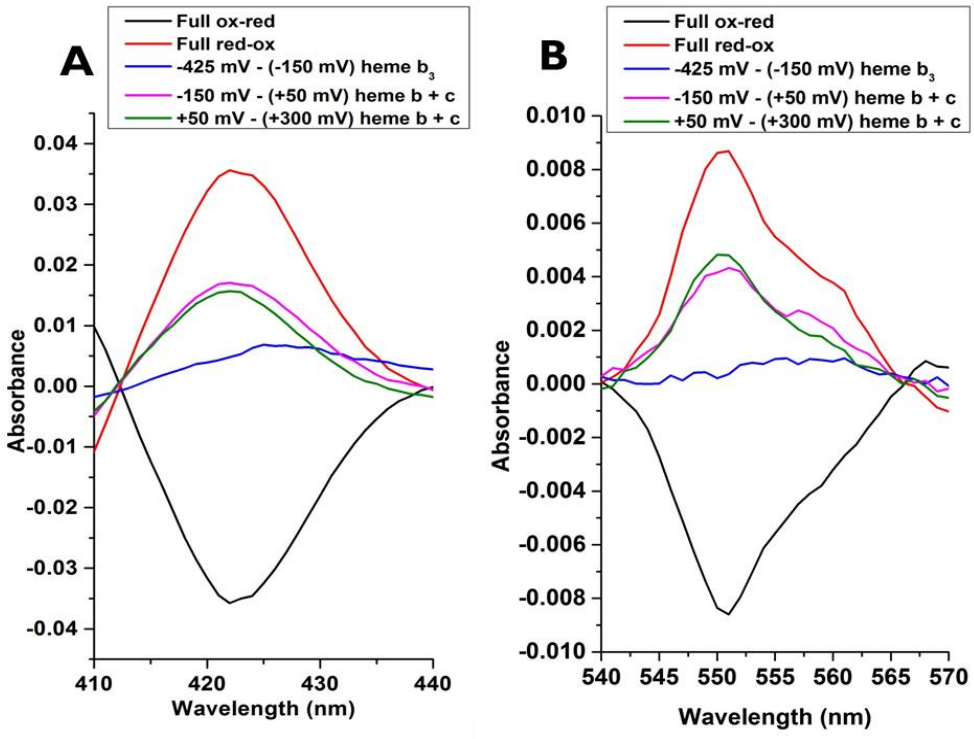

Figure 21 Investigation of the potentiometric titration of E122A mutant of cNOR by steps, **A)** Soret band **B)** alpha band at pH 7.5.

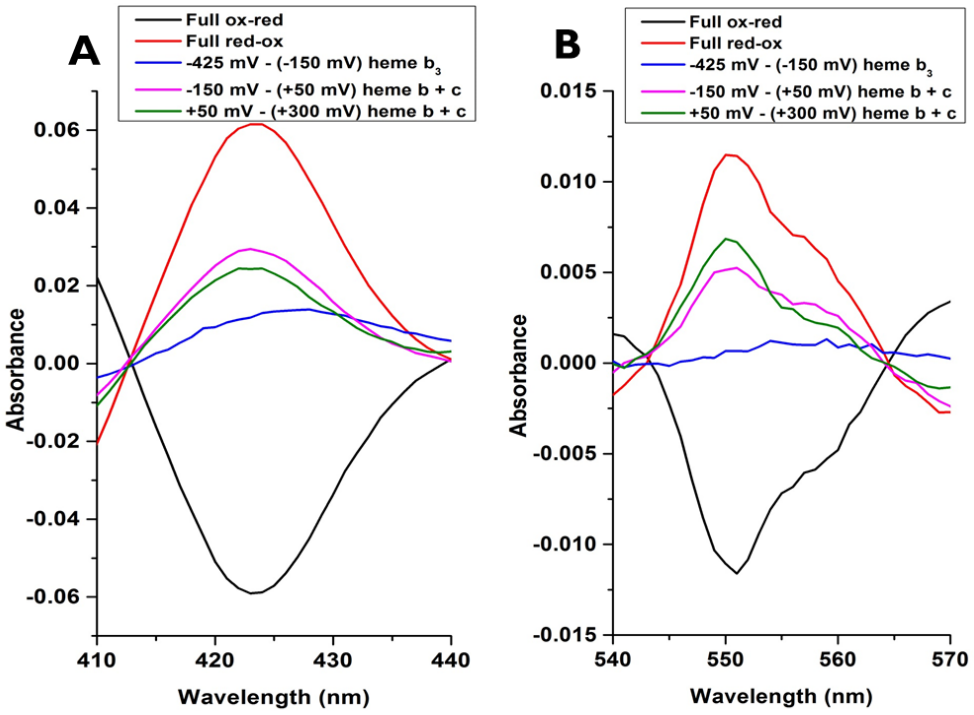

Figure 22 Investigation of the potentiometric titration of Y74F mutant of cNOR by steps, **A)** Soret band **B)** alpha band at pH 7.5.

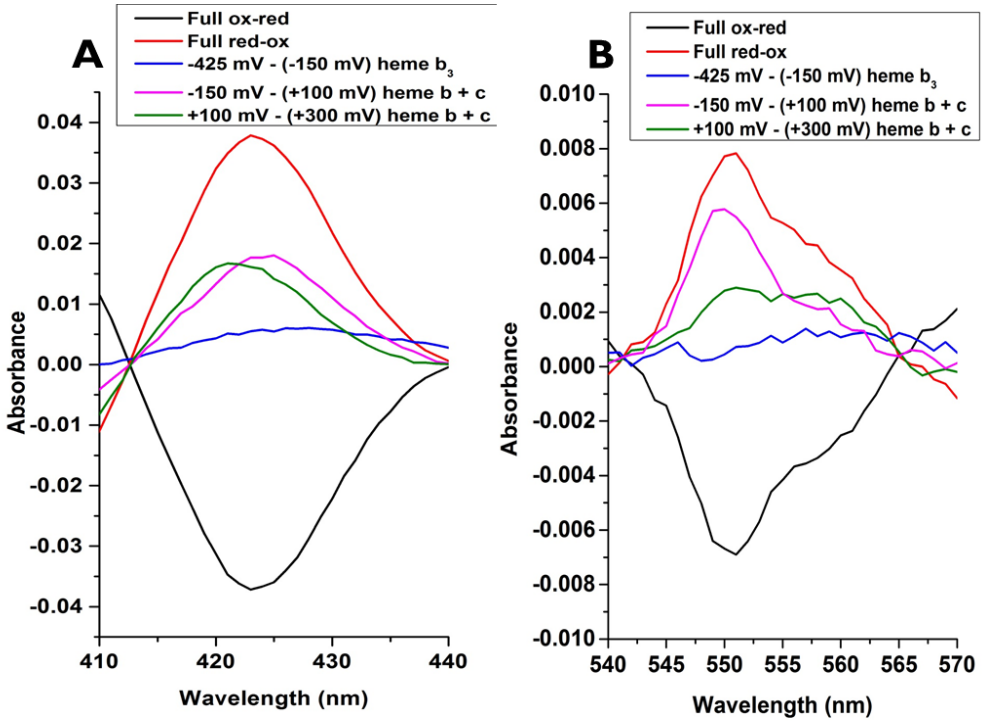

Figure 23 Investigation of the potentiometric titration of Y74S mutant of cNOR by steps, **A)** Soret band **B)** alpha band at pH 7.5

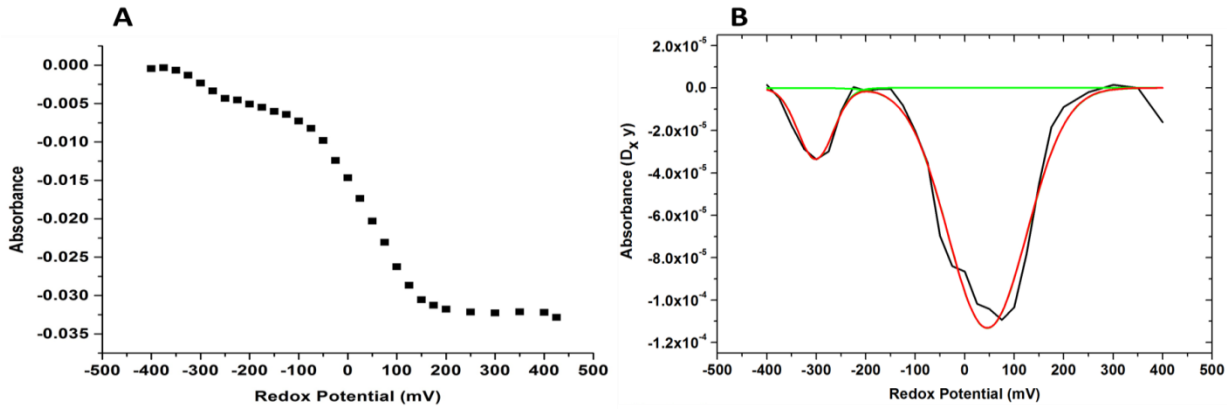

Figure 24 Potentiometric titration of E122A mutant at pH 7.5, **A)** Absorbance values from Soret band, **B)** Gaussian fitting of the first derivative of the absorbance values from Soret band

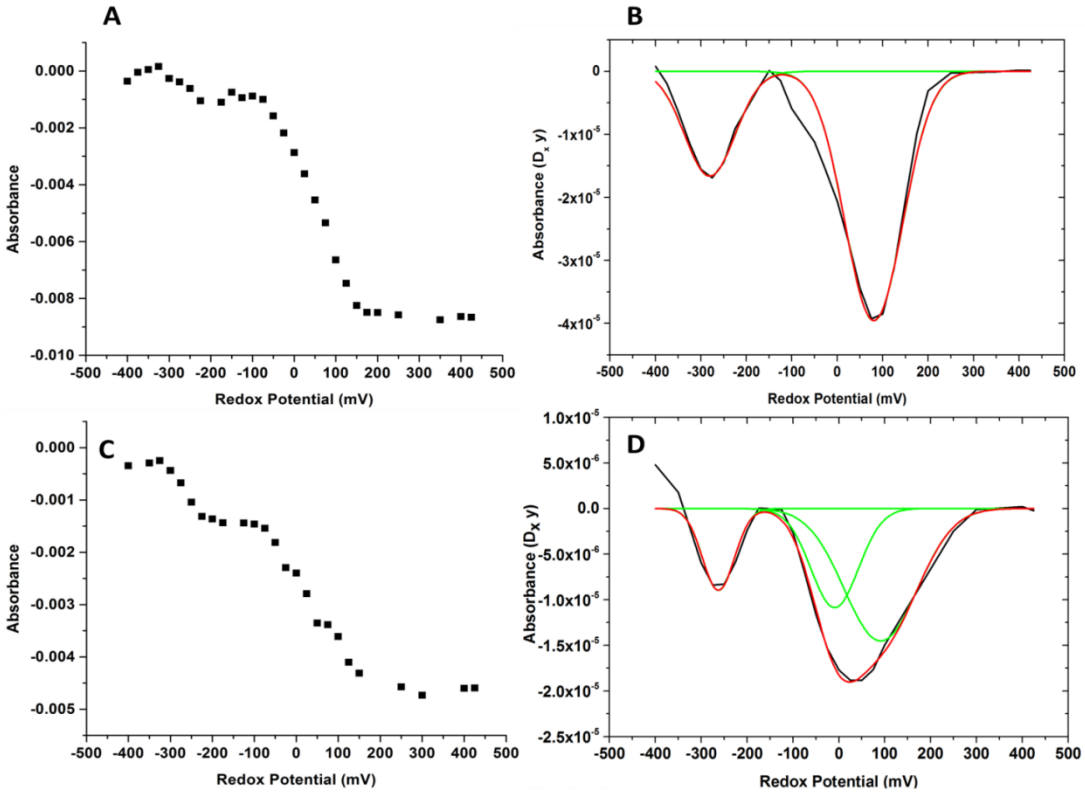

Figure 25 Potentiometric titration of wild E122A at pH 7.5, **A)** Absorbance values from alpha band at 551 nm, **B)** Gaussian fitting of the first derivative of the absorbance values from alpha band at 551 nm, **C)** Absorbance values from alpha band at 558 nm, **D)** Gaussian fitting of the first derivative of the absorbance values from alpha band at 558 nm

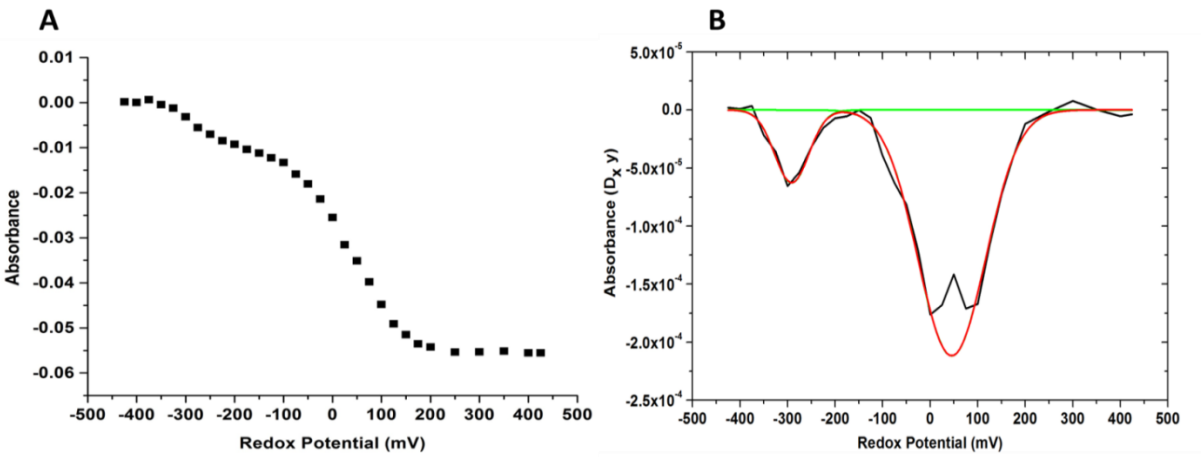

Figure 26 Potentiometric titration of Y74F mutant at pH 7.5, **A)** Absorbance values from Soret band, **B)** Gaussian fitting of the first derivative of the absorbance values from Soret band

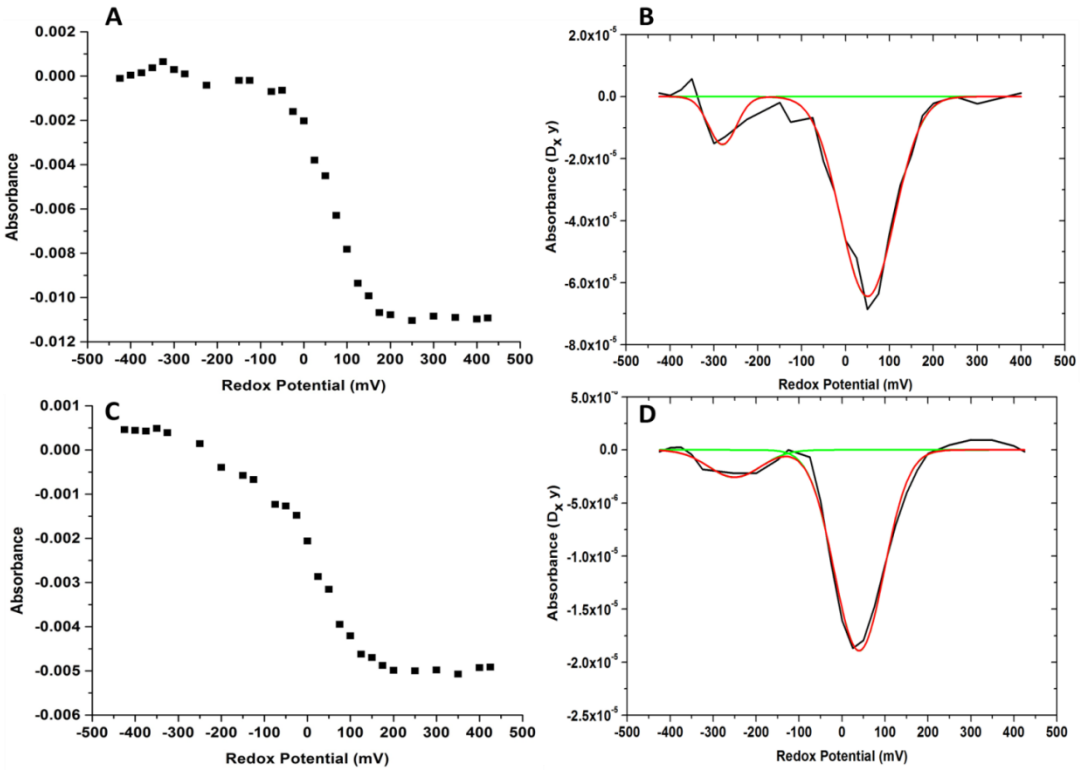

Figure 27 Potentiometric titration of Y74F at pH 7.5, **A)** Absorbance values from alpha band at 551 nm, **B)** Gaussian fitting of the first derivative of the absorbance values from alpha band at 551 nm, **C)** Absorbance values from alpha band at 558 nm, **D)** Gaussian fitting of the first derivative of the absorbance values from alpha band at 558 nm

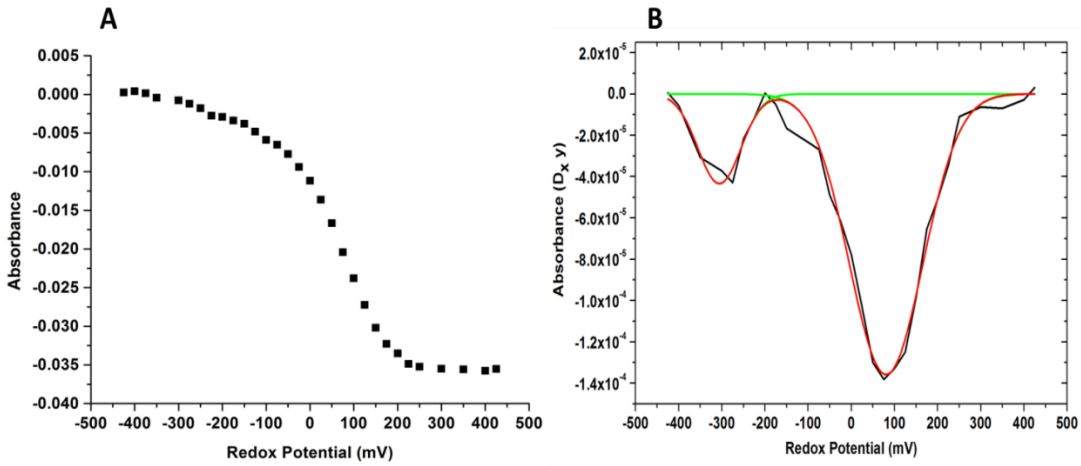

Figure 28 Potentiometric titration of Y74S mutant at pH 7.5, **A)** Absorbance values from Soret band, **B)** Gaussian fitting of the first derivative of the absorbance values from Soret band

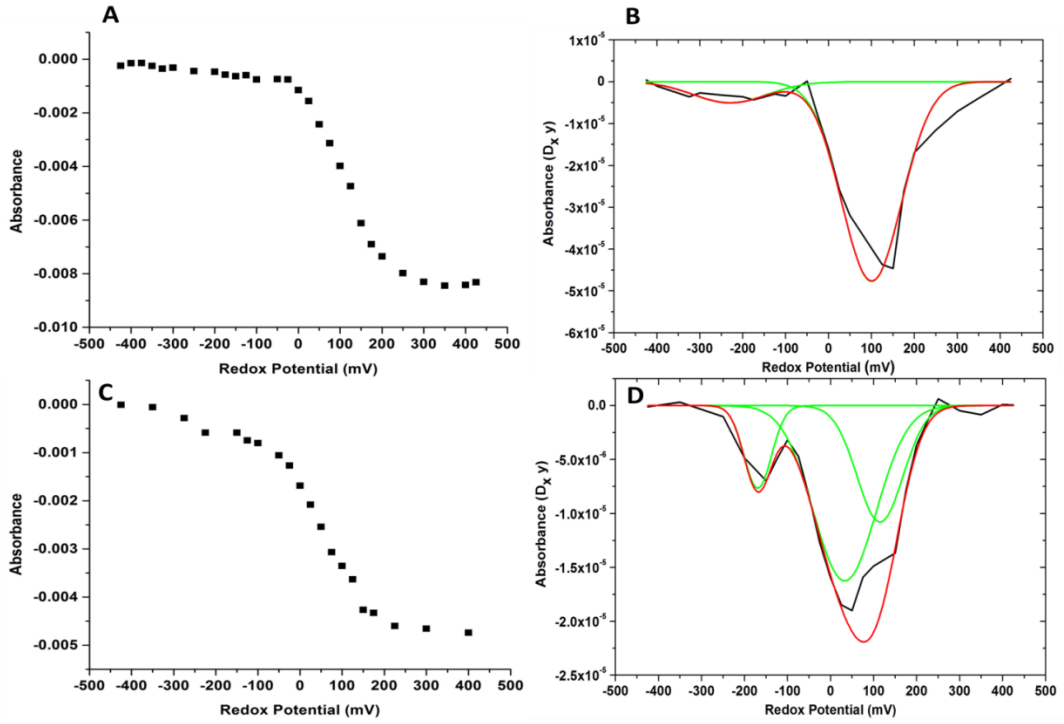

Figure 29 Potentiometric titration of wild Y74S at pH 7.5, **A)** Absorbance values from alpha band at 551 nm, **B)** Gaussian fitting of the first derivative of the absorbance values from alpha band at 551 nm, **C)** Absorbance values from alpha band at 558 nm, **D)** Gaussian fitting of the first derivative of the absorbance values from alpha band at 558 nm

Sinan Sabuncu

Investigation of enzymes from the respiratory chain by using electrochemical and spectroscopic techniques

Résumé

Le présent travail porte sur l'étude de deux protéines de la famille des oxydases à hème-fer par des techniques de spectroscopie et d'électrochimie. Le premier chapitre décrit l'étude du cytochrome *bo*$_3$ oxydase issue d'*E. coli*. Nous nous sommes intéressés à l'étude des interactions enzyme-quinone par l'utilisation de quinones avec des longueurs chaines isoprenyl différentes. Notre but est de mieux comprendre le rôle de la longueur de la chaine des quinones sur l'activité catalytique de l'enzyme et sur les propriétés redox des cofacteurs à hème. Dans l'étape suivante, on a étudié les résidues impliqués dans le site de liaison des quinones (haute affinité, Q_H). Plusieurs mutations de ces résidues sont étudiées pour mieux comprendre l'importance de chacun des résidues dans cette liaison. Dans la dernière partie de ce premier chapitre, la spectroscopie SEIRAS «spectroscopie d'absorption infrarouge exaltée de surface» est introduite comme une technique alternative pour l'étude des protéines membranaires. Dans le second chapitre, la protéine membranaire cNOR issue de *P. denitrificans* est étudiée. Nous nous sommes focalisés sur l'effet de différents environnements (pH, présence de protéo-liposomes) sur la stabilité de la cNOR. Pour ce faire, trois valeurs de pH (6.5, 7.5 et 8.5) sont choisies et quelques échantillons de cNOR sont reconstitués dans des protéo-liposomes. Enfin, le donneur de proton terminal (au centre binucléaire) dans la protéine cNOR était étudié. De plus, nous avons étudié les ligands des ions Ca^{2+} puisqu'il est proposéque le donneur de proton est situé proche de cette région.

Mots clés : spectroscopie infrarouge, électrochimie, titration potentiométrique, site de liaison de la quinone, *bo*$_3$ oxydase, cNOR.

Résumé en anglais

This thesis is focused on the study of two members of the heme-copper oxidase family by using spectroscopic and electrochemical techniques. In the first chapter cytochrome *bo*$_3$ oxidase from *E. coli* was studied. We focused on the quinone-enzyme interactions by using quinones with different isoprenyl chains. Our aim was to better understand the role of isoprenyl chain on the catalytic activity of the enzyme and the redox properties of the heme cofactors. In the next step we studied the residues that are suggested to be in the high-affinity (Q_H) quinone binding site. Several site-directed mutants of these residues were investigated in order to better understand the position of Q_H binding site and the importance of each residue. In the last part of this chapter surface-enhanced infrared absorption spectroscopy (SEIRAS) was introduced as an alternative technique to study the membrane proteins. In the second chapter cytochrome c dependent nitric oxide reducates (cNOR) from *P. denitrificans* was studied. We focused on the effect of different environment (pH, proteoliposomes) on the stability of cNOR. For that purpose three pH values (6.5, 7.5 and 8.5) was selected and some of the cNOR samples were reconstituted in liposomes. Finally, the terminal proton donor (to the binuclear center) in cNOR was investigated. We studied the ligands of the Ca^{2+} site in cNOR since it was suggested that the proton donor may be close to this area.

Keywords: Infrared spectroscopy, Electrochemistry, potentiometric titration, quinone binding site, *bo*$_3$ oxidase, cNOR